Temperature Dependence of Phonons in Elemental Cubic Metals Studied by Inelastic Scattering of Neutrons and X-Rays

Thesis by

Max G. Kresch

In Partial Fulfillment of the Requirements

for the Degree of

Doctor of Philosophy

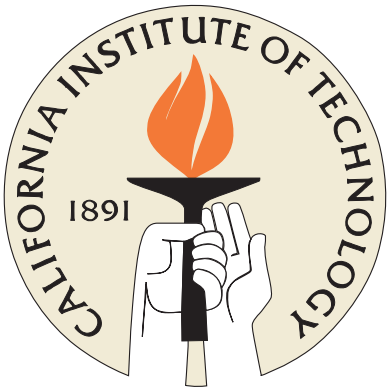

California Institute of Technology

Pasadena, California

2009

(Defended 5 December 2008)

To my wife, Agnes

Acknowledgments

Firstly, I thank my advisor, Brent Fultz. His advice was always insightful, and without his support this thesis would not exist.

Secondly, I thank my research group. They have been a constant source of answers and support. Former group members Olivier Delaire, Matt Lucas, Tabitha Swan-Wood, Alex Papandrew, Tim Kelley, and Jason Graetz have provided friendship and guidance — many of them both during and after their time at Caltech. Current group members Jiao Lin, Rebecca Stevens, Mike Winterrose, Chen Li, Hongjin Tan, Mike McKerns, Justin Purewal, Jorge Munoz, and Nick Stadie continue to make the Fultz lab a fun and fruitful place to work. Channing Ahn has always found time to lend an ear, give a recommendation, or help me find some device that would otherwise be hopelessly lost in the lab. To new and future members of the Fultz research group I wish the best of luck.

Thirdly, I thank my friends — both at Caltech and elsewhere. They have always been around to keep me sane while my work was trying to do otherwise. Near-weekly dinners with Tom and Susan Johnson, Mary Laura Lind, John McCorquodale, and Demetri Spanos have always been events to look forward to. Moreover, I thank John and Demetri for having spent many hours keeping me company, and for having made non-trivial contributions to my work. I also thank Jason Schaefer, who has always had time to listen to my complaints and then remind me of their relative unimportance. My friends have made my time at Caltech worthwhile.

Fourthly, I thank my family. Their love and support predates this work and will (I hope) persist long after its completion. My mother, my father, Klara, Mike, Anyu, Apu, and Sabba always had faith in me, and I could not have succeeded without it. In particular, my father always made time to talk to me about my work, and his questions and comments were extremely valuable.

Fifthly, I thank my wife, Agnes. For more than four years she has patiently provided support from halfway across the country. Without her love I would have never had the strength to complete this work.

Finally, I thank Spork. His affectionate moments have far exceeded his bitey ones.

Financial support for this thesis was provided by the United States Department of Energy and by the National Science Foundation.

Abstract

This thesis explores the temperature dependence of phonons in the cubic transition and nearly free electron metals through both experiment and simulation. Particular attention is paid to the entropic contributions of the phonons, and to their increased linewidths at high temperatures.

Measurements of the inelastic scattering of neutrons from face-centered-cubic (FCC) aluminum, lead, and nickel were performed at temperatures ranging from near absolute zero to roughly 80% of the melting temperature. Similarly, measurements of the nuclear resonant inelastic scattering of x-rays from body-centered-cubic (BCC) iron were made at temperatures from near zero to roughly 50% of the melting temperature. These experimental techniques allowed access to the entire phonon spectrum; and the experimental data were thus used to find the phonon spectra of these metals as a function of temperature. Given the phonon spectra and previous measurements of the temperature dependent thermal expansion and bulk modulus, the harmonic, quasiharmonic, and anharmonic phonon contributions to entropy were evaluated. Further, detailed consideration was made of the contributions of electrons, magnons, electron-phonon interactions, and vacancies to the entropy.

For the FCC metals aluminum and nickel, the anharmonic contributions of the phonons were small and negative; that is, the phonons did not shift as much as expected given the thermal expansion and bulk moduli. This was also the case for FCC lead; here, however, the anharmonic phonon contributions were larger. For BCC iron, even though the temperatures measured were far below the melting point, the anharmonic phonon contributions were found to be both large and positive. The agreement of the sums of the contributions with measured values of the total entropy was excellent for the nearly free metals aluminum and lead. For FCC nickel and BCC iron, the differences between the total and the sums of electronic and vibrational contributions were used to learn about the magnetic contributions to the entropy; and these contributions appear to be larger than those of the anharmonic phonons. In all of these metals, the contributions of anharmonicity were significantly larger than those of electron-phonon interactions and vacancies, and they were not negligible on the scale of the electronic entropy. We found that any serious consideration of the contributions to the total entropy of crystalline solids would be incomplete without consideration of the anharmonicity.

In aluminum, the best agreement between the sum of the components and the total entropy was

obtained using the damped phonon spectra (once corrected for instrument resolution). Tentatively, it seems that models which account for phonon broadening may lead to more accurate estimations of the phonon entropy than the widely accepted quasiharmonic model.

We have also considered some trends in FCC and BCC transition metals, as well as in FCC nearly free electron metals; to do so, we have supplemented our experimental data with some from other sources. Overall, we found relatively large variations in the anharmonic entropy of the BCC metals; whereas for the FCC metals the anharmonic entropy tended to be small and negative. The first nearest neighbors dominated the forces in the FCC metals, but for BCC metals the second nearest neighbors made significant contributions. Further, there were instabilities in the transverse forces in the first nearest neighbor shell for BCC metals, but not for FCC. Finally, we found that the shapes of the phonon spectra of the FCC metals were more consistent than those of their BCC counterparts — both across metals and as a function of temperature.

Given the similarities in the forces and anharmonic entropies in the FCC metals, we have performed a detailed study of their phonon linewidths using both experimental data and molecular dynamics simulations. The linewidths were quantified using quality factors, and these were scaled by the square root of the nuclear mass. For both the experimental and simulated data, we scaled the temperature at which the phonon data were collected by the melting temperature, and plotted the scaled qualities against this quantity. The curves so generated were all superlinear, and all fell within roughly the same region on the plot. This indicated that the ratio of anharmonic to harmonic forces was similar across the FCC metals. This was tested more directly using a ratio of anharmonic to harmonic forces taken from the potentials used for the molecular dynamics simulations. The simulations also indicated that the phonon linewidths were correlated with the thermal expansion of the materials. Since the forces in the FCC metals — as measured by the linewidths — are similar despite differing electronic structures, and since they are tied to the nuclear potential through their correlation with thermal expansion, we concluded that the phonon linewidths arise from the nuclear potential. That is, phonon linewidths in the FCC metals were found to be determined by phonon-phonon interactions, rather than by interactions of phonons with electrons or magnons.

Contents

List of Figures

List of Tables

Chapter 1

Introduction

1.1 General background and motivation

Despite great advances in both experimental and theoretical techniques, predicting phase diagrams of even elemental materials remains an active area of research. [1–10] Even at zero temperature and zero pressure, crystal structures are typically an input to *first-principles* calculations. The most obvious difficulty is the roughly unlimited number of available spatial configurations.[a] This is compounded as the number of constituents increases, and as more complicated phenomena, such as magnetism or superconductivity, become involved.

At non-zero temperatures and pressures, the energy alone is insufficient to determine phase stability. Thermal energy causes excitations from equilibrium (and the creation of quasi-particles), and there are myriad possible distributions of this energy over the (possibly myriad) degrees of freedom in the system. From basic thermodynamics, we know that the stability of a phase is determined by its Gibbs or Helmholtz free energy, $\mathcal{G}$ or $\mathcal{F}$ respectively:

$$\mathcal{G} = \mathcal{U} + PV - TS \,, \tag{1.1}$$

$$\mathcal{F} = \mathcal{U} - TS \,. \tag{1.2}$$

For elemental crystals, like those studied here, these energies determine temperatures and pressures at which melting, boiling, and sublimation occur. Additionally, solid-solid phase transitions are possible. In particular, it is fairly common for elemental metals to undergo phase changes under high pressures or at elevated temperatures. [11–20] Fig. 1.1 shows a generic pressure-temperature phase diagram for an element, with solid, liquid and gas phases. Fig. 1.2 shows the phase diagram for iron, where there exist multiple solid-solid phase transitions.

In multi-component alloys, the variety of phases available is combinatorially greater. Again, the

[a] There are only 14 Bravais lattice in three dimension; but there are 230 space groups and non-periodic structures as well.

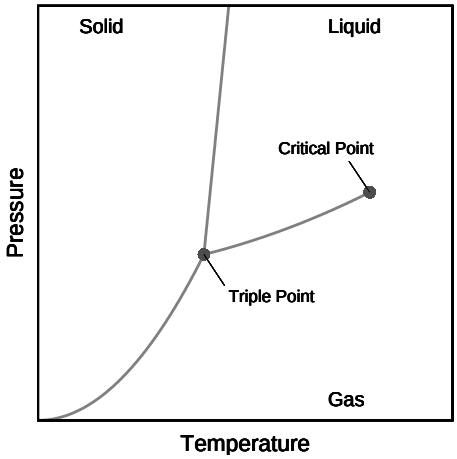

Figure 1.1: Generic phase diagram for a single component system (like an element). As the temperature increases the higher entropy gas and liquid phases are stabilized. Increasing pressure stabilizes the lower energy solid phase.

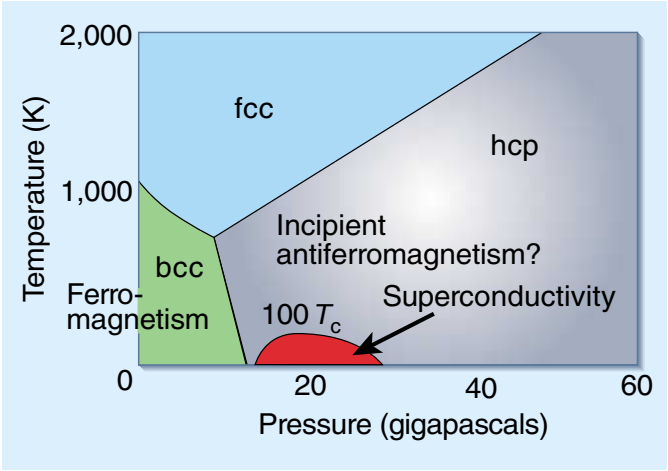

Figure 1.2: Phase diagram of iron at relatively low temperatures showing multiple solid phases. [11] The phase boundaries are determined not only by energetics, but also by entropic contributions of the various degrees of freedom of the system (electronic, nuclear, and magnetic). Interactions between these degrees of freedom also contribute, particularly around the superconducting region.

equilibrium phase is determined by minimization of the free energy. Phenomena such as martensitic phase transitions and spinodal decomposition also depend on the details of the energies and entropies of the phases. [22–24] Fig. 1.3 shows a binary phase diagram for aluminum and nickel, with a wide variety of phases including both FCC- and BCC-type structures.

It is critical to understand the contributions of the various degrees of freedom (quasi-particles and collective excitations) to the free energy (or entropy S, or heat capacity C...) of materials, and this too is an active field of inquiry. [13, 14, 25–42] Calculations of electronic structure using density functional theory frequently give an accurate account of the internal energy of a solid; however, accounting for the entropy is much more complicated. In a simple metal at low temperatures, the electrons dominate the entropy of the crystal. Defects and magnetism may also make sizable contributions to the entropy, and in polyatomic crystals, there is configurational entropy as well. At higher temperatures, the largest source of entropy is very commonly the vibrations of the nuclei about their equilibrium positions.

Most of solid state theory relies on the assumption that the oscillations of the nuclei about their equilibria are sufficiently small that the potential experienced by the nuclei is harmonic. Under this assumption, the phonon spectrum may be determined from first principles calculations. [43–49] Further, there exist closed form expressions for the free energy, entropy, and heat capacity of a harmonic solid, given the phonon spectrum. We know, however, that this assumption is untrue. Perhaps the most obvious contradiction is the existence of thermal expansion, which is precluded

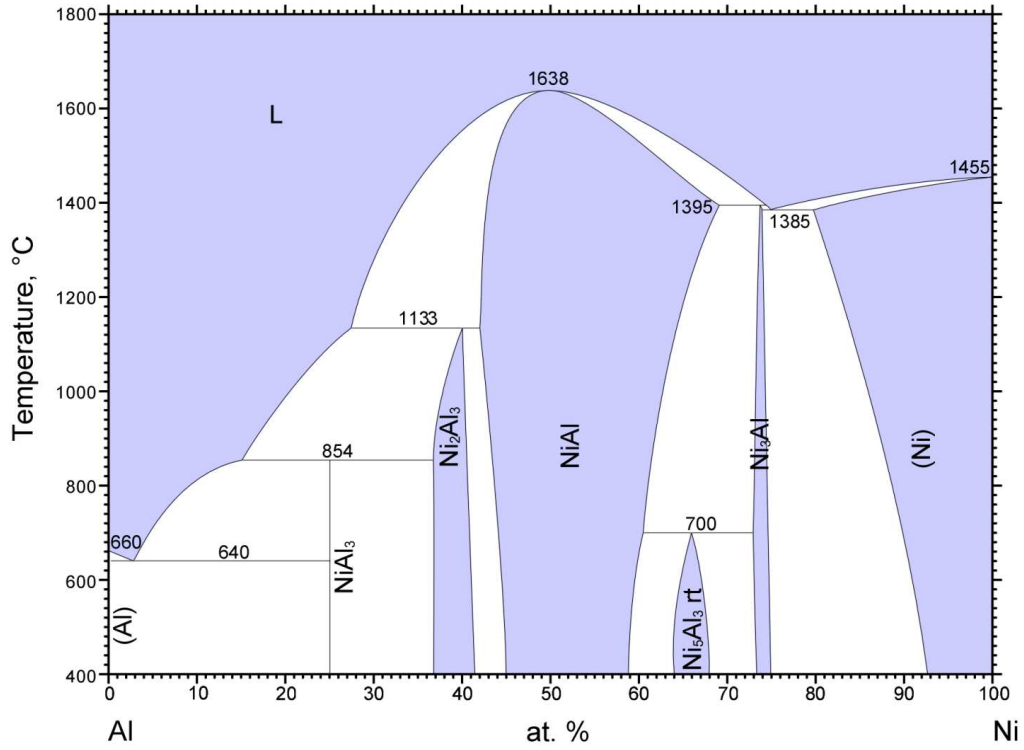

Figure 1.3: Binary phase diagram for aluminum and nickel. [21] On either end, there are disordered face-centered-cubic (FCC) solid solutions of the two constituents. Towards the center there are ordered compounds at and around 3/4, 3/5, 1/2, 3/8, and 1/4 aluminum atoms. Individually, both elements form are FCC; however, the equilibrium structures of their binary compounds are not always FCC-like.

under the harmonic approximation. [50–52] Additionally, the frequency of vibration is independent of the amplitude in a harmonic potential. [53] Therefore, if the primary effect of temperature on the oscillations of the nuclei is to increase their amplitudes, the vibrational spectrum in a harmonic solid would remain constant despite changes in temperature. Contrary to this prediction, experiments have shown that the temperature can have a significant impact on the phonon spectrum. [35–42, 54–60]

A relatively simple attempt to deal with this failure is called the *quasiharmonic approximation*. [36, 37] The idea, here, is that at fixed volume, the oscillations of the nuclei are indeed harmonic. It then remains only to find the appropriate harmonic potential at each volume (or at the corresponding temperature). In this model, there is a closed form expression for the phonon entropy, and it is simply the harmonic expression with the caveat that the phonon spectrum is now a function

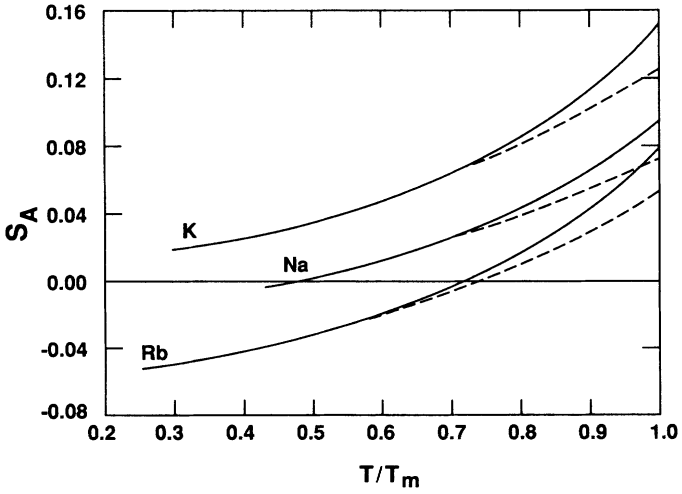

Figure 1.4: Anharmonic phonon entropy of the alkali metals taken from Wallace. [61] The total phonon entropy for these metals is around $10k_B$/atom, so the anharmonic entropy is less than 2% of the total phonon entropy. [61]

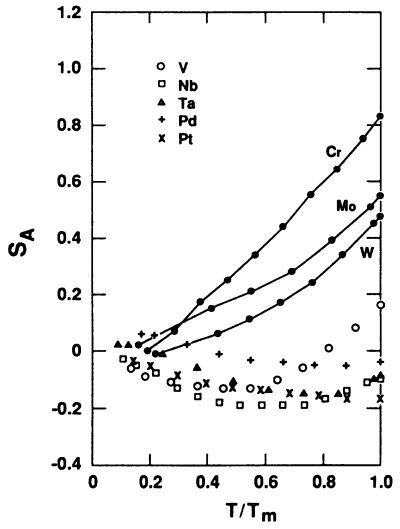

Figure 1.5: Anharmonic phonon entropy for a few transition metals taken from Eriksson *et al.* [36] In general, it is small relative to the total phonon entropy; however, this is not the case for Cr, Mo, and W.

of volume (or temperature). [36, 37] Alternatively, the *entropy of dilation*, $S_{\mathrm{ph,D}}$, may be found by taking the difference between the heat capacities at constant pressure and constant volume, C_P and C_V:

$$S_{\mathrm{ph,D}} = S_{\mathrm{ph,D}}(T) = \int_0^T \frac{C_P - C_V}{T'} dT' = \int_0^T \frac{9K_T\alpha^2}{\rho_N} dT' \,, \tag{1.3}$$

where T is the temperature, K_T is the isothermal bulk modulus, α is the linear coefficient, and ρ_N is the number density. In the quasiharmonic model, these two methods of determining the entropy should yield the same result; however, this is not always the case. Any entropy not accounted for by the quasiharmonic model is called *anharmonic* phonon entropy. For example, Fig. 1.4 shows that the quasiharmonic model is only a slight underestimate of the phonon entropy in the alkali metals potassium, sodium and rubidium; and Fig. 1.5 shows that the model gives only a slight overestimate of the entropy for vanadium, tantalum, palladium, and platinum. On the other hand, Fig. 1.5 also shows that the model grossly underestimates the phonon entropy for chromium, molybdenum and tungsten.

In addition to not accounting for all of the entropy, there are further failures of the quasiharmonic model. In spirit, the model is simple; however, accounting for the changes in energy of the phonons can become quite involved. It is not always the case that all of the phonon energies shift

proportionally, or even in the same direction, as the volume of the crystal changes. [39, 55] Further, the quasiharmonic model does not account for the shortened lifetimes of the phonons through electron-phonon and phonon-phonon interactions. Experimentally, these shortened lifetimes express themselves as non-zero spreads in the measured phonon energies. There exists quantum field theoretical techniques which allow calculation of phonon shifts and linewidths, and there has been a resurgence in their use in the last decade. [62–67] However, this method is very computationally intensive, and its accuracy is still unclear. In particular, it is based on perturbation theory and assumes nearly harmonic behavior. As such, the temperature dependencies it predicts for the phonons do not always match up with those seen in experiments.

1.2 Present work

The present work considers changes in the phonon spectrum of cubic metals as the temperature increases from absolute zero to near melting. We consider both the shifts in the fundamental energies, and the finite lifetimes of the phonons, as well as their effects on the thermodynamics.

In Part I we present the scientific background required to understand the rest of the text. Specifically, we start with a description of crystals and phonons, then move on to the various contributions to the entropy of a solid. After that, we consider neutron scattering in general, and time-of-flight chopper spectrometers in particular.

Part II describes the procedures used for analysis of the experimental data collected herein. This includes new and/or modified methods for determining the incident energy (without use of beam monitors), finding bad detectors, reducing experimental data to the the scattering function $S(Q, E)$, correcting for multiphonon- and multiple-scattering, analysis of phonon shifts and damping, and determination of Born–von Kármán (BvK) force constants from a measured phonon spectrum.

In Part III, we present neutron scattering experiments to determine phonon spectra in face-centered-cubic (FCC) aluminum, lead, and nickel as a function of temperature. Lattice parameters, interatomic force constants, phonon spectrum and entropies, mean energies, and mean quality factors are all extracted from the data. For aluminum and nickel, the softening of the phonon spectrum with increasing temperature is tied to force constants BvK models of the lattice dynamics. Thermal expansion and bulk modulus data from the literature in conjunction with the phonon spectrum are used to determine the harmonic, quasiharmonic, and anharmonic phonon entropies for these metals. All other contributions to the entropy are also assessed, and comparisons are made to experimental measurements of the total entropy. The effects of anharmonicity on the phonon spectrum and the entropy are discussed, with particular attention to the phonon line broadening seen at higher temperatures. Part IV presents the same sort of information for body-centered-cubic (BCC) iron, in addition to less detailed presentation of experimentally determined phonon spectra for the BCC

metals chromium and vanadium.

Trends across FCC and BCC metals are considered in Part V. In particular, commonality in the phonon linewidths of the FCC metals is explored. We find and present a simple empirical model based on the damped harmonic oscillator that gives a reasonable estimate of the phonon linewidths in the FCC metals studied. The experimental data is supplemented with data from molecular dynamics simulations, and these provide some access to the interatomic forces involved in the anharmonic phonon linewidths.

Finally, in Part VI, we summarize our results and offer some ideas for future avenues of research.

Part I

Background

In this part of the thesis, we examine some of the definitions and basic physics relevant to the rest of the work. We discuss crystals and their vibrational excitations, the division of the entropy into components, the theory of neutron scattering, and neutron scattering instruments.

Chapter 2

Notation

2.1 Indices

We will often use a bold letter for some non-scalar quantity, and the same letter, not bold, as an index. For example, we might have the component $\mathbf{v}_v$. We do this so that it will be easier to remember to what the index refers, and because we believe that the reader will be able to identify to which we are referring by context. Please note that any of these indices might be used for other purposes in other parts of the text, though we have made some effort to avoid this.

In an (albeit weak) attempt to appease serious mathematicians, we also point out the following: We will frequently use a dummy index i and a particular value of that dummy index interchangeably. For example, we might say "Atoms $\mathbf{a}$ are indexed by i, as in $\mathbf{a}_i$." This might be followed with something like "The i^{th} atom is at equilibrium," or "Atom $\mathbf{a}_i$ is at its equilibrium position." These statements should be taken to mean that for any particular value of i, the corresponding atom is at its equilibrium position. If a specific value of i *is* intended, it will be made clear. E.g., "Atom $\mathbf{a}_0$ is removed from the lattice."

2.2 Matrices

In order to distinguish between indices that yield elements of matrices,[a] and those that yield submatrices or elements of sets of matrices, we have adopted the following convention: Square brackets, as in $[\mathbf{M}_{ij}]$, indicate that $\mathbf{M}_{ij}$ is not a scalar. Indices on the outside of square brackets, as in $[\mathbf{M}_{ij}]_{kl}$, do yield a scalar. The argument of a function of a continuous variable is given in parentheses, thus $[\mathbf{M}_{ij}(v)]_{kl}$ is the kl^{th} element of the (non-scalar) ij^{th} $\mathbf{M}$ which is a continuous function of v.

For those familiar with previous expositions of lattice dynamics, please compare: Using our

[a] Here, the term *matrices* also includes vectors and tensors.

variable names, Venkataraman *et al.* [68] have this definition of the dynamical matrix:

$$D_{cc_1}\begin{pmatrix}\mathbf{q}\\ ss_1\end{pmatrix} = \frac{1}{\sqrt{M_s M_{s_1}}}\sum_{\ell} K_{cc_1}\begin{pmatrix}1 & \ell\\ s & s_1\end{pmatrix}\exp\left\{i\mathbf{q}\cdot\mathbf{x}\begin{pmatrix}\ell\\ s\end{pmatrix}\right\},$$

and we have:

$$\left[\mathbf{D}_{ss_1}(\mathbf{q})\right]_{cc_1} = \frac{1}{\sqrt{M_s M_{s_1}}}\sum_{\ell}\left[\mathbf{K}_{(1s)(\ell s_1)}\right]_{cc_1}\exp\left(i\mathbf{q}\cdot\left[\mathbf{x}_{(\ell s)}\right]\right), \tag{2.1}$$

where the index (ls) is a tuple, (l, s), and we have dropped the comma for brevity.

Chapter 3

Crystals and Phonons

This work is focused on the dynamics of nuclei in crystals, and we will have need of the following:

- A brief understanding of what constitutes a crystal.
- Some simplifications: periodic boundary conditions, the adiabatic approximation, and Taylor expansion of the nuclear potential.
- An understanding of the 1D quantum harmonic oscillator, and of how to decouple systems of classical, coupled harmonic oscillator. These concepts allow us to define phonons and the phonon density of states (DOS).
- The effects of anharmonicity on the phonon spectrum.

3.1 Crystals

Crystalline materials have a regular, repeating structure, and physicists tend to describe this with two sets of vectors. The elements of the first set are called *lattice vectors*, and in $\mathcal{D}$ dimensions, there will be $\mathcal{D}$ of them. The lattice vectors describe the repeat unit of the crystal. The *lattice* is the set of all integer linear combinations of the lattice vectors, and we denote elements of the lattice $[\mathbf{l}_i]$. We also call elements of the lattice *cell vectors*, as the cell vector of an atom points to the unit cell in which that atom is located. The elements of the second set are called *site vectors* or *sites*, and they give the positions of the atoms relative to the lattice. We denote the sites $[\mathbf{s}_i]$.[a] A crystal, then, consists of a lattice and sites:

$$\text{crystal} = \text{lattice} + \text{sites} \, . \tag{3.1}$$

Examples of simple crystals in 2 and 3 dimensions are shown in Figs. 3.1 and 3.2 respectively.

[a] We avoid using the terms 'basis' or 'basis-vectors' commonly used by crystallographers and physicists, as these terms already have clear meaning in linear algebra. In point of fact, the lattice vectors are a linear algebraic basis of the lattice.

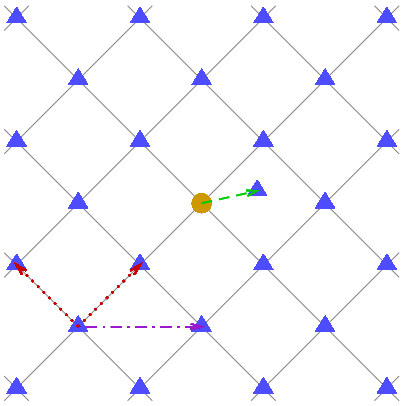

Figure 3.1: A 2D lattice, with lattice vectors shown in dotted red, and a cell vector shown in dash-dotted purple. The dashed green arrow shows the displacement of a particle from its equilibrium position. The orange circle is a site vector with zero length.

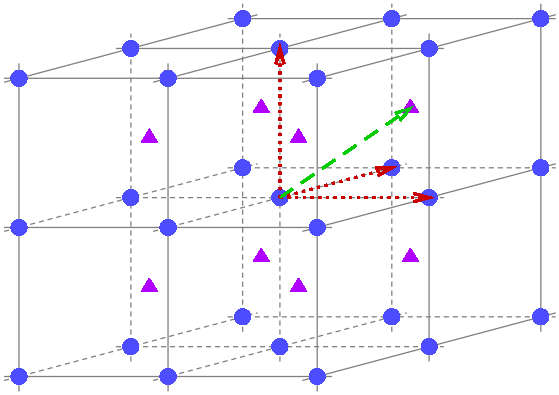

Figure 3.2: A 3D body centered cubic lattice, with lattice vectors shown in dotted red and site vectors shown in dashed green. (Two site vectors emanate from the same point on the lattice; but, one of them has zero length.)

The equilibrium position, $[\mathbf{x}_i]$ of any atom indexed i is:

$$[\mathbf{x}_i] = [\mathbf{l}_i] + [\mathbf{s}_i] \ , \tag{3.2}$$

and its instantaneous position $[\mathbf{r}_i]$ is given by:

$$[\mathbf{r}_i] = [\mathbf{x}_i] + [\mathbf{u}_i] = [\mathbf{l}_i] + [\mathbf{s}_i] + [\mathbf{u}_i] \ , \tag{3.3}$$

where $[\mathbf{u}_i]$ gives the displacement of the i^{th} atom from its equilibrium.

More details about crystal lattices (and reciprocal lattices) are available elsewhere.[50, 68, 69]

3.2 Approximations

As much as we would like the theory of crystalline solids to be exact, it appears to be far too complicated. The following approximations are instrumental to our understanding of the dynamics in these materials.

3.2.1 Periodic boundary conditions

In a typical empirical model of a metal, the forces extend out to on the order of ten nearest neighbors (10NN). Let us assume that we have a large cube with side length R filled with atoms, and that the atoms are arranged in a simple cubic lattice with lattice parameter a. (This is the structure as in Fig. 3.2 without the triangular markers.) Further, assume that any atom within $2a$ of the sides

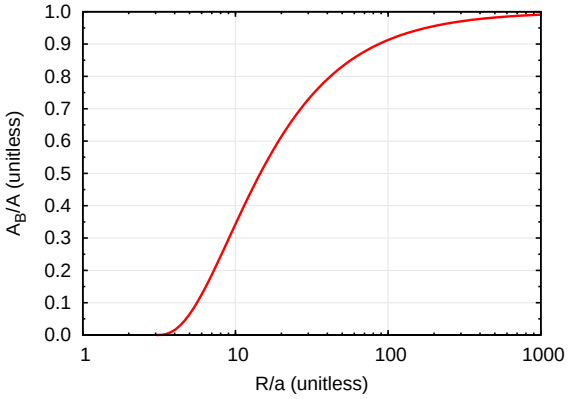

Figure 3.3: Approximate fraction of atoms that are in the bulk as described in § 3.2.1.

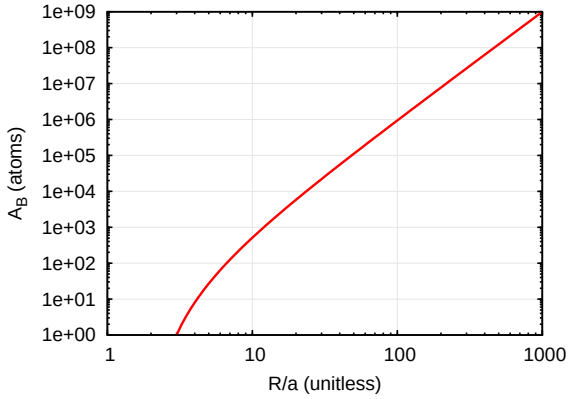

Figure 3.4: Approximate number of atoms in the bulk as described in § 3.2.1.

of the cube is part of the *surface* of the crystal, as opposed to being part of the *bulk*. The number density of the atoms in the crystal is approximately $1/a^3$, so the approximate number of atoms, $\mathcal{A}$, in the cube is given by:

$$\mathcal{A} = \left(\frac{R}{a}\right)^3 . \tag{3.4}$$

The number of atoms in the bulk $\mathcal{A}_{\mathrm{B}}$ is given by:

$$\mathcal{A}_{\mathrm{B}} = \left(\frac{R-2a}{a}\right)^3 . \tag{3.5}$$

Note that these are exact whenever R is an integer multiple of a.

Figs. 3.3 and 3.4 show respectively the fraction of atoms that are in the bulk portion of the crystal and the number of such atoms as a function of the length of the side of the crystal divided by the lattice parameter. From the figure, we see that in order to have less than 1% of the crystal be surface, we need around a billion atoms.

The point of all this is that when we need boundary conditions, it would be best if for any atom in our crystal, they approximated the existence of many other atoms in any direction. It would also be nice if we did not need to simulate billions of atoms. Periodic boundary conditions accomplish both of these tasks, and are represented as follows:

$$\left[\mathbf{r}_{([l+\mathcal{L}_i]\ s)}\right] = \left[\mathbf{r}_{(ls)}\right] , \tag{3.6}$$

where $\mathcal{L}_i$ is the number of unit cells in the direction of the i^{th} lattice vector. The one and two dimensional analogues are easy enough to visualize, where very long lines or planes of atoms become rings or tori. The same principle applies to three dimensions, but visualization is more difficult. In

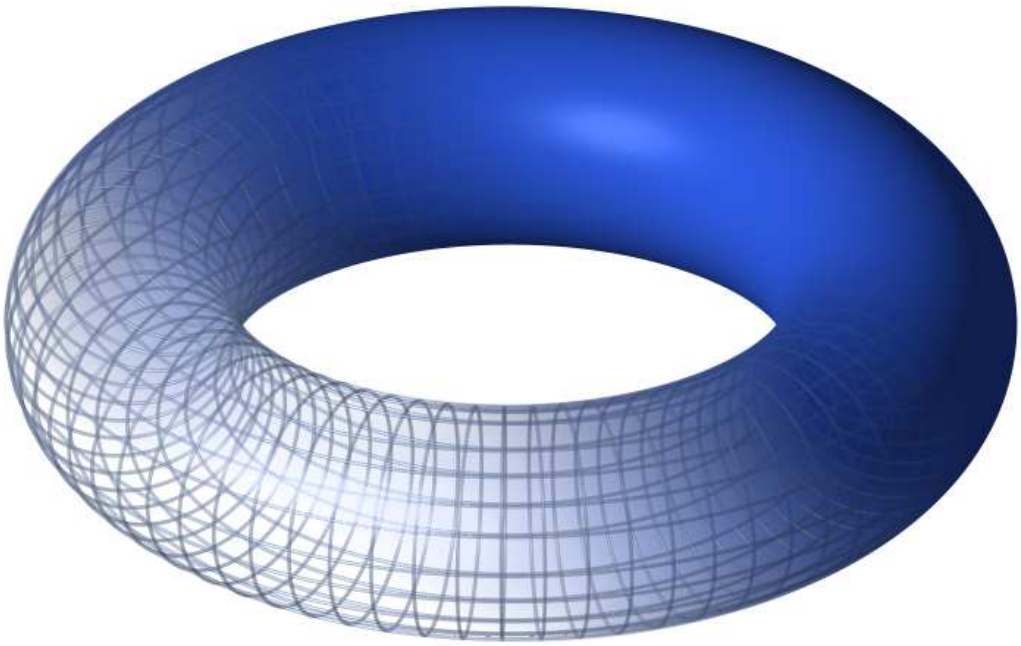

Figure 3.5: Imagining atoms at the intersections of the lines, the torus pictured above [70] is a geometric representation of periodic boundary conditions in two dimensions.

any case, the periodic boundary conditions allow representation of an infinite crystal with a small number of atoms.

More details about this approximation and its validity can be found in many standard texts on solid state physics or lattice dynamics. [50, 51, 68, 71, 72]

3.2.2 Adiabatic approximation

A typical crystal has on the order of 10^{23} particles, and the problem of understanding the detailed motions and interactions of all of them is hopelessly intractable. The greatest simplification possible would be a clean separation of the electronic and nuclear systems, with any (hopefully small) interactions accounted for in perturbation. This separation is accomplished with the *adiabatic* or *Born-Oppenheimer* approximation, which has been described in detail elsewhere. [50, 68, 73]

Briefly, the Hamiltonian, $\mathcal{H}$, for the system may be written as follows:

$$\mathcal{H} = \mathcal{T}_{\rm el} + \mathcal{T}_{\rm ph} + \mathcal{V} = \mathcal{T}_{\rm el} + \mathcal{T}_{\rm ph} + \mathcal{V}_{\rm el} + \mathcal{V}_{\rm ph} + \mathcal{V}_{\rm el-ph} \ , \tag{3.7}$$

where $\mathcal{T}$ denotes kinetic energy, $\mathcal{V}$ denotes the potential energy, and $_{\rm el}$ denotes electronic. The subscript $_{\rm ph}$ stands for 'phonon' (explained later) and it represents the contributions from the nuclei.

Finally, the subscript $_{\mathrm{el-ph}}$ denotes interactions between the electrons and nuclei.

We now exploit the fact that the mass of an electron, m_{e}, is much less than the mass of one of the nuclei, M. For a crystal of hydrogen, we have $\frac{m_{\mathrm{e}}}{M} = 5.446 \times 10^{-4}$, and for a more typical metallic crystal, say nickel, we have something more like $\frac{m_{\mathrm{e}}}{M} = 9.279 \times 10^{-6}$. The Hamiltonian may be expanded in powers of $\frac{m_{\mathrm{e}}}{M}$, and it is then evident that the responses of the electrons occur on a much shorter timescale than those of the nuclei. As a result, the electrons equilibrate quickly, and the nuclei experience a roughly constant cloud of electrons about themselves. Therefore, when considering the motion of the nuclei, we ignore the interactions between the electrons and other particles (including themselves). This gives the following approximate equation for the nuclear motion:

$$\mathcal{H}_{\mathrm{ph}} \quad \approx \quad \mathcal{T}_{\mathrm{ph}} + \mathcal{V}_{\mathrm{ph}} \; . \tag{3.8}$$

The interactions $\mathcal{V}_{\mathrm{el-ph}}$ may be treated in perturbation.

3.2.3 Expansion of the potential

In addition to simply not knowing the nuclear potential, we frequently can only successfully manipulate some portion of it. To this end, we employ a Taylor expansion:

$$\begin{aligned}
\mathcal{V}_{\mathrm{ph}} \quad &= \quad \mathcal{V}_{\mathrm{ph}}\Big|_{\mathbf{r}=\mathbf{x}} \\
&+ \quad \sum_{(lsc)} \left[\mathbf{K}_{(ls)}\right]_c \left[\mathbf{u}_{(ls)}\right]_c \\
&+ \quad \sum_{(lsc)} \sum_{(l_1 s_1 c_1)} \left[\mathbf{K}_{(ls)(l_1 s_1)}\right]_{cc_1} \left[\mathbf{u}_{(ls)}\right]_c \left[\mathbf{u}_{(l_1 s_1)}\right]_{c_1} \\
&+ \quad \sum_{(lsc)} \sum_{(l_1 s_1 c_1)} \sum_{(l_2 s_2 c_2)} \left[\mathbf{K}_{(ls)(l_1 s_1)(l_2 s_2)}\right]_{cc_1 c_2} \left[\mathbf{u}_{(ls)}\right]_c \left[\mathbf{u}_{(l_1 s_1)}\right]_{c_1} \left[\mathbf{u}_{(l_2 s_2)}\right]_{c_2} \\
&+ \quad \cdots \; ,
\end{aligned} \tag{3.9}$$

where we have defined:

$$\begin{aligned}
\left[\mathbf{K}_{(ls)}\right]_c \quad &\equiv \quad \left.\frac{\partial \mathcal{V}_{\mathrm{ph}}}{\partial \left[\mathbf{u}_{(ls)}\right]_c}\right|_{\mathbf{r}=\mathbf{x}} \; , \\
\left[\mathbf{K}_{(ls)(l_1 s_1)}\right]_{cc_1} \quad &\equiv \quad \left.\frac{\partial^2 \mathcal{V}_{\mathrm{ph}}}{\partial \left[\mathbf{u}_{(ls)}\right]_c \partial \left[\mathbf{u}_{(l_1 s_1)}\right]_{c_1}}\right|_{\mathbf{r}=\mathbf{x}} \; , \\
\left[\mathbf{K}_{(ls)(l_1 s_1)(l_2 s_2)}\right]_{cc_1 c_2} \quad &\equiv \quad \left.\frac{\partial^3 \mathcal{V}_{\mathrm{ph}}}{\partial \left[\mathbf{u}_{(ls)}\right]_c \partial \left[\mathbf{u}_{(l_1 s_1)}\right]_{c_1} \partial \left[\mathbf{u}_{(l_2 s_2)}\right]_{c_2}}\right|_{\mathbf{r}=\mathbf{x}} \; ,
\end{aligned} \tag{3.10}$$

and so on. The derivatives of the potential may be rewritten as matrices (or tensors), and we will use them in this form. As we will (presumably) not be dealing with strained samples, we assume that the coefficients of the first order term are zero. Most of our work is done in the harmonic or quasiharmonic approximations, dropping the third and higher order terms.

3.3 The quantum harmonic oscillator

The nuclear system has now been separated from the electronic one, and the next step is to analyze the motion of the nuclei. To this end, we first consider the motion of a single nucleus in a harmonic potential. This section borrows heavily from Griffiths. [74, pp. 31–37] Cohen-Tanoudji *et al.* [75] also have a clear presentation of this material.

In 1D, we may write the Hamiltonian for a single harmonic oscillator:

$$\mathcal{H} = \frac{p^2}{2M} + \frac{1}{2}Ku^2 = \frac{1}{2M}\left(\frac{\hbar}{i}\frac{\partial}{\partial u}\right)^2 + \frac{1}{2}M\omega^2 u^2 \ , \tag{3.11}$$

where $\omega \equiv \sqrt{\frac{K}{M}}$ is the classical frequency of the oscillator. We may then write the time-independent Schrödinger equation as follows:

$$\begin{aligned}\mathcal{H}\psi = \frac{1}{2M}\left[\left(\frac{\hbar}{i}\frac{\partial}{\partial u}\right)^2 + (M\omega u)^2\right]\psi = \\ \frac{1}{2}\left[\frac{1}{\sqrt{2M}}\left(\frac{\hbar}{i}\frac{\partial}{\partial u} - iM\omega u\right)\frac{1}{\sqrt{2M}}\left(\frac{\hbar}{i}\frac{\partial}{\partial u} + iM\omega u\right) + \right. \\ \left. \frac{1}{\sqrt{2M}}\left(\frac{\hbar}{i}\frac{\partial}{\partial u} + iM\omega u\right)\frac{1}{\sqrt{2M}}\left(\frac{\hbar}{i}\frac{\partial}{\partial u} - iM\omega u\right)\right]\psi = E\psi \ .\end{aligned} \tag{3.12}$$

We now define *creation* and *annihilation* operators:

$$\hat{\mathbf{a}}_\pm \equiv \frac{1}{\sqrt{2M}}\left(\frac{\hbar}{i}\frac{\partial}{\partial u} \pm iM\omega u\right) \ , \tag{3.13}$$

which allow us to write Schrödinger's equation for the oscillator in either this form: [b]

$$\left(\hat{\mathbf{a}}_\pm\hat{\mathbf{a}}_\mp \pm \frac{1}{2}\hbar\omega\right)\psi = E\psi \ . \tag{3.14}$$

Assume that the λ^{th} state of the oscillator, ψ_λ, is known. When we apply the creation or annihilation

[b] Another, possibly prettier option is $\frac{1}{2}\left(\hat{\mathbf{a}}_+\hat{\mathbf{a}}_- + \hat{\mathbf{a}}_-\hat{\mathbf{a}}_+\right)\psi = E\psi$.

operators to our state, we get a new solution to the Schrödinger equation:

$$\begin{aligned}\mathcal{H}\hat{\mathbf{a}}_{\pm}\psi_{\lambda} &= \left(\hat{\mathbf{a}}_{\pm}\hat{\mathbf{a}}_{\mp} \pm \frac{1}{2}\hbar\omega\right)\hat{\mathbf{a}}_{\pm}\psi_{\lambda} = \hat{\mathbf{a}}_{\pm}\left(\hat{\mathbf{a}}_{\mp}\hat{\mathbf{a}}_{\pm} \pm \frac{1}{2}\hbar\omega\right)\psi_{\lambda} \\ &= \hat{\mathbf{a}}_{\pm}\left(\hat{\mathbf{a}}_{\mp}\hat{\mathbf{a}}_{\pm} \mp \frac{1}{2}\hbar\omega \pm \hbar\omega\right) = \hat{\mathbf{a}}_{\pm}\left(E \pm \hbar\omega\right)\psi_{\lambda} \\ &= \left(E \pm \hbar\omega\right)\hat{\mathbf{a}}_{\pm}\psi_{\lambda} \ . \end{aligned} \tag{3.15}$$

Applications of the creation and annihilation operators, then, create new states with energy shifted by $\hbar\omega$.

The overall energy must be positive, so we may apply the annihilation operator until we reach the ground state, ψ_0. After that, we should get $\hat{\mathbf{a}}_{-}\psi_0 = 0$. Substituting ψ_0 into the Schrödinger equation, then, we get:

$$\left(\hat{\mathbf{a}}_{+}\hat{\mathbf{a}}_{-} + \frac{1}{2}\hbar\omega\right)\psi_0 = \frac{1}{2}\hbar\omega\psi_0 = E_0\psi_0 \ , \tag{3.16}$$

where we have used:

$$\hat{\mathbf{a}}_{+}\hat{\mathbf{a}}_{-}\psi_0 = \hat{\mathbf{a}}_{+}0 = 0 \ . \tag{3.17}$$

Thus, the entire spectrum of energies is given by:

$$E_{\lambda} = \left(\lambda + \frac{1}{2}\right)\hbar\omega \qquad \lambda \in \mathbb{N} \ . \tag{3.18}$$

3.4 Harmonic lattice dynamics

We have now briefly studied the quantum mechanical oscillations of a particle (nucleus) in a harmonic potential, and we wish to take our knowledge and apply it to a multi-dimensional, multi-particle system. To do so, we first review the mathematics of decoupled and normal modes, which allow us to take a single problem in many coupled variables and transform it into many problems, each in a single, uncoupled variable.

3.4.1 Decoupled modes

Occasionally, a difficult integral may sometimes be greatly simplified by a change of variables. Similarly, the problem of a system of coupled harmonic oscillators can be made simple by an appropriate coordinate transformation. First, we consider a system of two point particles of mass M connected to each other and to nearby walls by Hookean springs of stiffness K.

If we say that the displacement of the first particle from its equilibrium position is given by u_1,

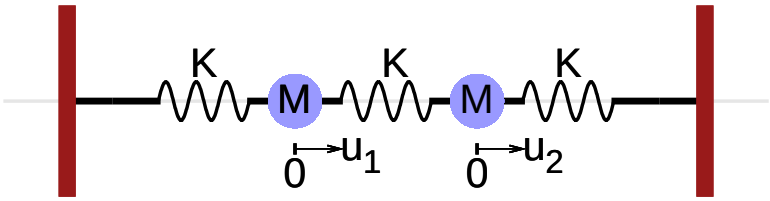

Figure 3.6: Coupled point particles with mass M, connected by springs of stiffness K. The displacements from equilibrium are given by $\mathbf{u}_i$.

and that of the second particle is given by u_2, we may write the equations of motion:

$$M\ddot{u}_1 + Ku_1 + K(u_1 - u_2) = 0 \,, \tag{3.19}$$

$$M\ddot{u}_2 + Ku_2 + K(u_2 - u_1) = 0 \,. \tag{3.20}$$

As with most differential equations, we may solve these by simply knowing the answer ahead of time. If we take:

$$u_j(t) = A_j \exp\left(i\omega_b t + \phi_b\right) \,, \tag{3.21}$$

where the A_j are amplitudes, the ω_b are frequencies, and the ϕ_b are phases,[c] and substitute it into the equations of motion, we get:

$$-\omega_b^2 M A_1 \exp\left(i\omega_b t + \phi_b\right) + 2KA_1 \exp\left(i\omega_b t + \phi_b\right) - KA_2 \exp\left(i\omega_b t + \phi_b\right) = 0 \,, \tag{3.22}$$

$$-\omega_b^2 M A_2 \exp\left(i\omega_b t + \phi_b\right) + 2KA_2 \exp\left(i\omega_b t + \phi_b\right) - KA_1 \exp\left(i\omega_b t + \phi_b\right) = 0 \,. \tag{3.23}$$

We may divide through by M times the exponential, and rewrite this as a matrix equation:

$$\begin{pmatrix} -\omega_b^2 + \frac{2K}{M} & -\frac{K}{M} \\ -\frac{K}{M} & -\omega_b^2 + \frac{2K}{M} \end{pmatrix} \begin{pmatrix} A_1 \\ A_2 \end{pmatrix} = 0 \,. \tag{3.24}$$

This is equivalent to an eigenvalue problem with eigenvalues ω_b^2:

$$\begin{pmatrix} \frac{2K}{M} & -\frac{K}{M} \\ -\frac{K}{M} & \frac{2K}{M} \end{pmatrix} \begin{pmatrix} A_1 \\ A_2 \end{pmatrix} = \omega_b^2 \begin{pmatrix} A_1 \\ A_2 \end{pmatrix} \,. \tag{3.25}$$

At this point, it is clear that there are two ω_b, which comes from $\mathcal{DA} = 1 \cdot 2 = 2$ (Again, $\mathcal{D}$ is the dimension and $\mathcal{A}$ is the number of atoms). We may find both eigenvalues by setting the determinant

[c] Note that the index on the frequencies and phases is different than the index on the displacement or the amplitude. This is because combined motion of the masses will give rise to the frequencies and phases.

of the matrix in Eq. 3.24 equal to zero:

$$\left(\omega_b^2 - \frac{2K}{M}\right)^2 - \left(\frac{K}{M}\right)^2 = 0 \; . \tag{3.26}$$

Taking the positive values for ω_b, this gives:

$$\omega_1 = \sqrt{\frac{K}{M} + \frac{2K}{M}} = \sqrt{\frac{3K}{M}} \; , \tag{3.27}$$

$$\omega_2 = \sqrt{-\frac{K}{M} + \frac{2K}{M}} = \sqrt{\frac{K}{M}} \; . \tag{3.28}$$

Substituting these eigenvalues back into the Eq. 3.25, we may find the eigenvectors:

$$\omega_1 \rightarrow \begin{pmatrix} -1 \\ 1 \end{pmatrix} \qquad , \qquad \omega_2 \rightarrow \begin{pmatrix} 1 \\ 1 \end{pmatrix} \; . \tag{3.29}$$

The decoupled modes of the system, then, are given by these eigenvalues and eigenvectors. In this case, the eigenvectors are orthogonal, so the decoupled modes are also *normal modes*. Let:

$$U_1 = u_1 - u_2 \quad , \quad \ddot{U}_1 = \ddot{u}_1 - \ddot{u}_2 \; , \tag{3.30}$$

$$U_2 = u_1 + u_2 \quad , \quad \ddot{U}_1 = \ddot{u}_1 + \ddot{u}_2 \; . \tag{3.31}$$

Then the sum and the difference of Eqs. 3.19 and 3.20 give respectively:

$$M(\ddot{u}_1 + \ddot{u}_2) + K(u_1 + u_2) = MU_2 + KU_2 = 0 \; , \tag{3.32}$$

$$M(\ddot{u}_1 - \ddot{u}_2) + 3K(u_1 - u_2) = MU_1 + 3KU_1 = 0 \; . \tag{3.33}$$

Thus, the eigenvectors provide us with a coordinate transformation that allows us to rewrite our original equations of motion in terms of two decoupled oscillators.

We now redo this for a more general system of oscillators. Let i, j label particles, and c, c_1 label Cartesian directions, then the displacement of the particle labeled i in the c direction is given by $[\mathbf{u}_i]_c$. We now construct the *mass matrix*, $\mathbf{M}$, such that:

$$[\mathbf{M}_{ij}]_{cc_1} = \delta_{ij}\delta_{cc_1}M_i \; . \tag{3.34}$$

For the example given above, we have $M_i = M$, so:

$$\mathbf{M} \;\; = \;\; \begin{pmatrix} M & 0 \\ 0 & M \end{pmatrix} \; . \tag{3.35}$$

Then it is clear that the force, $\mathbf{F}$ is given by $\mathbf{M\ddot{u}}$,or in our example:

$$\mathbf{F} = \begin{pmatrix} M & 0 \\ 0 & M \end{pmatrix} \begin{pmatrix} \ddot{u}_1 \\ \ddot{u}_2 \end{pmatrix} = \begin{pmatrix} M\ddot{u}_1 \\ M\ddot{u}_2 \end{pmatrix} . \tag{3.36}$$

Next, we construct the *stiffness matrix* $\mathbf{K}$. Each element $[\mathbf{K}_{ij}]_{cc_1}$ gives the force constant linking the motion of the i^{th} particle in the c direction to a response of the j^{th} particle in the c_1 direction. Going back to our two particle example, we have:

$$\mathbf{F} = -\mathbf{Ku} = -\begin{pmatrix} 2K & -K \\ -K & 2K \end{pmatrix} \begin{pmatrix} u_1 \\ u_2 \end{pmatrix} = -\begin{pmatrix} 2Ku_1 - Ku_2 \\ -Ku_1 + 2Ku_2 \end{pmatrix} . \tag{3.37}$$

The elements along the diagonal are frequently called *self force constants*, as they describe the forces felt by a particle when it is the only one displaced from equilibrium. In our example, displacing only the first mass leads to a restoring force $-Ku_1$ from the compression of the spring connecting the first mass to the second mass, and another restoring force $-Ku_1$ from the extension of the spring connecting the first mass to the wall.

Putting equations Eqs. 3.36 and 3.37 together, we recover Eqs. 3.19 and 3.20:

$$\mathbf{M\ddot{u}} = -\mathbf{Ku} , \tag{3.38}$$

$$\begin{pmatrix} M\ddot{u}_1 \\ M\ddot{u}_2 \end{pmatrix} = -\begin{pmatrix} 2Ku_1 - Ku_2 \\ -Ku_1 + 2Ku_2 \end{pmatrix} . \tag{3.39}$$

If we multiply the left and right of Eq. 3.38 by $\mathbf{M}^{-1}$, we get:

$$\ddot{\mathbf{u}} = -\mathbf{M}^{-1}\mathbf{Ku} . \tag{3.40}$$

The decoupled modes of the system, then, are found by diagonalization of the matrix $\mathbf{M}^{-1}\mathbf{K}$:

$$\mathbf{M}^{-1}\mathbf{K} = \begin{pmatrix} \frac{2K}{M} & \frac{-K}{M} \\ \frac{-K}{M} & \frac{2K}{M} \end{pmatrix} , \tag{3.41}$$

as in Eq. 3.25.

So long as all of the forces are subject to Newton's third law and are linear in the displacements, a decomposition into decoupled modes is possible;[d] however, if we wish the modes to be normal in the linear algebraic sense (i.e., for $\mathbf{M}^{-1}\mathbf{K}$ to have orthogonal eigenvectors) we need to impose further constraints. Fortunately, the symmetries of the crystal do this for us.

[d] Technically, other systems might also be decomposed into decoupled modes; however, this definition will cover all cases of interest to us.

3.4.2 Normal modes of a crystal

We now take what we have learned of decoupled modes in the previous section, and apply it to an arbitrary crystal structure, in arbitrary dimension. The mathematics is heavier, but the goal remains the same. We start out with the equations for a large system of coupled oscillators, and wish to end up with many equations, each for a single oscillator.

It is tempting to say that the problem is solved — why can't we simply diagonalize $\mathbf{M}^{-1}\mathbf{K}$? This approach poses a few problems. In a real crystal, we have on the order of 10^{23} atoms. Practically speaking, the diagonalization of $\mathbf{M}^{-1}\mathbf{K}$ is simply not possible. We will therefore exploit the fact that we have a crystal — not just an arbitrarily distributed group of atoms — in order to reduce the problem to manageable proportions. The periodic boundary conditions are critical in this regard.

Our $\mathcal{D}$-dimensional crystal has $\mathcal{A}$ atoms, and they are indexed by i (or j).[e] $\mathbf{x}$ is the $(\mathcal{A}\mathcal{D})$-vector[f] giving the equilibrium positions of the all the atoms in the crystal, and $[\mathbf{x}_i]$ is the equilibrium position vector for the i^{th} atom, a length $\mathcal{D}$ subvector of $\mathbf{x}$. If the cell vectors for all the atoms in the crystal are given by the $(\mathcal{A}\mathcal{D})$-vector $\mathbf{l}$, and similarly the site vectors by $\mathbf{s}$, we have:

$$\mathbf{x} = \mathbf{l} + \mathbf{s} \,, \tag{3.42}$$

$$[\mathbf{x}_i] = [\mathbf{l}_i] + [\mathbf{s}_i] \ . \tag{3.43}$$

We will want to exploit the translational symmetry of the lattice; therefore, we will also describe the i^{th} atom by indices to its cell and site vectors (ls). There are $\mathcal{L}$ cell vectors and $\mathcal{S}$ site vectors, thus we have $\mathcal{A} = \mathcal{L}\mathcal{S}$. Using the indices for the cell and site vectors, we may write:

$$\left[\mathbf{x}_{(ls)}\right] = [\mathbf{l}_l] + [\mathbf{s}_s] \ , \tag{3.44}$$

such that $\left[\mathbf{x}_{(ls)}\right]$ is the position vector for the $(ls)^{\text{th}}$ atom, $[\mathbf{l}_l]$ its cell vector, and $[\mathbf{s}_s]$ its site vector. Finally, $\mathbf{u}$ gives the displacement of all atoms from their equilibria, such that the instantaneous positions of all the atoms are given by $\mathbf{r}$, with:

$$\mathbf{r} = \mathbf{x} + \mathbf{u} \,, \tag{3.45}$$

$$[\mathbf{r}_i] = [\mathbf{x}_i] + [\mathbf{u}_i] \ , \tag{3.46}$$

$$\left[\mathbf{r}_{(ls)}\right] = [\mathbf{l}_l] + [\mathbf{s}_s] + \left[\mathbf{u}_{(ls)}\right] \ . \tag{3.47}$$

Note that the instantaneous position and the displacement must be indexed by the tuple (ls), whereas the cell vector and the site vector require only their respective indices, l and s, separately.

Let $[\mathbf{K}_{ij}]$ represent the $\mathcal{D} \times \mathcal{D}$ force constant matrix connecting the i^{th} and the j^{th} atoms, then

[e] We apologize that i is doing double duty as $\sqrt{-1}$ and as an index in this section.
[f] This is meant to indicate a vector of length $\mathcal{A}\mathcal{D}$.

we may write out $\mathbf{K}$ explicitly as follows:

$$\mathbf{K} = \begin{pmatrix} [\mathbf{K}_{11}] & [\mathbf{K}_{12}] & \cdots & [\mathbf{K}_{1\mathcal{A}}] \\ [\mathbf{K}_{21}] & [\mathbf{K}_{22}] & \cdots & [\mathbf{K}_{2\mathcal{A}}] \\ \vdots & \vdots & \ddots & \vdots \\ [\mathbf{K}_{\mathcal{A}1}] & [\mathbf{K}_{\mathcal{A}2}] & \cdots & [\mathbf{K}_{\mathcal{A}\mathcal{A}}] \end{pmatrix} = \tag{3.48}$$

$$\begin{pmatrix} \left[\mathbf{K}_{(11)(11)}\right] & \left[\mathbf{K}_{(11)(12)}\right] & \cdots & \left[\mathbf{K}_{(11)(1\mathcal{S})}\right] & \left[\mathbf{K}_{(11)(21)}\right] & \cdots & \left[\mathbf{K}_{(11)(\mathcal{L}\mathcal{S})}\right] \\ \left[\mathbf{K}_{(12)(11)}\right] & \left[\mathbf{K}_{(12)(12)}\right] & \cdots & \left[\mathbf{K}_{(12)(1\mathcal{S})}\right] & \left[\mathbf{K}_{(12)(21)}\right] & \cdots & \left[\mathbf{K}_{(12)(\mathcal{L}\mathcal{S})}\right] \\ \vdots & \vdots & \ddots & \vdots & \vdots & \ddots & \vdots \\ \left[\mathbf{K}_{(1\mathcal{S})(11)}\right] & \left[\mathbf{K}_{(1\mathcal{S})(12)}\right] & \cdots & \left[\mathbf{K}_{(1\mathcal{S})(1\mathcal{S})}\right] & \left[\mathbf{K}_{(1\mathcal{S})(21)}\right] & \cdots & \left[\mathbf{K}_{(1\mathcal{S})(\mathcal{L}\mathcal{S})}\right] \\ \left[\mathbf{K}_{(21)(11)}\right] & \left[\mathbf{K}_{(21)(12)}\right] & \cdots & \left[\mathbf{K}_{(21)(1\mathcal{S})}\right] & \left[\mathbf{K}_{(21)(21)}\right] & \cdots & \left[\mathbf{K}_{(21)(\mathcal{L}\mathcal{S})}\right] \\ \vdots & \vdots & \ddots & \vdots & \vdots & \ddots & \vdots \\ \left[\mathbf{K}_{(\mathcal{L}\mathcal{S})(11)}\right] & \left[\mathbf{K}_{(\mathcal{L}\mathcal{S})(12)}\right] & \cdots & \left[\mathbf{K}_{(\mathcal{L}\mathcal{S})(1\mathcal{S})}\right] & \left[\mathbf{K}_{(\mathcal{L}\mathcal{S})(21)}\right] & \cdots & \left[\mathbf{K}_{(\mathcal{L}\mathcal{S})(\mathcal{L}\mathcal{S})}\right] \end{pmatrix}. \tag{3.49}$$

Let us also make the submatrices explicit:

$$[\mathbf{K}_{ij}] = \left[\mathbf{K}_{(ls)(l_1s_1)}\right] = \begin{pmatrix} \left[\mathbf{K}_{(ls)(l_1s_1)}\right]_{11} & \left[\mathbf{K}_{(ls)(l_1s_1)}\right]_{12} & \cdots & \left[\mathbf{K}_{(ls)(l_1s_1)}\right]_{1\mathcal{D}} \\ \left[\mathbf{K}_{(ls)(l_1s_1)}\right]_{21} & \left[\mathbf{K}_{(ls)(l_1s_1)}\right]_{22} & \cdots & \left[\mathbf{K}_{(ls)(l_1s_1)}\right]_{2\mathcal{D}} \\ \vdots & \vdots & \ddots & \vdots \\ \left[\mathbf{K}_{(ls)(l_1s_1)}\right]_{\mathcal{D}1} & \left[\mathbf{K}_{(ls)(l_1s_1)}\right]_{\mathcal{D}2} & \cdots & \left[\mathbf{K}_{(ls)(l_1s_1)}\right]_{\mathcal{D}\mathcal{D}} \end{pmatrix}. \tag{3.50}$$

We now wish to look at the equation of motion of the i^{th} or $(ls)^{\text{th}}$ atom. This involves a summation over a row of $\mathbf{M^{-1}K}$ and a column of $\mathbf{u}$. In particular, we move in steps that are $\mathcal{D}$ elements wide, performing matrix-vector multiplication of the $\mathcal{D} \times \mathcal{D}$ matrix $\left[\mathbf{M^{-1}K}_{(ls)(l_1s_1)}\right]$ onto the $\mathcal{D}$-vector $\left[\mathbf{u}_{(l_1s_1)}\right]$ and summing up the resulting vectors:

$$\left[\ddot{\mathbf{u}}_{(ls)}\right] = -\sum_{(l_1s_1)} \left[\mathbf{M^{-1}K}_{(ls)(l_1s_1)}\right] \left[\mathbf{u}_{(l_1s_1)}\right] . \tag{3.51}$$

The mass depends only on the site vector and we may explicitly write into our equation the appropriate matrix element from $\mathbf{M^{-1}}$:

$$\left[\ddot{\mathbf{u}}_{(ls)}\right] = -\sum_{(l_1s_1)} \frac{1}{M_{s_1}} \left[\mathbf{K}_{(ls)(l_1s_1)}\right] \left[\mathbf{u}_{(l_1s_1)}\right] . \tag{3.52}$$

We believe that the solutions will take the form of plane waves. From the symmetries of the crystal, we know that for two atoms with the same site vector, only the phase of their oscillations may differ. This means that the polarization vectors, $[\boldsymbol{\epsilon}_{bs}(\mathbf{q})]$ will not be indexed by l. Here, the b is the *branch index*. As for b in §3.4.1, we see that we have $b \in \{1, 2, \cdots, \mathcal{DS}\}$. Similarly, the

amplitudes of the motions cannot depend on the cell vector. Thus, we make the following guess for the solutions to the equation of motion:

$$\begin{aligned}\left[\mathbf{u}_{(ls)}\right] &= \sqrt{M_s}\exp\left(i\mathbf{q}\cdot\left[\mathbf{x}_{(ls)}\right]-\omega_b(\mathbf{q})t\right)\left[\boldsymbol{\epsilon}_{bs}(\mathbf{q})\right] \\ &= \sqrt{M_s}\exp\left(i\mathbf{q}\cdot\left([\mathbf{l}_l]+[\mathbf{s}_s]\right)-\omega_b(\mathbf{q})t\right)\left[\boldsymbol{\epsilon}_{bs}(\mathbf{q})\right]\ , \end{aligned} \tag{3.53}$$

where $\mathbf{q}$ is the wavevector for the normal mode and the amplitude of the mode is folded into the polarization vector.

We may break up the exponential into a product:

$$\left[\mathbf{u}_{(ls)}\right] = \sqrt{M_s}\exp\left(i\mathbf{q}\cdot[\mathbf{s}_s]\right)\exp\left(i\mathbf{q}\cdot[\mathbf{l}_l]\right)\exp\left(-i\omega_b(\mathbf{q})t\right)\left[\boldsymbol{\epsilon}_{bs}(\mathbf{q})\right]\ . \tag{3.54}$$

In this form it is easy to see that the first and second time derivatives of the displacements are as follows:

$$\left[\dot{\mathbf{u}}_{(ls)}\right] = -i\omega_b(\mathbf{q})\left[\mathbf{u}_{(ls)}\right]\ , \tag{3.55}$$

$$\left[\ddot{\mathbf{u}}_{(ls)}\right] = -\omega_b^2(\mathbf{q})\left[\mathbf{u}_{(ls)}\right]\ . \tag{3.56}$$

We now substitute these back into the equation of motion:

$$\begin{aligned}&-\omega_b^2(\mathbf{q})\sqrt{M_s}\exp\left(i\mathbf{q}\cdot[\mathbf{s}_s]\right)\exp\left(i\mathbf{q}\cdot[\mathbf{l}_l]\right)\exp\left(-i\omega_b(\mathbf{q})t\right)\left[\boldsymbol{\epsilon}_{bs}(\mathbf{q})\right] = \\ &-\sum_{s_1}\frac{1}{M_{s_1}}\sum_{l_1}\left[\mathbf{K}_{(ls)(l_1s_1)}\right]\sqrt{M_{s_1}}\exp\left(i\mathbf{q}\cdot[\mathbf{s}_{s_1}]\right)\exp\left(i\mathbf{q}\cdot[\mathbf{l}_{l_1}]\right)\exp\left(-i\omega_b(\mathbf{q})t\right)\left[\boldsymbol{\epsilon}_{bs_1}(\mathbf{q})\right]\ . \end{aligned} \tag{3.57}$$

Dividing both sides of the equation by $\sqrt{M_s}$ and the exponentials, and collecting terms, we get:

$$\begin{aligned}&\omega_b^2(\mathbf{q})\left[\boldsymbol{\epsilon}_{bs}(\mathbf{q})\right] = \\ &\sum_{s_1}\frac{\exp\left\{i\mathbf{q}\cdot\left([\mathbf{s}_{s_1}]-[\mathbf{s}_s]\right)\right\}}{\sqrt{M_sM_{s_1}}}\sum_{l_1}\left[\mathbf{K}_{(ls)(l_1s_1)}\right]\exp\left\{i\mathbf{q}\cdot\left([\mathbf{l}_{l_1}]-[\mathbf{l}_l]\right)\right\}\left[\boldsymbol{\epsilon}_{bs_1}(\mathbf{q})\right]\ . \end{aligned} \tag{3.58}$$

We note that any $\mathcal{D}\times\mathcal{D}$ submatrix of the force constant matrix $[\mathbf{K}_{ij}]$ connecting the atoms i and j depends only on the distance between two atoms, not on their absolute positions. Therefore, we fix one of the atoms into the first unit cell. [g]

$$\ell \rightarrow 1\ , \tag{3.59}$$

$$\left[\mathbf{K}_{(ls)(l_1s_1)}\right] \rightarrow \left[\mathbf{K}_{(1s)(l_1s_1)}\right]\ . \tag{3.60}$$

[g] In practice, there is sometimes reason to use a *calculational cell* that contains $\mathcal{U}$ repeat units of the crystal where $\mathcal{U}>1$ (i.e., more than one *primitive unit cell*). In this case, we are adding up the same force constants $\mathcal{U}$ times, once for each copy of the repeat unit that appears in the calculational cell. Thus, we must divide our result by $\mathcal{U}$ in order to get the correct squared frequencies.

With periodic boundary conditions, or an infinite lattice, it is clear that the difference of any two cite vectors is itself a site vector. Therefore, we have:

$$\sum_{l_1} \mathbf{q} \cdot ([\mathbf{l}_{l_1}] - [\mathbf{l}_l]) \rightarrow \sum_{\ell} \mathbf{q} \cdot [\mathbf{l}_\ell] \ , \tag{3.61}$$

and we may thus replace the cell vectors in the exponential with a new cell vector, $[\mathbf{l}_\ell]$:

$$\omega_b^2(\mathbf{q}) \left[\boldsymbol{\epsilon}_{bs}(\mathbf{q})\right] = \sum_{s_1} \frac{\exp\left\{i\mathbf{q} \cdot ([\mathbf{s}_{s_1}] - [\mathbf{s}_s])\right\}}{\sqrt{M_s M_{s_1}}} \sum_{\ell} \left[\mathbf{K}_{(1s)(\ell s_1)}\right] \exp\left(i\mathbf{q} \cdot [\mathbf{l}_\ell]\right) \left[\boldsymbol{\epsilon}_{bs_1}(\mathbf{q})\right] \ . \tag{3.62}$$

At this point, it is traditional to define the *dynamical matrix*, $[\mathbf{D}_{ss_1}(\mathbf{q})]$ as follows:

$$[\mathbf{D}_{ss_1}(\mathbf{q})] = \frac{\exp\left\{i\mathbf{q} \cdot ([\mathbf{s}_{s_1}] - [\mathbf{s}_s])\right\}}{\sqrt{M_s M_{s_1}}} \sum_{\ell} \left[\mathbf{K}_{(1s)(\ell s_1)}\right] \exp\left(i\mathbf{q} \cdot [\mathbf{l}_\ell]\right) . \tag{3.63}$$

Thus, the we have reduced our problem to one of solving the following equation:

$$\omega_b^2(\mathbf{q}) \left[\boldsymbol{\epsilon}_{bs}(\mathbf{q})\right] = \sum_{s_1} \left[\mathbf{D}_{ss_1}(\mathbf{q})\right] \left[\boldsymbol{\epsilon}_{bs_1}(\mathbf{q})\right] \ . \tag{3.64}$$

For clarity, we explicitly write $\mathbf{D}$ in matrix form:

$$\mathbf{D}(\mathbf{q}) = \begin{pmatrix} [\mathbf{D}_{11}(\mathbf{q})] & [\mathbf{D}_{12}(\mathbf{q})] & \cdots & [\mathbf{D}_{1\mathcal{S}}(\mathbf{q})] \\ [\mathbf{D}_{21}(\mathbf{q})] & [\mathbf{D}_{22}(\mathbf{q})] & \cdots & [\mathbf{D}_{2\mathcal{S}}(\mathbf{q})] \\ \vdots & \vdots & \ddots & \vdots \\ [\mathbf{D}_{\mathcal{S}1}(\mathbf{q})] & [\mathbf{D}_{\mathcal{S}2}(\mathbf{q})] & \cdots & [\mathbf{D}_{\mathcal{S}\mathcal{S}}(\mathbf{q})] \end{pmatrix} , \tag{3.65}$$

where:

$$[\mathbf{D}_{ss_1}(\mathbf{q})] = \begin{pmatrix} [\mathbf{D}_{ss_1}(\mathbf{q})]_{11} & [\mathbf{D}_{ss_1}(\mathbf{q})]_{12} & \cdots & [\mathbf{D}_{ss_1}(\mathbf{q})]_{1\mathcal{D}} \\ [\mathbf{D}_{ss_1}(\mathbf{q})]_{21} & [\mathbf{D}_{ss_1}(\mathbf{q})]_{22} & \cdots & [\mathbf{D}_{ss_1}(\mathbf{q})]_{2\mathcal{D}} \\ \vdots & \vdots & \ddots & \vdots \\ [\mathbf{D}_{ss_1}(\mathbf{q})]_{\mathcal{D}1} & [\mathbf{D}_{ss_1}(\mathbf{q})]_{\mathcal{D}2} & \cdots & [\mathbf{D}_{ss_1}(\mathbf{q})]_{\mathcal{D}\mathcal{D}} \end{pmatrix} , \tag{3.66}$$

and has eigenvectors:

$$[\boldsymbol{\epsilon}_b(\mathbf{q})] = \begin{pmatrix} [\boldsymbol{\epsilon}_{b1}(\mathbf{q})] \\ [\boldsymbol{\epsilon}_{b2}(\mathbf{q})] \\ \vdots \\ [\boldsymbol{\epsilon}_{b\mathcal{S}}(\mathbf{q})] \end{pmatrix} . \tag{3.67}$$

Thus we may write:

$$\mathbf{D}(\mathbf{q})\left[\boldsymbol{\epsilon}_b(\mathbf{q})\right] = \omega_b^2(\mathbf{q})\left[\boldsymbol{\epsilon}_b(\mathbf{q})\right] \ , \tag{3.68}$$

and see that the problem of finding the decoupled modes is now a problem of diagonalizing $\mathbf{D}(\mathbf{q})$ at a large number of $\mathbf{q}$, where $\hbar\omega_b(\mathbf{q})$ is the energy of the state associated with $\boldsymbol{\epsilon}_b(\mathbf{q})$.

For every $\mathbf{q}$, we get $\mathcal{DS}$ squared frequencies; thus, in order to have the same number of eigenvalues as $\mathbf{M}^{-1}\mathbf{K}$ we must have $\frac{\mathcal{DA}}{\mathcal{DS}} = \frac{\mathcal{A}}{\mathcal{S}} = \mathcal{L}$ q-points. The exact constraint on the values of $\mathbf{q}$ comes from the periodic boundary conditions described briefly in § 3.2.1. It may be shown that $\mathbf{D}$ is Hermitian, and as a result its eigenvectors are orthogonal. [51]

For the purpose of practical calculations, we frequently have:

$$\mathbf{K} = \sum_k \left[\mathbf{K}_k\right] , \tag{3.69}$$

where the k indexes shells of neighbors. As all of the relevant operations performed in this section have been linear, we may simply substitute the sum in wherever there is a $\mathbf{K}$. This property can be exploited to find the gradient of the dynamical matrix with respect to changes in a coefficient of $\mathbf{K}$ as is described in § 8.3.

Practically speaking, we have converted the problem of diagonalizing a matrix with on the order of $10^{23} \times 10^{23}$ elements to one of diagonalizing a matrix with on the order of 10×10 or, for a structure with more than 20 atoms per unit cell, 100×100 elements. For a crystal with only one site, a very high quality calculation of the frequency spectrum might require diagonalization at 1,000,000 q-points.

For the interested reader, myriad texts about the theory of lattice dynamics, including derivations of the dynamical matrix and its properties, are available. [51, 68, 71, 72]

3.5 The quantum harmonic oscillator revisited: phonons

We have shown that for an arbitrary crystal structure, we may decouple the oscillations into normal modes. In $\mathcal{D}$ dimensions, with $\mathcal{A}$ atoms, we find the normal coordinates U_j, with $j \in \{1, 2, \cdots, \mathcal{DA}\}$, and then solve the 1D quantum harmonic oscillator for each of the U_j. If the classical frequencies are ω_j, the quantized spectrum is then given by:

$$E_{j\lambda} = \left(\lambda + \frac{1}{2}\right)\hbar\omega_j \qquad \lambda \in \mathbb{N} \, . \tag{3.70}$$

One way to look at this, is to say that there are $\mathcal{DA}$ modes, and at any time, each mode j may be in any state λ, with energy given by Eq. 3.70. Another way follows. We note that for the j^{th}

mode, the difference between successive energy levels is always $\hbar\omega_j$. We posit the existence of a quantized excitation called a *phonon* (of type j), which has precisely this energy, and we say that the λ^{th} excited state actually corresponds to the existence of λ phonons (of type j). The meanings of the names 'creation' and 'annihilation' operator are now clear — respectively, these operators create or annihilate a phonon.

At least in the case of a harmonic crystal, phonon thermodynamics is specified completely by the distribution of phonon frequencies or the *phonon density of states*, $g(E)$:

$$g(E) \quad = \quad \frac{1}{\mathcal{DA}} \sum_{j}^{\mathcal{DA}} \delta\left[E - \hbar\omega_j\right] . \tag{3.71}$$

Or, using the $\mathbf{q}$ and the branch index b, we have:[h]

$$g(E) \quad = \quad \frac{1}{\mathcal{DSL}} \sum_{\mathbf{q}}^{\mathcal{L}} \sum_{b}^{\mathcal{DS}} \delta\left[E - E_b(\mathbf{q})\right] , \tag{3.72}$$

where $E_b(\mathbf{q}) \equiv \hbar\omega_b(\mathbf{q})$.

As we may have an arbitrary number of phonons in any state λ we see that phonons are bosons.[i] In a crystal, at a fixed temperature and volume, phonons are created and destroyed so as to minimize the Helmholtz free energy $\mathcal{F}$. This may be expressed as follows:

$$\left(\frac{\partial \mathcal{F}}{\partial \mathcal{P}_E}\right)_{T,V} = 0 , \tag{3.73}$$

where $\mathcal{P}_E$ is the number of phonons at energy E. We may identify the quantity on the left of Eq. 3.73 as the chemical potential, μ. Since this equation is true for phonons of all energies, we see that for phonons, $\mu = 0$. [76]

Finally, the mean thermal occupancy of any phonon state, $n_E(T)$, is governed by Bose-Einstein statistics, and is given as follows:

$$n_E = n_E(T) = \frac{1}{e^{\beta E} - 1} , \tag{3.74}$$

where $\beta = \frac{1}{k_{\text{B}} T}$, T is the temperature, and k_{B} is Boltzmann's constant.

[h] A reminder, the number of q-points is $\mathcal{L}$.

[i] More technically, they are *composite* bosons; that is, they are made up of other elementary particles and the agglomeration displays the statistics characteristic of bosons.

3.6 Anharmonic lattice dynamics

Thus far, we have only considered harmonic potentials; however, the failures of a harmonic model of a crystal are both considerable and well known. [50, 52] Briefly, we paraphrase the summary given by Brüesch. [51, pp. 162–163] Without anharmonicity:

- There is no thermal expansion.
- Force constants and elastic constants are independent of temperature.
- The specific heats at constant pressure or volume are equal.
- There is an infinite thermal conductivity, and measured phonon peaks would have no linewidths, because the phonons do not interact.

The effects of anharmonicity can be treated, through perturbation theory, though the accuracy of these techniques requires further testing. For the perturbed wavefunctions and energy levels of a single anharmonic quantum oscillator, Cohen-Tanoudji *et al.* have an excellent account. [75] Perturbing the potential of a 3D crystal is significantly more complicated, and we will only summarize some of the results and point to some literature.

The result of an anharmonic perturbation to the potential is that the measured energies of the phonons are shifted and broadened. The measured energy is given by:

$$E_b(\mathbf{q}) = \hbar \left[\omega_b(\mathbf{q}) + \Delta\omega_b(\mathbf{q})\right] \ , \tag{3.75}$$

and it has a peak width of $2\Gamma_b(\mathbf{q})$.

We now summarize the various contributions to the shifts and linewidths; not because we will use this level of math directly, but because we will discuss calculations of this type made by others. A disinterested reader may skip to the next section with little or no cost to the readability of the remainder of the manuscript, and the interested reader may look elsewhere for details.[51, 62–64, 77, 78]

The shift may be broken into quasiharmonic, third, and fourth order contributions:

$$\Delta\omega_b(\mathbf{q}) = \Delta^{\mathrm{Q}}\omega_b(\mathbf{q}) + \Delta^3\omega_b(\mathbf{q}) + \Delta^4\omega_b(\mathbf{q}) \ . \tag{3.76}$$

The quasiharmonic contribution to the shift is given as follows:

$$\Delta^{\mathrm{Q}}\omega = -\gamma\omega\frac{\Delta V}{V} \ , \tag{3.77}$$

where V is the volume and $\gamma = \gamma_b(\mathbf{q})$ is the Grüneisen parameter:

$$\gamma = -\frac{1}{2\omega} \sum_{(sc)} \sum_{(l_1 s_1 c_1)} \sum_{(l_2 s_2 c_2)} \left[\mathbf{K}_{(1s)(l_1 s_1)(l_2 s_2)}\right]_{cc_1c_2} \left[\boldsymbol{\epsilon}_{bs}\right]_c \left[\boldsymbol{\epsilon}_{bs_1}\right]_{c_1} \times \left(\left[\mathbf{x}_{(1s)}\right]_{c_2} - \left[\mathbf{x}_{(l_2 s_2)}\right]_{c_2}\right) \exp\left\{i\mathbf{q} \cdot \left(\left[\mathbf{x}_{(1s)}\right] - \left[\mathbf{x}_{(l_1 s_1)}\right]\right)\right\} . \tag{3.78}$$

For the sake of readability, we have subsumed the $\mathbf{q}_i$ and b_i dependence of ω and γ into a single number i. (E.g. $\gamma = \gamma_b(\mathbf{q})$ and $\omega_1 = \omega_{b_1}(\mathbf{q_1})$.) We do this for the remainder of this section. Likewise for the mean occupation factor for bosons, n (see Eq. 3.74). Further, we allow the $\mathbf{q}_i$ dependence of the polarization vectors to be indicated by the associated b_i. (E.g. $[\boldsymbol{\epsilon}_b] = [\boldsymbol{\epsilon}_b(\mathbf{q})]$ and $[\boldsymbol{\epsilon}_{b_1}] = [\boldsymbol{\epsilon}_{b_1}(\mathbf{q_1})]$.) The third order contribution to the shift, then, is given by:

$$\Delta^3\omega = -\frac{18}{\hbar^2} \sum_{\mathbf{q}_1 b_1} \sum_{\mathbf{q}_2 b_2} \left|\left[\mathbf{D}_{bb_1b_2}(\mathbf{q}, \mathbf{q_1}, \mathbf{q_2})\right]\right|^2 \left\{\mathbb{P}\left(\frac{n_1 + n_2 + 1}{\omega_1 + \omega_2 + \omega}\right) + \mathbb{P}\left(\frac{n_1 + n_2 + 1}{\omega_1 + \omega_2 - \omega}\right) + \mathbb{P}\left(\frac{n_2 - n_1}{\omega_1 - \omega_2 + \omega}\right) + \mathbb{P}\left(\frac{n_2 - n_1}{\omega_1 - \omega_2 - \omega}\right)\right\} , \tag{3.79}$$

where the $\mathbb{P}$ denotes the principal value,[79, p. 12] and is frequently approximated as follows:

$$\mathbb{P}\left(\frac{1}{v}\right) = \lim_{\epsilon \to 0} \frac{v}{v^2 + \epsilon^2} . \tag{3.80}$$

The fourth order term is considerably simpler:

$$\Delta^4\omega = \frac{12}{\hbar} \sum_{\mathbf{q}_1 b_1} \left[\mathbf{D}_{bbb_1b_1}(\mathbf{q}, -\mathbf{q}, \mathbf{q_1}, -\mathbf{q_1})\right] \{2n_1 + 1\} . \tag{3.81}$$

There is also a third order contribution to the linewidth:

$$\Gamma = -\frac{18\pi}{\hbar^2} \sum_{\mathbf{q}_1 b_1} \sum_{\mathbf{q}_2 b_2} \left|\left[\mathbf{D}_{bb_1b_2}(\mathbf{q}, \mathbf{q_1}, \mathbf{q_2})\right]\right|^2 \times \{(n_1 + n_2 + 1)\left[\delta(\omega_1 + \omega_2 - \omega) - \delta(\omega_1 + \omega_2 + \omega)\right] + (n_2 - n_1)\left[\delta(\omega_1 - \omega_2 - \omega) - \delta(\omega_1 - \omega_2 + \omega)\right]\} . \tag{3.82}$$

In the above equations, the n express the thermal occupations of the modes, and the delta functions express conservation of energy. Most of the physics is hidden in the $\mathbf{D}$, which, very roughly, correspond to Fourier transforms of the terms in the Taylor expansion of the potential. For

the third order term, we have:

$$[\mathbf{D}_{bb_1b_2}(\mathbf{q},\mathbf{q_1},\mathbf{q_2})] = \frac{1}{3!}\left(\frac{\hbar}{2N}\right)^{\frac{3}{2}} \times \sum_{(lsc)}\sum_{(l_1s_1c_1)}\sum_{(l_2s_2c_2)} \frac{\exp\left\{i\left(\mathbf{q}\cdot[\mathbf{s}_s]+\mathbf{q}_1\cdot[\mathbf{s}_{s_1}]+\mathbf{q}_2\cdot[\mathbf{s}_{s_2}]\right)\right\}}{\left(M_sM_{s_1}M_{s_2}\right)^{\frac{1}{2}}} \times \frac{\left[\boldsymbol{\epsilon}_{bs}\right]_c\left[\boldsymbol{\epsilon}_{b_1s_1}\right]_{c_1}\left[\boldsymbol{\epsilon}_{b_2s_2}\right]_{c_2}}{\left[\omega\omega_1\omega_2\right]^{\frac{1}{2}}} \left[\mathbf{K}_{(1s)(l_1s_1)(l_2s_2)}\right]_{cc_1c_2} \exp\left\{i\left(\mathbf{q}\cdot[\mathbf{l}_l]+\mathbf{q}_1\cdot[\mathbf{l}_{l_1}]+\mathbf{q}_2\cdot[\mathbf{l}_{l_2}]\right)\right\}. \tag{3.83}$$

In addition to the Fourier transform, we see that we also have inner products of all the polarization vectors of the modes, as well as weights relating to the masses of the nuclei and their frequencies of oscillation. According to Brüesch, "an analogous expression holds for the coefficients of [the fourth order term]." [51, p. 231]

The real challenge is to come up with the coefficients for the third and fourth order force constant matrices. Information about them comes from a variety of sources, including thermal expansion; temperature, pressure, and strain dependencies of elastic constants and moduli (higher order elastic constants); experimentally determined Grüneisen parameters and Debye-Waller factors; etc. Even with all of the above information their evaluation remains terribly complicated. See, for example, Leibfried and Ludwig. [80]

Chapter 4

Components of the Entropy of a Solid

To make the problem of finding the entropy of the solid tractable, we assume that the states of the system may be split into combinations of independent subsystems of states such that:

$$S = k_{\mathrm{B}} \ln \Omega \approx k_{\mathrm{B}} \ln \left(\prod_i \Omega_i \right) = k_{\mathrm{B}} \sum_i \ln \left(\Omega_i \right) = \sum_i S_i \ , \tag{4.1}$$

where Ω is the number of states of the system, Ω_i is the number of states of the subsystem i, and S_i is the entropy of subsystem i. Especially at high temperatures, it may be necessary to correct for the interactions between the subsystems. These corrections represent differences between simplified models and reality, and may thus be positive or negative. They are called 'entropy' nevertheless.

For a non-magnetic, crystalline solid, the total entropy, S, may be broken up into contributions from electrons, S_{el}, phonons, S_{ph}, and their interactions, $S_{\mathrm{el-ph}}$, with the phonon entropy usually dominant at high temperatures. For a polyatomic solid the configurational entropy, S_{cf}, is also significant, but for crystals of a pure element the configurational contribution arises from defects, and is usually quite small. In a magnetic solid, the spins contribute to the entropy through their configurations as well as their dynamics; however we will group all of this under the electronic entropy. Thus, we have:

$$S = S_{\mathrm{ph}} + S_{\mathrm{el}} + S_{\mathrm{el-ph}} + S_{\mathrm{cf}} \ . \tag{4.2}$$

First, we investigate the contributions of the phonons. The entropy for a group of non-interacting bosons is derived in Appendix B. As the chemical potential for phonons is zero, their entropy is given by:

$$S_{\mathrm{ph}} = S_{\mathrm{ph}}(T, T') = 3k_{\mathrm{B}} \int dE g_{T'} \left[(n_T + 1) \ln \left(n_T + 1 \right) - n_T \ln \left(n_T \right) \right] , \tag{4.3}$$

where both the phonon DOS at temperature T', $g_{T'}$, and the mean occupancy for bosons at temperature T, n_T, are also functions of energy E. In a truly harmonic crystal, the phonon states would remain unchanged with temperature; [50] therefore, the only temperature dependence in Eq. 4.3 would come from n_T. Thus, we calculate the harmonic phonon entropy, $S_{\rm ph,H}$, at a temperature T by using the $T' = 0$ K phonon spectrum and the occupancy at T into Eq. 4.3. In an experiment, we may determine directly the temperature dependence of the phonon DOS. It can be shown that to leading order, using Eq. 4.3 with the phonon spectrum from temperature T and the occupancy at temperature T yields the total phonon entropy. [36, 81]

We know, that real solids are not perfectly harmonic (see § 3.6). For one, in a real solid, the crystal volume changes with temperature, Classically, we may find the entropy associated with dilation of the lattice, $S_{\rm ph,D}$ by looking at the difference between the heat capacities at constant pressure and at constant volume, C_P and C_V respectively: [82]

$$S_{\rm ph,D} = S_{\rm ph,D}(T) = \int_0^T \frac{C_P - C_V}{T'} dT' = \int_0^T \frac{9K_T\alpha^2}{\rho_N} dT' \ , \tag{4.4}$$

where K_T is the isothermal bulk modulus, α is the linear coefficient of thermal expansion, and ρ_N is the number density, all of which are temperature dependent. From Eq. 4.4, we see that the increased entropy allows expansion despite the associated energy cost exacted by the elastic forces (as represented by the bulk modulus) of the crystal.

The *quasiharmonic entropy*, $S_{\rm ph,Q}$ is given by the sum of the harmonic and dilational contributions to the phonon entropy:

$$S_{\rm ph,Q} = S_{\rm ph,H} + S_{\rm ph,D} \ . \tag{4.5}$$

Any additional changes of the phonon entropy with increasing temperature are termed the *anharmonic entropy*, $S_{\rm ph,A}$, so

$$S_{\rm ph} = S_{\rm ph,H} + S_{\rm ph,D} + S_{\rm ph,A} = S_{\rm ph,Q} + S_{\rm ph,A} \ . \tag{4.6}$$

It is sometimes also useful to consider the *nonharmonic* phonon entropy, $S_{\rm ph,NH}$, which is the sum of the dilation and anharmonic contributions

$$S_{\rm ph,NH} = S_{\rm ph,D} + S_{\rm ph,A} = S_{\rm ph} - S_{\rm ph,H} \ . \tag{4.7}$$

The entropy for non-interacting fermions is derived in Appendix B, and the electronic entropy is

given as follows:

$$S_{\rm el} = S_{\rm el}(T,T') = -k_{\rm B}\int dE G_{T'}\left[(1-f_T)\ln(1-f_T) + f_T\ln(f_T)\right] , \tag{4.8}$$

where $G_{T'} = G_{T'}(E)$ is the electron DOS at temperature T' and the mean occupation for Fermions at temperature T is given by:

$$f_T = f_T(E) = \frac{1}{e^{\beta(E-\mu)}+1} . \tag{4.9}$$

The Fermi energy $E_{\rm f}$ is often a good approximation of the chemical potential, μ, of the electrons; however, we will use:

$$N_{\rm el} = \int G_T(E) f_T(E) dE , \tag{4.10}$$

where N_{el} is the number of electrons,[a] to find the chemical potential more precisely. This can make a difference in metals like iron and nickel which have their Fermi level at the top of the d-band, for example.

For a non-magnetic material, divisions similar to those made for the phonon entropy may also be made for the electronic entropy:

$$S_{\rm el} = S_{\rm el,G} + S_{\rm el,D} , \tag{4.11}$$

where $S_{\rm el,G}$ is the ground state electron entropy and $S_{\rm el,D}$ is the electronic entropy associated with changes in the electron DOS from dilation of the lattice. Both of these contributions to the electronic entropy originate with non-interacting electrons. $S_{\rm el,G}$ is found using Eq. 4.8 with the T' =0 K electron DOS and the temperature dependence coming only from f_T. To find $S_{\rm el,D}$, we use Eq. 4.8 with the electron DOS for the volume corresponding to T, and subtract the ground state term.

For a ferromagnetic material,[b] $G_T(E)$ is ferromagnetic at low temperatures, and paramagnetic at high temperatures. Regardless, we will sometimes use a non-magnetic DOS at all temperatures, and we denote this, $G_T^{\rm NM}(E)$. The electronic entropy must also include a term for the entropy associated with electron spins, $S_{\rm el,M}$:

$$S_{\rm el} = S_{\rm el,G} + S_{\rm el,M} + S_{\rm el,D} . \tag{4.12}$$

Just as in the non-magnetic case, $S_{\rm el,G}$ is determined using $G_0(E)$ in Eq. 4.8. The sum $S_{\rm el,M} + S_{\rm el,D}$ includes the effects of lattice dilation, spin dynamics, and the precipitous rise in the Fermi level at

[a] In practical calculations, this is frequently the number of valence electrons per unit cell, and is dependent on the particular potential used.

[b] We will not be considering in detail antiferromagnets or more complicated magnetic materials in this thesis.

the Curie temperature. To within the errors of our calculations,[c] $S_{\mathrm{el,G}}$ gives a lower bound on the electronic entropy. Spin dynamics and short range magnetic order make getting an upper bound more difficult. The former would cause us to underestimate the electronic entropy, and the latter to overestimate. In so much as these two errors cancel one another, the non-magnetic electronic entropy, $S_{\mathrm{el,NM}}$, calculated using Eq.4.8 with the non-magnetic electronic DOS, $G_T^{\mathrm{NM}}(E)$, gives a reasonable upper bound on the electronic entropy.[d] Thus, we have:

$$S_{\mathrm{el,G}} \lesssim S_{\mathrm{el}} \lesssim S_{\mathrm{el,NM}} \ . \tag{4.13}$$

Here, $S_{\mathrm{el,NM}}$ includes the entropy due to dilation of the lattice, and we suggest the following approximation for the dilational contribution to the electronic entropy of a magnetic material:

$$S_{\mathrm{el,D}} \approx S_{\mathrm{el,NM}} - S_{\mathrm{el,G,NM}} \ , \tag{4.14}$$

where $S_{\mathrm{el,G,NM}}$ is the entropy found by using $G_0^{\mathrm{NM}}(E)$ in Eq. 4.8. Roughly, this should give some account of the effects of the expansion of the lattice as separated from spin fluctuations and the rise in the Fermi level at the Curie temperature.

We now consider interactions between electrons and phonons. The electron-phonon entropy is separated into two parts:

$$S_{\mathrm{el-ph}} = S_{\mathrm{el-ph,na}} + S_{\mathrm{el-ph,ad}} \ . \tag{4.15}$$

The non-adiabatic electron-phonon entropy, $S_{\mathrm{el-ph,na}}$, which dominates at low temperatures, is associated with the velocities of the nuclei and gives the mixing of the electron ground states from the nuclear motion. At higher temperatures, the adiabatic electron-phonon entropy, $S_{\mathrm{el-ph,ad}}$, dominates. It arises from the displacements of the nuclei, and accounts for the thermal shifts of electron states caused by averaged nuclear motions. These contributions to the entropy have been discussed in greater detail.[25, 26, 28–30, 37, 38] There should also be a contribution to the electron-phonon entropy from the dilation of the lattice; however, we expect this to be negligible.

Putting this all together, we have:

$$S \approx S_{\mathrm{ph,H}} + S_{\mathrm{ph,D}} + S_{\mathrm{ph,A}} + S_{\mathrm{el,G}} + S_{\mathrm{el,D}} + S_{\mathrm{el,M}} + S_{\mathrm{el-ph,ad}} + S_{\mathrm{el-ph,na}} + S_{\mathrm{cf}} \ . \tag{4.16}$$

[c] According to Wallace, [37] these may be as large as 10%.

[d] We will examine this in greater detail in our discussions of iron and nickel.

Chapter 5

Neutron Scattering

The primary means of investigating the structure and dynamics of crystals is through their scattering of incident radiation. A very basic picture of what goes on in a scattering experiment is shown in Fig. 5.1. There is a source of radiation, a sample, and a detector. Depending on what we know about the source, and on what we measure in the detector, we may garner information about the sample by analyzing the differences between the incident and detected radiation.

Our study of iron was performed using x-rays from a synchotron source, and this type of experiment is discussed in Chapter 12. We treat neutron scattering separately and up front because it applies to our studies of both aluminum and nickel, for which thermal neutrons from a spallation source were used, and because it is a prerequisite for parts of the chapters on data analysis.

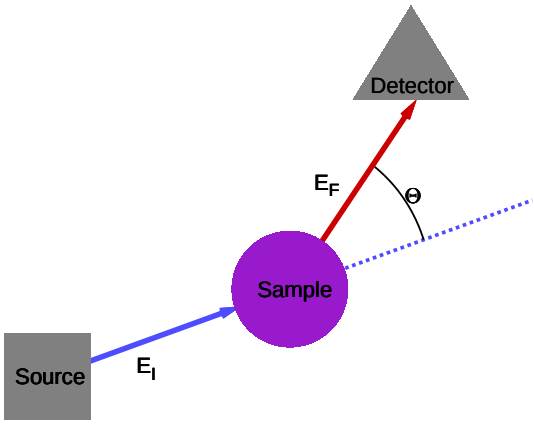

Figure 5.1: A very basic depiction of a scattering experiment. Radiation leaves the source, and interacts with the sample. Radiation is captured at the detector. The scattering angle Θ and the energy acquired by the sample $E = E_{\mathrm{I}} - E_{\mathrm{F}}$ are two things that might be measured in such an experiment.

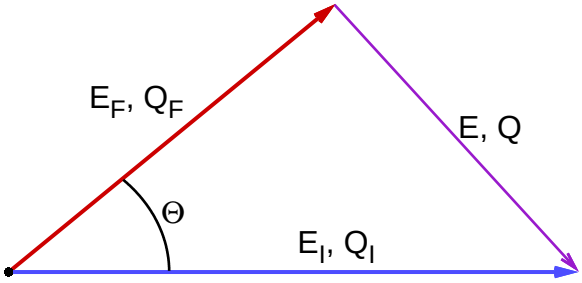

Figure 5.2: Depiction of the energies and wavevectors involved in a scattering experiment. The incident radiation has energy and wavevector E_{I} and $\mathbf{Q}_{\mathrm{I}}$, the outgoing E_{F} and $\mathbf{Q}_{\mathrm{F}}$, and the energy and wavevector *transferred* to the sample are given by $E = E_{\mathrm{I}} - E_{\mathrm{F}}$ and $\mathbf{Q} = Q_{\mathrm{I}} - Q_{\mathrm{F}}$.

5.1 General theory of neutron scattering

The theory of neutron scattering has been discussed in great detail elsewhere; [83–85] and here we do little more than briefly summarize some of the major results. Where applicable, equation numbers for Squire's book [83] are provided.

Modulo some details about particular instruments, the quantity measured in a neutron scattering experiment is the number of neutrons that are scattered into some spread of solid angle $d\Omega$ centered around Ω, with some spread of final energies dE_{F} centered around E_{F}. We expect the number of neutrons arriving per unit time at any given solid angle Ω and energy E_{F} to be proportional to the flux of the incident neutrons, Φ_{I}, as well as to the spreads in energy and solid angle:

$$\frac{\text{number of neutrons scattered towards } \Omega \, , E_{\mathrm{F}}}{\text{unit time}} \quad = \quad \left(\frac{d^2\sigma}{d\Omega dE_{\mathrm{F}}}\right) \Phi_{\mathrm{I}} d\Omega dE_{\mathrm{F}} \, , \tag{5.1}$$

or:

$$\left(\frac{d^2\sigma}{d\Omega dE_{\mathrm{F}}}\right) \quad = \quad \frac{\text{number of neutrons scattered towards } \Omega \, , E_{\mathrm{F}}}{\text{unit time}} \frac{1}{\Phi_{\mathrm{I}} d\Omega dE_{\mathrm{F}}} \tag{5.2}$$

(Squires, Eq. 1.11), where $\left(\frac{d^2\sigma}{d\Omega dE_{\mathrm{F}}}\right)$, which has units of area per energy, is known as the *double-differential cross-section*. Using Fermi's golden rule [74, 75, 83] to describe transition probabilities between states of the scattering system, and the Fermi pseudopotential [83, 84] to describe the interaction of the neutron and the nucleus, we arrive at a very general expression for the double differential scattering cross-section:

$$\left(\frac{d^2\sigma}{d\Omega dE_{\mathrm{F}}}\right) \quad = \quad \frac{Q_{\mathrm{F}}}{Q_{\mathrm{I}}} \frac{1}{2\pi\hbar} \sum_{ij} \mathrm{a}_i \mathrm{a}_j \int \langle \exp\{-i\mathbf{Q} \cdot [\mathbf{r}_j(0)]\} \exp\{i\mathbf{Q} \cdot [\mathbf{r}_i(t)]\} \rangle \, e^{-i\omega t} dt \tag{5.3}$$

(Squires, Eq. 2.59), where $\mathbf{Q}_{\mathrm{I}}$, $\mathbf{Q}_{\mathrm{F}}$, $\mathbf{Q}$, $\mathbf{r}_i$, a_i, ω, and t are the initial and final neutron wavevectors, the wavevector transfer, the instantaneous position and scattering length of the atom indexed i, angular frequency, and time, respectively. The angle brackets indicate a thermal average.

It is traditional to separate the scattering into coherent and incoherent contributions. Generally, we do not deal with isotopically pure samples; therefore, we need to average over the scattering lengths for different isotopes weighted by their natural frequencies. To do this, we:

- Break the sum into one over $i = j$ and another over $i \neq j$.
- Use $\langle \mathrm{a}_i \mathrm{a}_j \rangle = \langle \mathrm{a}_i \rangle \langle \mathrm{a}_j \rangle$ for $i \neq j$.
- Add and subtract an $i = j$ term to get rid of the $i \neq j$ condition on the sum.

This yields:

$$\left(\frac{d^2\sigma^{\rm inc}}{d\Omega dE_{\rm F}}\right) = \frac{Q_{\rm F}}{Q_{\rm I}}\frac{1}{2\pi\hbar}\sum_i \frac{\sigma_i^{\rm inc}}{4\pi}\int \langle \exp\{-i\mathbf{Q}\cdot[\mathbf{r}_i(0)]\}\exp\{i\mathbf{Q}\cdot[\mathbf{r}_i(t)]\}\rangle\, e^{-i\omega t}dt\ , \quad (5.4)$$

$$\left(\frac{d^2\sigma^{\rm coh}}{d\Omega dE_{\rm F}}\right) = \frac{Q_{\rm F}}{Q_{\rm I}}\frac{1}{2\pi\hbar}\sum_{ij} \langle {\rm a}_i\rangle\langle {\rm a}_j\rangle \int \langle \exp\{-i\mathbf{Q}\cdot[\mathbf{r}_j(0)]\}\exp\{i\mathbf{Q}\cdot[\mathbf{r}_i(t)]\}\rangle\, e^{-i\omega t}dt \quad (5.5)$$

(Compare to Squires, Eqs. 2.68, 2.69), where we have used $\sigma_i^{\rm inc} = 4\pi\left(\langle {\rm a}_i^2\rangle - \langle {\rm a}_i\rangle^2\right)$. The first equation depends only on the motions of a single atom i at a time. It thus gives the *incoherent scattering*. The second equation, then, is the coherent scattering, and it depends on the motions of both atoms i and j. We also have $\sigma^{\rm coh} = 4\pi\langle {\rm a}_i\rangle^2$; however, we may not insert this into the above equation for the coherent scattering unless we have a monatomic system.

5.2 Neutron scattering from crystals

Assuming a crystalline structure allows us to make further progress in developing theoretical expressions for the neutron scattering cross section. The exponentials from Eqs. 5.4 and 5.5 that involve the instantaneous positions of the atoms may be broken up into time-dependent and time-independent parts, using:

$$[\mathbf{r}_i(t)] = [\mathbf{x}_i] + [\mathbf{u}_i(t)] = \left[\mathbf{x}_{(ls)}\right] + \left[\mathbf{u}_{(ls)}(t)\right]\ , \quad (5.6)$$

where $\mathbf{r}_i$, $\mathbf{x}_i$, and $\mathbf{u}_i$ are respectively the instantaneous position, equilibrium position, and displacement of atom i. Therefore, we may write:

$$\left(\frac{d^2\sigma^{\rm inc}}{d\Omega dE_{\rm F}}\right) = \frac{Q_{\rm F}}{Q_{\rm I}}\frac{1}{2\pi\hbar}\sum_{ls} \frac{\sigma_s^{\rm inc}}{4\pi}\int \left\langle \exp\left\{-i\mathbf{Q}\cdot\left[\mathbf{u}_{(ls)}(0)\right]\right\}\exp\left\{i\mathbf{Q}\cdot\left[\mathbf{u}_{(ls)}(t)\right]\right\}\right\rangle e^{-i\omega t}dt\ , \quad (5.7)$$

$$\left(\frac{d^2\sigma^{\rm coh}}{d\Omega dE_{\rm F}}\right) = \frac{Q_{\rm F}}{Q_{\rm I}}\frac{1}{2\pi\hbar}\sum_{(ls)}\sum_{(l_1s_1)} \langle {\rm a}_s\rangle\langle {\rm a}_{s_1}\rangle \exp\left\{-i\mathbf{Q}\cdot\left(\left[\mathbf{x}_{(ls)}\right] - \left[\mathbf{x}_{(l_1s_1)}\right]\right)\right\}$$
$$\times \int \left\langle \exp\left\{-i\mathbf{Q}\cdot\left[\mathbf{u}_{(l_1s_1)}(0)\right]\right\}\exp\left\{i\mathbf{Q}\cdot\left[\mathbf{u}_{(ls)}(t)\right]\right\}\right\rangle e^{-i\omega t}dt\ , \quad (5.8)$$

where we have used the fact that the (isotopically averaged) scattering lengths must be a function of the site alone. We may further simplify the equations by fixing one of the atoms to be in the first

cell:

$$\left(\frac{d^2\sigma^{\rm inc}}{d\Omega dE_{\rm F}}\right) = \frac{Q_{\rm F}}{Q_{\rm I}}\frac{\mathcal{L}}{2\pi\hbar}\sum_s \frac{\sigma_s^{\rm inc}}{4\pi}\int \langle \exp\{-i\mathbf{Q}\cdot[\mathbf{u}_s(0)]\}\exp\{i\mathbf{Q}\cdot[\mathbf{u}_s(t)]\}\rangle\, e^{-i\omega t}dt\ , \quad (5.9)$$

$$\left(\frac{d^2\sigma^{\rm coh}}{d\Omega dE_{\rm F}}\right) = \frac{Q_{\rm F}}{Q_{\rm I}}\frac{\mathcal{L}}{2\pi\hbar}\sum_\ell \sum_{ss_1}\langle \mathrm{a}_s\rangle\langle \mathrm{a}_{s_1}\rangle \exp\{-i\mathbf{Q}\cdot[\mathbf{l}_\ell]\}\exp\{-i\mathbf{Q}\cdot([\mathbf{s}_s]-[\mathbf{s}_{s_1}])\}$$
$$\times\int \left\langle \exp\{-i\mathbf{Q}\cdot[\mathbf{u}_{s_1}(0)]\}\exp\left\{i\mathbf{Q}\cdot\left[\mathbf{u}_{(\ell s)}(t)\right]\right\}\right\rangle e^{-i\omega t}dt\ , \quad (5.10)$$

where we have dropped the cell index whenever it was fixed to be 1.

It is traditional, here, to define two operators, $\hat{\mathbf{U}}$ and $\hat{\mathbf{V}}$:

$$\hat{\mathbf{U}}_s \equiv -i\mathbf{Q}\cdot[\mathbf{u}_s(0)]\ , \quad (5.11)$$

$$\hat{\mathbf{V}}_{(\ell s)} \equiv i\mathbf{Q}\cdot\left[\mathbf{u}_{(\ell s)}(t)\right]\ . \quad (5.12)$$

Using the following results:

$$\left\langle \exp\left\{\hat{\mathbf{U}}_{(l_1 s_1)}\right\}\exp\left\{\hat{\mathbf{V}}_{(ls)}\right\}\right\rangle = \exp\left\langle\frac{1}{2}\left(\hat{\mathbf{U}}^2_{(l_1 s_1)}+\hat{\mathbf{V}}^2_{(ls)}\right)\right\rangle \exp\left\langle\hat{\mathbf{U}}_{(l_1 s_1)}\hat{\mathbf{V}}_{(ls)}\right\rangle\ , \quad (5.13)$$

$$\langle\hat{\mathbf{U}}^2_s\rangle = \langle\hat{\mathbf{V}}^2_{(\ell s)}\rangle \quad (5.14)$$

(Compare to Squires, Eqs. 3.23–3.35), we may write the two cross-sections as follows:

$$\left(\frac{d^2\sigma^{\rm inc}}{d\Omega dE_{\rm F}}\right) = \frac{Q_{\rm F}}{Q_{\rm I}}\frac{\mathcal{L}}{2\pi\hbar}\sum_s \frac{\sigma_s^{\rm inc}}{4\pi}\exp\left\langle\hat{\mathbf{U}}^2_s\right\rangle\int \exp\left\langle\hat{\mathbf{U}}_s\hat{\mathbf{V}}_s\right\rangle e^{-i\omega t}dt\ , \quad (5.15)$$

$$\left(\frac{d^2\sigma^{\rm coh}}{d\Omega dE_{\rm F}}\right) = \frac{Q_{\rm F}}{Q_{\rm I}}\frac{\mathcal{L}}{2\pi\hbar}\sum_\ell \sum_{ss_1}\langle \mathrm{a}_s\rangle\langle \mathrm{a}_{s_1}\rangle \exp\{-i\mathbf{Q}\cdot[\mathbf{l}_\ell]\}\exp\{-i\mathbf{Q}\cdot([\mathbf{s}_s]-[\mathbf{s}_{s_1}])\}$$
$$\times\exp\left\langle\frac{1}{2}\left(\hat{\mathbf{U}}^2_{s_1}+\hat{\mathbf{U}}^2_s\right)\right\rangle\int \exp\left\langle\hat{\mathbf{U}}_{s_1}\hat{\mathbf{V}}_{(\ell s)}\right\rangle e^{-i\omega t}dt \quad (5.16)$$

(Compare to Squires, Eqs. 3.127, 3.36).

We now expand $\exp\left\langle\hat{\mathbf{U}}_{s_1}\hat{\mathbf{V}}_{(\ell s)}\right\rangle$:

$$\left(\frac{d^2\sigma^{\rm inc}}{d\Omega dE_{\rm F}}\right) = \frac{Q_{\rm F}}{Q_{\rm I}}\frac{\mathcal{L}}{2\pi\hbar}\sum_s \frac{\sigma_s^{\rm inc}}{4\pi}\exp\left\langle\hat{\mathbf{U}}^2_s\right\rangle\int \sum_{\mathcal{P}}\frac{1}{\mathcal{P}!}\left\langle\hat{\mathbf{U}}_s\hat{\mathbf{V}}_s\right\rangle^{\mathcal{P}} e^{-i\omega t}dt\ , \quad (5.17)$$

$$\left(\frac{d^2\sigma^{\rm coh}}{d\Omega dE_{\rm F}}\right) = \frac{Q_{\rm F}}{Q_{\rm I}}\frac{\mathcal{L}}{2\pi\hbar}\sum_\ell \exp\{-i\mathbf{Q}\cdot[\mathbf{l}_\ell]\}\sum_{ss_1}\langle \mathrm{a}_s\rangle\langle \mathrm{a}_{s_1}\rangle \exp\{-i\mathbf{Q}\cdot([\mathbf{s}_s]-[\mathbf{s}_{s_1}])\}$$
$$\times\exp\left\langle\frac{1}{2}\left(\hat{\mathbf{U}}^2_{s_1}+\hat{\mathbf{U}}^2_s\right)\right\rangle\int \sum_{\mathcal{P}}\frac{1}{\mathcal{P}!}\left\langle\hat{\mathbf{U}}_{s_1}\hat{\mathbf{V}}_{(\ell s)}\right\rangle^{\mathcal{P}} e^{-i\omega t}dt\ . \quad (5.18)$$

Each term in the series represents scattering involving $\mathcal{P}$ phonons.

In the rest of this section, we give results for the Debye-Waller factor, Bragg and 1-phonon

scattering, and then develop the expression for multiphonon scattering, all for an arbitrary crystal structure.

5.2.1 The Debye-Waller factor

The Debye-Waller factor is related to the mean-squared displacement, determines the ratio of elastic to inelastic scattering intensity, and is given by $\exp(2W_s)$, with:

$$W_s = -\frac{1}{2}\left\langle \hat{\mathbf{U}}_s^2 \right\rangle = \frac{\hbar}{4M_s\mathcal{L}} \sum_b \frac{\left|\mathbf{Q}\cdot[\boldsymbol{\epsilon}_{bs}]\right|^2}{\omega_b} \langle 2n_b + 1\rangle \tag{5.19}$$

(Squires, Eq. 3.74). For a large enough crystal the spectrum of frequencies is continuous, and we may convert the sum over branches to an integral:

$$W_s = \frac{\hbar}{4M_s\mathcal{L}} \mathcal{D}\mathcal{L} \int \left\langle \left|\mathbf{Q}\cdot[\boldsymbol{\epsilon}_{bs}]\right|^2 \right\rangle_{\omega=\omega_b} \frac{g_s(\omega)}{\omega} \langle 2n_\omega + 1\rangle d\omega \ . \tag{5.20}$$

In 3D, for a monatomic cubic crystal, we have:

$$\left\langle \left|\mathbf{Q}\cdot[\boldsymbol{\epsilon}_{bs}]\right|^2 \right\rangle_{\omega=\omega_b} = \frac{1}{3}Q^2 \ . \tag{5.21}$$

Thus, Eq. 5.20 can be rewritten as follows:

$$W = \frac{\hbar Q^2}{4M} \int \frac{g(\omega)}{\omega} \langle 2n + 1\rangle d\omega \tag{5.22}$$

(Compare to Squires, Eq. 3.66). This is frequently used as an approximation for other crystals as well, including polyatomic ones:

$$W_s = \frac{\hbar Q^2}{4M_s} \int \frac{g_s(\omega)}{\omega} \langle 2n + 1\rangle d\omega \ . \tag{5.23}$$

5.2.2 Elastic scattering

To find the elastic scattering, we set $\mathcal{P} = 0$ in Eqs. 5.17 and 5.18:

$$\left(\frac{d^2\sigma^{\rm inc}}{d\Omega dE_{\rm F}}\right)_0 = \frac{Q_{\rm F}}{Q_{\rm I}} \frac{\mathcal{L}}{2\pi\hbar} \sum_s \frac{\sigma_s^{\rm inc}}{4\pi} e^{-2W_s} \int e^{-i\omega t} dt \ , \tag{5.24}$$

$$\left(\frac{d^2\sigma^{\rm coh}}{d\Omega dE_{\rm F}}\right)_0 = \frac{Q_{\rm F}}{Q_{\rm I}} \frac{\mathcal{L}}{2\pi\hbar} \sum_\ell \exp\{-i\mathbf{Q}\cdot[\mathbf{l}_\ell]\} \sum_{ss_1} \langle \mathrm{a}_s\rangle\langle \mathrm{a}_{s_1}\rangle \exp\{-i\mathbf{Q}\cdot([\mathbf{s}_s] - [\mathbf{s}_{s_1}])\}$$
$$\times e^{-W_{s_1} - W_s} \int e^{-i\omega t} dt \ . \tag{5.25}$$

The $\frac{1}{2\pi\hbar}$ time the integrals yield delta functions in E, and the sum over ℓ also gives a delta function:

$$\left(\frac{d^2\sigma^{\rm inc}}{d\Omega dE_{\rm F}}\right)_0 = \frac{Q_{\rm F}}{Q_{\rm I}}\mathcal{L}\sum_s \frac{\sigma_s^{\rm inc}}{4\pi}e^{-2W_s}\delta(E)\ , \tag{5.26}$$

$$\left(\frac{d^2\sigma^{\rm coh}}{d\Omega dE_{\rm F}}\right)_0 = \frac{Q_{\rm F}}{Q_{\rm I}}\mathcal{L}\frac{(2\pi)^{\mathcal{D}}}{V_{\mathbf{q}}}\sum_{\mathbf{q}}\delta(\mathbf{Q}-\mathbf{q})\left|\sum_s \langle {\rm a}_s\rangle e^{-i\mathbf{Q}\cdot[\mathbf{s}_s]}e^{-W_s}\right|^2\delta(E)\ . \tag{5.27}$$

Finally, we integrate over $E_{\rm F}$, to get:

$$\left(\frac{d\sigma^{\rm inc}}{d\Omega}\right)_0 = \frac{\mathcal{L}}{4\pi}\sum_s \sigma_s^{\rm inc}e^{-2W_s}\ , \tag{5.28}$$

$$\left(\frac{d\sigma^{\rm coh}}{d\Omega}\right)_0 = \mathcal{L}\frac{(2\pi)^{\mathcal{D}}}{V_{\mathbf{q}}}\sum_{\mathbf{q}}\delta(\mathbf{Q}-\mathbf{q})\left|\sum_s \langle {\rm a}_s\rangle e^{-i\mathbf{Q}\cdot[\mathbf{s}_s]}e^{-W_s}\right|^2 \tag{5.29}$$

(Compare to Squires, Eqs. 3.137, 3.75 & 3.76), where the delta-function forced $Q_{\rm I} = Q_{\rm F}$. The first equation gives the incoherent elastic scattering, and it is closely related to the Debye-Waller factor and the mean-squared displacement. The second is the coherent elastic scattering, or Bragg scattering, and it carries information about the crystal structure.

5.2.3 1-phonon scattering

To find the 1-phonon scattering, we set $\mathcal{P} = 1$ in Eqs. 5.17 and 5.18.

$$\left(\frac{d^2\sigma^{\rm inc}}{d\Omega dE_{\rm F}}\right)_1 = \frac{Q_{\rm F}}{Q_{\rm I}}\frac{\mathcal{L}}{2\pi\hbar}\sum_s \frac{\sigma_s^{\rm inc}}{4\pi}e^{-2W_s}\int \langle \hat{\mathbf{U}}_s\hat{\mathbf{V}}_s\rangle e^{-i\omega t}dt\ , \tag{5.30}$$

$$\left(\frac{d^2\sigma^{\rm coh}}{d\Omega dE_{\rm F}}\right)_1 = \frac{Q_{\rm F}}{Q_{\rm I}}\frac{\mathcal{L}}{2\pi\hbar}\sum_\ell \exp\left\{-i\mathbf{Q}\cdot[\mathbf{l}_\ell]\right\}\sum_{ss_1}\langle {\rm a}_s\rangle\langle {\rm a}_{s_1}\rangle \exp\left\{-i\mathbf{Q}\cdot([\mathbf{s}_s]-[\mathbf{s}_{s_1}])\right\}$$
$$\times e^{-W_{s_1}-W_s}\int \langle \hat{\mathbf{U}}_{s_1}\hat{\mathbf{V}}_{\ell s}\rangle e^{-i\omega t}dt\ . \tag{5.31}$$

Using:

$$\langle \hat{\mathbf{U}}_{s_1}\hat{\mathbf{V}}_{\ell s}\rangle = \frac{\hbar}{2\mathcal{L}}\sum_b\left(\frac{1}{M_{s_1}M_s}\right)^{\frac{1}{2}}\frac{\mathbf{Q}\cdot[\boldsymbol{\epsilon}_{bs}]\,\mathbf{Q}\cdot[\boldsymbol{\epsilon}_{bs_1}]}{\omega_b}$$
$$\times\left\{\exp\left(-i\mathbf{q}\cdot[\mathbf{l}_\ell]+i\omega_b t\right)\langle n_b+1\rangle + \exp\left(i\mathbf{q}\cdot[\mathbf{l}_\ell]-i\omega_b t\right)\langle n_b\rangle\right\} \tag{5.32}$$

(Compare to Squires, Eqs. 3.105–3.108), we have:

$$\left(\frac{d^2\sigma^{\rm inc}}{d\Omega dE_{\rm F}}\right)_1 = \frac{Q_{\rm F}}{Q_{\rm I}}\frac{1}{2\pi}\sum_s\frac{\sigma_s^{\rm inc}}{8\pi}e^{-2W_s}\int\sum_b\frac{1}{M_s}\frac{|\mathbf{Q}\cdot[\boldsymbol{\epsilon}_{bs}]|^2}{\omega_b}$$
$$\times\left\{\exp\left(i\omega_b t\right)\langle n_b+1\rangle + \exp\left(-i\omega_b t\right)\langle n_b\rangle\right\}e^{-i\omega t}dt\ , \tag{5.33}$$

$$\left(\frac{d^2\sigma^{\rm coh}}{d\Omega dE_{\rm F}}\right)_1 = \frac{Q_{\rm F}}{Q_{\rm I}}\frac{1}{4\pi}\sum_\ell \exp\left\{-i\mathbf{Q}\cdot[\mathbf{l}_\ell]\right\}\sum_{ss_1}\langle \mathrm{a}_s\rangle\langle \mathrm{a}_{s_1}\rangle \exp\left\{-i\mathbf{Q}\cdot([\mathbf{s}_s]-[\mathbf{s}_{s_1}])\right\}$$
$$\times e^{-W_{s_1}-W_s}\int\sum_b\left(\frac{1}{M_{s_1}M_s}\right)^{\frac{1}{2}}\frac{\mathbf{Q}\cdot[\boldsymbol{\epsilon}_{bs}]\,\mathbf{Q}\cdot[\boldsymbol{\epsilon}_{bs_1}]}{\omega_b}$$
$$\times\left\{\exp\left(-i\mathbf{q}\cdot[\mathbf{l}_\ell]+i\omega_b t\right)\langle n_b+1\rangle+\exp\left(i\mathbf{q}\cdot[\mathbf{l}_\ell]-i\omega_b t\right)\langle n_b\rangle\right\}e^{-i\omega t}dt\ . \quad (5.34)$$

Here, $\frac{1}{2\pi}$ times the integrals yield delta functions in ω, and the sum over ℓ also gives delta functions in $\mathbf{q}$ and $\mathbf{q}_1$:

$$\left(\frac{d^2\sigma^{\rm inc}}{d\Omega dE_{\rm F}}\right)_1 = \frac{Q_{\rm F}}{Q_{\rm I}}\frac{1}{8\pi}\sum_s\frac{\sigma_s^{\rm inc}}{M_s}e^{-2W_s}$$
$$\times\sum_b\frac{\left|\mathbf{Q}\cdot[\boldsymbol{\epsilon}_{bs}]\right|^2}{\omega_b}\left\{\delta(\omega-\omega_b)\langle n_b+1\rangle+\delta(\omega+\omega_b)\langle n_b\rangle\right\}\ , \quad (5.35)$$

$$\left(\frac{d^2\sigma^{\rm coh}}{d\Omega dE_{\rm F}}\right)_1 = \frac{Q_{\rm F}}{Q_{\rm I}}\frac{(2\pi)^{\mathcal{D}}}{2V_{\mathbf{q}}}\sum_{\mathbf{q}_1}\sum_b\left|\sum_s\frac{\langle \mathrm{a}_s\rangle}{\sqrt{M_s}}\left(\mathbf{Q}\cdot[\boldsymbol{\epsilon}_{bs}]\right)e^{-i\mathbf{Q}\cdot[\mathbf{s}_s]}e^{-W_s}\right|^2$$
$$\times\frac{1}{\omega_b}\{\delta(\mathbf{Q}-\mathbf{q}-\mathbf{q}_1)\langle n_b+1\rangle\,\delta(\omega-\omega_b)+\delta(\mathbf{Q}+\mathbf{q}-\mathbf{q}_1)\langle n_b\rangle\,\delta(\omega+\omega_b)\} \quad (5.36)$$

(Squires, Eqs. 3.138, 3.120). In both expressions, the first term corresponds to the creation of, and the second term to annihilation of one phonon.

We may further simplify the expression for the incoherent cross-section. With $x=\hbar\omega\beta$, we use:

$$\langle n(\omega)+1\rangle = \frac{e^x}{e^x-1}=\frac{1}{1-e^{-x}}=\frac{-1}{e^{-x}-1}=-\langle n(-\omega)\rangle\ , \quad (5.37)$$

to write:

$$\left(\frac{d^2\sigma^{\rm inc}}{d\Omega dE_{\rm F}}\right)_1 = \frac{Q_{\rm F}}{Q_{\rm I}}\frac{\mathcal{D}\mathcal{L}}{8\pi}\sum_s\frac{\sigma_s^{\rm inc}}{M_s}e^{-2W_s}\frac{g_s(\omega)}{\omega}\frac{1}{1-e^{-\hbar\omega\beta}}\left\langle\left|\mathbf{Q}\cdot[\boldsymbol{\epsilon}_{bs}]\right|^2\right\rangle_{\omega=\omega_b}\ , \quad (5.38)$$

where $g_s(\omega)$ is the *partial phonon DOS* for vibrations of atoms at site s. We have also taken $g_s(-\omega)=g_s(\omega)$, and used the fact that for some function f_s:

$$\sum_b f_s(\omega_b)=\mathcal{D}\mathcal{L}\int g_s(\omega)f_s(\omega)d\omega\ . \quad (5.39)$$

In 3D, for a monatomic cubic crystal, we have $\mathcal{D}=3$ and $\left\langle\left|\mathbf{Q}\cdot[\boldsymbol{\epsilon}_{bs}]\right|^2\right\rangle_{\omega=\omega_b}=\frac{1}{3}Q^2$. Therefore:

$$\left(\frac{d^2\sigma^{\rm inc}}{d\Omega dE_{\rm F}}\right)_1 = \frac{Q_{\rm F}}{Q_{\rm I}}\frac{\mathcal{L}\sigma^{\rm inc}}{8\pi M}\frac{g(\omega)}{\omega}\frac{1}{1-e^{-\hbar\omega\beta}}Q^2e^{-2W}\ . \quad (5.40)$$

Again, we point out that $\left\langle\left|\mathbf{Q}\cdot[\boldsymbol{\epsilon}_{bs}]\right|^2\right\rangle_{\omega=\omega_b}=\frac{1}{3}Q^2$ is frequently not a bad approximation for other

crystal structures; therefore:

$$\left(\frac{d^2\sigma^{\rm inc}}{d\Omega dE_{\rm F}}\right)_1 \approx \frac{Q_{\rm F}}{Q_{\rm I}}\frac{\mathcal{L}}{8\pi\omega}\frac{Q^2}{1-e^{-\hbar\omega\beta}}\sum_s \frac{\sigma_s^{\rm inc}}{M_s}e^{-2W_s}g_s(\omega)\ . \tag{5.41}$$

The factor modifying multiplying the DOS is a simplified version of the *neutron weight factor*, which modulates the scattering from polyatomic crystals.

5.2.4 Multiphonon scattering

A neutron interacting with a sample may actually produce or annihilate (or some combination thereof) more than one phonon at a time. Like the 0- and 1-phonon scattering, these processes can be either coherent or incoherent. The *incoherent approximation* is the assumption that for numbers of phonons $\mathcal{P} > 1$, the coherent scattering is well approximated by the incoherent scattering multiplied by the ratio of the coherent and incoherent cross-sections, $\frac{\sigma^{\rm coh}}{\sigma^{\rm inc}}$.[83, 84, 86]

From Eq. 5.17, we see that the incoherent scattering cross-section for site s and $\mathcal{P}$ phonons is proportional to the Fourier transform $\left\langle \hat{\mathbf{U}}_s\hat{\mathbf{V}}_s\right\rangle^{\mathcal{P}}$:

$$\frac{1}{2\pi}\int \left\langle \hat{\mathbf{U}}_s\hat{\mathbf{V}}_s\right\rangle^{\mathcal{P}} e^{-i\omega t}dt = \mathcal{FT}\left\{\left\langle \hat{\mathbf{U}}_s\hat{\mathbf{V}}_s\right\rangle^{\mathcal{P}}\right\}. \tag{5.42}$$

For $\mathcal{P} \geq 1$, we may rewrite this in the following form:

$$\frac{1}{2\pi}\int \left\langle \hat{\mathbf{U}}_s\hat{\mathbf{V}}_s\right\rangle^{\mathcal{P}} e^{-i\omega t}dt = \mathcal{FT}\left\{\left\langle \hat{\mathbf{U}}_s\hat{\mathbf{V}}_s\right\rangle^{\mathcal{P}-1}\left\langle \hat{\mathbf{U}}_s\hat{\mathbf{V}}_s\right\rangle\right\}. \tag{5.43}$$

The Fourier transform of the product may be rewritten as a convolution (denoted with $*$) of the Fourier transforms of the multiplicands, yielding a recursion relation for the multiphonon scattering:

$$\begin{aligned}\frac{1}{2\pi}\int \left\langle \hat{\mathbf{U}}_s\hat{\mathbf{V}}_s\right\rangle^{\mathcal{P}} e^{-i\omega t}dt &= \mathcal{FT}\left\{\left\langle \hat{\mathbf{U}}_s\hat{\mathbf{V}}_s\right\rangle^{\mathcal{P}-1}\right\} * \mathcal{FT}\left\{\left\langle \hat{\mathbf{U}}_s\hat{\mathbf{V}}_s\right\rangle\right\} \\ &= \mathcal{FT}\left\{\left\langle \hat{\mathbf{U}}_s\hat{\mathbf{V}}_s\right\rangle^{\mathcal{P}-1}\right\} * \frac{1}{2\pi}\int \left\langle \hat{\mathbf{U}}_s\hat{\mathbf{V}}_s\right\rangle e^{-i\omega t}dt\ .\end{aligned} \tag{5.44}$$

We have already determined the integral on the far right, thus the problem of determining the multiphonon scattering is *solved*, given that we know the 1-phonon scattering. We denote $\mathcal{P}$ convolutions with $*^{\mathcal{P}}$, so that:

$$\frac{1}{2\pi}\int \left\langle \hat{\mathbf{U}}_s\hat{\mathbf{V}}_s\right\rangle^{\mathcal{P}} e^{-i\omega t}dt = \left[\frac{1}{2\pi}\int \left\langle \hat{\mathbf{U}}_s\hat{\mathbf{V}}_s\right\rangle e^{-i\omega t}dt\right] *^{\mathcal{P}} \left[\frac{1}{2\pi}\int \left\langle \hat{\mathbf{U}}_s\hat{\mathbf{V}}_s\right\rangle e^{-i\omega t}dt\right]\ . \tag{5.45}$$

Comparing Eqs. 5.30 and 5.40, we have for the case of a monatomic cubic lattice in 3D:

$$\frac{1}{2\pi}\int \left\langle \hat{\mathbf{U}}\hat{\mathbf{V}} \right\rangle e^{-i\omega t}dt \quad = \quad \frac{1}{2\pi}\frac{\pi\hbar Q^2}{M}\frac{g(\omega)}{\omega}\frac{1}{1-e^{-\hbar\omega\beta}} \; . \tag{5.46}$$

If we multiply the top and bottom of this equation by γ_0:

$$\gamma_0 = \int \frac{g(\omega)}{\omega}\langle 2n+1\rangle d\omega \; , \tag{5.47}$$

then we have:

$$\frac{1}{2\pi}\int \left\langle \hat{\mathbf{U}}\hat{\mathbf{V}} \right\rangle e^{-i\omega t}dt \quad = \quad \left[\frac{\hbar Q^2}{2M}\int \frac{g(\omega)}{\omega}\langle 2n+1\rangle d\omega\right]\frac{g(\omega)}{\gamma_0\omega}\frac{1}{1-e^{-\hbar\omega\beta}} \; . \tag{5.48}$$

The factor in brackets is precisely the Debye Waller factor, $2W$, as given in Eq. 5.22, and we define the remaining factor to be $S_1(\omega)$. We thus rewrite this equation as:

$$\frac{1}{2\pi}\int \left\langle \hat{\mathbf{U}}\hat{\mathbf{V}} \right\rangle e^{-i\omega t}dt \quad = \quad 2WS_1(\omega) \; . \tag{5.49}$$

If we make the following definition:

$$S_{\mathcal{P}}(\omega) \quad \equiv \quad S_{\mathcal{P}-1}(\omega) * S_1(\omega) = S_1(\omega) *^{\mathcal{P}} S_1(\omega) \; , \tag{5.50}$$

then, from Eq. 5.45, we have:

$$\begin{aligned} \frac{1}{2\pi}\int \left\langle \hat{\mathbf{U}}_s\hat{\mathbf{V}}_s \right\rangle^{\mathcal{P}} e^{-i\omega t}dt \quad &= \quad [2WS_1(\omega)] *^{\mathcal{P}} [2WS_1(\omega)] \\ &= \quad (2W)^{\mathcal{P}}\left[S_1(\omega) *^{\mathcal{P}} S_1(\omega)\right] = (2W)^{\mathcal{P}}S_{\mathcal{P}}(\omega) \; . \end{aligned} \tag{5.51}$$

Substituting this into the $\mathcal{P}^{\text{th}}$ order term from Eq. 5.17 and rearranging, we have:

$$\begin{aligned} \frac{1}{\mathcal{L}}\frac{Q_{\text{I}}}{Q_{\text{F}}}\frac{4\pi}{\sigma^{\text{inc}}}\left(\frac{d^2\sigma^{\text{inc}}}{d\Omega dE_{\text{F}}}\right)_{\mathcal{P}} \quad &= \quad \frac{1}{\hbar}\frac{(2W)^{\mathcal{P}}}{\mathcal{P}!}e^{-2W}S_{\mathcal{P}}(\omega) \\ &= \quad \frac{1}{\hbar}S_{\mathcal{P}}(Q)S_{\mathcal{P}}(\omega) \\ &\equiv \quad \frac{1}{\hbar}S_{\mathcal{P}}(Q,\omega) \equiv S_{\mathcal{P}}(Q,E) \; . \end{aligned} \tag{5.52}$$

If we define $S_0(E) = \delta(E)$, then we may write:

$$\frac{1}{\mathcal{L}}\frac{Q_{\text{I}}}{Q_{\text{F}}}\frac{4\pi}{\sigma^{\text{inc}}}\left(\frac{d^2\sigma^{\text{inc}}}{d\Omega dE_{\text{F}}}\right) \quad = \quad e^{-2W}\sum_{\mathcal{P}=0}^{\infty}\frac{(2W)^{\mathcal{P}}}{\mathcal{P}!}S_{\mathcal{P}}(E) \equiv S(Q,E) \; . \tag{5.53}$$

$S(Q,E)$ is called the *scattering function*, *response function*, *scattering law*, or the *dynamic structure*

factor, and is generally the quantity that we wish to extract from a given scattering experiment. Finally, we note that the ratio of the intensity of the elastic to the inelastic scattering is given by $\frac{1}{\exp(2W)-1}$.

5.2.5 Scattering from a damped harmonic oscillator

In the same way that we expressed changes in the phonon frequencies due to perturbations to the harmonic potential in § 3.6, it is possible to find expressions for the double-differential scattering cross-section in the presence of anharmonicity. The perturbed *frequency response* turns out to be that of a damped harmonic oscillator, with the measured frequency given by $\omega_b(\mathbf{q}) + \Delta\omega_b(\mathbf{q})$ and with half width $\Gamma_b(\mathbf{q})$.

For a single damped harmonic oscillator (DHO), we have the following expression for the response function: [84]

$$S_1^{\mathrm{DHO}}(Q,E) = Q^2 e^{-2W} \frac{1}{M\pi\mathcal{Q}\omega'\omega} \frac{1}{\left(\frac{\omega'}{\omega} - \frac{\omega}{\omega'}\right)^2 + \left(\frac{1}{\mathcal{Q}}\right)^2} \frac{1}{1-e^{-\hbar\beta\omega}} , \tag{5.54}$$

where the equation of motion for the oscillator was given by $\omega'^2 u + \frac{C}{M}\dot{u} + \ddot{u} = 0$. Here, C is the damping coefficient, K is a harmonic force constant, $\omega' \equiv \sqrt{\frac{K}{M}}$ is the natural frequency of the oscillator, and $\mathcal{Q} \equiv \frac{\omega'}{C/M} = \frac{\omega'}{2\Gamma}$ is the quality factor.[a]

If we have $\mathcal{L}$ independent oscillators, each with the same quality factor, the response function is given by:

$$\begin{aligned} S_1^{\mathrm{DHO}}(Q,E) &= Q^2 e^{-2W} \frac{1}{M\omega} \frac{1}{1-e^{-\hbar\beta\omega}} \frac{1}{\mathcal{L}} \sum_i \frac{1}{\pi\mathcal{Q}\omega_i} \frac{1}{\left(\frac{\omega_i}{\omega} - \frac{\omega}{\omega_i}\right)^2 + \left(\frac{1}{\mathcal{Q}}\right)^2} \\ &= Q^2 e^{-2W} \frac{1}{M\omega} \frac{1}{1-e^{-\hbar\beta\omega}} \int \frac{g(\omega')}{\pi\mathcal{Q}\omega'} \frac{d\omega'}{\left(\frac{\omega'}{\omega} - \frac{\omega}{\omega'}\right)^2 + \left(\frac{1}{\mathcal{Q}}\right)^2} . \end{aligned} \tag{5.55}$$

That is, we measure an integral transform of the harmonic phonon spectrum with the damped harmonic oscillator function, B:

$$B(\mathcal{Q},\omega',\omega) = \frac{1}{\pi\mathcal{Q}\omega'} \frac{1}{\left(\frac{\omega'}{\omega} - \frac{\omega}{\omega'}\right)^2 + \frac{1}{\mathcal{Q}^2}} . \tag{5.56}$$

The dependence on wavevector transfer of the response for an independent oscillator is identical to that for a cubic crystal. Thus, provided that the quality factor is actually the same for all of the modes, this expression should hold for a monatomic cubic crystal as well (modulo a constant of proportionality). In general, this provision is not true; however, it does appear to be true *on average* in some crystals.

[a] We apologize for the similarity between Q for wavevector transfer and $\mathcal{Q}$ for quality.

Chapter 6

Time-of-flight Neutron Chopper Spectrometers

In this chapter, we briefly explain the concepts of direct-geometry, time-of-flight chopper spectrometry, make comparisons to the more widely use triple axis spectrometer, and describe in some detail the two instruments used for the neutron scattering studies of aluminum and nickel presented in this work.

6.1 Spallation neutron sources

Although chopper spectrometers may be built on reactor sources, they are more commonly found at spallation sources. As all of the studies presented here were performed at spallation sources, we focus our discussion on these types of instruments.

A schematic of a spallation source is given in Fig. 6.1. Generally, the process starts with the acceleration of reasonably massive charge particles (usually H^- ions) to energies on the order of 100 MeV or more in a *linear accelerator*. The ions are then stripped of electrons and bunched together

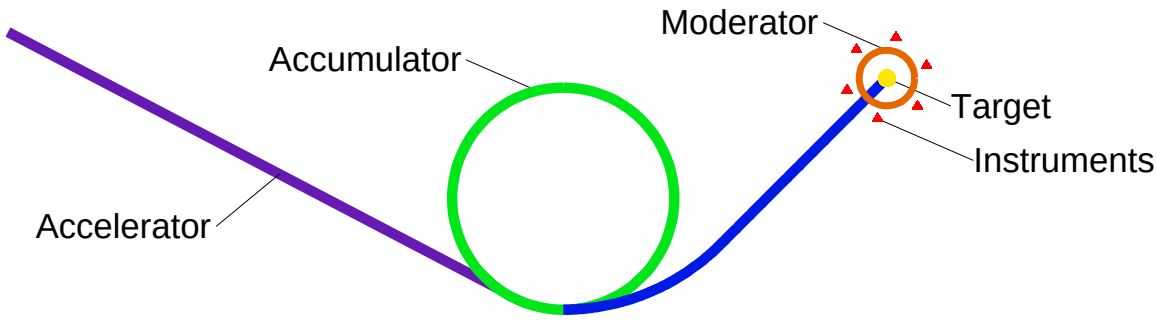

Figure 6.1: Schematic of a spallation source. Charged particles are accelerated, accumulated, and then directed into a heavy metal target. The particles cause spallation neutrons to come out in all directions, passing through the moderator and into the instruments.

into pulses in an *accumulator ring*, and directed at a heavy metal target. As the protons hit nuclei in the target, neutrons are *spalled* in all directions. In a circle about the target are *moderators*, in which the fast neutrons interact inelastically with the moderator material and are *thermalized*. Typically, moderators use materials rich in hydrogen, such as water or solid methane, because it is a strong scatterer of neutrons and has a high average energy transfer per collision. On the other side of the moderators are suites of instruments, optimized for different types of scientific experiments.

For all instruments, the neutrons exit the moderator in small pulses at known times, and this timing is fundamental to the operation of a chopper spectrometer.

6.2 Direct geometry, time-of-flight, chopper spectrometers

Fig. 6.2 shows a schematic of a direct-geometry, time-of-flight chopper spectrometer. Each pulse of neutrons leaves the moderator at a known time, τ_0. They then pass through the *T0* and *E0* (or *Fermi*) *choppers*. These are rotating cylinders with slits that are phased to allow only neutrons of a certain velocity, v_{I}, pass through. The T0 chopper stops fast neutrons (with MeV energies) and γ-rays The Fermi chopper provides the monochromatization, occasionally with a contribution from the T0 chopper. Having two choppers can stop some fast and slow neutrons that would otherwise pass through chopper openings intended respectively for previous or subsequent pulses.

The neutrons that pass through the choppers impinge upon the sample, where they might be

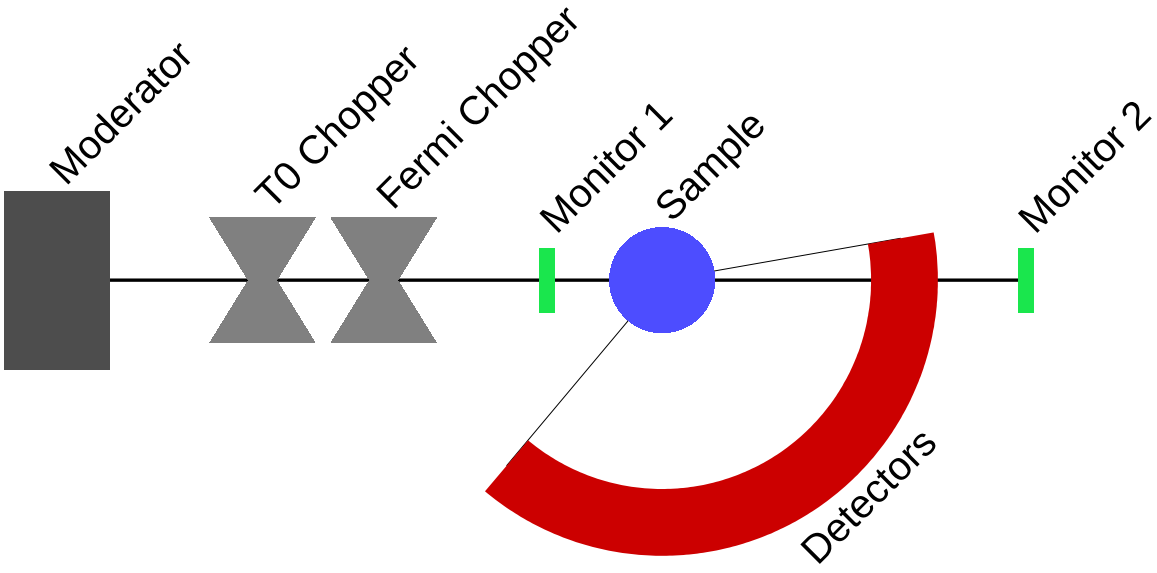

Figure 6.2: Schematic of a direct-geometry, time-of-flight chopper spectrometer. Neutrons of a wide range of energies leave the moderator. The T0 and E0 (or *Fermi*) choppers monochromatize the beam. The neutrons then scatter off of the sample and travel into the detectors. The monitors may be used to determine accurately the incident energy (spectrum) of the neutrons.

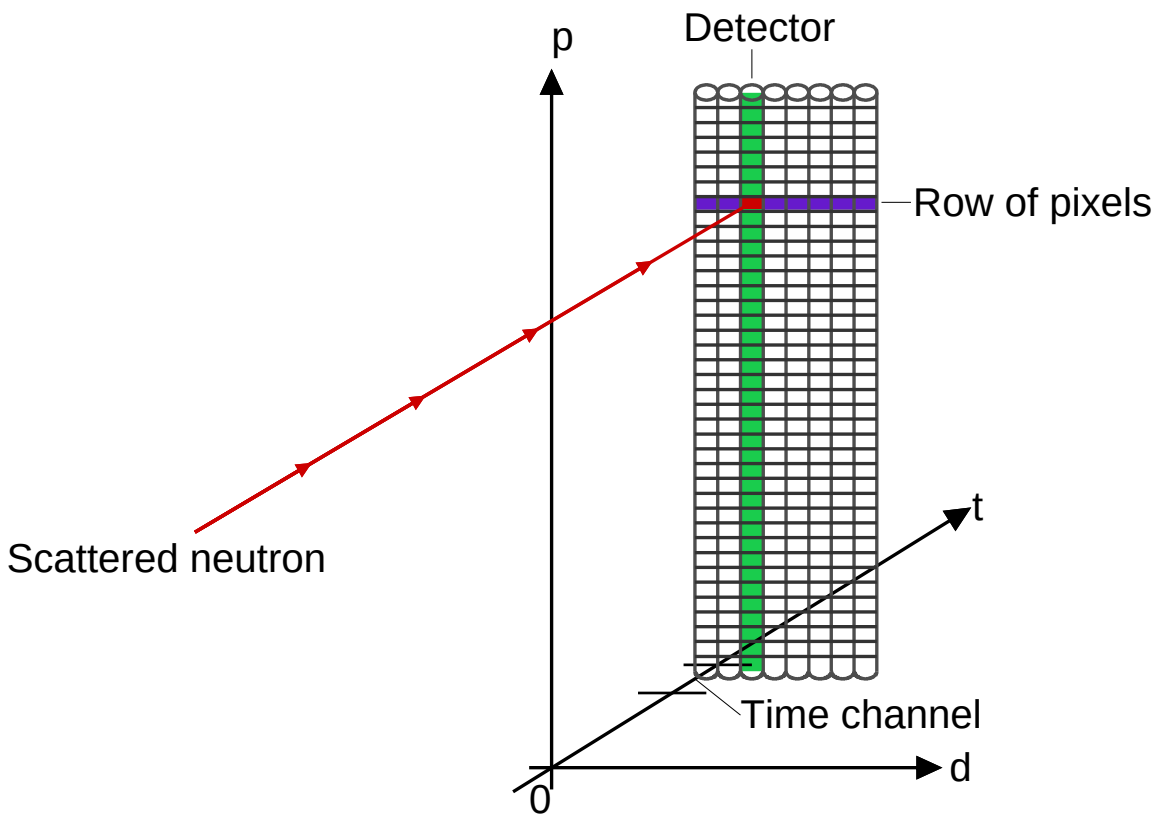

Figure 6.3: Schematic of a scattered neutron entering a typical detector module. The module consists of a batch of detectors. Each detector, then, has a number of pixels. Finally, each pixel has time channels. These are indexed by d, p, and t, respectively. Frequently, the detector modules are positioned radially around the sample, forming a sort of cylinder. In this case, all the pixels in a row in a given detector module are approximately equidistant from the sample. Pixels in different rows, however, are at different distances from the sample. On older instruments the detectors are not pixelated.

elastically or inelastically scattered — possibly more than once. Since the time the neutrons arrived at the moderator and the distance from the moderator to the sample are known, and the velocities of the neutrons are determined by the choppers, we may determine the time at which the neutrons arrive at the sample, τ_{I}.

Some fraction of the neutrons that have made it to the sample will be scattered towards the detectors. The arrival of a neutron into a time-channel in a pixel in a detector in a *detector module* is depicted in Fig. 6.3 The modules are frequently arranged cylindrically about the sample, like the detectors in Fig. 6.2.

We now know the time and velocity of the neutrons when they arrived at the sample, and the time and location of their arrival in the banks of detectors, and we may use all of this information to determine the initial and final energies and wavevectors of the neutrons. The initial values are

straightforward, we have:

$$E_{\mathrm{I}} = \frac{m_{\mathrm{n}}}{2} v_{\mathrm{I}}^2 \,, \tag{6.1}$$

$$\mathbf{Q}_{\mathrm{I}} = \frac{m_{\mathrm{n}}}{\hbar} \mathbf{v}_{\mathrm{I}} \,, \tag{6.2}$$

where, $|\mathbf{v}_{\mathrm{I}}|$ is determined by the chopper frequencies and its direction is determined by the location of the moderator.[a] For the final values, we consider an instrument that lacks pixelated detectors. If we assume that a neutron arrives at a detector, d, in a time τ_d, and that the distance from the sample to the center of the detector is L_d, we have:

$$E_{\mathrm{F}} = \frac{m_{\mathrm{n}}}{2} \left(\frac{L_d}{\tau_d} \right)^2 \,, \tag{6.3}$$

$$Q_{\mathrm{F}} = \frac{m_{\mathrm{n}}}{\hbar} \frac{L_d}{\tau_d} \,. \tag{6.4}$$

The angle, Θ_d at which the center of a particular detector is located is frequently tabulated along with L_d, allowing us to find the direction of $\mathbf{Q}_{\mathrm{F}}$. Frequently, on an instrument that has pixelated detectors, only the distance from the center of the detector to the pixel, L_p, is tabulated in addition to L_d and Θ_d. In this case, we have:

$$E_{\mathrm{F}} = \frac{m_{\mathrm{n}}}{2} \left(\frac{L_{dp}}{\tau_{dp}} \right)^2 \,, \tag{6.5}$$

$$Q_{\mathrm{F}} = \frac{m_{\mathrm{n}}}{\hbar} \frac{L_{dp}}{\tau_{dp}} \,, \tag{6.6}$$

where $L_{dp} = \sqrt{L_d^2 + L_p^2}$ is the distance and τ_{dp} is the time for the neutron to travel from the sample to the pixel. The direction of $\mathbf{Q}_{\mathrm{F}}$ is determined through the scattering angle, $\Theta_{dp} = \arccos\left(\frac{L_d}{L_{dp}} cos(\Theta_d) \right)$.[b] Fig. 6.4 is a schematic of some of the relevant angles, times, and distances for a direct geometry, time-of-flight, chopper spectrometer.

The energy, E, and wavevector $\mathbf{Q}$, transferred to the sample, then, are given by:

$$E = E_{\mathrm{I}} - E_{\mathrm{F}} \,, \tag{6.7}$$

$$\mathbf{Q} = \mathbf{Q}_{\mathrm{I}} - \mathbf{Q}_{\mathrm{F}} \,. \tag{6.8}$$

The relationship of the initial, final, and transferred wavevectors was depicted in Fig. 5.2. If the sample is a single crystal, the direction of $\mathbf{Q}$ is related to the actual wavevector transferred to the sample through the orientation of the crystal. For a polycrystalline sample, like those used for the

[a] More accurate methods of determining the initial energy of the neutrons are discussed in Chapter 7.

[b] We have assumed that the detectors are oriented perpendicular to the initial velocities of the neutrons. If this is not the case, more involved geometry is required, as well as additional information about the experimental setup.

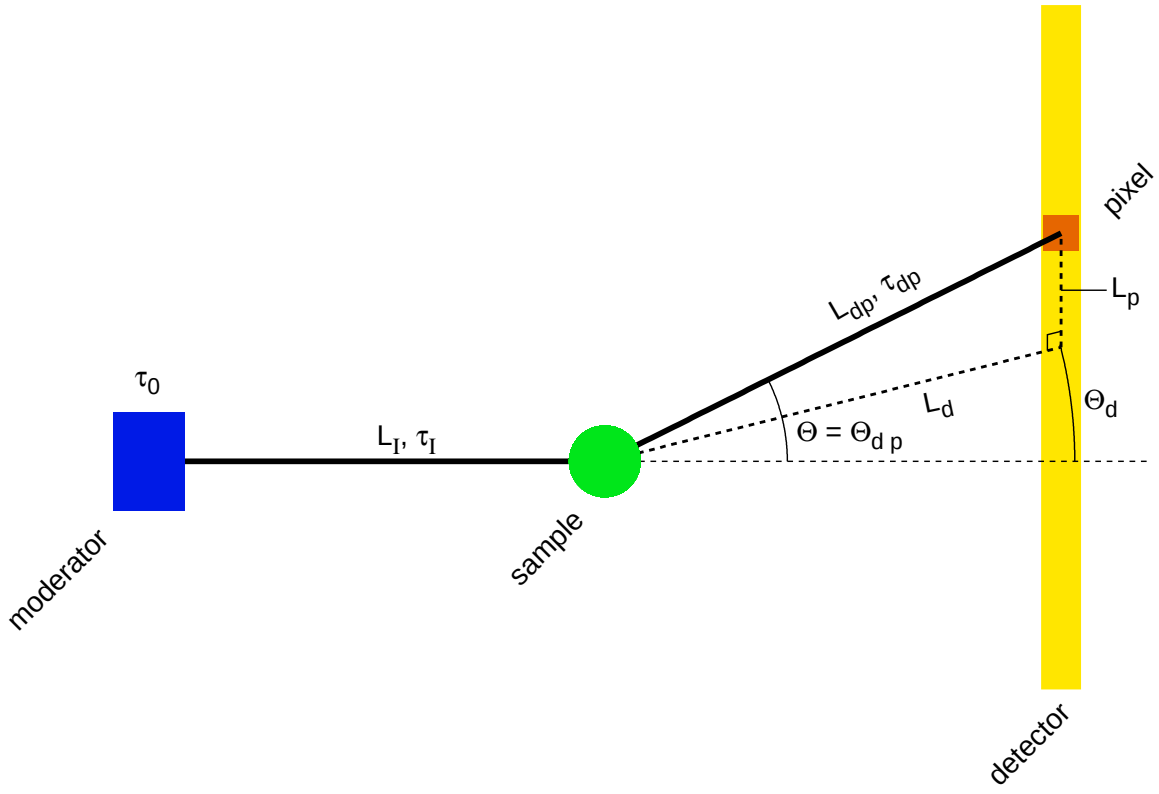

Figure 6.4: Another schematic of a direct geometry, time-of-flight, chopper spectrometer; this one showing some of the times, distances and, angles relevant to the analysis of a measurement. The neutron leaves the moderator at $\tau_0 = 0$, and travels a distance $L_{\rm I}$ in time $\tau_{\rm I}$, in order to arrive at the sample. Here, it is scattered an angle $\Theta = \Theta_{dp}$ in the direction of a pixel in a detector that is located at an angle Θ_d to the incident neutron beam in the plane containing the centers of the detectors. The distance from the sample to the center of the detector is L_d, and from there to the pixel L_p, so that the total distance is $L_{dp} = \sqrt{L_d^2 + L_p^2}$; and the neutron travels this distance in time τ_{dp}. From this information and the initial neutron energies, we may determine energies and wavevectors of the scattered neutrons and, in turn, of the excitations in the sample.

studies presented here, the direction of $\mathbf{Q}$ is not measurable. Rather, we measure an average over neutrons that have the same $Q = |\mathbf{Q}|$. Fig. 6.5 shows an example of the region in $Q-E$ space sampled in a time-of-flight neutron chopper experiment. The large portion of reciprocal space sampled in a time-of-flight experiment makes it a superior technique for measuring the phonon DOS.

6.3 Time-of-flight vs. triple-axis

Pioneered by Bertram Brockhouse,[c] the triple-axis spectrometer has been the workhorse of inelastic neutron scattering since its advent in the mid 1950s. If the purpose of an experiment is to measure the dispersion relations for phonons or magnons, there is no better technique. Similarly if the

[c]He won the 1994 Nobel Prize for his work.

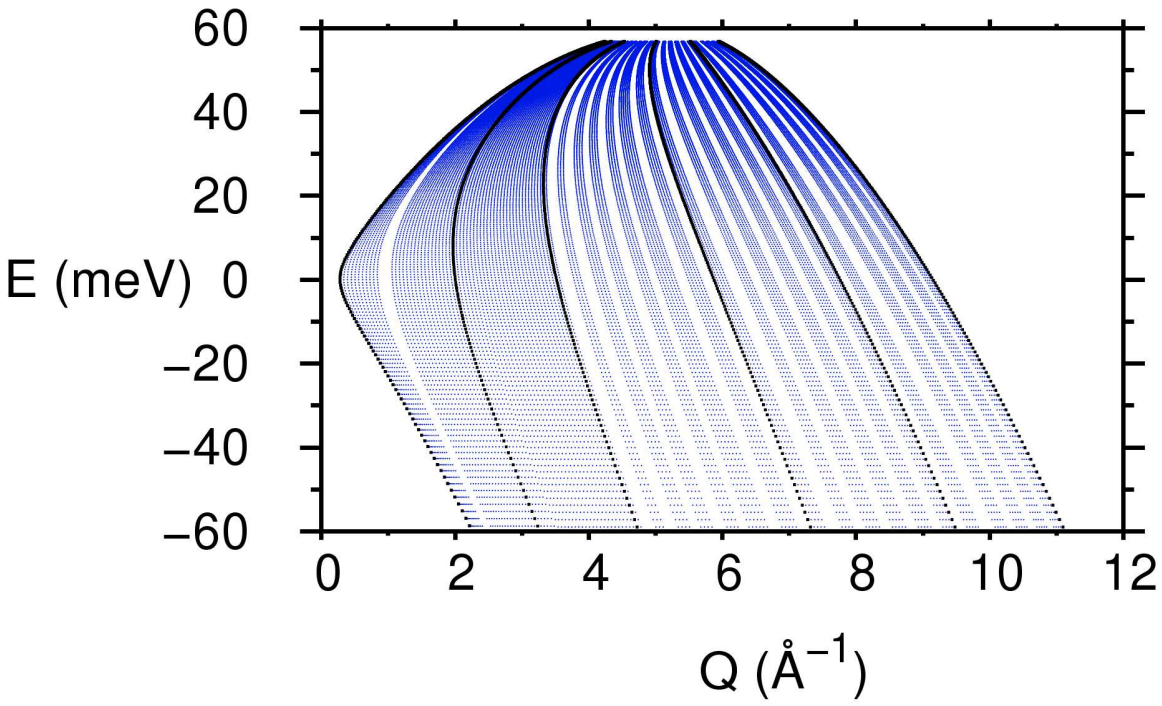

Figure 6.5: Region sampled in Q and E on LRMECS (described in § 6.4) for an incident energy of 60.0 meV. Each light blue point in the plot corresponds to one time-of-flight in one detector. The spacing of the points in time-of-flight was constant; however, in energy the spacing gets larger as we move from positive to negative energy transfers, *i.e.*, there is better resolution for phonon creation than for phonon annihilation. The darker black points are contours of constant angle. Specifically, they are at 2.4°, 21.0°, 37.8°, 64.2°, 92.4°, and 117.6° from left to right. The gaps are either spaces between detector modules or missing/broken detectors.

purpose of the experiment is to investigate the properties of some particular phonon, magnon, or excitation.

A schematic of a triple-axis spectrometer is shown in Fig. 6.6. Typically, neutrons from a nuclear reactor reach the moderator where they are thermalized. They then travel to a crystal monochromator, which selects neutrons with a particular energy that continue along to the sample. The neutrons are scattered in the sample, and some fraction of those scattered proceed to the analyzer. At the analyzer, neutrons with a particular final energy are scattered toward the detector, where they are, one hopes, detected. The sample may be rotated about the monochromator, the analyzer about the sample, the detector about the analyzer, and the sample about its center, with those angles (respectively Θ_0, Θ_1, Θ_2, and Θ_s as shown in Fig. 6.6) defining the incident and final energies and wavevectors of the neutrons.

For a sample which is a single crystal, the technique thus provides a direct measurement of the scattering intensity for excitations with some fixed energy $E = E_\mathrm{I} - E_\mathrm{F}$ and wavevector transfer $\mathbf{Q} = \mathbf{Q}_\mathrm{I} - \mathbf{Q}_\mathrm{F}$. Typically, scans are performed in either constant energy or constant wavevector, the

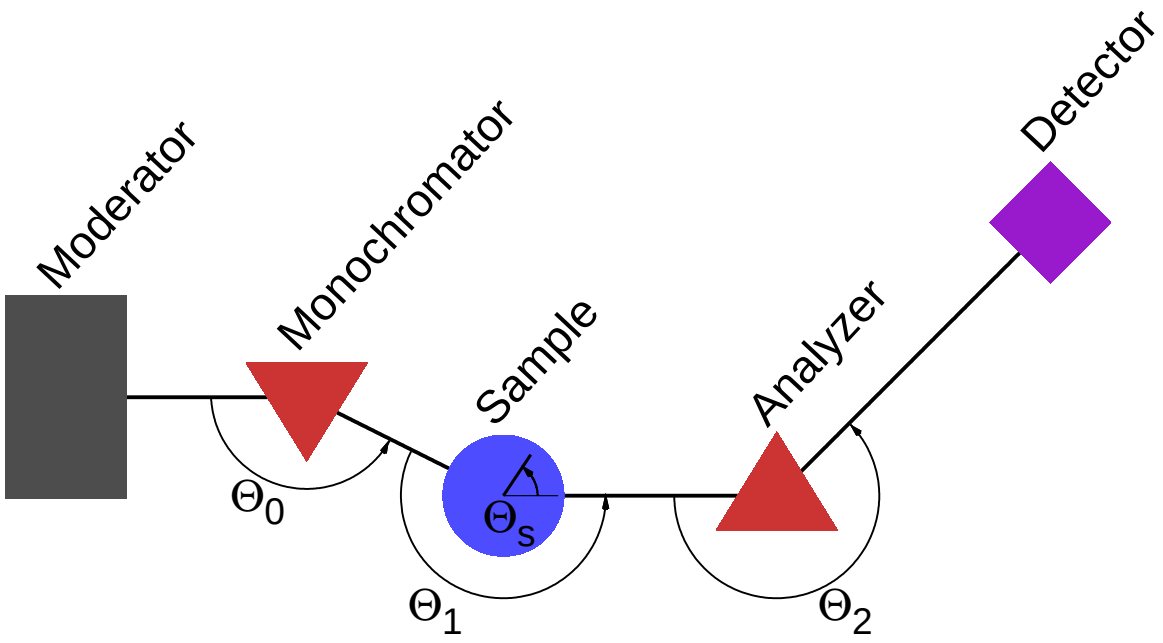

Figure 6.6: Schematic of a 3-axis spectrometer. Neutrons exit the moderator, and are monochromatized by a single crystal. They then enter the sample, where they are scattered. The analyzer crystal then monochromatizes the outgoing neutrons before they head to the detector. Typically, the sample may be rotated about the monochromator, the analyzer about the sample, and the detector about the analyzer. Additionally, the sample might be rotated in place.

latter providing the dispersion in some particular direction in the reciprocal space of the sample. Measurements of the phonon dispersions in some small number of directions are thus feasible, and may be used to optimize some model of the lattice dynamics in the sample — usually to allow a calculation of the phonon DOS. Since the phonon DOS is an average over the entire reciprocal space, a time-of-flight chopper spectrometer provides a much more direct measurement.

6.4 Instruments used

The three instruments used in this work were the Low Resolution Medium Energy Chopper Spectrometer (LRMECS) at the Intense Pulsed Neutron Source (IPNS) at Argnonne National Lab (ANL), Pharos (not an acronym, but rather a reference to the lighthouse of Alexandria) at the Los Alamos Neutron Science Center (LANSCE) at Los Alamos National Laboratory (LANL), and the wide-Angle ChoppeR Spectrometer (ARCS) at the Spallation Neutron Source (SNS) at Oak Ridge National Laboratory (ORNL). LRMECS and Pharos were used for both the aluminum and nickel experiments, and ARCS for the lead experiment. Schematics are given in Figs. 6.7 and 6.8, and some of the more general details are given in Table 6.1.

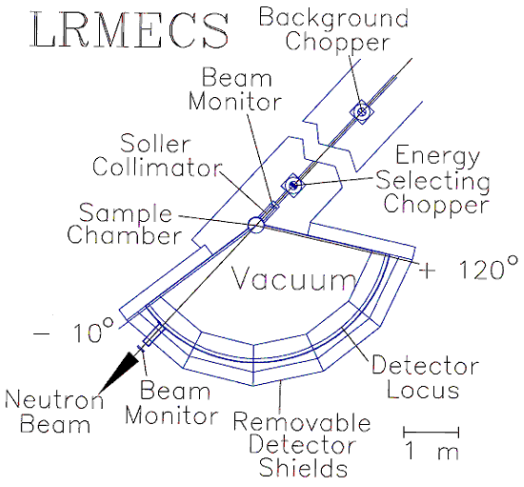

Figure 6.7: Schematic of LRMECS.

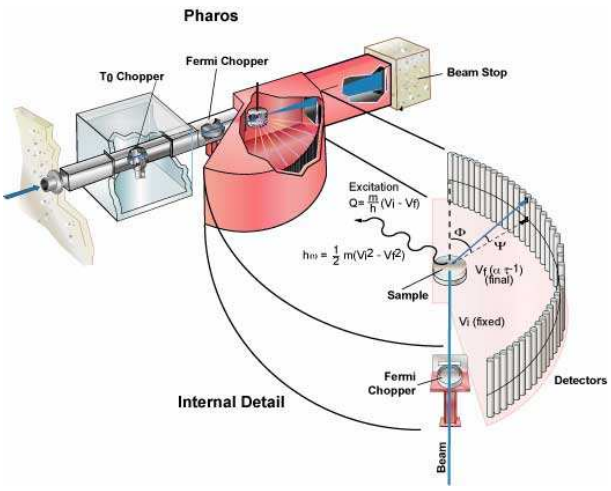

Figure 6.8: Schematic of Pharos.

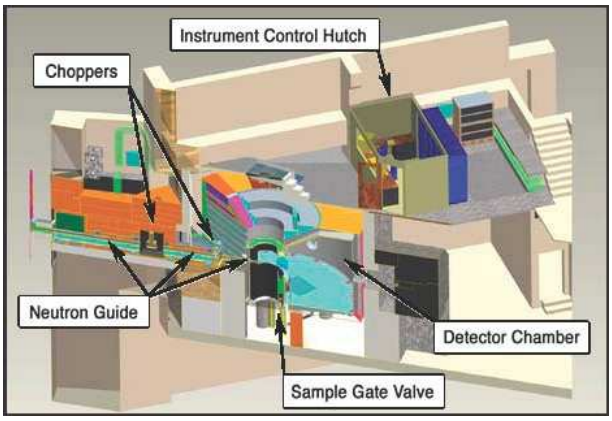

Figure 6.9: Schematic of ARCS.

Quantity	**LRMECS**	**Pharos**	**ARCS**
moderator type	Liquid CH_4 at 100 K	Liquid H_2O at 283 K	Liquid H_2O, ambient
detector type	^{3}He	^{3}He	^{3}He
number of detectors	148	376	920
detector heights	$\Theta_d < 25^\circ \rightarrow 0.229$ m	1.0 m	high angles $\rightarrow$ 1.0 m
	$\Theta_d \geq 25^\circ \rightarrow 0.457$ m	0.25 m	low angles $\rightarrow$ 0.25 m
pixels per detector	NA	40	128 or 256
pixel size	NA	0.025 m	$\frac{1}{128}$ m or $/\frac{1}{256}$ m
L_{I}	8.1 m	20.00 m	13.6 m
$\langle L_d \rangle$	2.5 m	4.13 m	3 m
T0 chopper position	$\sim$ 6.5 m	14.0 m	9 m
E0 chopper position	7.6 m	18.0 m	11.6 m
1$^{\mathrm{st}}$ monitor position	7.65 m	NA	11.825 m
2$^{\mathrm{nd}}$ monitor position	11.34 m	NA	18.5 m
beam size	0.05 m $\times$ 0.10 m	0.05 m $\times$ 0.075 m	0.05 m $\times$ 0.05 m
$\langle \Delta\Theta_d \rangle$	0.6°	0.4°	0.48°
angular range	$-7.2^\circ < \Theta_d < -2.4^\circ$, $2.4^\circ < \Theta_d < 117.6^\circ$	$-10.9^\circ < \Theta_d < -1.7^\circ$ $1.77^\circ < \Theta_d < 147.07^\circ$	$-28.1^\circ < \Theta_d < -3^\circ$ $3^\circ < \Theta_d < 135^\circ$

Table 6.1: Some details about LRMECS, Pharos, and ARCS. $\langle L_d \rangle$ is the modal distance from the sample to the detectors. All other positions are given relative to the moderator. $\langle \Theta_d \rangle$ is the modal angular step between detectors. The ARCS water moderator is decoupled, and the number of pixels in its detectors may be varied.

.

Part II

Data Analysis and Computation

Analytical and computational techniques for simplifying and interpreting data from time-of-flight chopper spectrometers are presented here. New or modified procedures are presented in the following sections: §7.1.1, §7.2.2, §7.4.2, §8.1.2, §8.2, and §8.3.1.2.

Chapter 7

From Raw Data to S(Q,E)

Up to this point, we have considered some general formulas relating the double differential cross-section or the dynamic structure factor to the elementary excitations in a solid. In this chapter, we present methods by which the actual measured quantities are related to the theoretical quantities presented in Chapter 5.

As discussed in § 6.2, the information available to us in a direct geometry, neutron time-of-flight chopper spectrometer experiment are the time-of-flight τ of the neutron, the distance from the moderator to the sample, L_{I}, and the distance, L_{dp}, from sample to a pixel indexed p (in a detector indexed d). Using these, we must determine the initial and final energy of the neutrons, E_{I} and E_{F}, and the amount of energy absorbed by the sample $E = E_{\mathrm{I}} - E_{\mathrm{F}}$. We know approximately the direction of the incident neutron beam, so given its energy we may also determine its wavevector, $\mathbf{Q}_{\mathrm{I}}$. If we also consider the scattering angle, Θ, which is determined by the locations of the pixel and sample, we may determine the final wavevector of the neutron $\mathbf{Q}_{\mathrm{F}}$, and the *wavevector transfer*, $\mathbf{Q} = \mathbf{Q}_{\mathrm{I}} - \mathbf{Q}_{\mathrm{F}}$.

The goal of this chapter is to describe in detail the process by which the raw data acquired on a direct geometry, time-of-flight, chopper spectrometer is converted to a physically meaningful quantity, such as the dynamic structure factor $S(\mathbf{Q}, E)$. We present both commonly used and new techniques. At a minimum, the following operations (or analogous ones) must be performed:

- Detector masking and efficiency corrections
- Determination of the incident energy
- Normalization of the data
- Transformation to physical coordinates
- Removal of background scattering

In practice, these operations are usually performed once for each data set. In reality, the results from

some of these operations affect the others, and iterating over the operations to find a self consistent solution might be more accurate.

A final note before we begin: Technically, the removal of multiply scattered neutrons belongs to this chapter, as this type of scattering involves the geometry of the instrument, and is not part of the dynamic structure factor. Corrections for multiple scattering are frequently skipped all together, and the multiple scattering correction presented in this text is coupled to the determination of the phonon DOS. As such, we delay discussion of this correction until § 8.1.

7.1 Detector masking and efficiency corrections

On LRMECS and Pharos, the neutron detectors are based on the helium conversion reaction:

$$n + {}^3\mathrm{He} \rightarrow {}^3\mathrm{H} + {}^1\mathrm{H} + 0.764 \text{ MeV} . \tag{7.1}$$

The detectors are hollow tubes with a voltage across them, filled with ^{3}He. When a neutron hits the detector, it undergoes the above reaction, which in turn causes a cascade of charged particles. These charged particles are then detected as a current flow at the terminals on the detector.

In order to calibrate the detectors, it is very helpful to perform an experiment where the same number of neutrons will reach each detector. Fig. 7.1 shows a measurement of the scattering from vanadium made on LRMECS. Pure vanadium is a highly incoherent scatterer of thermal neutrons, with coherent and incoherent neutron scattering cross-sections of $\sigma^{\mathrm{coh}} = 0.0184$ barns and $\sigma^{\mathrm{inc}} = 5.08$ barns, respectively. As such, measurements of the scattering from vanadium are well suited to the purpose of neutron instrument calibration. Although it is possible to measure the vanadium with a fixed incident neutron energy, all of the detector calibrations in this text were performed using a *white beam* measurement of vanadium.

The efficiency of the detector depends on its electronics, at least in so much as faulty electronics may cause it to cease working altogether. We assume that this is completely accounted for by the elimination of bad detectors.[a] The efficiency of the detector also depends on the pressure of the ^{3}He gas that it contains, as well as on the energy of the particle it is detecting. We assume that these two contributions are independent. Thus, the probabilities, Υ_{dt}, of detecting neutrons in detectors indexed by d and time channels indexed by t are given by:[b]

$$\Upsilon_{dt} = \Upsilon_t \Upsilon_d , \tag{7.2}$$

[a] It is likely that other effects from the electronics get taken care of fortuitously when we correct for the pressure-dependence of the detector efficiency.

[b] Given that neutrons have arrived at the detector at some times and that they *should* be detected. We will not be considering probabilities that neutrons get registered in the wrong detectors or time channels.

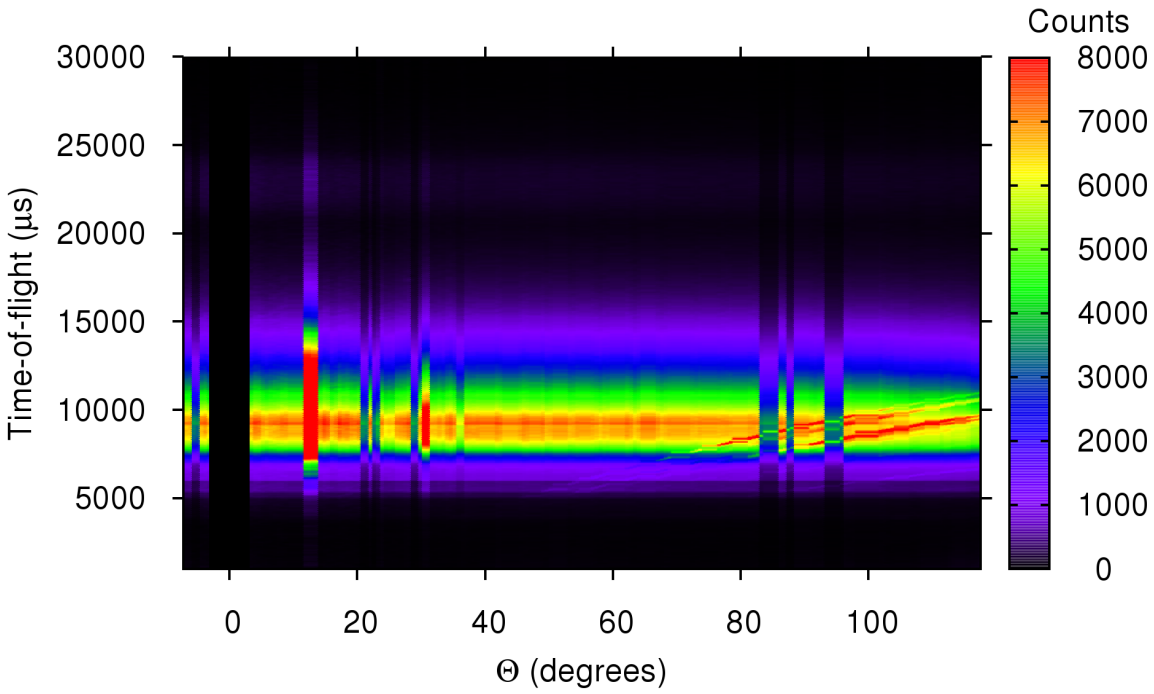

Figure 7.1: Vanadium data from LRMECS. Because vanadium is a purely incoherent scatterer, the angular dependencies of the data must come from somewhere other than the sample. (Technically, the inelastic scattering increase with increasing Q; however, the elastic scattering completely dominates this contribution.) The black bar around $\Theta = 0$ is because there are no detectors there. The near horizontal streaks at the higher angles are probably Bragg scattering from somewhere in the sample well. The vertical streaks are the variations in detector efficiency for which we must correct.

where Υ_t gives the energy-dependent probabilities and Υ_d gives the pressure-dependent ones.

Here, we consider a scheme for automatically determining which detectors are unusable, as well as methods for correcting for the energy- and pressure-dependencies of the detectors.

7.1.1 Masking bad detectors

Instrument scientists sometimes provide a list (called a *mask*) of the detectors that are not working properly, but these lists can get lost, or be out of date. Further, the bad detectors are usually found by hand, which is only feasible so long as the numbers of detectors on an instrument are sufficiently small. Thus, automating the task of finding the bad detectors is desirable. The problem here is that it is not at all obvious a-priori which detectors are good and which are bad. Operating under the assumption that the data should vary relatively smoothly from detector to detector, we may automate the removal of some bad detectors. Thus, the measurement of vanadium is used for finding the detector mask.

Before doing anything more involved, we make note of any detectors with exactly zero counts. This is a highly unlikely measurement in a facility geared towards the production of neutrons. This

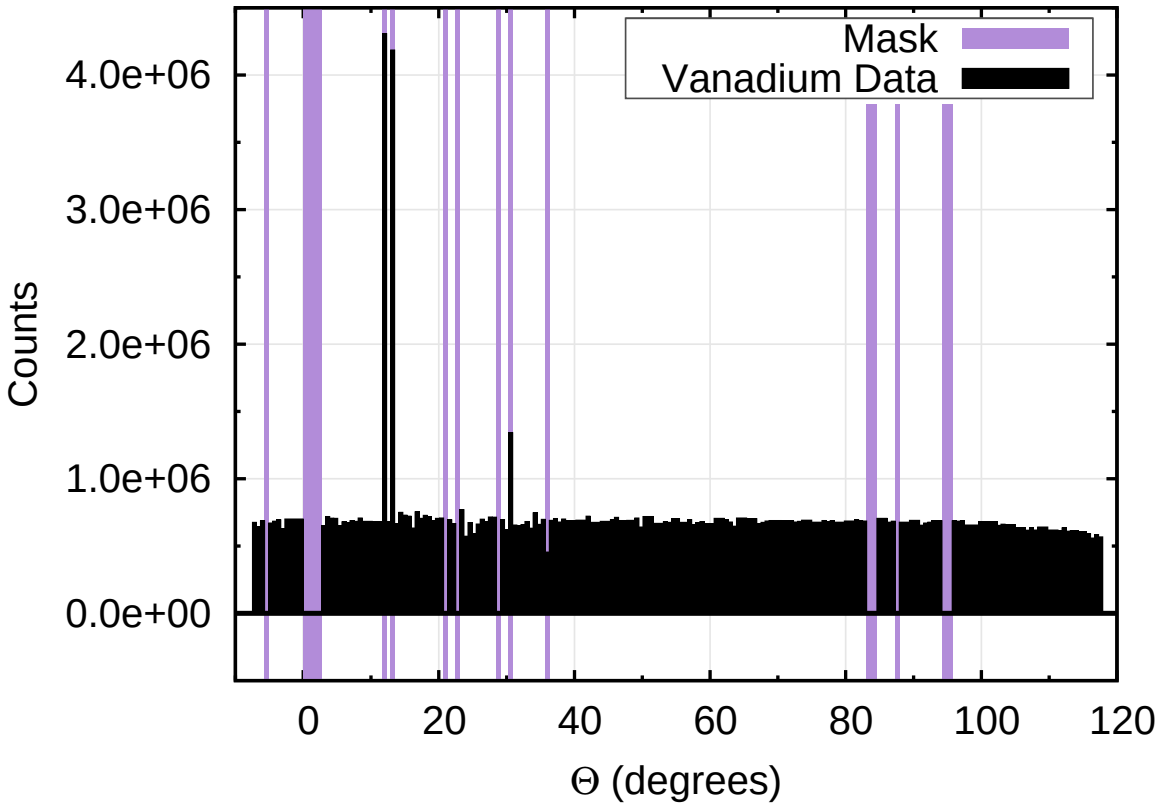

Figure 7.2: Vanadium data from LRMECS, summed over time-of-flight, is shown in black. Two *hot* detectors are clearly visible at around 12°, and absent or broken detectors are visible throughout. The lighter, purple bars show masked detectors. (Note that the the vanadium plate is oriented at 145° to the beam, and that this is why the detectors at high angles have decreasing intensity. *Dark angle* corrections based on simple models of neutron absorption are commonly used, but the details are not presented here.)

part of the correction should be performed directly on both the scattering from vanadium, and from the sample of interest; in case a detector has failed suddenly in between the measurements.

We now attempt to iteratively find detectors with unreasonable numbers of counts. We choose a final threshold for keeping a detector — for example, we might require that no detector has more than 10% more counts than the mean number of counts in a detector.[c] We should not immediately find the mean number of counts in a detector and throw out all detectors which deviate from that value by more than 10%. For an extreme example, imagine that there are 10 detectors and that a perfect experiment would yield 10 counts per detector. Further, imagine that the measured number of counts in each detector is 10, with the exception of one detector where we found 1 count, and another where we found 1,000 counts.[d] The mean number of counts per detector is 108, and the

[c] Unlike finding detectors with zero counts, it is not possible to perform this part of the corrections with data from the sample of interest unless it is a totally incoherent scatterer. If it is coherent, the Bragg scattering will not vary smoothly with angle.

[d] This example is not absurd. The collected counts are stored digitally, and an error in a single bit may change the number of counts by orders of magnitude.

percent errors between the 1 count, the 1,000 count, and the 10 count detectors and the mean are -100%, 825%, and -91%, respectively. If we blindly apply our 10% criterion, we have no detectors left.

Instead, we iterate, each time finding the detector with the maximum and the minimum counts. If these deviate from the mean by more than our threshold, they are masked, if neither of them deviate by this amount, our mask is complete. In our example, the 1 and 1,000 count detectors are eliminated in the first round. Once that is done, the mean number of counts goes to 10, and we mask no other detectors.

In practice, a threshold of about 20% deviation from the mean number of counts seems to work quite well for LRMECS data, as seen in Fig. 7.2. The technique has yet to be applied to Pharos data, where the detectors are pixelated; however, it seems that it should work either by summing the counts over the pixels, or by treating each individual pixel as a detector was treated here.[e] This scheme is by no means perfect, but it is often a good starting point for the removal of bad detectors.

7.1.2 Energy-dependent detector efficiency

As a rule of thumb, the probabilities of a neutron being detected, Υ_t, are proportional to the amount of time the neutron spends in the detector. This, in turn, is inversely proportional to the final velocity of the neutron, $v_{\rm F}$. If the mean distance through the detector is given by $\langle L_{\rm det}\rangle$, then we have approximately:

$$\Upsilon_t \propto \frac{\langle L_{\rm det}\rangle}{v_{\rm F}} \propto \frac{\langle L_{\rm det}\rangle}{\sqrt{E_{\rm F}}} \; , \tag{7.3}$$

where $v_{\rm F}$ is the final neutron velocity. Noting that $v_{\rm F} = \frac{L_{dp}}{\tau_{dp}}$, where τ_{dp} is the time-of-flight for the neutron to travel from the sample to a pixel (in a detector), we have:

$$\Upsilon_t \propto \tau_{dp} \; . \tag{7.4}$$

This may also be seen in the following way. The probabilities of detection are the same as the probabilities of absorption, which are approximately given as follows:

$$\begin{aligned} \Upsilon_t &\propto 1 - \exp\left(-\rho_{\rm He}\sigma^{\rm abs}\langle L_{\rm det}\rangle\right) \\ &\approx 1 - \left[1 - \left(\rho_{\rm He}\sigma^{\rm abs}\langle L_{\rm det}\rangle\right) + \frac{1}{2}\left(\rho_{\rm He}\sigma^{\rm abs}\langle L_{\rm det}\rangle\right)^2 + \cdots\right] \\ &\approx \rho_{\rm He}\sigma^{\rm abs}\langle L_{\rm det}\rangle \; , \end{aligned} \tag{7.5}$$

[e] The former is the proper choice if the failure of a pixel indicates that the detector in which it resides has also failed.

where ρ_{He} is the number density of the ^{3}He atoms in the detector, and σ^{abs} is their absorption cross-section. Since $\sigma^{\mathrm{abs}} \propto \frac{1}{v_{\mathrm{F}}} \propto \frac{1}{\sqrt{E_{\mathrm{F}}}}$, [83, 84] we find again that the absorption of neutrons in the detector is proportional to τ_{dp} or inversely proportional to the square root of the energy.

In principle, the efficiency of the detectors as a function of energy could be measured;[f] however, it is often provided by the detector manufacturer. In any case, given Υ_t, the measured intensity as a function of time-of-flight, detector ID, and pixel ID, I''_{dpt}, is scaled accordingly:

$$I'_{dpt} = \frac{I''_{dpt}}{\Upsilon_t} \, , \tag{7.6}$$

where I'_{dpt}, then, is the intensity corrected for the energy-efficiency of the detectors.

7.1.3 Pressure-dependent detector efficiency

As seen in Eq. 7.5, the efficiency of the detectors depends upon the density, and thus, the pressure of the ^{3}He in the tubes. Here, we correct the data for variations of the pressure in the detectors. The measurement of a vanadium sample gives intensity as a function of detector, pixel, and time-channel; but we are not interested in the time-of-flight as we have already corrected for the energy-efficiency of the detectors. Two simple possibilities for reducing the data to a function of detector only are to (1) Sum over the time-of-flight coordinate, or (2) Select the time-of-flight, τ_{e}, that corresponds to the neutrons traveling from the moderator to the pixels with energy E_{I}:

$$\tau_{\mathrm{e}} \equiv \frac{L_{\mathrm{I}} + L_{dp}}{L_{\mathrm{I}}} \tau_{\mathrm{I}} \, , \tag{7.7}$$

where $\tau_{\mathrm{I}} = \tau - \tau_{dp}$ is the time-of-flight for the neutron to travel from the moderator to the sample. The supposed advantage of the latter method is that E_{I} is most relevant to the experiment. In reality, we will be measuring neutrons with a variety of energies, and, if we are doing an inelastic experiment, we will care in particular about those with energies *not* equal to the incident energy. Additionally, the sum over time-of-flight means that we have a much larger set of data to work with. For these two reasons, the sum over all time channels is likely a better choice.

LRMECS has un-pixelated detectors, and on Pharos there may not be sufficient intensity in a pixel for its efficiency to be corrected individually. Further, the pixels in a detector all share the same ^{3}He gas. Because of this, we assume that the efficiency depends only on the detector, and not

[f] One way to do this would be to make many measurements of vanadium at different incident energies; however this is generally considered too costly. As a result, the efficiencies provided by the manufacturer are commonly used. An alternative is to make a single measurement of the vanadium spectrum with either a monochromatic or white-beam incident neutron spectrum. (Presumably the monochromatic beam would have the same energy as for subsequent measurement of the sample.) In so much as the inelastic scattering spectrum of vanadium approximates the inelastic spectrum of the sample to be measured, the monochromatic run will weight the counts at different energies appropriately. In practice, it seems more likely that the benefits of the greatly increased intensity of the white beam far outweigh the benefits derived from similarities between the spectrum of the sample and that of vanadium.

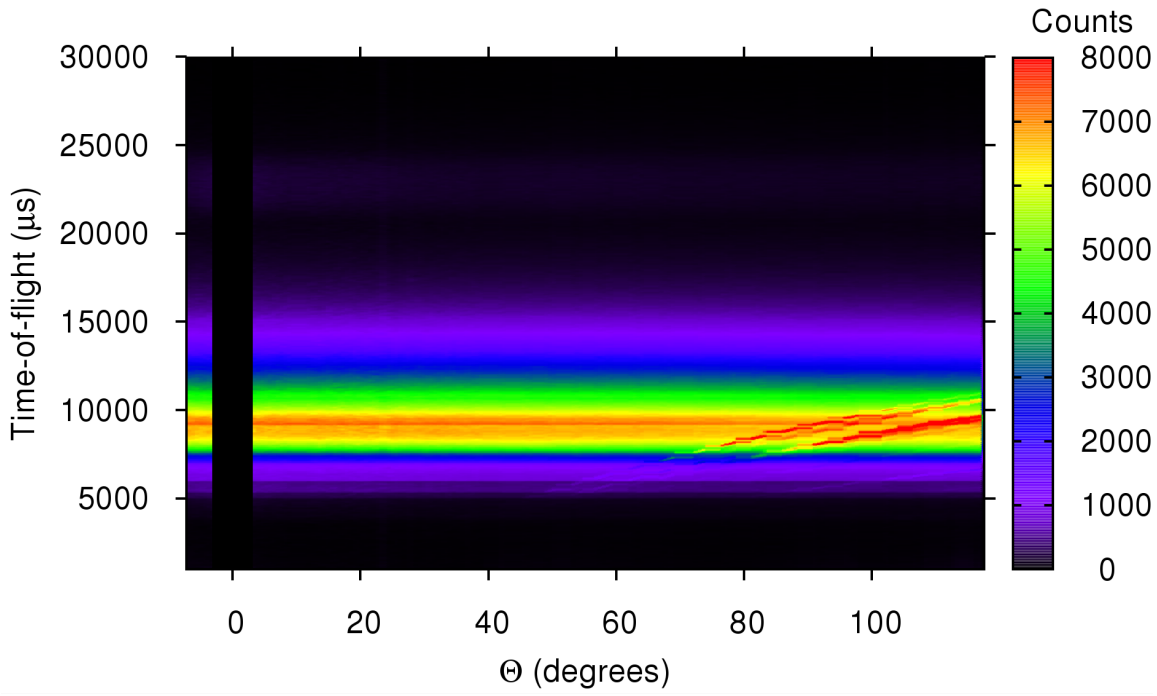

Figure 7.3: Vanadium data from LRMECS, as seen in Fig. 7.1, but corrected for detector efficiencies. The black bar around $\Theta = 0$ is because there are no detectors there. The Bragg scattering at the higher angles is still visible, but the other variations have been accounted for. The correction derived from and applied to the vanadium data will be applied to our experimental data as well.

on the pixel. The probabilities, then, for the pressure-efficiency of the detectors are given as follows:

$$\Upsilon_d = \frac{\sum_p \sum_t I''^{\text{van}}_{dpt}}{\sum_d \sum_p \sum_t I''^{\text{van}}_{dpt}} , \tag{7.8}$$

and the intensity, corrected for both energy- and pressure-dependencies, I_{dpt}, is given by:

$$I_{dpt} = \frac{I'_{dpt}}{\Upsilon_d} = \frac{I''_{dpt}}{\Upsilon_d \Upsilon_t} = \frac{I''_{dpt}}{\Upsilon_{dt}} . \tag{7.9}$$

The vanadium data from LRMECS, shown uncorrected in Fig. 7.1, are shown in Fig. 7.3, once the detector efficiency corrections have been applied.

7.1.4 Solid-angle of the pixels

Since the detectors are straight tubes, and the pixels have equal length along those tubes, pixels at different heights cover different amounts of solid-angle. The solid angles covered may be calculated and corrected for analytically; or they may be corrected for by performing the procedure for the

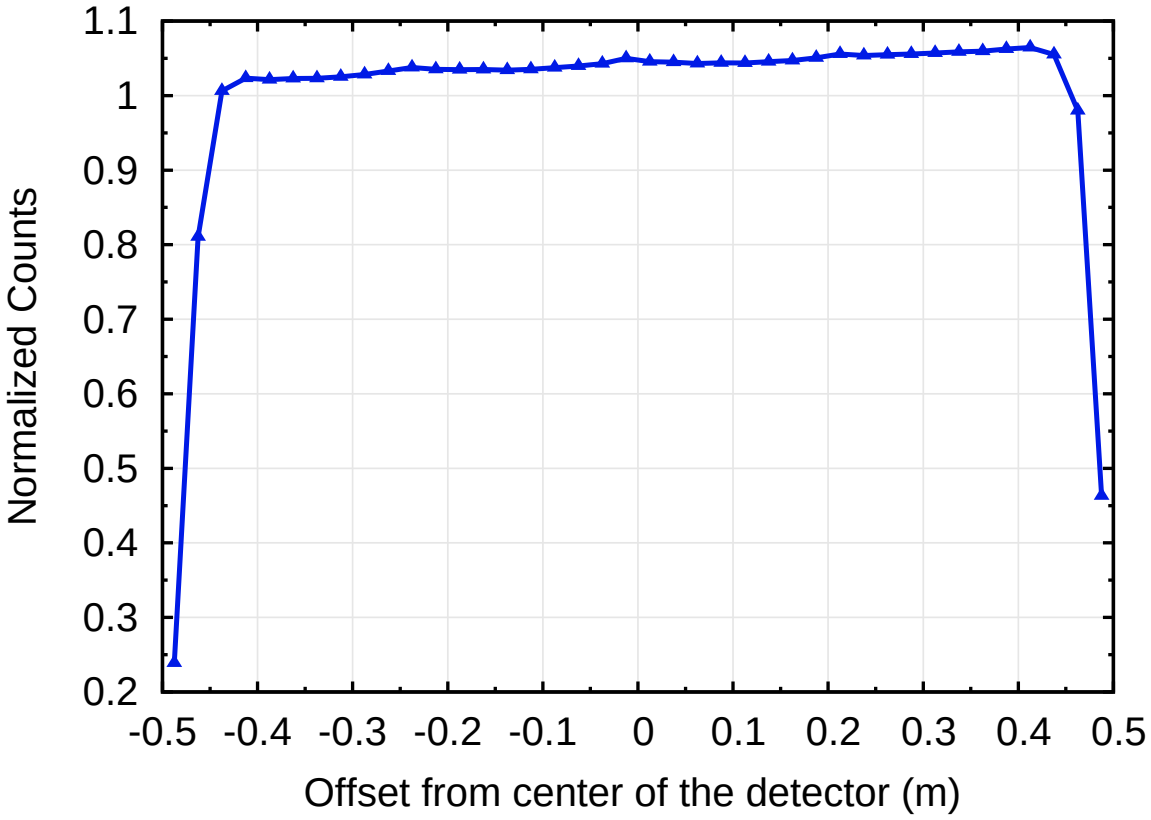

Figure 7.4: Counts from vanadium as a function of the offset of a pixel from the center of the detector, normalized such that the mean number of counts per pixel is 1. Presumably there are differences because of the different solid angle subtended by each pixel; however, in reality, this effect is quite small. The drop in intensity at the ends of the detector is probably due to shielding by the detector mounts, rather than differences in solid-angle coverage.

pressure-efficiency of the detectors, but with sums over detectors at equal distances to the sample, rather than over pixels. In either case, this is typically a very small correction on LRMECS and Pharos, as seen in Fig. 7.4, which shows normalized intensity as a function of the offset of the pixel from the center of the detector. The correction can be more significant on ARCS, where the detectors are stacked three rows tall.

7.2 Determination of the incident energy

As seen in § 6.2, the incident energy is nominally determined by the rotation frequencies of the T0 and Fermi choppers; however, in practice it is more accurate to determine the incident neutron energy from the data itself. Here, we present two methods for doing this.

7.2.1 Using monitors

The traditional way to find the incident energy is very simple. Two special detectors, called monitors, are used to measure the incident neutron spectrum. They are located at different points along the path the incident neutrons would take were they not scattered, and we assume that the neutrons counted in the monitors have traveled there from the moderator without interacting with anything along the way. Presumably, if the choppers are working properly, the spectrum in either monitor consists of a large peak, as is seen in Fig. 7.5

Some sort of fit to the peaks is performed, and the time required for the neutrons to reach the monitor is extracted from the fit. In Fig. 7.5, the fit to the peaks was parabolic, but fits with Gaussian or other lineshapes are also possible. Given the fits, we may calculate a single value that is our estimate of E_{I}, as follows:

$$E_{\mathrm{I}} = \frac{m_{\mathrm{n}}}{2}\left(\frac{L_{\mathrm{mon}}}{\tau_{\mathrm{mon}}}\right)^2 , \tag{7.10}$$

where m_{n} is the neutron mass, L_{mon} is the distance between the two monitors, and τ_{mon} is the difference between the two times-of-flight determined by the fits. For the LRMECS data shown in Fig. 7.5, $\tau_{\mathrm{mon}} = 1107.98\ \mu$s, and $L_{\mathrm{mon}} = 3.732$ m; thus the experimentally determined incident energy is given by:

$$E_{\mathrm{I}} = \frac{1.67\times10^{-27}\ \mathrm{kg}}{2}\left(\frac{3.73\ \mathrm{m}}{1107.98\times10^{-6}\ \mathrm{s}}\right)^2 = 9.50\times10^{-21}\ \mathrm{J} = 59.30\ \mathrm{meV}\ . \tag{7.11}$$

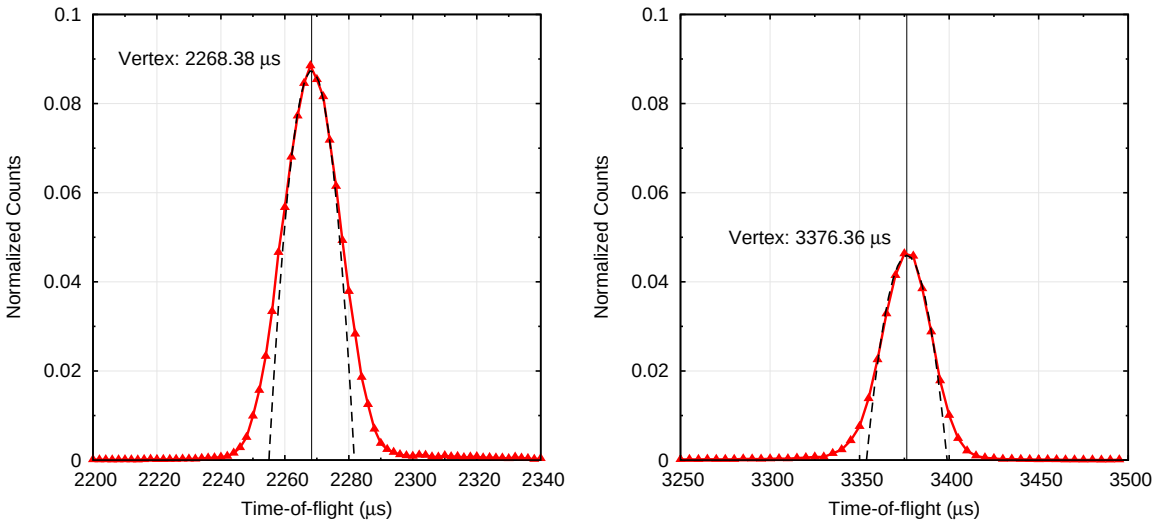

Figure 7.5: Counts in the first and second beam monitors on LRMECS. The data, shown with markers, were fit to parabolas, shown by the dashed line. The vertices of the parabolas allow us to make an estimate of the incident energy.

The nominal incident energy (from the chopper settings) was 60.00 meV, which is in error by a little over 1%.

7.2.2 Using scattered data

Some instruments have no monitors, or have broken monitors, and the following procedure allows determination of the incident energy using the scattered neutron counts. More generally, we should be able to use the scattered neutrons to help with determination of the incident energy even if there are monitors, or to help with refinement of the instrument and sample geometry.

We wish to determine the incident energy of the neutrons from the corrected intensity, I_{dpt}. Our procedure rests primarily on the assumptions that an elastic peak exists at all angles and that the scattering will be the strongest in the elastic peak — both of which are usually satisfied. On most instruments, the detectors are grouped together in modules, like the one seen in Fig. 6.3. Here, we will assume that the centers of all the detectors are equidistant from the sample, and that all the pixels in a given row are also equidistant from the sample. This is generally not the case; however, it is easy to adjust this method to work detector bank by detector bank, where these positional constraints are usually met.

In the past, where monitors were wanting, the incident energy was determined by finding the intensity as a function of time-of-flight only, without regard to the varying sample to pixel distances:

$$I_t = \sum_d \sum_p I_{dpt} \ . \tag{7.12}$$

This spectrum was then fit to a Gaussian, or some other function, and the incident energy was taken to be the maximum (or the mean, etc.). This is shown in Fig. 7.6. The vertex is at 6587.260μs, and given the distance from the moderator to the detectors is $L_{\mathrm{I}} + L_{dp} \sim 24.013$m, we get an incident energy:

$$E_{\mathrm{I}} = \frac{1.675 \times 10^{-27} \text{ kg}}{2} \left(\frac{24.013 \ m}{6587.260 \times 10^{-6} \ s} \right)^2 = 1.112 \times 10^{-20} \text{ J} = 69.461 \text{ meV} \ . \tag{7.13}$$

To make a more accurate estimate, we will consider sums over the intensity at constant distance from the sample. Given our assumption about detector banks, this means we may sum over detectors to get intensity as a function of time-of-flight and pixel:

$$I_{pt} \equiv \sum_d I_{dpt} \ . \tag{7.14}$$

In a fixed pixel, $p = p^*$, we find the time-of-flight channel that corresponds to the maximum counts and then fit a parabola (or some other function) to a few of the closely surrounding points. The

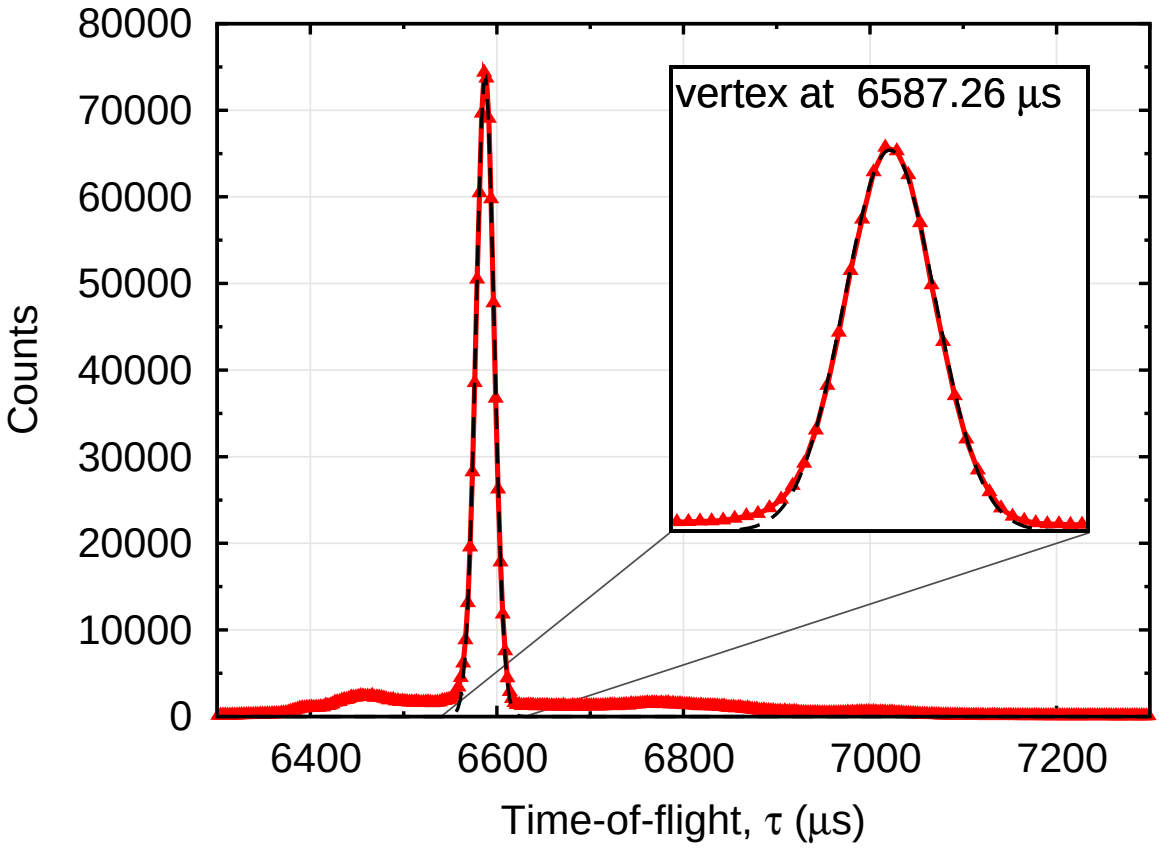

Figure 7.6: Intensity summed over detectors and pixels, I_t, from nickel at room temperature as measured on Pharos. The red triangles are the data, and the black, dashed line shows a fit of a Gaussian to the peak. The inset shows a closeup of the fit, and the time-of-flight at the vertex is taken to correspond to the incident energy.

.

time-of-flight at the vertex of the parabola, $[\tau_{\mathrm{e}}]_{p^*}$, is taken to correspond to the incident energy, $[E_{\mathrm{e}}]_{p^*}$, as seen in the row of pixels:

$$[E_{\mathrm{e}}]_{p^*} = \frac{m_{\mathrm{n}}}{2}\left(\frac{L_{p^*}}{[\tau_{\mathrm{e}}]_{p^*}}\right)^2 , \tag{7.15}$$

where L_{p^*} is the distance from the moderator to the row of pixels. Finally, we take the incident energy, E_{I} to be the average of these over all rows of pixels:

$$E_{\mathrm{I}} = \langle [E_{\mathrm{e}}]_p \rangle = \frac{\sum_p [E_{\mathrm{e}}]_p}{\sum_p 1} = \frac{\sum_p \frac{m_{\mathrm{n}}}{2}\left(\frac{L_p}{[\tau_{\mathrm{e}}]_p}\right)^2}{\sum_p 1} , \tag{7.16}$$

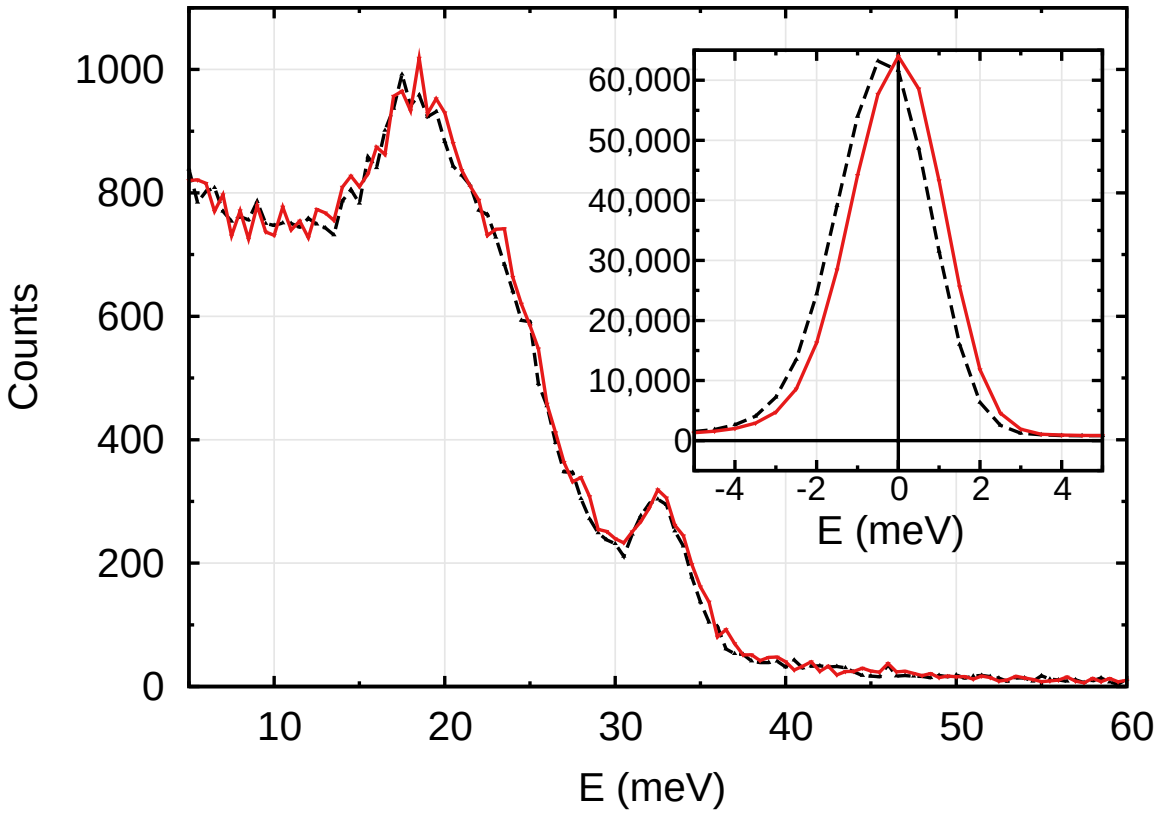

Figure 7.7: Scattering as a function of the energy transferred to the sample. The dashed black curve was found with the incident energy determined by sums over both detectors and pixels, the solid red curve by sums over detectors only. The differences in the inelastic scattering (5+ meV) seem small; however, they are systematic, and will have an effect on the phonon DOS. In particular, the errors in the estimation of the incident energy are likely to cause an underestimate of the high energy cutoff of the phonon spectrum, which will impact our calculations of thermodynamic quantities like the phonon entropy. At elastic energies (inset) the differences are more apparent; with the solid red curve clearly centered around 0 meV, and the dashed black curve incorrectly shifted.

where the denominator gives the number of rows of pixels. In this fashion, we get:

$$E_{\mathrm{I}} = 69.517 \text{ meV} . \tag{7.17}$$

In this case, the change in the incident energy is relatively small; however, the effects on the calculated spectrum are larger. The data here are quite high quality, and larger discrepancies can be expected for lower quality data sets. Fig. 7.7 shows the scattering as a function of the energy transferred to the sample, $E = E_{\mathrm{F}} - E_{\mathrm{I}}$, with E_I determined by sums over detectors and pixels, or by sums over detectors only.

Since most newer instruments (like ARCS) have monitors, which are probably better suited for the determination of the incident spectrum, this sort of procedure could be adopted for fine-tuning our understanding of the instrument geometry. Specifically, it could be used to find the distances

from the sample to the pixels, given an incident energy determined via the scattering in the monitors. To do so, we invert Eq. 7.15, and use the calculated incident energy in order to determine the sample to pixel distance:

$$L_{p^*} = \left(\frac{2E_{\mathrm{I}}}{m_{\mathrm{n}}}\right)^{\frac{1}{2}} [\tau_{\mathrm{e}}]_{p^*} \ . \tag{7.18}$$

Although there is probably not enough intensity on Pharos to actually perform this procedure pixel by pixel (e.g., not summed over detectors), there likely will be on newer instruments (again, like ARCS).

7.3 Normalization

Frequently, we will collect data on more than one sample, and we will wish to compare these measurements. In order to do so, we need a way to estimate the number of neutrons that have hit the sample, whether they were scattered or not.

Normalization of the data is generally quite straight forward. On an instrument with a monitor, we simply divide the data through by the summed intensity in said monitor. On an instrument without a monitor, the integrated proton current is often used as a proxy. Fig. 7.8 indicates that this works reasonably well.

7.4 Transformation to physical coordinates

The data measured measured in a typical neutron scattering experiment conflates information about the instrument with information about the sample. We wish now to try and separate these two pieces of information. In this section, we will discuss the conversion of the data to physical coordinates such as the scattering angle Θ, the energy transfer E, or the momentum transfer $\mathbf{Q}$, that are independent of the geometry of the instrument.

7.4.1 Rebinning

The most commonly used method of transforming the data from instrument to physical coordinates is through a technique called *rebinning*. In particular, the raw data is rebinned in multiple steps; first into counts as a function of detector, pixel, and energy, I_{dpE}; then of scattering angle and energy transfer, $I_{\Theta E}$; and finally of momentum and energy transfer, I_{QE}.[g] The first two of these steps are roughly orthogonal, so we might group them and say that the data is rebinned twice.[h] We will give

[g] With a sample that is a single crystal, we get $I_{\mathbf{Q}E}$, where the measured wavevector transfer is a vector quantity. This does not have a large effect on the procedures outlined here, other than to make their explanation more tedious.

[h] Remember, the data is *already binned* in hardware.

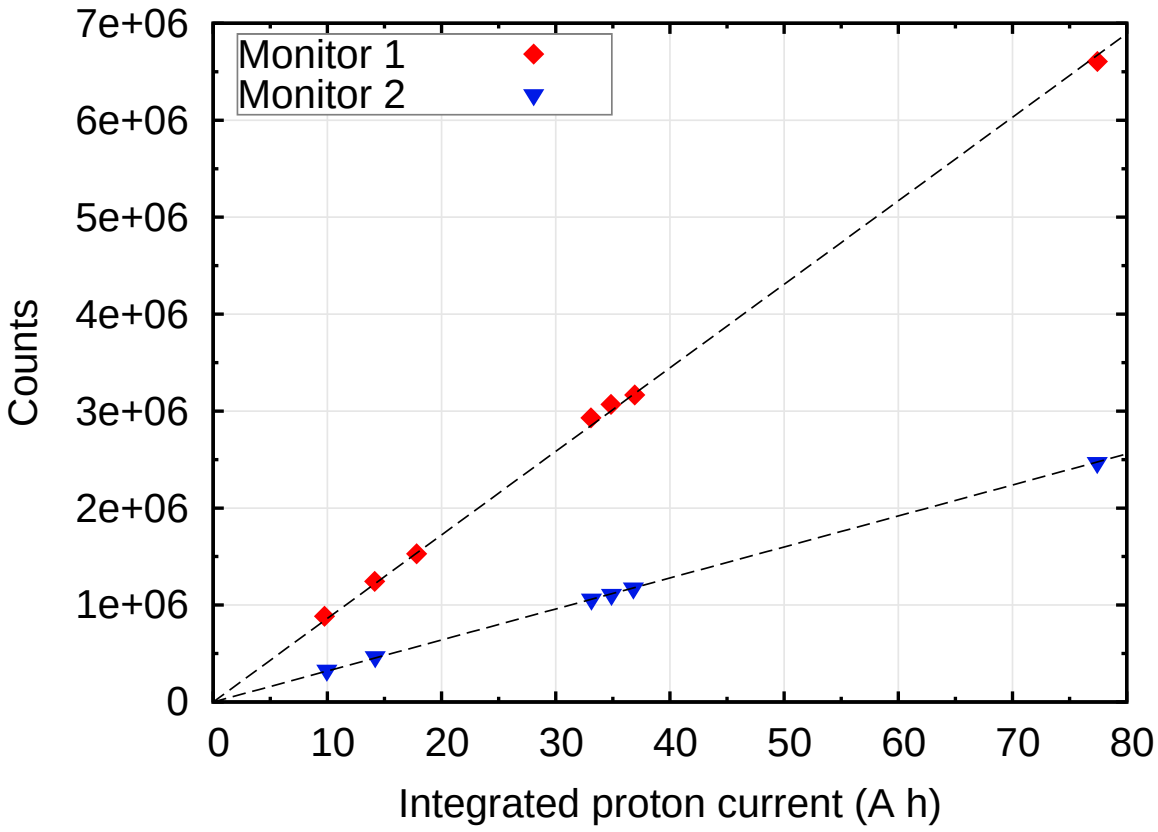

Figure 7.8: Integrated proton current versus integrated counts in the monitors for Pharos. The red diamonds are counts from monitor 1, which is between the T0 and E0 choppers, and the blue triangles are from monitor 2, which is between the E0 chopper and the sample. The dashed black lines are linear fits to the data, constrained to go through 0. The dependence is quite linear, indicating that the integrated proton current is a good proxy for use in normalization of data.

a 2D example of rebinning, but this technique is also used for higher dimensional data sets.

The data is considered to be a histogram on a regular rectangular grid in the current coordinate system, with axes x and y. We measure the counts within some rectangle (bin) in the x-y system, and wish to know how many counts that corresponds to for a bin in the target u-v coordinate system. To estimate this, we transform each of the 4 corners of our bin in x and y into the u-v coordinate system, and then connect the transformed corners with straight lines, forming a 4-sided polygon. This is shown in Fig. 7.9. Each bin in the u-v system contains some fraction of the area of the polygon, and those bins receive counts in proportion to that fraction. If the transformation is highly structured — which is usually the case in a physical experiment — this procedure leads to systematic errors in the placement of counts in the new coordinate system. This is also shown in Fig. 7.9.

7.4.2 Analytical coordinate transformation

In this section, we propose an alternative method of treating neutron scattering data from a powder sample as measured on a direct-geometry, time-of-flight, chopper spectrometer. Proof of principle has been performed using LRMECS data; however, the technique should be generalizable to other instruments — there is nothing in the method that precludes generalization to single crystals and/or inverse geometry instruments. The approximations involved are superior to those made in rebinning. Throughout the section, data from LRMECS are used because the instrument is relatively simple for a time-of-flight chopper spectrometer. In particular, its detectors are not pixelated, and are all approximately the same distance from the sample.

The method involves two steps. We first account for the differences between a count in Θ-τ space and one in Q-E-space. Once this *reweighting* is complete, we take as input pairs of Q and E and

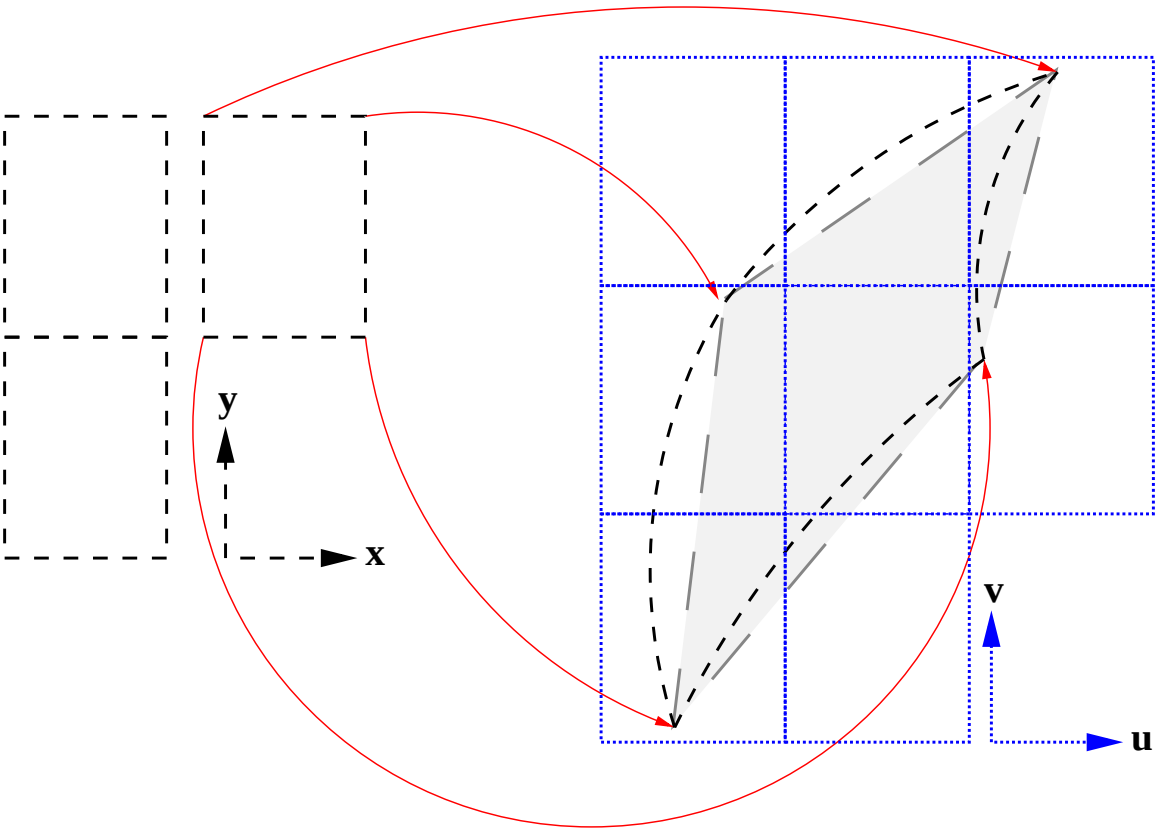

Figure 7.9: Rebinning from x and y to u and v. The short-dashed black rectangles depict bins in the x-y coordinate system, and the dotted blue in the u-v system. The solid red arrows show the transformation of the corners of a bin in the x-y coordinate system to points in the u-v system. Connecting those transformed corners with straight lines forms the long-dashed, shaded, gray polygon in the u-v system; whereas an exact transformation would yield the black dashed curve, which shares the same corner points. Each bin in the u-v system contains some fraction of the area of the gray polygon, and those bins receive counts in proportion to that fraction. Here, then, the rebinned intensity is being systematically shifted to lower v and to higher u.

linearly interpolate to give $I(Q,E)$.[i]

7.4.2.1 Reweighting

Here, we will consider data only as a function of detector and time-of-flight, because the detectors on LRMECS are not pixelated. Further, for LRMECS, there is a one-to-one correspondence between a detector, and a scattering angle so we may write:

$$I_{dt} = I_{\theta t} \ , \tag{7.19}$$

where θ indexes scattering angle. On LRMECS, some of the detectors are located at negative scattering angles. For a powder sample, the sign of the scattering angle is irrelevant.[j] Further, on LRMECS, it so happens that for each detector at negative scattering angle Θ^- there is an identical detector at $\Theta^+ = |\Theta^-|$. We assume these to be independent measurements of the same quantity, and thus take:

$$I_{\theta t} = \frac{I_{\theta^- \ t} + I_{\theta^+ \ t}}{2} \ , \tag{7.20}$$

for all detectors that have matching positive- and negative-angle instances.[k]

The intensity $I_{\theta t}$, when properly normalized, gives the probability of a neutron arriving in the area of Θ-τ space covered by the detector(s) indexed by θ and t. We wish to know the probability of finding a neutron arriving in the associated region of Q-E space. For LRMECS, it is (at least approximately) true that all of the scattering angle and time-of-flight bins cover the same area in Θ-τ space; however, it is by no means true that they all cover the same area in Q-E space. The first thing to do, then, is to reweight the probabilities by the areas in the two coordinate systems:

$$I_{QE} = \frac{|\mathcal{R}_{\theta t}|}{|\mathcal{R}_{QE}|} I_{\theta t} \ , \tag{7.21}$$

where $|\mathcal{R}_{\theta t}|$ gives the area of a bin in Θ-τ space, and $|\mathcal{R}_{QE}|$ its area in Q-E space.[l] We will continue to use abbreviated notation in the subscripts: $Q = Q_{\theta t}$ and $E = E_t$.

The area in Θ-τ space is a known quantity. If $\Delta\tau$ is the width of a time channel, and $\Delta\Theta$ is the width of a detector (in scattering angle), then the area in Θ-τ space is given by their product:

$$|\mathcal{R}_{\theta t}| = \Delta\Theta \ \Delta\tau \ , \tag{7.22}$$

[i] Here, we use $I(Q,E)$ as opposed to I_{QE} because the the linear interpolation provides a continuous function of inputs Q and E.

[j] For a single crystal, the sign matters, and we simply skip these first steps.

[k] In a sense, the repeated detector angles are a complication rather than a simplification. Without them, there is no need to combine counts from different detectors.

[l] Care must be taken here that none of the area in Θ-τ space, $|\mathcal{R}_{\theta t}|$, has been accounted for in the detector efficiency corrections — in particular, in a correction for the solid angle subtended by the pixels.

In theory, the area in Q-E space is also easy to find, it is given by:

$$|\mathcal{R}_{QE}| = \iint_{\mathcal{R}_{QE}} dQdE \ . \tag{7.23}$$

The problem is that we don't know how to write the region of integration, $\mathcal{R}_{QE}$, explicitly. Therefore, we use:

$$|\mathcal{R}_{QE}| = \iint_{\mathcal{R}_{\Theta\tau}} |\mathbf{J}| d\Theta d\tau = \iint_{\mathcal{R}_{\Theta\tau}} \begin{vmatrix} \frac{dQ}{d\Theta} & \frac{dQ}{d\tau} \\ \frac{dE}{d\Theta} & \frac{dE}{d\tau} \end{vmatrix} d\Theta d\tau \ , \tag{7.24}$$

where $|\mathbf{J}|$ is the determinant of the *Jacobian matrix*, [87] $\mathbf{J}$, and $\mathcal{R}_{\Theta\tau}$ is the region of integration in ϕ-T space, which is the rectangle formed by the points (Θ, τ), $(\Theta, \tau + \Delta\tau)$, $(\Theta + \Delta\Theta, \tau)$, and $(\Theta + \Delta\Theta, \tau + \Delta\tau)$. Integrating Eq. 7.24 is feasible, but messy and uninstructive. Thus, the details are given in Appendix C. Here we present the result of the indefinite integral:

$$\begin{aligned} |\mathcal{R}_{QE}| = \frac{-\hbar^2 Q_{\mathrm{I}}^3}{6m_{\mathrm{n}}} \Bigg\{ & 3\cos(\Theta)\sin^2(\Theta)\mathrm{arcsinh}\left(\frac{\frac{Q_{\mathrm{F}}}{Q_{\mathrm{I}}} - \cos(\Theta)}{\sin(\Theta)}\right) \\ & + \left[\left(\frac{Q_{\mathrm{F}}}{Q_{\mathrm{I}}}\right)^2 - 2\frac{Q_{\mathrm{F}}}{Q_{\mathrm{I}}}\cos(\Theta) + 1\right]^{\frac{1}{2}} \left[2\left(\frac{Q_{\mathrm{F}}^2}{Q_{\mathrm{I}}^2}\right)^2 - \frac{Q_{\mathrm{F}}}{Q_{\mathrm{I}}}\cos(\Theta) - 3\cos^2(\Theta) + 2\right] \Bigg\} \Bigg|_{\mathcal{R}_{\Theta\tau}} \ , \end{aligned} \tag{7.25}$$

where in terms of τ and τ_{I}, we have

$$\frac{Q_{\mathrm{F}}}{Q_{\mathrm{I}}} = \frac{L_d \tau_{\mathrm{I}}}{L_{\mathrm{I}}(\tau - \tau_{\mathrm{I}})} \ , \tag{7.26}$$

where L_d is the distance from the sample to the detector.[m] The vertical bar at the end of Eq. 7.25 indicates that the function must be evaluated over the appropriate region in Θ-τ.

7.4.2.2 Coordinate mapping

Now that we have the area $|\mathcal{R}_{QE}|$, we may reweight our data using Eq. 7.21. What then remains is to generate a map that connects the axes of the old coordinate system, Θ and τ, to the axes in the new coordinate system, Q and E. Considering that many analysis codes require data in a certain format, and that we believe that our data informs us about the space in between the hardware bins as well as the bins, we would like a general way to get $I(Q, E)$ for any pair of Q and E within the overall region sampled. Moreover, we would like to do so without any loss of resolution. (Nor with any gain.) A relatively simple way to do this is to take a pair of Q and E as user input, map them back to the instrument coordinates, find the smallest simplex which encloses the point of interest, and linearly interpolate between those points.

[m] For pixelated detectors, we would use L_{dp}

This method assumes that the data has been preprocessed, so that for any given τ and Θ pair, there exists only one value of $I_{\tau\Theta}$. (On LRMECS, for example, we took care of this when we combined counts in detectors at equivalent positive and negative angles.) Given that this preprocessing has been done, we use:

$$\Theta = \arccos\left(\frac{Q_{\mathrm{I}}^2 + Q_{\mathrm{F}}^2 - Q^2}{2Q_{\mathrm{I}}Q_{\mathrm{F}}}\right), \tag{7.27}$$

to map Q back to Θ and its index θ^*. Then, we use:

$$\tau = \sqrt{\frac{m_{\mathrm{n}}}{2}}\left(\frac{L_{\mathrm{I}}}{\sqrt{E_{\mathrm{I}}}} + \frac{L_d}{\sqrt{E_{\mathrm{F}}}}\right), \tag{7.28}$$

to map E back to τ, and its index t^*. Determining t^* and Θ^* and finding the enclosing simplex efficiently is a matter of having the original data in an appropriate data structure, such as a kD-tree or an R-tree. [88–90]

If the data is highly structured in τ and Θ, care needs to be taken to avoid cases where the smallest enclosing simplex is not well defined. For example, if the data points form a rectangle centered about τ and Θ, which three points should be used to form an enclosing simplex? Here, careless choices might lead to a discontinuous representation of the data.

In point of fact, the geometry and electronics on LRMECS are such that τ and Θ have a regular, gridded structure.[n] In this case, the *native* data structure proves to be the most efficient for mapping from the user's Q and E to the instrument coordinates. As such, we implemented a minor variation on the scheme outlined above. Since τ and Θ form a regular grid, we may transform the Q-E pair into τ and Θ, and use simple arithmetic to determine the nearest neighboring points:

$$t^* = \mathrm{floor}\left(\frac{\tau^* - \tau_1}{\Delta\tau}\right), \tag{7.29}$$

$$\theta^* = \mathrm{floor}\left(\frac{\Theta^* - \Theta_1}{\Delta\Theta}\right), \tag{7.30}$$

where τ_1 and Θ_1 are the first elements arrays containing time-of-flight and scattering angle, respectively. The four corners of a rectangle that encloses the point of interest, then, are given by (t^*, θ^*), $(t^*, \theta^* + 1)$, $(t^* + 1, \theta^*)$, and $(t^* + 1, \theta^* + 1)$.

The astute reader will have noticed that linearly interpolating over a rectangle is not strictly possible.[o] One solution would be to quadratically interpolate. Instead, we calculate the mean value of the counts at the four corners of the rectangle, and take that to be the number of counts at the center of the rectangle. We then interpolate over the triangles, as is shown in Fig.7.10. Fig. 7.11

[n] Actually, the data are gridded slightly irregularly, but the required modifications of the algorithms are not very instructive.

[o] Simply because three points define a plane.

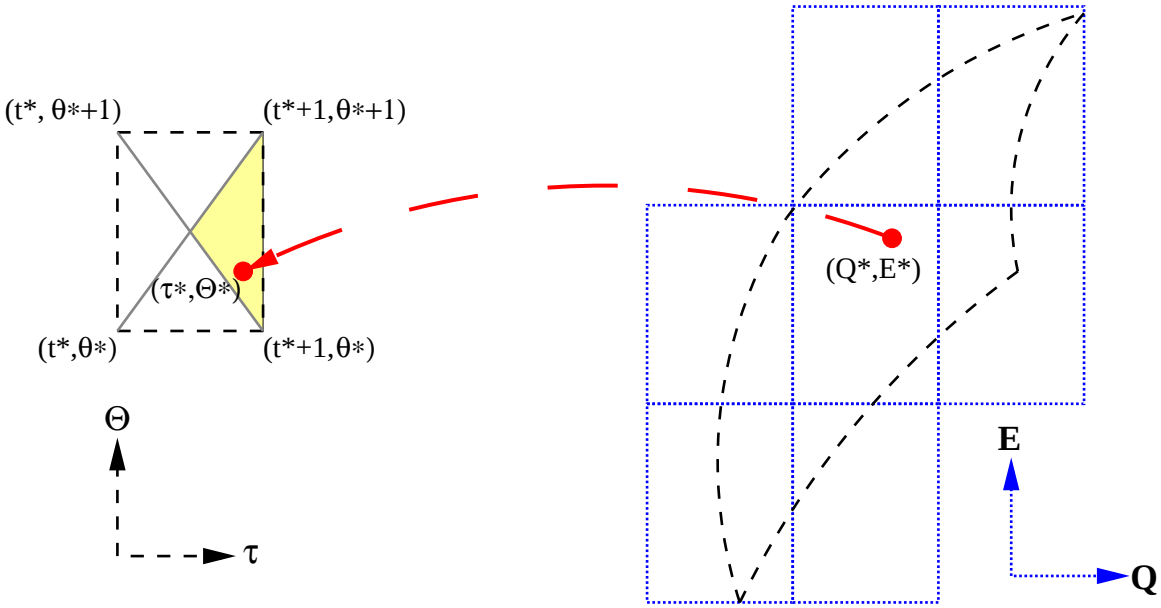

Figure 7.10: Interpolation for LRMECS data. The point of interest is given in red, and it is shown in the Θ-τ and the E-Q coordinate systems on the left and the right respectively, with the long-dashed, red arrow representing the transformation. The bins from the hardware are shown by the short-dashed, black rectangle in Θ-τ, and the short-dashed, black curvy figure in Q-E. The two solid gray lines cross at the center of the rectangle, and we assign the mean of the counts at the corners of the rectangle to this point. The yellow, shaded region represents the linear interpolation surface which gives the value of the intensity for the point of interest.

shows nickel data, measured on LRMECS, that has been analyzed with both the rebinning and the analytical coordinate transformation methods described above.

7.5 Removal of background scattering

Occasionally, it is thought that a measurement of the background is unnecessary because the sample container and mount will not scatter enough neutrons to merit it. On the contrary, it is not only the sample container and mount that contribute to the background scattering, but also the instrument itself.

For this reason, it is always critical to make a measurement of the background. Assuming such a measurement, I^{b} has been made, we simply subtract it from the measurement of the sample, I^{s}:

$$I(Q,E) = I^{\mathrm{s}}(Q,E) - fI^{\mathrm{b}}(Q,E)\ . \tag{7.31}$$

As some fraction of the neutrons which were scattered by the instrument and sample environment are now scattered by the sample it is common to subtract only a fraction, f of the measured background. Usually, samples are designed to scatter between 10% and 20% of neutrons; thus, we normally have

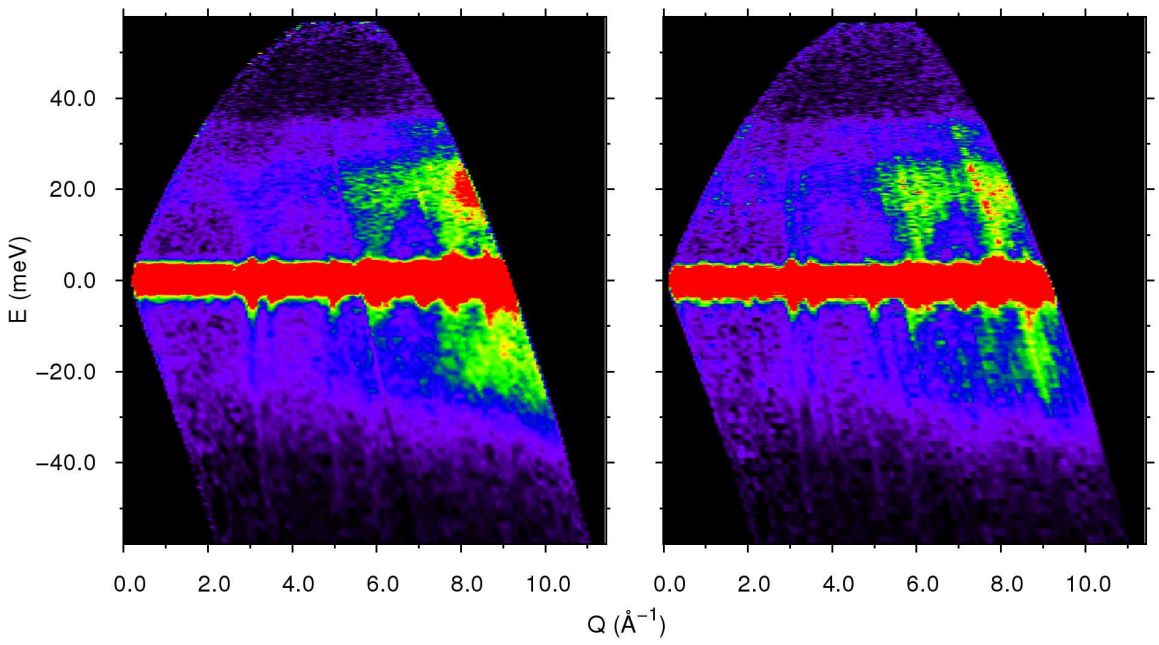

Figure 7.11: Comparison of $I(Q, E)$ for nickel as measured on LRMECS and as calculated with with the analytical coordinate transformation on the left and with rebinning on the right. In so much as it was possible, the two analyses were performed so as to be comparable. For example, the plotted data have the same numbers of points in Q and E. The plot on the left should be considered no more than proof-of-principle, and there are noticeable defects in the analysis. Namely, the calculation of the incident energy was not quite correct, and the resulting spectrum is skewed off center. Regardless, the plot on the right shows a great deal more streaking along lines of constant angle (See Fig. 6.5. For LRMECS, this corresponds to counts in single detector).

$0.8 < f < 1.0$.

Although the removal of background scattering could be performed with the raw data; it is frequently only done at this stage in the analysis process. A disadvantage of this strategy is that it might compound certain types of systematic errors in the data analysis. An advantage is that the intensity, up to now, has always remained positive, which can aid in the speed and ease of the analysis process.

Another variation is to remove separately the measured background I^{b} and the *time-of-flight-independent* background.[p] Changes in the background may occur on time scales similar to a single measurement. For example, the neighboring instrument may be running while I^{s} is being measured, but not during measurement of I^{b}. The correction for this is often performed even before the corrections for detector efficiencies, and it entails selecting a region in time of flight where the counts are only ambient noise, finding the average number of counts in this region, and subtracting that from the data. The rest of the removal of background scattering remains the same.

[p]This is frequently called the *time-independent* background; however, that is a gross misnomer. It is precisely the time dependence of the background for which it attempts to correct; albeit for times that are on a longer scale than the time-of-flight.

Chapter 8

Processing S(Q,E)

Once $S(Q, E)$ is determined to the best of our abilities,[a] we frequently wish to extract further information about the structure or dynamics of our sample. In this chapter, we present methods for determining the phonon DOS and the lattice parameter from the scattering. We also consider methods for characterizing phonon linewidths and the interatomic potential, given a phonon spectrum.

8.1 Finding the phonon DOS

There are two commonly used methods for extracting the phonon spectrum from inelastic neutron scattering data. Both methods are designed to separate 1-phonon from multiphonon scattering, which is the simultaneous creation or annihilation of many phonons by 1 neutron. This is to be distinguished from multiple scattering, in which a neutron is scattered by a phonon (or phonons) and then at some later time is scattered again. The two are qualitatively different, as multiphonon scattering is a property of the sample alone, but multiple scattering may involve the sample environment and the instrument.

The first method presented is called the Fourier-log method and corrects only for the multiphonon scattering. The second is an iterative procedure, and it has been modified to also correct approximately for multiply scattered neutrons.

8.1.1 Fourier-log method

Here, we assume that the measured scattering $I(Q, E)$, is given by the dynamic structure factor, $S(Q, E)$, with the energy dependent portion convolved[b] with some resolution function $Z(Q, E)$. We

[a] Since we have not yet corrected for multiple scattering, we are technically still dealing with $I(Q, E)$. [91–93] We will only concern ourselves with this distinction in § 8.1.2, where we will actually attempt to make such a correction.

[b] This must really be a convolution — as opposed to some other integral transform — in order for this method to work. In particular, this means that the resolution function must be independent of the energy transferred to the sample, E'; *e.g.*, a Gaussian with $\sigma = 2$ meV, as opposed to a Gaussian with $\sigma = \frac{1}{\sqrt{E'}}$.

use Eq. 5.15 to express this as follows:

$$I(Q,E) \quad \propto \quad Z(Q,E) * \left[e^{-2W} \mathcal{FT}\left\{ \exp \langle \hat{\mathbf{U}}\hat{\mathbf{V}} \rangle \right\} \right] , \tag{8.1}$$

where we have taken advantage of the fact that $S(Q,E)$ is proportional to $\mathcal{FT}\left\{ \langle \hat{\mathbf{U}}\hat{\mathbf{V}} \rangle \right\}$. We may pull the Debye-Waller factor through, and then take the inverse Fourier transform of both sides, converting the convolution into a product:

$$\begin{aligned} \mathcal{FT}^{-1}\{I(Q,E)\} &\propto e^{-2W} \mathcal{FT}^{-1}\left\{ Z(Q,E) * \mathcal{FT}\left\{ \exp \langle \hat{\mathbf{U}}\hat{\mathbf{V}} \rangle \right\} \right\} \\ &\propto e^{-2W} \mathcal{FT}^{-1}\{Z(Q,E)\} \mathcal{FT}^{-1}\left\{ \mathcal{FT}\left\{ \exp \langle \hat{\mathbf{U}}\hat{\mathbf{V}} \rangle \right\} \right\} \\ &\propto e^{-2W} \mathcal{FT}^{-1}\{Z(Q,E)\} \exp \langle \hat{\mathbf{U}}\hat{\mathbf{V}} \rangle . \end{aligned} \tag{8.2}$$

We now take the logarithm of both sides:

$$\log \left[\mathcal{FT}^{-1}\{I(Q,E)\} \right] \quad \sim \quad -2W + \log \left[\mathcal{FT}^{-1}\{Z(Q,E)\} \right] + \langle \hat{\mathbf{U}}\hat{\mathbf{V}} \rangle . \tag{8.3}$$

We subtract $\log \left[\mathcal{FT}^{-1}\{Z(Q,E)\} \right] - 2W$ from both sides, and take the Fourier transform:

$$\begin{aligned} \mathcal{FT}\left\{ \langle \hat{\mathbf{U}}\hat{\mathbf{V}} \rangle \right\} &\sim \mathcal{FT}\left\{ \log \left[\frac{\mathcal{FT}^{-1}\{I(Q,E)\}}{\mathcal{FT}^{-1}\{Z(Q,E)\}} \right] + 2W \right\} \\ &\sim \mathcal{FT}\left\{ \log \left[\frac{\mathcal{FT}^{-1}\{I(Q,E)\}}{\mathcal{FT}^{-1}\{Z(Q,E)\}} \right] \right\} + 2W\delta(E) . \end{aligned} \tag{8.4}$$

In the case that $Z(Q,E) = Z(Q)Z(E) = e^{2W} Z(E)$ — that is, the Q dependent part of the resolution function is determined only by the Debye-Waller factor — we have:

$$\mathcal{FT}\left\{ \langle \hat{\mathbf{U}}\hat{\mathbf{V}} \rangle \right\} \quad \sim \quad \frac{1}{2W} \mathcal{FT}\left\{ \log \left[\frac{\mathcal{FT}^{-1}\{I(Q,E)\}}{\mathcal{FT}^{-1}\{Z(E)\}} \right] \right\} + 2W\delta(E) . \tag{8.5}$$

The advantage of this method is that it is direct, and that for sufficiently simple[c] resolution functions, you may correct for $Z(Q,E)$ as you find the DOS. This is not the case for time-of-flight chopper spectrometers; however, this is the type of procedure used for the nuclear resonant inelastic x-ray scattering data presented in Chapter 12.

8.1.2 Iterative method, with correction for multiple scattering

Here, we wish to deal with only inelastic scattering, so we must first remove any elastic scattering from the data. This is done by assuming an E^2 energy dependence of the phonon DOS, which leads

[c] Read, energy transfer independent.

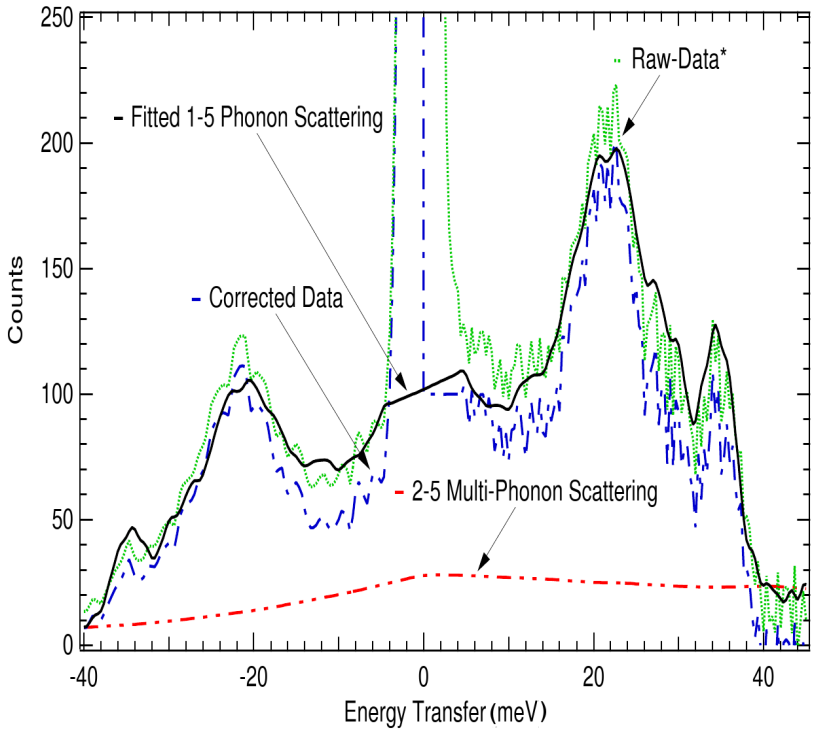

Figure 8.1: A typical determination of the multiphonon-scattering using data that has been binned into angle banks. The green dotted line labeled "Raw-Data" shows $I(E)$ as determined by experiment. The solid black line labeled "Fitted 1-5 Phonon Scattering" is the best fit to the data. (This should be compared to the fit in Fig. 8.4.) Figure taken from Swan-Wood. [94]

to inelastic scattering at low energies of the following form:

$$I(E) = \frac{\zeta_0 E}{1 - \exp\left(-\beta E\right)} \,, \tag{8.6}$$

where the constant ζ_0 is determined by matching the function to the experimentally measured scattering, just past the edges of the elastic peak. The peak, then, is replaced with a scattering in the form of Eq. 8.6.

Once the elastic scattering has been removed we analyze the remaining, inelastic scattering to determine the phonon DOS. This method of finding the DOS is iterative, and it is the approach we have used for the neutron measurements of aluminum and nickel presented herein. The process has been described previously,[92, 95] but we present some modifications here. Namely, in the past, the correction has either been used for incoherent scattering measured on a triple-axis spectrometer at a single value of Q,[92] or for time-of-flight neutron scattering data, where the data has been binned into angle-banks. [13, 14, 22–24, 54, 95–99] Fig. 8.1 shows a typical best fit to data obtained in this fashion. Here, the correction is performed with data that is a function of Q, not angle bank; and an approximate correction for multiple scattering has also been added.

Corrections for multiple scattering have been performed in many ways, from subtracting a constant from the data, [92] to full Monte-Carlo simulations. [100] At high temperatures, the former does not account for the slope of the scattering past the high energy cutoff of the phonon DOS. The latter can be computationally intensive, and requires details of the shape of the sample and the instrument. Here we take an approach of intermediate complexity.

In § 5.2.4, we developed an expression for the multiphonon scattering, which showed that the $\mathcal{P}$-phonon scattering can be written as a convolution of the 1- and the $(\mathcal{P}-1)$-phonon scattering. Briefly, we consider the physical meaning of this. Let $\Upsilon_{\mathcal{P}}(E)$ be the probability of an event where the neutron loses energy E to $\mathcal{P}$ phonons. If all of the 1-phonon scattering processes are statistically independent, and if a 2-phonon process is made up of two 1-phonon processes, then we have the probability of a 2-phonon process where a neutron loses E' to one phonon and E'' to another is given by:

$$\Upsilon_2(E', E'') = \Upsilon_1(E')\Upsilon_1(E'') \; . \tag{8.7}$$

In an experiment, however, we only see the resulting neutron energy loss, $E = E' + E''$, which gives $E'' = E - E'$. There may be many combinations of two 1-phonon processes that produce this energy loss, and the intensity that we see will correspond to a sum over all of these possibilities:

$$\Upsilon_2(E) = \sum_{E'} \Upsilon_1(E')\Upsilon_1(E - E') \; . \tag{8.8}$$

In the limit of a continuous energy expression, we have a convolution. For $\mathcal{P}$-phonons, this is expressed by the recursion relation:

$$\Upsilon_{\mathcal{P}}(E) = \int_{E'} \Upsilon_1(E')\Upsilon_{\mathcal{P}-1}(E - E')dE' \; . \tag{8.9}$$

The point of this discussion is that we have actually said very little about the underlying scattering processes — simply that we believe them to be statistically independent. As such, we expect the same reasoning to apply to multiply scattered neutrons. That is, for both multiple scattering and multiphonon scattering, a $\mathcal{P}$-phonon scattering profile involves a convolution of the single-phonon scattering profiles with the $(\mathcal{P}-1)$-phonon profile.

Additionally, the $\mathcal{P}$-phonon probability function for multiple scattering will have position and momentum dependencies. (These do not appear for multiphonon scattering processes.) Sears, *et al.*, [92] argue that the integrals for multiple scattering are related to those for the multiphonon scattering through slowly varying functions of Q and E. Here we take these functions to be constants, $\zeta_{\mathcal{P}}$. In essence, we make the approximation that the position and momentum dependencies can be

factored out. Thus:

$$I(Q,E) = N' \left[\sum_{\mathcal{P}=1}^{\infty} (1+\zeta_{\mathcal{P}}) S_{\mathcal{P}}(Q,E) \right] , \tag{8.10}$$

where $I(Q,E)$ is the experimentally-determined total scattering (including multiple scattering), $S_{\mathcal{P}}(Q,E)$ is the $\mathcal{P}$-phonon scattering (both creation and annihilation), and N' is a normalization constant.[d] (When we stripped the elastic peak from the data, the dominant multiple elastic scattering is removed, so the index $\mathcal{P}$ in Eq. 8.10 starts at 1 rather than 0.)

We now make the incoherent approximation: [83]

$$S_{\mathcal{P}}^{\mathrm{coh}}(Q,E) = \frac{\sigma^{\mathrm{coh}}}{\sigma^{\mathrm{inc}}} S_{\mathcal{P}}^{\mathrm{inc}}(Q,E) . \tag{8.11}$$

Note that this does not really apply to the 1-phonon scattering; nevertheless, it is common to apply this equation to the 1-phonon terms as well as all higher orders. The last step in our procedure will be to assess any error this has introduced into our analysis. This allows us to write:

$$I(Q,E) = N' \left(1 + \frac{\sigma^{\mathrm{coh}}}{\sigma^{\mathrm{inc}}} \right) \left[\sum_{\mathcal{P}=1}^{\infty} (1+\zeta_{\mathcal{P}}) S_{\mathcal{P}}^{\mathrm{inc}}(Q,E) \right] . \tag{8.12}$$

Our next assumption is that $\zeta_{\mathcal{P}} = \zeta'_{\mathrm{ms}}$ for all $\mathcal{P} \geq 2$, where ζ'_{ms} is a single constant that relates the multiple scattering to the multiphonon scattering. Thus:

$$I(Q,E) = N' \left(1 + \frac{\sigma^{\mathrm{coh}}}{\sigma^{\mathrm{inc}}} \right) \left[(1+\zeta_1) S_1^{\mathrm{inc}}(Q,E) + \sum_{\mathcal{P}=2}^{\infty} (1+\zeta'_{\mathrm{ms}}) S_{\mathcal{P}}^{\mathrm{inc}}(Q,E) \right] . \tag{8.13}$$

Since the multiphonon scattering drops off rapidly with increasing $\mathcal{P}$, this approximation will only have a small effect on our results. Collecting some terms into the normalization constant, we have:

$$I(Q,E) = N \left[S_1^{\mathrm{inc}}(Q,E) + (1+\zeta_{\mathrm{ms}}) S_{2+}^{\mathrm{inc}}(Q,E) \right] , \tag{8.14}$$

where $N = N' \left(1 + \sigma^{\mathrm{coh}}/\sigma^{\mathrm{inc}} \right) (1+\zeta_1)$ is the new normalization constant, and $1+\zeta_{\mathrm{ms}} \equiv (1+\zeta'_{\mathrm{ms}})/(1+\zeta_1)$. Also, for notational convenience, we have introduced:

$$S_{j+}(Q,E) \equiv \sum_{\mathcal{P}=j}^{\infty} S_{\mathcal{P}}(Q,E) . \tag{8.15}$$

The reason that the 1-phonon scattering has a different constant than the higher order scattering is that there are much stronger kinematic restrictions on the 1-phonon scattering than on the higher

[d] Again, we note that $I(Q,E)$ is distinct from the scattering function, $S(Q,E)$, which does not include multiple scattering.

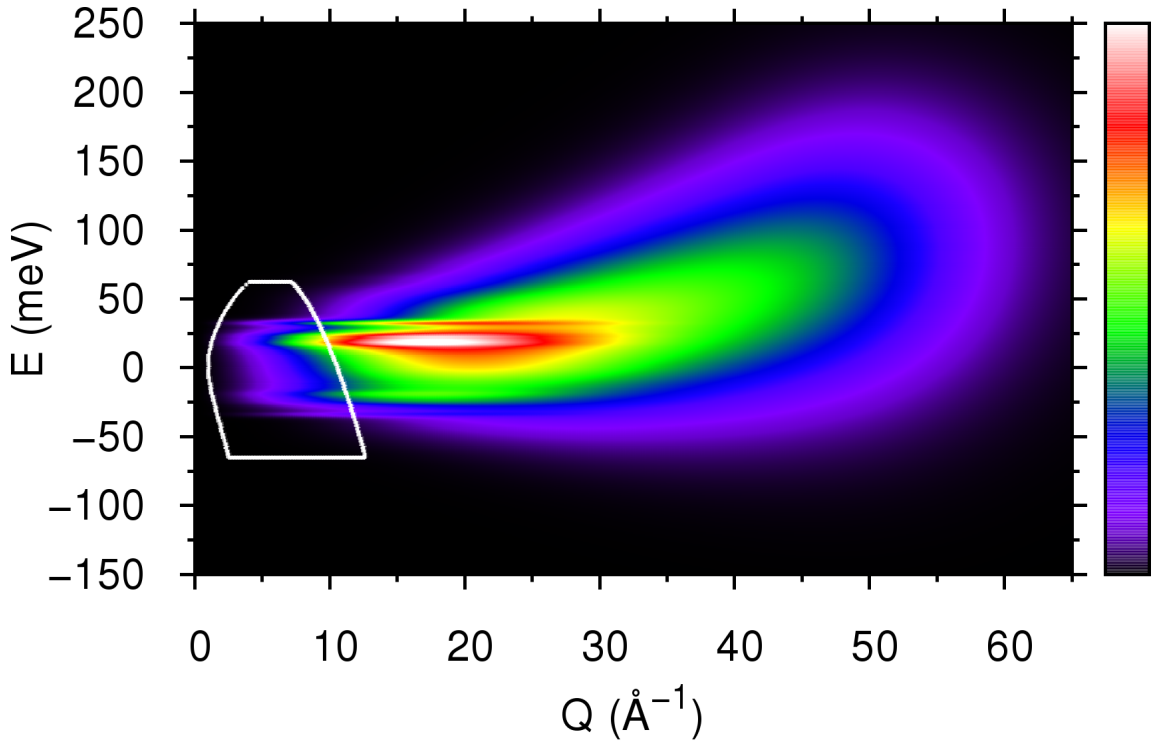

Figure 8.2: $S^{\text{inc}}(Q, E)$ for nickel at 300 K calculated from the phonon DOS. This includes multi-phonon processes of all orders, but not multiple scattering. The white polygon borders the region sampled if the incident energy is roughly 70 meV, and if there is no multiple scattering. The 1-phonon scattering — including a transverse and a longitudinal peak — can be seen on top of the multiphonon *background* at $-40 < E < 40$. It is quite dim for $Q < 10$, becomes bright red and white for $10 < Q < 30$, then fades out again at $Q > 30$. Clearly the ratio of 1-phonon to multi-phonon scattering decreases dramatically with increasing Q. If we allow for multiple scattering, a neutron might be involved in processes outside the white polygon such that sums over the energy and momentum transferred would allow us to detect it. This could change the ratio of 1-phonon to multiphonon scattering as seen in an experiment from that expected when considering only the region in the white polygon.

orders. That is, a neutron may not lose more energy than it has in a single scattering event; however, a neutron may gain energy in a first event, and then lose this energy *in addition to* its initial energy in a subsequent event. This is shown in Fig. 8.2, where the region outlined in white are the total energy and momentum transfers that we are capable of measuring. Processes from within the outlined region may scatter a neutron out of our detection range; but, another process may return that neutron to the outlined region, where we detect it.

For a cubic crystal, and a fixed value of ζ_{ms}, we can now find the DOS by solving Eq. 8.14 in the manner described by Sears, *et al.* [92] Since we do not know the value of ζ_{ms} a-priori, we generate a list of possible values, and solve for the DOS at each one. For nickel, as seen in Chapter 11, values of ζ_{ms} between 0.0 and 2.0 were tested. It then remains to select the *best* DOS from those generated with the different ζ_{ms}. This is done by minimizing a penalty function constructed to find the DOS

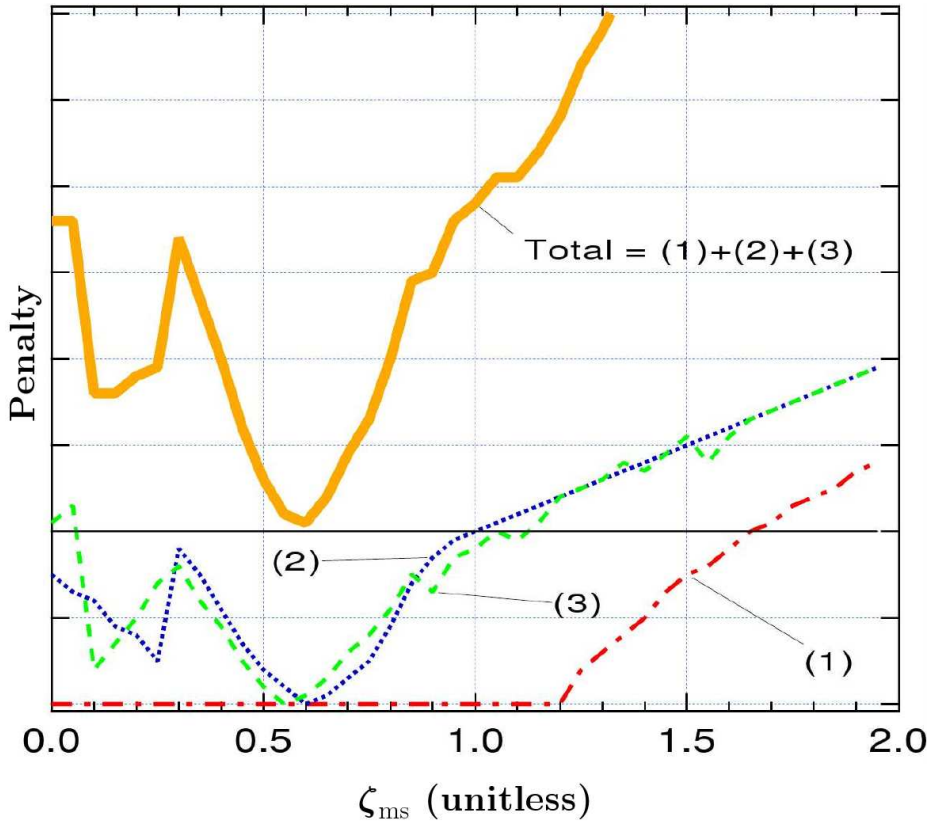

Figure 8.3: Penalty functions for nickel at 300 K, as defined in the text. The dash-dotted line (1) relates to the overall fit, the dotted line (2) relates to the noise near the incident energy, and the dashed line (3) relates to the slope near the incident energy. The solid line is the sum of these three contributions (offset).

that produces $S(E)$ that best satisfies the following conditions:

(1)

$$\frac{1}{N}\sum_{Q} I(Q,E) = \sum_{Q}\left[S_1^{\rm inc}(Q,E) + (1+\zeta_{\rm ms})S_{2+}^{\rm inc}(Q,E)\right] , \tag{8.16}$$

where the sum over Q is basically the application of the incoherent approximation to the data. (Details of the summation over Q are given in Appendix D.) With simplified notation:

$$\frac{I(E)}{N} \;=\; S_1^{\rm inc}(E) + (1+\zeta_{\rm ms})S_{2+}^{\rm inc}(E) \; . \tag{8.17}$$

(2) The experimental noise at energy transfers near the incident energy oscillates about the value $(1+\zeta_{\rm ms})S_{2+}^{\rm inc}(E)$.

(3) At energy transfers near the incident energy, the slope of a linear fit to the experimental noise

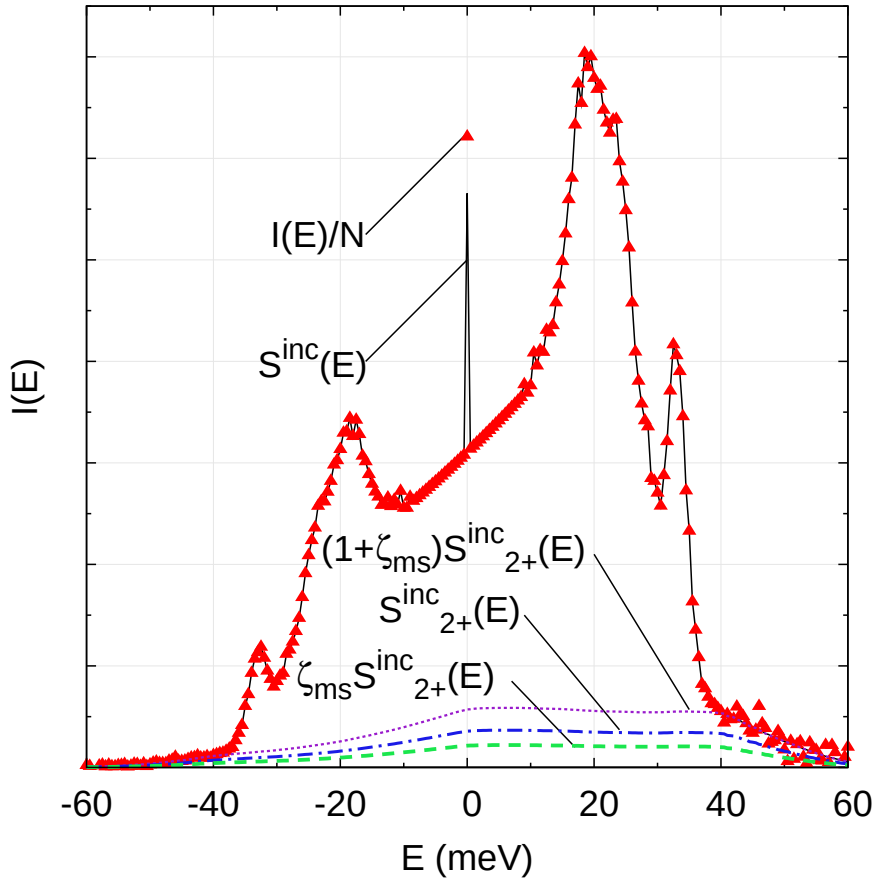

Figure 8.4: Best fit to scattering for nickel at 300 K. The triangles are the normalized experimental scattering, $I(E)/N$. The solid line shows the fit, $S_1^{\rm inc}(E) + (1+\zeta_{\rm ms})S_{2+}^{\rm inc}(E)$. The dashed line is the multiple scattering, $\zeta_{\rm ms}S_{2+}^{\rm inc}(E)$. The dash-dotted line is the multiphonon scattering, $S_{2+}^{\rm inc}(E)$. The dotted line is the sum, $(1+\zeta_{\rm ms})S_{2+}^{\rm inc}(E)$. The point at $E = 0$ is not used in the fitting procedure.

matches the slope of a linear fit to $(1+\zeta_{\rm ms})S_{2+}^{\rm inc}(E)$.

These three criteria are based on our experiences trying to fit data generated from known phonon spectra with known values of $\zeta_{\rm ms}$. These three criteria are correlated, but are not identical. In particular, (1) will be well satisfied whenever the DOS has no cutoff, even though this is undesirable. On the other hand, if there is no cutoff, the noise at energy transfers near the incident energy will not oscillate about the sum of the multiphonon and multiple scattering contributions — e.g. (2) will not be satisfied. This, in turn, does not imply that (3) is not satisfied. If the two linear fits are parallel, (3) is satisfied, regardless of (2). For nickel at 300 K, these three contributions and their sum are shown in Fig. 8.3.

Fig. 8.4 shows the best fit to the normalized scattering, $I(E)/N$ for nickel at 300 K, which had $\zeta_{\rm ms} = 0.6$. Finding a DOS from experimental scattering always involves some art; this procedure attempts to limit that art to the construction of a suitable penalty function. The phonon DOS

obtained this way were fit with a Born–von Kármán model, from which all phonon contributions to the scattering, both coherent and incoherent, were calculated. With these results, and with the final value for $\zeta_{\rm ms}$, the calculation was checked against the measured scattering, which showed that the effects of assuming all the scattering to be incoherent were negligible. The procedure has been applied successfully to cubic metals, including nickel and aluminum as studied in this work.

8.2 Shift and linewidth analysis of the DOS

As mentioned in § 3.6, the phonons in a metallic solid are expected undergo a shift to lower energies, and to broaden, with increasing temperature. The shift might be approximated as a constant multiplier, $\Delta^{\rm s}$, applied to all phonon energies E:

$$E \rightarrow \Delta^{\rm s} E \ . \tag{8.18}$$

Broadening of the phonons is expected to take the form of a damped harmonic oscillator function, $B = B(\mathcal{Q}, E', E)$ centered about energy E':

$$B(\mathcal{Q}, E', E) = \frac{1}{\pi \mathcal{Q} E'} \frac{1}{\left(\frac{E'}{E} - \frac{E}{E'}\right)^2 + \frac{1}{\mathcal{Q}^2}} \ . \tag{8.19}$$

Note that the quality factor, $\mathcal{Q}$, is related to the full width at half maximum, 2Γ of the phonon peaks as follows:

$$\frac{1}{\mathcal{Q}} \approx \frac{2\Gamma}{E} \ . \tag{8.20}$$

Using Eqs. 8.18 and 8.19, we see that the high temperature phonon DOS may be approximated as a function of the low temperature DOS, with only two free parameters, $\Delta^{\rm s}$ and $\mathcal{Q}$:

$$g_T(E) = B \odot g_0(\Delta^{\rm s} E') = \int B(\mathcal{Q}, E', E) g_0(\Delta^{\rm s} E') dE' \ , \tag{8.21}$$

where g_T is the phonon DOS at temperature T and g_0 is the zero temperature DOS. The integral transform of the DOS is very similar to a convolution and we denote it with $\odot$. What we measure in an experiment is $Z \odot B \odot g_0$, but assuming that there is no broadening at 0 K, Eq. 8.21 gives $B \odot (Z \odot g_0)$. Thus, the equation is valid for use with the experimentally determined phonon DOS in so far as we believe the following:

$$Z \odot B \approx B \odot Z \ . \tag{8.22}$$

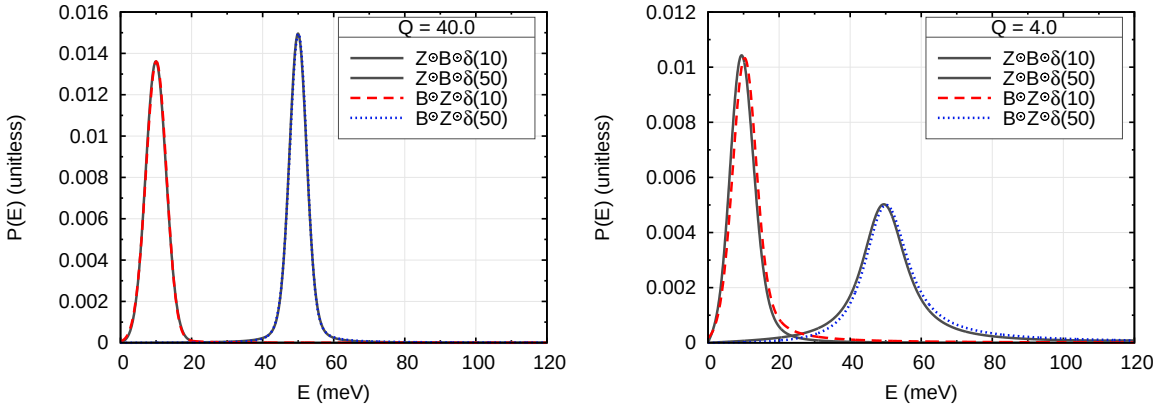

Figure 8.5: Solid gray lines show $Z \odot B$ for $g(E) = \delta(E = 10 \text{ meV}) = \delta(10)$ and $g(E) = \delta(E = 50 \text{ meV}) = \delta(50)$. $B \odot Z$ for $g(E) = \delta(10)$ and $g(E) = \delta(50)$ are shown by the dashed red and the dotted blue curves, respectively. The left-hand plot was produced with a relatively high quality factor, $\mathcal{Q} = 40.0$, such that most of the broadening is given by Z. In this case $B \odot Z$ and $Z \odot B$ are almost identical. In the right-hand plot, $\mathcal{Q} = 4.0$, which is representative of some of the lower quality phonon spectra presented here. Here, the differences between $B \odot Z$ and $Z \odot B$ are just beginning to be noticeable.

This is approximately true when $\mathcal{Q}$ is large. This can be seen in Fig. 8.5, which shows $B \odot Z$ and $Z \odot B$ for $\mathcal{Q} \in \{40, 4\}$.

At any temperature, the best $\mathcal{Q}$ and Δ^s for the experimental DOS may be determined through a least squares algorithm. At least within reasonable ranges for the parameters — $0.7 \leq \Delta^s \leq 1.1$ and $0.1 \leq \mathcal{Q} \leq 1000$ — the problem has only one minimum. A representative plot of the least squares error is given in Fig. 8.6. As a result, we may thus easily find the optimal shift and the quality factor.

The shifts Δ^s may be compared to the ratios of the mean phonon energies, $\langle E \rangle_T / \langle E \rangle_0$ as determined from the DOS:

$$\frac{\langle E \rangle_T}{\langle E \rangle_0} = \frac{\int E g_T dE}{\int E g_0 dE} \,. \tag{8.23}$$

Experimentally, we do not have access to 0 K, so we use in its place the lowest temperatures we can measure. For neutron measurements, this frequently works out to be about 10 K.

8.3 Born–von Kármán fits to the DOS

Once the phonon DOS has been determined, we may try and learn about the interatomic forces which give rise to it. A relatively simple way to do this is with a Born–von Kármán (BvK) model of

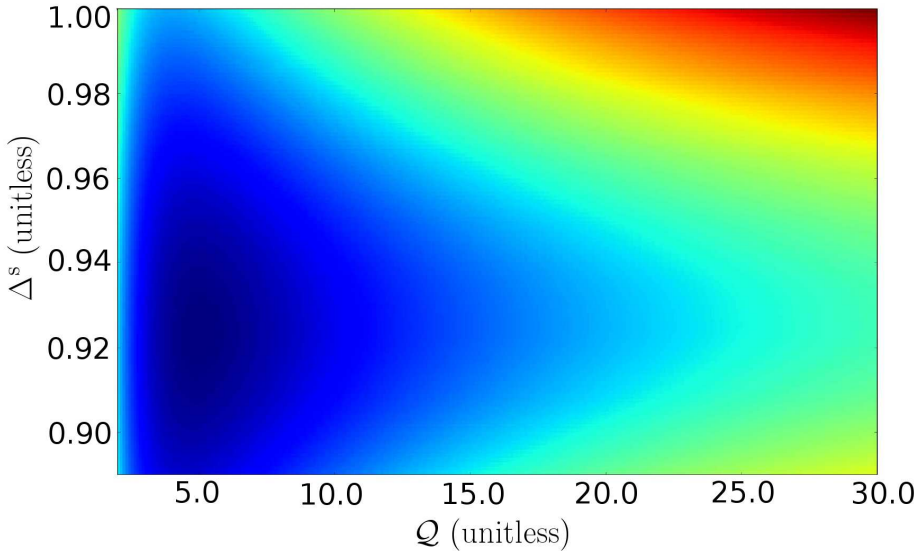

Figure 8.6: Close-up of least squares error as a function of $\mathcal{Q}$ and Δ^s for nickel using Eq. 8.21 with 300 K the lower and 1275 K the higher temperature. The lighter red corresponds to larger errors and the darker blue to smaller, the optimum values being roughly $\mathcal{Q} = 5.1$ and $\Delta^s = 0.92$. The same trends continue for (at least) $0.1 \leq \mathcal{Q} \leq 1000.0$ and $0.7 \leq \Delta^s \leq 1.1$, thus, we may easily take the path of steepest decent to the optima.

the lattice dynamics.[e] The theory underlying these models was described in § 3.4.2. Here we discuss methods for fitting these models to real data and simple ways of interpreting the results.

8.3.1 Fitting real data

Although the statistical noise of a neutron measurement of the DOS can make fitting difficult, neither this, nor any of the other problems quite generally associated with modeling of data, will be the subject here. Rather, we focus on the fact that on its own, a BvK model cannot reproduce instrument or anharmonic broadening of the phonon spectrum, and on means for getting around this shortcoming. Here, we present both derivative-free and gradient methods for fitting the DOS.

8.3.1.1 Derivative-free methods

If we are willing to forgo the use of derivatives, adjusting a BvK model to account for instrument and anharmonic broadening of the phonons is quite simple. The penalty function, Y, for optimization is constructed by direct comparison of the experimentally determined phonon DOS, g^{exp} and the *computed DOS*, which is found through an integral transformation of the DOS from BvK, g^{bvk}.

[e] These models are also useful for the so-called *neutron-weight correction*[23, 98, 101] that is required when interpreting the scattering from a polyatomic sample.

Specifically:

$$Y = \int_E \left[g^{\text{exp}}(E) - Z \odot B \odot g^{\text{bvk}}(E) \right]^2 dE \; . \tag{8.24}$$

In practice, the experimental and computed DOS are frequently manipulated as histograms, in which case the integral is replaced with a sum.

8.3.1.2 Gradient methods

If we wish to cut down on function evaluations and use a gradient in our optimization, we write the dynamical matrix as a sum of matrices $\mathbf{D}_k$ multiplied by independent force constants K_k, as was briefly discussed in the text around Eq. 3.69:

$$\mathbf{D}(\mathbf{q}) = \sum_k K_k \left[\mathbf{D}_k(\mathbf{q}) \right] \; . \tag{8.25}$$

The force constants, K_k, are actually the parameters to be varied, whereas the matrices $\mathbf{D}_k$ will remain unchanged.[f]

We may exploit this structure with a result from linear algebra. If the dynamical matrix has eigenvectors $[\boldsymbol{\epsilon}_b(\mathbf{q})]$ and eigenvalues $\Lambda_b(\mathbf{q}) = \omega_b^2(\mathbf{q})$, then the derivative of the eigenvalue with respect to a small change in the force constants is given by[102]:

$$\frac{\partial \Lambda_b}{\partial K_k} \quad = \quad \boldsymbol{\epsilon}_b^{\mathbf{T}} \mathbf{D}_k \boldsymbol{\epsilon}_b \; , \tag{8.26}$$

where we have dropped the $\mathbf{q}$ dependencies for clarity.

In theory, we could now take the derivative of the DOS with respect to a change in an eigenvalue, and the penalty with respect to a change in the DOS, apply the chain rule, and have the derivative of the penalty function with respect to a change in a force constant:

$$\frac{\partial Y}{\partial K_k} \quad = \quad \left(\frac{\partial Y}{\partial g^{\text{bvk}}(E)} \right) \left(\frac{\partial g^{\text{bvk}}(E)}{\partial \Lambda_b^{\text{bvk}}} \right) \left(\frac{\partial \Lambda_b^{\text{bvk}}}{\partial K_k} \right) \; , \tag{8.27}$$

where the first partial derivative on the right can be found by inspecting Eq. 8.24. The second partial derivative on the right can be found by differentiating Eq. 3.71, which gives the density of states as a sum over delta functions. In practice, however, the derivative of a delta-function is poorly defined; thus, using Eq. 8.27 successfully can be quite difficult.

An alternative is to think of the experimentally determined phonon DOS as a probability distribution, and to draw a uniform sample of squared frequencies that follow it. This still leaves us with

[f] The number of independent constants K_k and the shapes of the matrices $\mathbf{D}_k$ are largely determined by the point-group symmetries of the lattice. A method for numerically determining these constraints on the force constants is outlined in Appendix E.

the problem of modeling instrument and anharmonic broadening of the spectrum, and two methods of handling this follow.

The first method is to *undo* the broadening of the experimentally determined phonon DOS. That is, we assume knowledge of Z and B (or, at least, of $Z \odot B$), and we then find $(Z \odot B)^{-1}$, so that:

$$g'^{\exp}(E) = (Z \odot B)^{-1} g^{\exp}(E) \; . \tag{8.28}$$

The problem with this sort of technique is that $B \odot Z$ is usually very poorly conditioned, *i.e.*, for fixed $Z \odot B$, there exist many choices of $g'^{\exp}(E)$ that satisfy Eq. 8.28 equally well. In so much as the integral transformation represented by $\odot$ is like a convolution, this is no surprise. One way around this difficulty is with regularization techniques such as Tikhonov regularization.[103]

Assuming that our *deconvolution* is successful,[g] we may then draw a uniform sample of *experimentally determined eigenvalues*, $\Lambda^{\exp}$ from the distribution $(Z \odot B)^{-1} g^{\exp}(E)$, and construct the following penalty function:

$$Y = \sum_{\mathbf{q},b} \left[\Lambda_b^{\exp}(\mathbf{q}) - \Lambda_b^{\text{bvk}}(\mathbf{q}) \right]^2 \; . \tag{8.29}$$

Then the change in the penalty with a change in a force constant is given by:

$$\begin{aligned} \frac{\partial Y}{\partial K_k} &= \left(\frac{\partial Y}{\partial \Lambda_b^{\text{bvk}}} \right) \left(\frac{\partial \Lambda_b^{\text{bvk}}}{\partial K_k} \right) \\ &= 2 \sum_{\mathbf{q},b} \left[\Lambda_b^{\text{bvk}}(\mathbf{q}) - \Lambda_b^{\exp}(\mathbf{q}) \right] \boldsymbol{\epsilon}_b^{\mathbf{T}} \mathbf{D}_k \boldsymbol{\epsilon}_b \; . \end{aligned} \tag{8.30}$$

Note that in an experiment we may not actually know to which branch b and momentum transfer $\mathbf{q}$ a particular eigenvalue $\Lambda^{\exp}$ belongs. We circumvent this difficulty by sorting both the experimental and simulated eigenvalues before comparison. Let there be an index i such that $\Lambda_i < \Lambda_{i+1}$, and such that each i corresponds to one and only one pair $(\mathbf{q} \; , \; b)$, then we may write:

$$\frac{\partial Y}{\partial K_k} = 2 \sum_i \left[\Lambda_i^{\text{bvk}} - \Lambda_i^{\exp} \right] \boldsymbol{\epsilon}_i^{\mathbf{T}} \mathbf{D}_k \boldsymbol{\epsilon}_i \; . \tag{8.31}$$

In the second method, we *apply* the broadening $Z \odot B$ to the eigenvalues determined with the BvK model. The advantage of this method is that it allows use of a gradient, but requires no matrix inversion. Because the method is somewhat involved, we give the steps in bullet form and motivate them below. We:

- find the eigenvalue $\Lambda_b^{\text{bvk}}(\mathbf{q})$ from simulation
- assume that the square root of the eigenvalue $\omega_b^{\text{bvk}}(\mathbf{q}) = \sqrt{\Lambda_b^{\text{bvk}}(\mathbf{q})}$ represents the argument

[g] Actually, an inverse integral transform.

to a delta-function, $\delta\left[\omega_b^{\rm bvk}(\mathbf{q})\right]$

- apply the instrument and anharmonic broadening to the delta function to generate a distribution $Z \odot B \odot \delta\left[\omega_b^{\rm bvk}(\mathbf{q})\right]$
- draw from the distribution a sample with elements $\omega_{bj}^{\rm bvk}(\mathbf{q})$ (Note the new index, j)
- square the elements of the sample to get $\Lambda_{bj}^{\rm bvk}(\mathbf{q}) = \left[\omega_{bj}^{\rm bvk}(\mathbf{q})\right]^2$

The complexity of the method stems almost entirely from the need to apply $Z \odot B$ to the simulated results. Firstly, we must apply the broadening $Z \odot B$ to a specific value rather than to a distribution. As mentioned before, this is necessary because we taking a derivative of the DOS with respect to a change in an eigenvalue is non-trivial. Secondly, the broadening $Z \odot B$ is known for a frequency ω, not for an eigenvalue ω^2. As a result, we have to take a square root before applying the broadening. Squaring things afterward simplifies finding the change in the penalty with respect to a change in a force constant.

We may now construct a penalty function by comparing $\Lambda_{bj}^{\rm bvk}(\mathbf{q})$ with a sample drawn from the experimentally determined phonon DOS, $\Lambda_{bj}^{\rm exp}(\mathbf{q})$:

$$Y = \sum_{\mathbf{q},b,j} \left[\Lambda_{bj}^{\rm exp}(\mathbf{q}) - \Lambda_{bj}^{\rm bvk}(\mathbf{q})\right]^2 \ . \tag{8.32}$$

The change in the penalty with respect to a change in a force constant is given by:

$$\frac{\partial Y}{\partial K_k} \ = \ \left(\frac{\partial Y}{\partial \Lambda_{bj}^{\rm bvk}}\right)\left(\frac{\partial \Lambda_{bj}^{\rm bvk}}{\partial \Lambda_b^{\rm bvk}}\right)\left(\frac{\partial \Lambda_b^{\rm bvk}}{\partial K_k}\right) \ . \tag{8.33}$$

As in the previous method, we assume an index i such that $\Lambda_i < \Lambda_{i+1}$, and such that each i corresponds to one and only one pair ($\mathbf{q}$, b). We also assume an index l such that $\Lambda_l < \Lambda_{l+1}$, and such that each i corresponds to one and only one triplet ($\mathbf{q}$, b , j). We may then write:

$$\begin{aligned} \frac{\partial Y}{\partial K_k} \ &= \ \left(\frac{\partial Y}{\partial \Lambda_l^{\rm bvk}}\right)\left(\frac{\partial \Lambda_l^{\rm bvk}}{\partial \Lambda_i^{\rm bvk}}\right)\left(\frac{\partial \Lambda_i^{\rm bvk}}{\partial K_k}\right) \\ &= \ 2\sum_{l,i}\left[\Lambda_l^{\rm bvk} - \Lambda_l^{\rm exp}\right]\left(\frac{\partial \Lambda_l^{\rm bvk}}{\partial \Lambda_i^{\rm bvk}}\right)\boldsymbol{\epsilon}_i^{\mathbf{T}}\mathbf{D}_k\boldsymbol{\epsilon}_i \ . \end{aligned} \tag{8.34}$$

It remains to determine the derivative of one of the resample eigenvalues Λ_l with respect to a change in one of the Λ_i. One way to do this is to evaluate it numerically. In order to be able to compare the simulation to the experiment, the Λ_i must be quite densely packed; therefore:

$$\frac{\partial \Lambda_l^{\rm bvk}}{\partial \Lambda_i^{\rm bvk}} \ \approx \ \frac{\Lambda_{l+1}^{\rm bvk} - \Lambda_l^{\rm bvk}}{\Lambda_{i+1}^{\rm bvk} - \Lambda_i^{\rm bvk}} \ . \tag{8.35}$$

8.3.1.3 Comparison of methods

The fitting methods presented fall into two major classes, those that used analytical derivatives and those that do not. The advantages of the former are directness and the fact that only one function evaluation is required per optimization step. The disadvantage is that analytical derivatives can be complicated, costly or even impossible determine. In the past, only the derivative-free methods have been used for optimizing BvK models to a phonon DOS.

More specifically, for a BvK model, a gradient based technique requires determination of the eigenvectors as well as the eigenvalues. In practice, the extra time spent determining the eigenvectors is made up by the decreased number of function evaluations per optimization step. Additionally, if we are trying to do an optimization of $S(Q, E)$ rather than the DOS, or if we have a polyatomic system, we have to calculate the eigenvectors anyways.

Regardless of the choice of methods, the problem of fitting force constants to a DOS is not convex.[65] Any procedure, then, only guarantees a local optimum. It is currently too computationally intensive to search the entire force constant parameter space, which may include well over ten parameters. That said, simulated annealing, genetic algorithms, and other global optimization chicanery will probably yield better results than simply running any of these local optimizations on its own.

The last point we make is about the broadening of the spectrum, which we have done by transforming the DOS, and also by transforming each phonon frequency separately. Fig. 8.7 shows that the two methods yield similar, but by no means identical results. At least part of the difference is related to the operation of binning the eigenvalues into a density of states. Although transforming the DOS is somewhat more intuitive than broadening each phonon frequency individually, the latter is probably more reflective of the underlying physics. For example, in the case of a neutron experiment, a single neutron will be scattered by a particular phonon with some linewidth.

8.3.2 Longitudinal and transverse force constants

Each force constant tensor connects two atoms with a *bond*, and we will frequently want to look at the force projected onto the bond direction. Unlike the generalized tensorial force constants, the *longitudinal* force has a clear physical interpretation — it tells us about how strongly the two bonded atoms attract each other. Moreover, from model to model there is often great variation in the generalized constants; however, if the models are at all realistic, the longitudinal force constants are very likely to be similar. (See Table 9.3, in § 9.5, for example.) The transverse force constants are less robust to changes in model, but are also sometimes of interest.

Given an interatomic force constant tensor, $\mathbf{K}$, and the bond with equilibrium separation, $\mathbf{x}$, to

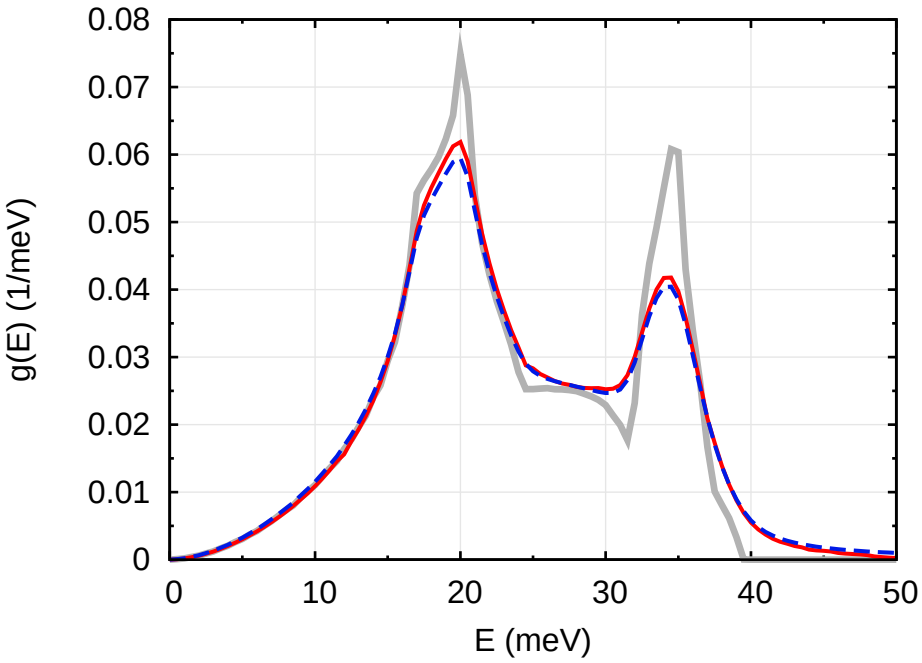

Figure 8.7: The solid, light gray line in the background shows a phonon DOS, g, from a BvK model of aluminum with no anharmonic broadening. The blue dashed line is $Z \odot B \odot g$. The solid red line is also from the same BvK model but with the eigenvalues have been broadened as in the second method presented in § 8.3.1.2. In order to focus on the anharmonic broadening, the calculations were performed assuming an instrument with perfect resolution, *i.e.*, $Z = \mathbf{1}$. The differences in the 2 methods of broadening the DOS are clearly visible in the taller peaks; but will have only a small impact on thermodynamic calculations that depend on the phonon spectrum. Also, at least some of the disparity between the spectra has to do with the binning of the phonon frequencies that was done to determine their density.

which it belongs, we may find the longitudinal force constant as follows:

$$\mathcal{K} = \frac{\mathbf{x}^{\mathrm{T}}\mathbf{K}\mathbf{x}}{\mathbf{x}^{\mathrm{T}}\mathbf{x}} \,. \tag{8.36}$$

Since there is an entire 2D subspace that is orthogonal to the bond direction, finding a transverse force constant is more complicated. Often, we may skirt this difficulty by comparing $\mathcal{K}$ to the eigenvalues of $\mathbf{K}$. If the forces are axial, then one of the eigenvectors will be in the longitudinal direction and its eigenvalue will match $\mathcal{K}$. We then take the remaining $\mathcal{D}-1$ (two, in 3D) eigenvalues to be transverse, and average them to obtain a single transverse force constant.

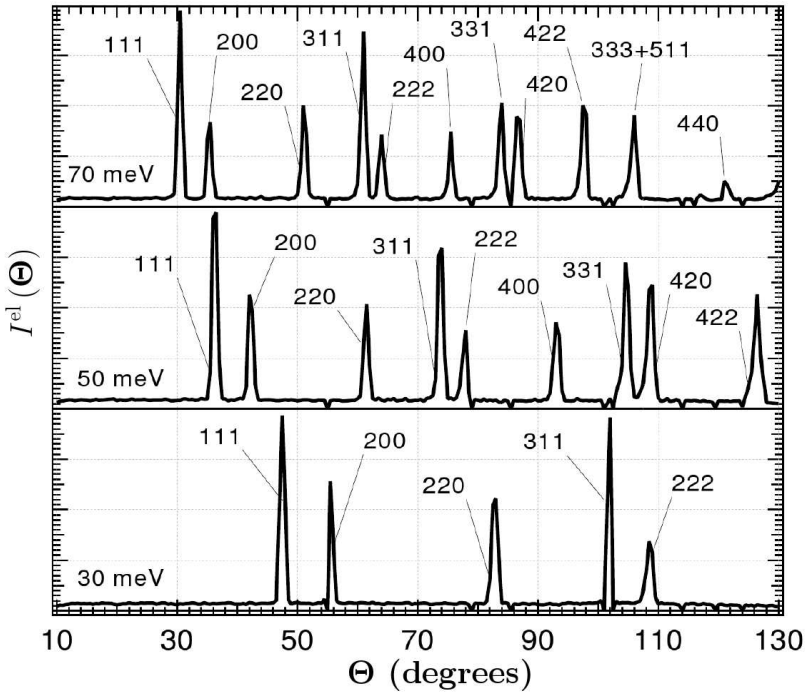

Figure 8.8: Indexed diffraction patterns from polycrystalline nickel at room temperature with incident neutron energies of 30, 50, and 70 meV. The corrected intensity, $I(\Theta, E)$, was summed over energies from -2.5 to 2.5 meV. Each peak can be fit and, the vertex of the fit used in Bragg's Law to determine a lattice parameter. The resulting parameters for the 70 meV pattern were used in a Nelson-Riley plot shown in Fig. 8.9. As an aside, the fact that the ratios of the peak heights are similar for the different incident energies indicates that the nickel sample was not textured crystallographically.

8.4 Finding the lattice parameter

Along with the inelastic scattering which yields the phonon spectrum, a measurement of a polycrystalline sample on an time-of-flight chopper spectrometer also yields Bragg scattering.[h] This can be seen in Fig. 7.11, where the bumps in the red line at $E = 0$ are actually Bragg peaks. The quality of the diffraction patterns is much less than those from dedicated neutron or x-ray diffractometers. Nevertheless, it is still possible to obtain reasonable estimates of quantities such as lattice parameters, given a known structure. A relatively simple method for finding the lattice parameter follows.

First, we wish to separate the elastic and the inelastic scattering. To do so, we simply sum over a range of energies that we consider to be in the elastic region, for example, from -2.5 to 2.5 meV:

$$I^{\mathrm{el}}(\Theta) = \sum_{E=-2.5}^{+2.5} I(\Theta, E) \; . \tag{8.37}$$

[h]This requires that the sample is a coherent scatterer of neutrons.

$I^{\mathrm{el}}(\Theta)$, then, is our diffraction pattern, like the ones shown in Fig.8.8.

Once we have the diffraction pattern, we may fit the peaks with parabolae, or some other function, and use the Θ-coordinate at the vertex in Bragg's law:

$$a(\Theta) = \frac{\lambda\sqrt{(h^2+k^2+l^2)}}{\sin(\Theta/2)} \,, \tag{8.38}$$

where λ_{I} is the wavelength of the incident (and outgoing, since it is elastic scattering) neutrons, and h, k, l are the Miller indices [50, 52, 104] for the peak.

Unfortunately, the different peaks are very likely to yield different lattice parameters. Thusfar, the largest errors in the estimation of the lattice parameter have come from displacements of the sample from its assumed position.[i] To some extent, we may correct for this by noting that for scattering of $\Theta = 180°$, the displacements of the sample have no effect on the peak position. In fact, the relative error in the lattice parameter should go linearly to zero as follows:[104]

$$\frac{\Delta a}{a} \propto \frac{\cos^2(\Theta/2)}{\sin(\Theta/2)} \,. \tag{8.39}$$

Nelson and Riley,[104, 105] suggested a slightly modified relationship:

$$\frac{\Delta a}{a} \propto \frac{\cos^2(\Theta/2)}{\sin(\Theta/2)} + 2\frac{\cos^2(\Theta/2)}{\Theta} \,, \tag{8.40}$$

which is the form used in Fig. 8.9 in order to find lattice parameters for nickel at 10, 300, 575, 875, and 1275 K.

A more robust method of diffraction analysis would be to create a parametrized model of the sample and its environment that includes sample positioning, lattice parameters, crystallite orientation and strain distributions, etc. and to then perform an optimization of the model to the data. This sort of procedure, when applied to diffraction patterns, is commonly called *Rietveld refinement*.[106] It is the technique of choice for diffraction data taken on dedicated neutron or x-ray diffractometers; however, it is rarely (if ever) applied to diffraction data from chopper spectrometers.

[i] The *displacements* may also be due simply to the non-zero thickness of the sample.

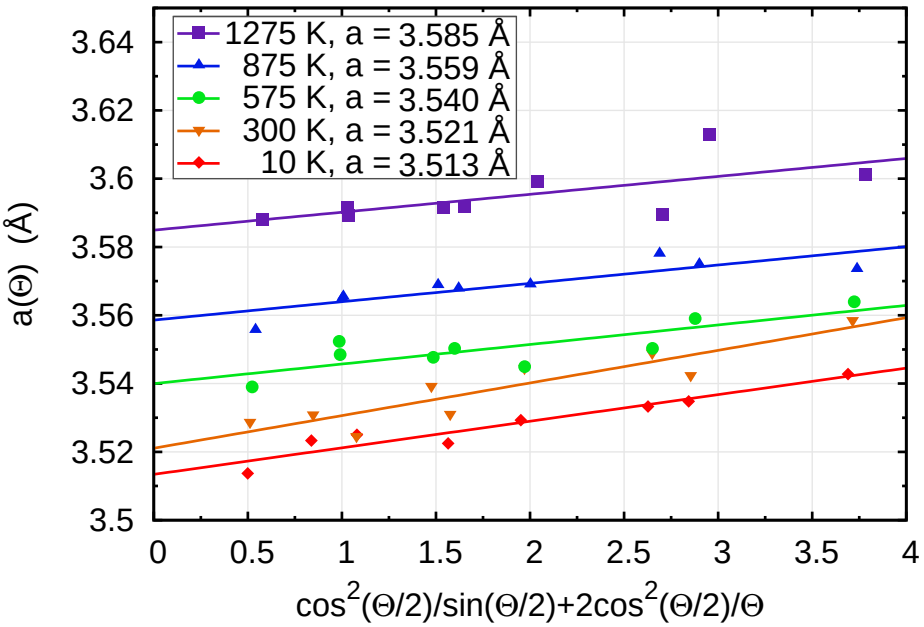

Figure 8.9: Nelson Riley plot for nickel from data measured at 10, 300, 575, 875 and 1275 K on Pharos. The corrected data, $I(\Theta, E)$, were summed over energies from -2.5 to 2.5 meV to get the diffraction patterns. (Shown in Fig. 11.1) The peaks were fit to parabolas, and the Θ coordinates of the vertices were used as Θ for the markers. The nominal lattice parameter for each vertex was determined using Bragg's law. The lines are linear fits to the markers at a given temperature. Error due to displacement of the sample goes to zero at $\Theta = 180°$, thus, the $a(\Theta)$-intercept represents the best estimate of the lattice parameter. The 10 K was taken in a displex refrigerator, at 300 K on a sample stick, and for the remaining temperatures in a furnace. For the three furnace measurements, the sample was not moved, and the similar slopes of the lines reflect this fact.

Part III

Phonons in FCC Metals at Elevated Temperatures

Inelastic neutron scattering measurements of polycrystalline aluminum, lead, and nickel are presented here, with specific attention paid to high temperature effects on phonons. The three sections on analysis and computation are quite similar, with the following exceptions: § 10.3.3 describes problems only relevant to the measurement of lead and §,11.3.6 describes spin polarized electronic sctructure calculations relevant only to nickel.

Chapter 9

Aluminum

9.1 Introduction

On account of its abundance and the favorable thermal and mechanical properties of its alloys, aluminum is one of the most widely used metals for industrial and engineering applications. Its melting temperature of 933 K is relatively low, and the thermodynamic stability of aluminum at elevated temperatures is of technological and scientific importance. Because of its simple electronic structure, aluminum metal is frequently used as a test case for theoretical models of crystals and their thermodynamics. [15, 43, 44, 66, 107–112]

Aluminum is non-magnetic, so the majority of its entropy comes from phonons. In turn, the majority of its phonon entropy, S_{ph}, can be attributed to harmonic oscillations of the nuclei about their equilibrium positions. The 'quasiharmonic' phonon entropy $S_{\mathrm{ph,Q}}$ includes both the harmonic phonon entropy, and the entropy due to a decrease in phonon frequencies (softening) as the crystal expands. Measurements of phonon dispersions in body centered cubic metals [16, 39, 54, 55, 113, 114] have shown that the quasiharmonic model is often insufficient to explain the temperature dependence of the phonon entropy. For example, $S_{\mathrm{ph,Q}}$ is an overestimate of the phonon entropy in both niobium [36] and vanadium [54], but a severe underestimate for chromium. [36] There is less experimental data on the high temperature trends in phonons and phonon entropy in face-centered cubic metals, although recent work has shown that the phonons in nickel are slightly stiffer than predicted by the expansion of the lattice against the bulk modulus. [35]

Aluminum has one natural isotope, ^{27}Al, and scatters thermal neutrons coherently. There have been a number of measurements of its phonon dispersions using neutron triple-axis spectrometers [56, 115–118], and other work using x-ray diffuse scattering. [119, 120] The phonon dispersions at 80 and 300 K measured with inelastic neutron scattering by Stedman *et al.* [118] have been used frequently, sometimes to generate phonon DOS. [43, 44, 65, 121, 122]

Previous measurements of phonons in aluminum at temperatures above 300 K were limited to small numbers of momentum transfers. Because aluminum is a coherent scatterer, such measure-

ments sampled only small numbers of phonon states, and are not optimal for determining the phonon density-of-states that is so important for thermodynamics. Nevertheless, Larsson *et al.* [56] found that some phonon frequencies shifted by approximately 15% between temperatures of 298 K and 932 K. They found phonon linewidths to increase at temperatures above 600 K. Peterson *et al.* [120] also suggested that the longitudinal modes are anharmonic.

Energy shifts and lifetime broadening of phonons in aluminum and other FCC metals have been studied theoretically. [62–64, 123–125] Björkman *et al.*, using a pseudopotential model, [124] show how electron-phonon interactions shorten phonon lifetimes in aluminum. Using Born–von Kármán fits to neutron data in conjunction with measurements of second and third order elastic constants, Zoli *et al.* calculated the shifts [62] and lifetime broadening [64] of the phonons in aluminum at temperatures below room temperature. More generally, understanding the contributions of quasiparticles and collective excitations to the free energy, entropy, and heat capacity of crystalline solids is an active area of research. [25, 26, 31–33, 36–38, 126–128]

Here we present results from inelastic neutron scattering measurements of the phonon DOS of aluminum at temperatures of 10, 150, 300, 525, and 775 K. We use these results to determine the phonon contributions to the entropy of aluminum, and we assess the other entropic contributions, finally obtaining excellent agreement with the total thermodynamic entropy. The overall softening of the phonons is found to be caused by a monotonic temperature dependence of the 1NN, 2NN, and 3NN force constants, with the 1NN force constants decreasing approximately 10% over the temperature range of measurement. The purely anharmonic part of the phonon entropy, not accounted for by the expansion of the lattice, is approximately $-0.07\ k_{\mathrm{B}}$/atom at 775 K. Additionally, we quantify the temperature dependence of the energy widths and shifts of the phonons, and we attribute the anharmonic effects to phonon-phonon interactions.

9.2 Experiment

9.2.1 Sample preparation

Clean aluminum shot of 99.99% purity was arranged to cover maximally the interior of a thin walled, rectangular, aluminum pan, whose height, width and depth were approximately 10.0, 7.0 and 0.5 cm. The ratio of singly- to multiply-scattered neutrons was designed to be approximately 10:1.

9.2.2 Neutron scattering measurements

The first set of inelastic neutron scattering measurements was performed on LRMECS. The aluminum pan was mounted at 45° to the incident neutron beam, and measurements were made at 10, 150, 300, 525, and 775 K. Measurements were also made on the empty aluminum pan at all

temperatures, to allow for some removal of background scattering. For the lower temperatures, 10, 150, and 300 K, the sample was mounted in a displex refrigerator. For the higher temperatures, the sample was mounted in a low background, electrical resistance furnace designed for vacuum applications. In both cases, temperature was monitored with several thermocouples, and is believed accurate to within 5 K over the bulk of the sample.

In order to achieve a nominal energy of 60 meV for the incident neutrons, the T0 chopper was set to 90 Hz, and the E0 chopper to 150 Hz. The counts from neutrons taking between 2400 and 6000 μs to reach the sample from the moderator were stored in bins of width 4 μs. Incident neutron energies for the different temperatures determined from scattering in the monitors ranged from 59.0 to 59.2 meV (details in § 7.2.1). The experimentally determined full width at half maximum resolution in angle was approximately 1°. All measurements were roughly 8 hours in duration, and included approximately 750,000 counts.

A second set of measurements was made on Pharos. Another displex refrigerator was used for a measurement at 10 K, and the same furnace was used for a measurement at 775 K. The same aluminum sample was used, again mounted at an angle of 45° to the incident neutron beam. The data acquisition system was set to fill time bins spaced every 2.5μs from 5500 to 9000 μs. Data were collected for a minimum of four hours at each temperature, giving on the order of one million counts. The T0 and E0 choppers were set to 40 Hz and 300 Hz respectively, for a nominal incident energy of 70 meV. There are no monitors on Pharos, but the incident energies calculated from the data ranged from 69.3 to 69.4 meV (details in § 7.2.2).

For both instruments, the energy resolution function, $Z(E, E')$, was assumed to be Gaussian in energy:

$$Z(E, E') = \frac{1}{\sigma_i(E')\sqrt{2\pi}} \exp\left\{ -\frac{1}{2}\left[\frac{E - E'}{\sigma_i(E')} \right]^2 \right\} . \tag{9.1}$$

The standard deviations, σ_i, were assumed to decrease linearly from the elastic line to the incident energy, and our expressions for two instruments are given here:

$$\begin{aligned} \sigma_{\mathrm{LRMECS}}(E') &\approx -0.0071E' + 1.2744,\ E_{\mathrm{I}} = 60.0 \text{ meV} , \\ \sigma_{\mathrm{Pharos}}(E') &\approx -0.0091E' + 1.0620,\ E_{\mathrm{I}} = 70.0 \text{ meV} , \end{aligned} \tag{9.2}$$

where E' and the $\sigma_i(E')$ are in meV.

Table 9.1: Experimentally determined lattice parameter, a, of aluminum and shifts of the aluminum phonon energies as a function of temperature. Fits of the 10 K DOS to the high temperature DOS by scaling of the energy and integral transformation with the damped oscillator function yield the relative frequency shifts Δ^{s} (Eq. 9.6). $\langle E\rangle_T/\langle E\rangle_{10}$ are ratios of the first moments of the DOS (Eq. 9.8). Values in square brackets are from Pharos data.

T (K)	$a \pm 0.01$ (Å)	Δ^{s}	$\langle E\rangle_T/\langle E\rangle_{10}$	$S_{\mathrm{ph}} \pm 0.03$	(k_{B}/atom)
10	4.041	1.000	1.000	0.001	[0.001]
150	4.045	0.995	0.990	1.628	-
300	4.056	0.977	0.964	3.462	-
525	4.079	0.954	0.941	5.146	-
775	4.111	0.952	0.941	6.332	[6.306]

9.3 Analysis and computation

Details of the data reduction procedures used here are given in Chapter 7, with rebinning described in § 7.4.1. The correction for multiple- and multiphonon scattering was described in § 8.1.2. For diffraction, determination of the quality factors, and fitting of BvK models, see § 8.4, § 8.2, and § 8.3.1.2, respectively.

9.3.1 General data reduction

The raw data from both instruments, in time-of-flight and scattering angle Θ were first normalized using the counts in the beam monitor for LRMECS, and the integrated proton current for Pharos. Bad detectors were identified and masked, and the data were corrected for detector efficiency using a measurement of vanadium, an incoherent scatterer. At each temperature, the measured scattering from the empty aluminum pan was subtracted from the data, reduced by 10% to account for the self-shielding of the sample. The data were then binned to get intensity, $I(\Theta, E)$, as a function of scattering angle, Θ, and energy, E, transferred to the sample. Approximately, Θ ranged from 10° to 120° with a bin width of 0.75°, and E ranged from −60.0 to 60.0 meV with a bin width of 0.5 meV for both instruments.

9.3.2 Elastic scattering: *in-situ* neutron diffraction

By summing the LRMECS data from −5.0 to 5.0 meV, in-situ neutron diffraction patterns were obtained. Lattice parameters were determined from these data using Nelson–Riley [104, 105] plots, and are listed in Table 9.1. Their thermal trends are consistent with thermal expansion data.

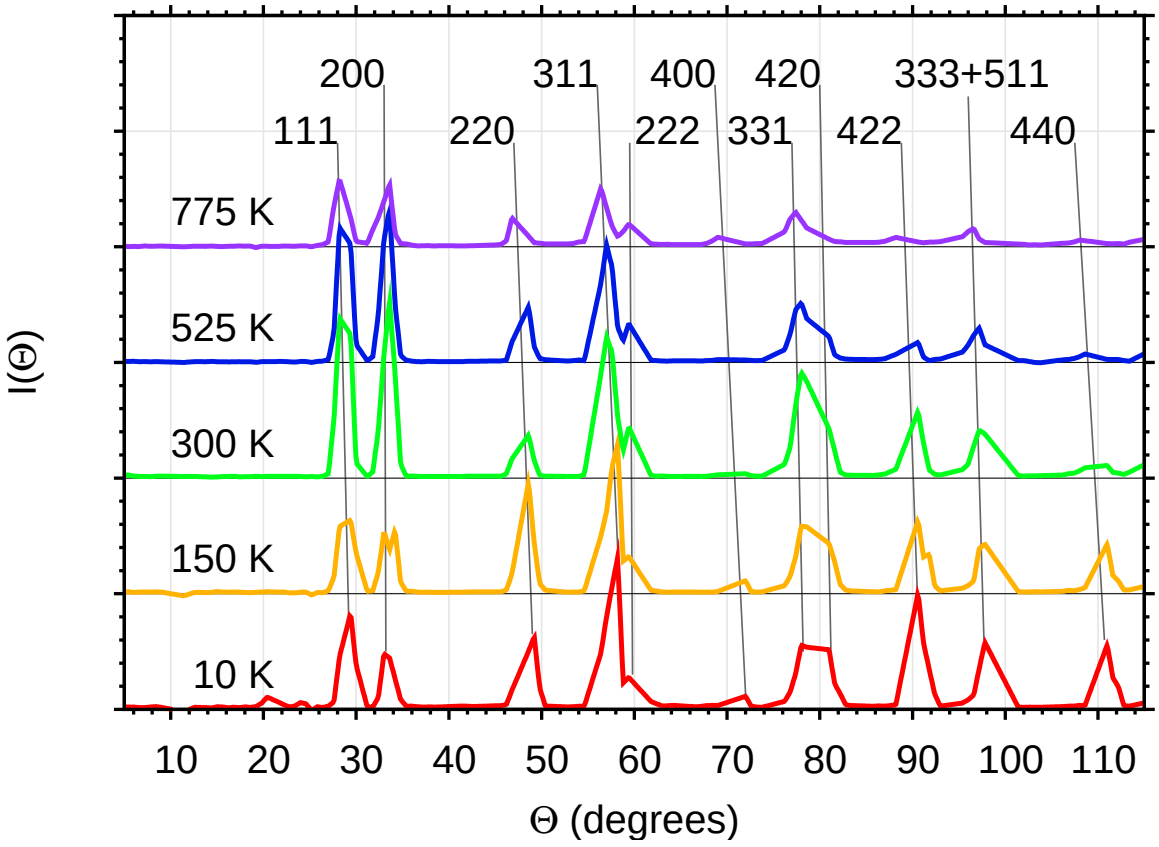

Figure 9.1: Diffraction patterns from aluminum at temperatures as indicated. Despite their appearance, these were used to determine the lattice parameters shown in Table 9.1.

9.3.3 Inelastic scattering: S(Q,E) and the phonon DOS

Data reduced to $I(\Theta, E)$ were then rebinned into intensity, $I(Q, E)$, where Q is the momentum transferred to the sample. For both instruments, Q ranged from 0.0 to 12 Å^{-1}, with a binwidth of about 0.075 Å^{-1}. The elastic peak was removed below 8 meV and replaced by a function of the following form:

$$I(E) \approx \frac{\zeta_0 E}{1 - \exp(-\beta E)} , \tag{9.3}$$

where the constant ζ_0 was determined from the inelastic scattering just past the elastic peak. Here, we have assumed that the phonon DOS is proportional to E^2 in the low energy regime, as in a Debye model. The phonon DOS were then extracted from the scattering, making the thermal corrections and corrections for multiphonon and multiple scattering, as described in § 8.1.2. These phonon DOS are shown by markers and lines in Fig. 9.2, and by the markers in Figs. 9.3.

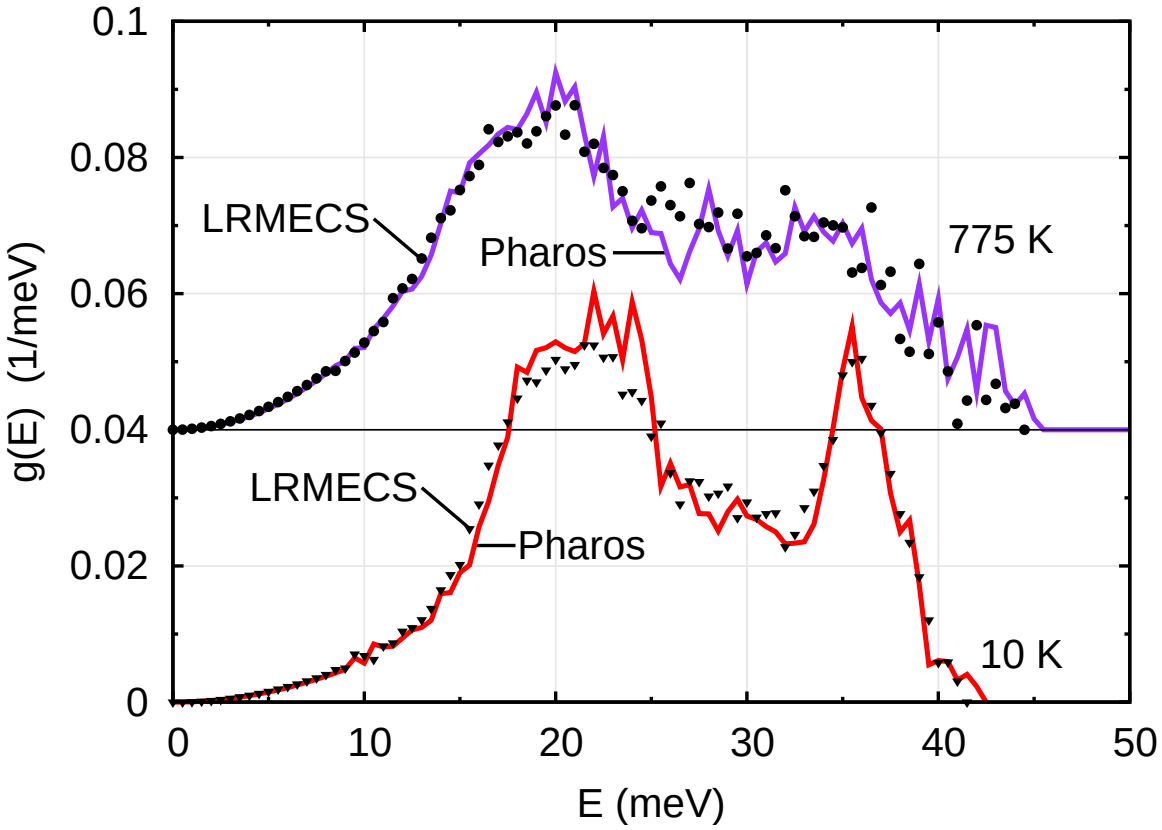

Figure 9.2: Phonon DOS of aluminum at temperatures as indicated. The markers show the experimentally determined DOS from LRMECS, and the lines show the DOS from Pharos.

9.3.4 Phonon shifts and broadening

With increasing temperature, the phonon peaks in a metallic solid typically broaden and undergo a shift to lower energies. These shifts were approximated as a constant multiplier, Δ^{s}, applied to all phonon energies E:

$$E \rightarrow \Delta^{\mathrm{s}} E \,. \tag{9.4}$$

The broadening of the phonons was assumed to take the form of a damped harmonic oscillator function, $B(\mathcal{Q}, E', E)$ centered about energy E': [84]

$$B(\mathcal{Q}, E', E) = \frac{1}{\pi \mathcal{Q} E'} \frac{1}{\left(\frac{E'}{E} - \frac{E}{E'}\right)^2 + \frac{1}{\mathcal{Q}^2}} \,. \tag{9.5}$$

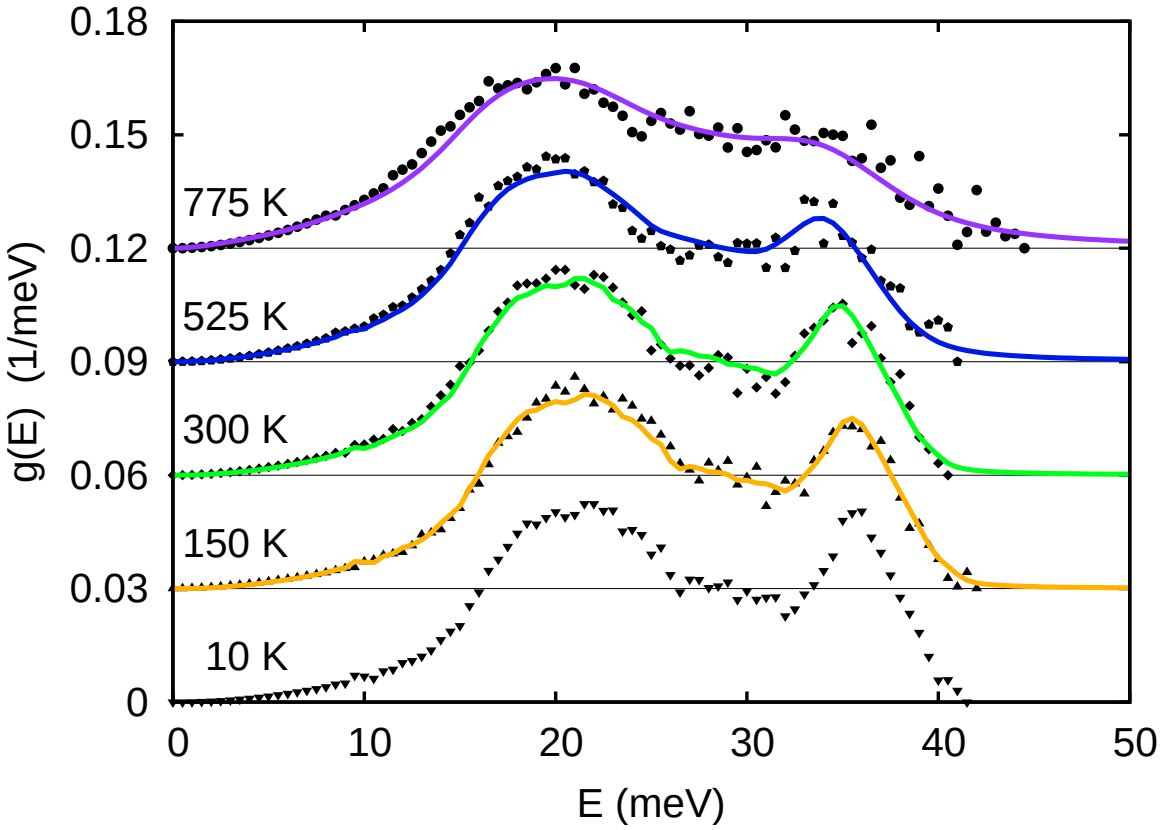

Figure 9.3: Phonon DOS of aluminum at temperatures as indicated. The markers show the experimentally determined DOS, and the lines the best fits of the 10 K DOS to the high temperature DOS by scaling of the energy and intrgral transform with the damped oscillator function as a kernel (Eq. 9.6).

Using Eqs. 9.4 and 9.5, the high temperature phonon DOS was approximated as a function of the low temperature DOS, with only two free parameters, Δ^s and $\mathcal{Q}$:

$$g_T(E) = B(\mathcal{Q}, E', E) \odot g_{10}(\Delta^s E') \,, \tag{9.6}$$

where g_T is the phonon DOS at temperature T, and $\odot$ denotes an integral transform that is similar to a convolution. (The subscript 10, as in 10 K, refers to the lowest temperature data from this set of experiments.)

At each temperature, the best $\mathcal{Q}$ and Δ^s for the experimental DOS were determined through a least squares algorithm. The $\mathcal{Q}$ so determined are shown in Fig. 9.4, and the fits to the phonon DOS are shown in Fig. 9.3. The inverse of the quality factor was well described by a quadratic function of T:

$$\frac{1}{\mathcal{Q}} \approx 3.523 \times 10^{-7}\, T^2 \,, \tag{9.7}$$

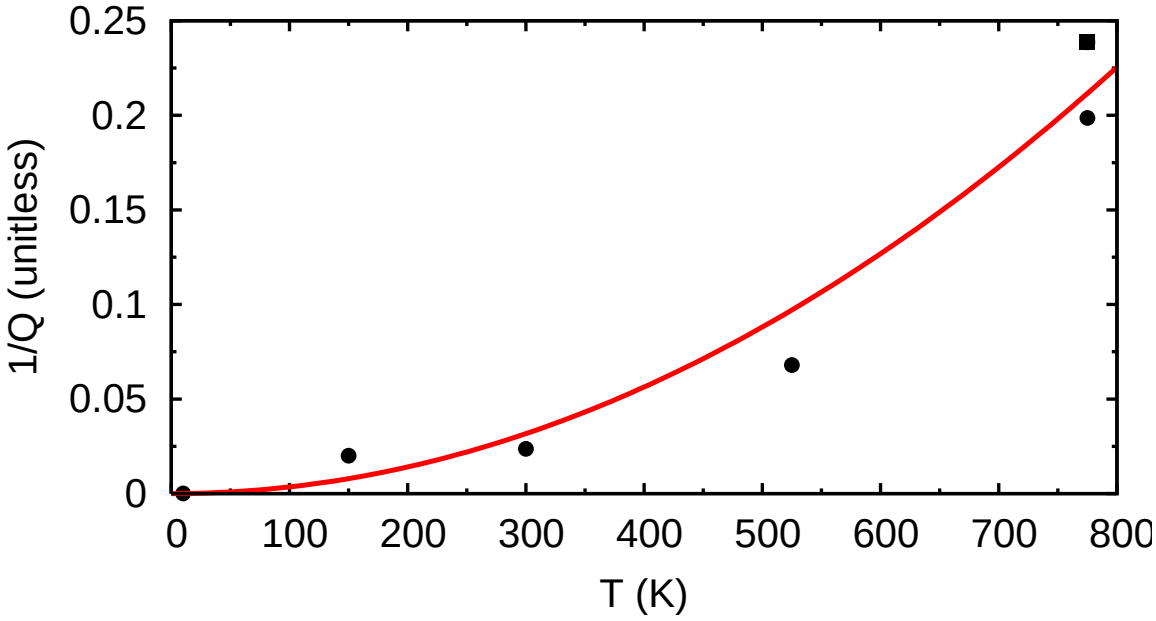

Figure 9.4: Markers show the inverse of the quality factor, $1/\mathcal{Q}$, as a function of temperature for aluminum phonons, circles are LRMECS data, and the square is Pharos data. The line is a parabolic fit (Eq. 9.7).

where T is in degrees Kelvin. The shifts $\Delta^{\rm s}$ are given in Table 9.1, along with the ratios of the mean phonon energies, $\langle E\rangle_T/\langle E\rangle_{10}$, as determined from the DOS:

$$\frac{\langle E\rangle_T}{\langle E\rangle_{10}} = \frac{\int E\; g_T(E)\; dE}{\int E\; g_{10}(E)\; dE}\;. \tag{9.8}$$

9.3.5 Born–von Kármán models of the lattice dynamics

In a second analysis, the phonon DOS were fit with Born–von Kármán models of the lattice dynamics. [68, 71, 72, 129] Tensorial force constants to the 3NN shell were determined with a gradient search method. For the higher temperatures, where there is significant anharmonic broadening, these models were sufficiently accurate. At lower temperatures, however, they were unable to reproduce the shape of the DOS. For the DOS at 10, 150, and 300 K, axially-symmetric force constants from 4NN through 8NN shells were also optimized. These showed little change with temperature, so they were averaged and kept constant for a final round of optimization.

To account for the thermal and instrument broadening, the frequencies, ω, calculated as the square root of each eigenvalue of the dynamical matrix, were taken to be the arguments of delta functions in energy, $\delta\left(E-\hbar\omega\right)$. Each delta function was transformed using the damped harmonic oscillator function of Eq. 8.19, and the Gaussian instrument resolution function given by Eqs. 9.1

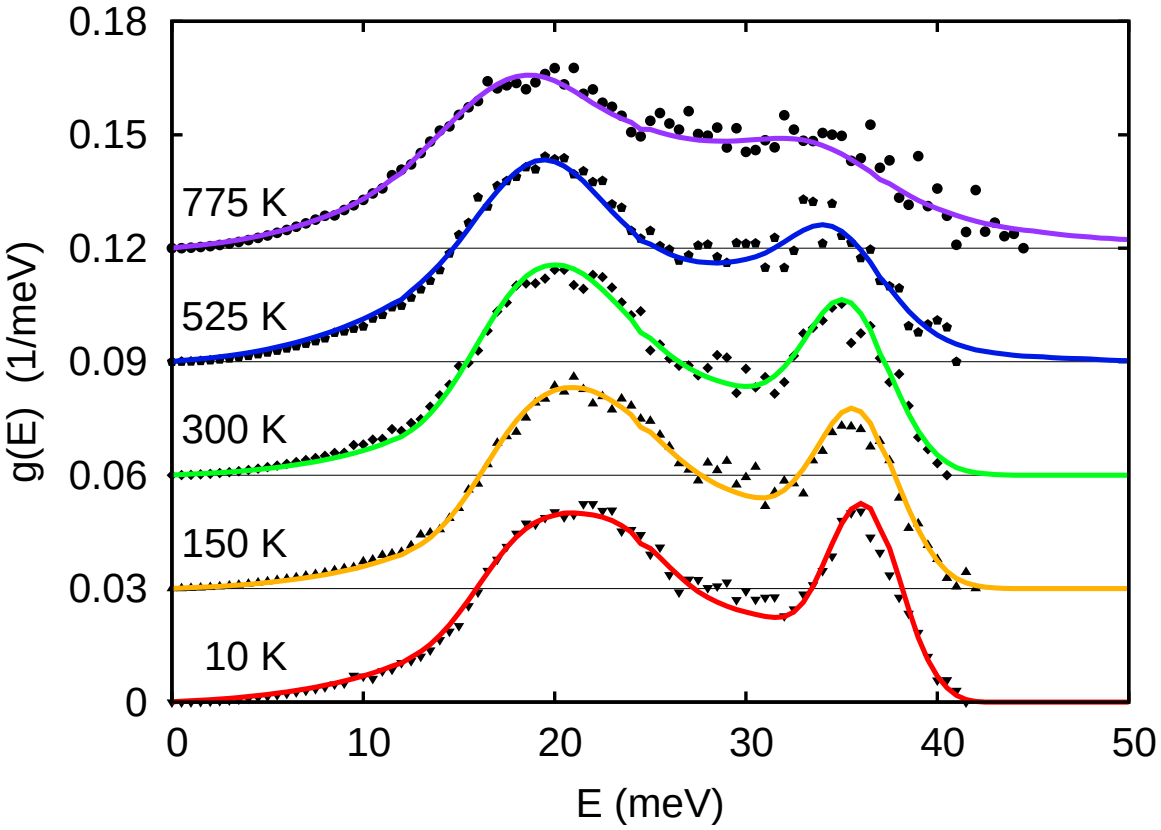

Figure 9.5: Phonon DOS of aluminum at temperatures as indicated. The markers show the experimentally determined DOS, and the lines the best BvK models found by fitting the data.

and 9.2. The force constants so determined are listed in Table 9.2, and the best fits to the DOS at all temperatures are shown in Fig. 9.5.

The longitudinal force constants were found by projecting the tensor onto the bond vectors $\langle xyz \rangle$. The 3×3 force constant tensors were then diagonalized. The longitudinal force constant was matched to one of the eigenvalues and the average transverse constant was taken to be the mean of the remaining eigenvalues. Longitudinal force constants to 3NN are shown in Fig. 9.6, and the averaged transverse force constants out to 3NN are shown in Fig. 9.7. The XNN longitudinal force constants, $\mathcal{K}_X(T)$, decrease with increasing temperature approximately as:

$$\mathcal{K}_1(T) = 21.022 - 2.559 \times 10^{-3}\ T\ , \tag{9.9}$$

$$\mathcal{K}_2(T) = \ \ 2.463 - 7.384 \times 10^{-4}\ T\ , \tag{9.10}$$

$$\mathcal{K}_3(T) = -0.862 - 2.066 \times 10^{-4}\ T\ , \tag{9.11}$$

where T is in degrees Kelvin and $\mathcal{K}_X(T)$ is in N/m. The fits are also shown in Fig. 9.6.

Table 9.2: Optimized tensor force constants in N/m as a function of temperature for FCC aluminum. They are given in a Cartesian basis, where $< xyz >$ is the bond vector for the given tensor components.

	$< xyz >$	10 K	150 K	300 K	525 K	775 K
$[\mathbf{K}_1]_{xx}$	$< 110 >$	10.112	9.708	9.708	10.542	10.112
$[\mathbf{K}_1]_{xy}$		11.148	10.697	10.378	9.232	8.970
$[\mathbf{K}_1]_{zz}$		−1.356	−1.201	−2.059	−3.370	−3.463
$[\mathbf{K}_2]_{xx}$	$< 200 >$	2.454	2.408	2.224	1.972	1.956
$[\mathbf{K}_2]_{yy}$		−0.532	−0.508	−0.367	−0.148	−0.144
$[\mathbf{K}_3]_{xx}$	$< 211 >$	−0.634	−0.636	−0.635	−0.707	−0.706
$[\mathbf{K}_3]_{xy}$		−0.185	−0.301	−0.294	−0.301	−0.299
$[\mathbf{K}_3]_{yy}$		−0.298	−0.183	−0.181	−0.225	−0.222
$[\mathbf{K}_3]_{yz}$		−0.149	−0.147	−0.148	−0.151	−0.151
$[\mathbf{K}_4]_{xx}$	$< 220 >$	0.273	0.273	0.273	0.000	0.000
$[\mathbf{K}_4]_{xy}$		−0.051	−0.051	−0.051	0.000	0.000
$[\mathbf{K}_4]_{zz}$		0.324	0.324	0.324	0.000	0.000
$[\mathbf{K}_5]_{xx}$	$< 310 >$	0.469	0.469	0.469	0.000	0.000
$[\mathbf{K}_5]_{xy}$		0.090	0.090	0.090	0.000	0.000
$[\mathbf{K}_5]_{yy}$		0.229	0.229	0.229	0.000	0.000
$[\mathbf{K}_5]_{zz}$		0.199	0.199	0.199	0.000	0.000
$[\mathbf{K}_6]_{xx}$	$< 222 >$	0.144	0.144	0.144	0.000	0.000
$[\mathbf{K}_6]_{xy}$		−0.110	−0.110	−0.110	0.000	0.000
$[\mathbf{K}_7]_{xx}$	$< 321 >$	−0.061	−0.061	−0.061	0.000	0.000
$[\mathbf{K}_7]_{xy}$		0.032	0.032	0.032	0.000	0.000
$[\mathbf{K}_7]_{xz}$		0.016	0.016	0.016	0.000	0.000
$[\mathbf{K}_7]_{yy}$		−0.088	−0.088	−0.088	0.000	0.000
$[\mathbf{K}_7]_{yz}$		0.011	0.011	0.011	0.000	0.000
$[\mathbf{K}_7]_{zz}$		−0.105	−0.105	−0.105	0.000	0.000
$[\mathbf{K}_8]_{xx}$	$< 400 >$	−0.536	−0.536	−0.536	0.000	0.000
$[\mathbf{K}_8]_{yy}$		−0.117	−0.117	−0.117	0.000	0.000

9.3.6 *Ab-initio* phonon calculations

In a third computational effort, we used the plane-wave code VASP [130, 131] to calculate the electronic DOS of aluminum as a function of unit cell volume. The calculations used projector augmented plane waves and the Perdew-Burke-Ernzerhof generalized gradient approximation. [133] A conventional FCC cell was used, and it was relaxed using the 'accurate' setting for the kinetic energy cutoff, with a $20 \times 20 \times 20$ Monckhorst-Pack q-point grid. [134] The relaxed volume (which matched the experimentally determined volume to better than 0.2%) was taken to be the 0 K volume of the unit cell, and the values of the linear coefficient of thermal expansion from Wang *et al.* [107] were used to determine the volumes at temperatures corresponding to our experiments. At each of these volumes, the electronic DOS was determined on a larger, $70 \times 70 \times 70$ q-point grid. The electronic DOS at 10 and 775 K are shown in Fig. 9.8.

The interatomic forces and the phonons were calculated from first principles in the direct method

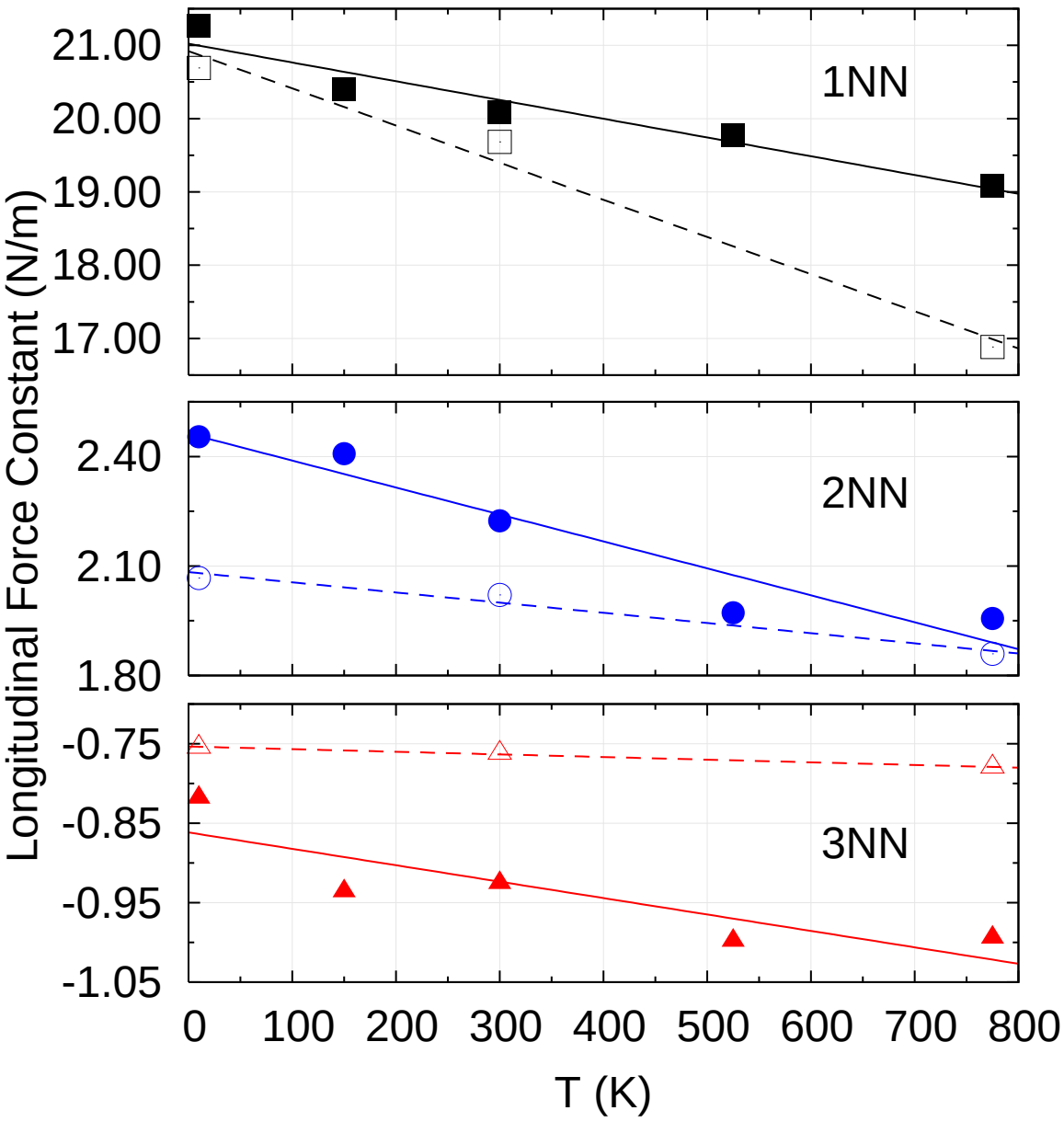

Figure 9.6: Longitudinal force constants for FCC aluminum as a function of temperature. Filled markers and solid lines are from BvK fits, unfilled markers and dashed lines are from calculations using VASP [130, 131] and PHON [132]. The fits to the BvK force force constants are given by Eqs. 9.9, 9.10, and 9.11. For the BvK models, the higher order force constants were fixed as described in the text.

using VASP in conjunction with the program PHON [132]. At volumes consistent with the temperatures 0, 300, and 775 K, the total energy was minimized for a $4 \times 4 \times 4$ (64 atom) super-cell with a $4 \times 4 \times 4$ electronic q-point grid. A single displacement whose length was 1% of the interatomic separation was used, and testing showed that the effects of the size of the displacement on the calculated force constants was negligible. The longitudinal and average transverse force constants were

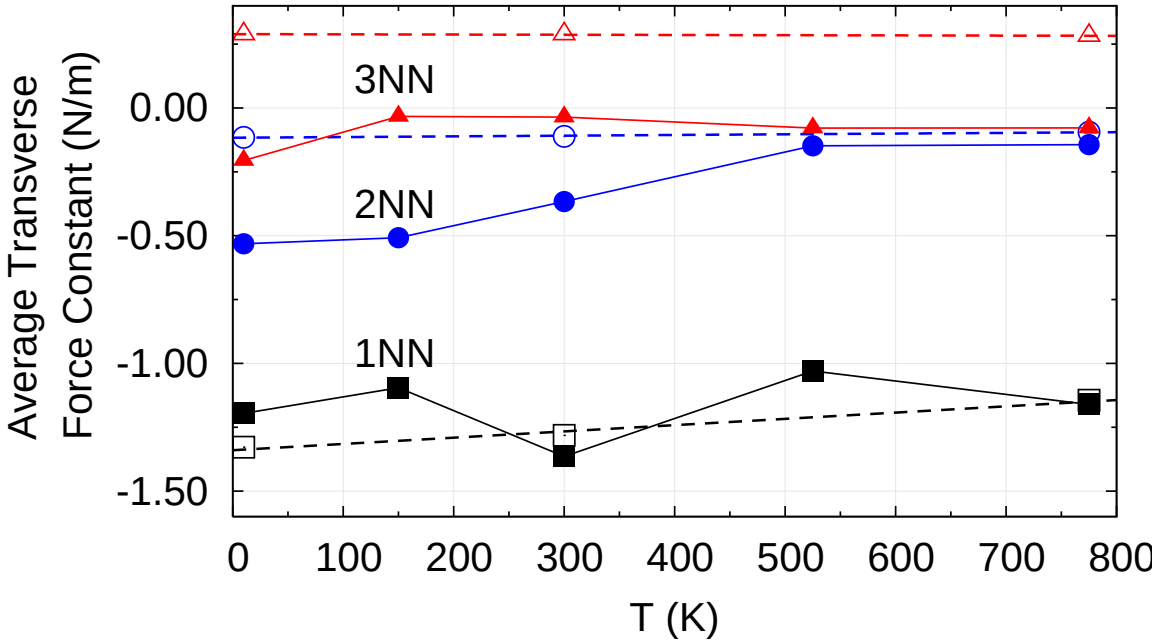

Figure 9.7: Averaged transverse force constants for FCC aluminum as a function of temperature. Filled markers and solid lines are from BvK fits, unfilled markers and dashed lines are from calculations using VASP [130, 131] and PHON [132].

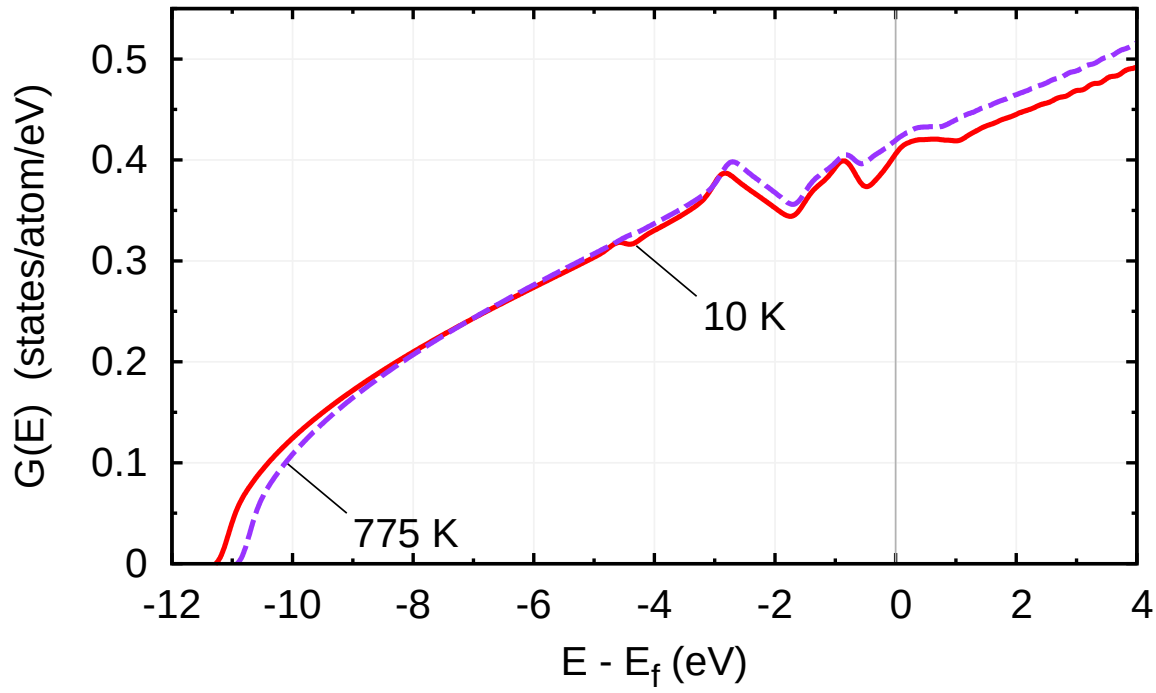

Figure 9.8: Electronic DOS of FCC aluminum at 10 K and 775 K, showing the effects of the expansion of the lattice with increasing temperature. E_{f} is the Fermi energy.

determined as for the BvK models, and are shown in Figs. 9.6 and 9.7 respectively. The values of the longitudinal force constants to 3NN at 0 K are given in Table 9.3.

9.4 Results

The force constants obtained from BvK models need not be unique, especially for more distant nearest-neighbor shells and for off-bond directions. [65] Nevertheless, Wallis *et al.* found that their BvK models for aluminum showed reasonable agreement with pseudopotential calculations for longitudinal force constants of the first three nearest-neighbor shells. [65] Table 9.3 presents the longitudinal force constants from the pseudopotential and empirical models (at 0 and 80 K, respectively) of Wallis *et al.*, from the empirical model (at 80 K) of Gilat *et al.*, from our empirical model (at 10 K), and from our plane-wave calculations (at 0 K). The table shows remarkable agreement of the major longitudinal force constants, giving confidence in our values of these force constants as a function of temperature.

As seen in Fig. 9.6, thermal changes in the 1NN force constants are dominant, and are expected to have the largest effect in shifting the DOS to lower energies with increasing temperature. The transverse force constants shown in Fig. 9.7 have small changes with temperature. They have negative signs, indicating some instability in the off-bond directions. At all temperatures, the magnitudes of both the longitudinal and transverse force constants decrease rapidly with increasing distance in the first two or three shells. The behavior of the fit force constants for longer bonds is less structured, possibly due to noise in the data and the difficulty in fitting parameters that have smaller impacts on the DOS. Nevertheless, fluctuations of sign could be consistent with Friedel oscillations in Al. [65]

The frequencies of the transverse modes and longitudinal modes have slightly different temperature dependencies, leading to modest differences in the second and third columns of Table 9.1. Stedman *et al.* [121] reported $\langle E \rangle_{300} / \langle E \rangle_{80} = 0.98$, which seems in reasonable agreement with the value of 0.969, obtained as the average of our values at 10 and 150 K. A previous study by

Table 9.3: Longitudinal force constants, $\mathcal{K}_X$ for the XNN shell in units of N/m as determined by BvK models and *ab-initio* calculations. Data from Wallis *et al.* [65] and Gilat *et al.* [122] are also tabulated.

Force Constant	Wallis Pseudopotential (0 K)	Wallis Empirical (80 K)	Gilat (80 K)	Present Study BvK (10 K)	Present Study Plane wave (0 K)
$\mathcal{K}_1$	21.70	24.60	21.55	21.26	20.69
$\mathcal{K}_2$	2.60	2.68	2.45	2.45	2.07
$\mathcal{K}_3$	-0.86	-0.68	-0.92	-0.82	-0.75

Larsson *et al.* [56] found significantly larger shifts in the mean frequency at higher temperatures: $\langle E\rangle_{775}/\langle E\rangle_{300} = 0.925$[a] where we find $\langle E\rangle_{775}/\langle E\rangle_{300} = 0.976$, perhaps because these early results were based on the central energies of broadened phonon peaks, and also because the much greater region of Q-space sampled in the present measurements gives a better average of the phonon softening.

From the values of $1/\mathcal{Q}$ shown in Fig. 9.4, at the highest energy of the phonons, 38.0 meV, we find maximum values of the full width at half maximum $2\Gamma = E/\mathcal{Q}$ to be approximately 0, 0.8, 0.9, 2.6, and 7.5 meV at the temperatures 10, 150, 300, 525, and 775 K respectively. This broadening seems consistent with the experimental values reported by Larsson *et al.* [56] Linewidths due to phonon-phonon interactions for aluminum at 300 K were calculated by Zoli *et al.* using an empirical force constant model. [64] They find a maximum 2Γ of about 1.5 meV for the longitudinal modes in the [111] direction, which is also in reasonable agreement with our data. In all cases, the linewidths appear to increase with increasing phonon energy.

Examples of phonon DOS from BvK models, damped BvK models, and reduction of experimental data are shown in Fig. 9.9. Especially at high temperatures, these DOS yield slightly different phonon entropies. To leading order in anharmonic perturbation theory, the phonon entropy is given by the quasiharmonic formula (Eq. 4.3) with the shifted energies. [37, 38] This would correspond to using our undamped BvK models. Calculating the entropy using the undamped BvK models gives a total entropy that is larger than that obtained from reduced experimental data. As the phonon linewidths increase, a particular phonon can be created or annihilated over a wider spectrum of energies. The damping function of Eq. 8.19, causes an increase in the mean phonon energy, and, thus, a decrease in phonon entropy. To minimize data manipulations, we report the entropy from reduced experimental data. We did not correct for the effects of instrument resolution broadening, which causes us to overestimate the phonon entropy by as much as 0.03 k_{B}/atom. This is not included in our estimates of the error.

9.5 Discussion

The harmonic and quasiharmonic contributions to the phonon entropy, $S_{\mathrm{ph,H}}$ and $S_{\mathrm{ph,Q}}$ were determined using Eq. 4.3. For the former, the spectrum measured at 10 K was assumed a good approximation of the 0 K phonon DOS. To find the contribution of lattice dilation to the phonon entropy, $S_{\mathrm{ph,D}}$, we used Eq. 4.4 with the temperature dependent isothermal bulk modulus found by He *et al.*, [135] and the temperature dependent lattice parameter and linear coefficient of thermal expansion

[a] Here, we have used the formula from Ref. [38] with $\langle E\rangle_{300}$ from our experiment.

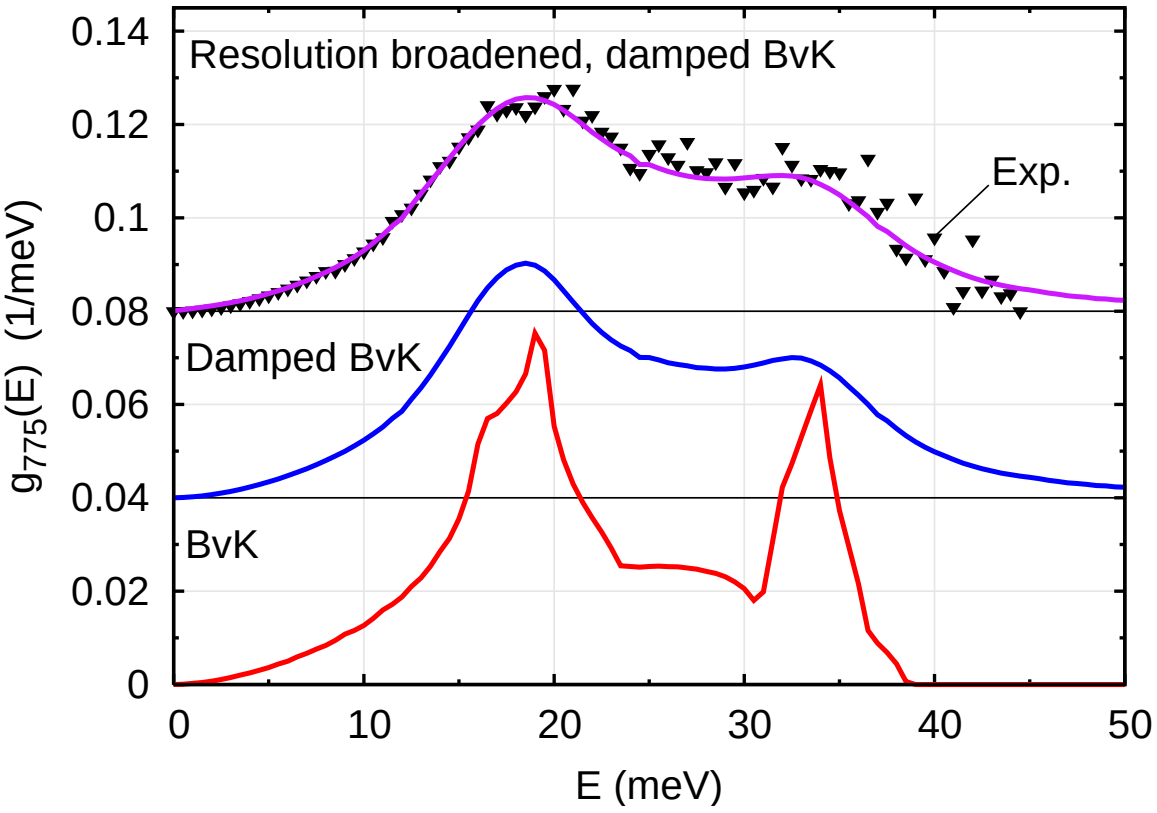

Figure 9.9: Phonon DOS for aluminum at 775 K. Markers show the experimental data. Lines show BvK models without damping, with damping, and with both damping and instrument resolution broadening, in the bottom, middle and top curves respectively.

for a 'real crystal' found by Wang *et al.*. [107] Specifically:

$$\begin{aligned} S_{\rm ph} &= S_{\rm ph}(T) = S_{\rm ph}(T,T)\ , \\ S_{\rm ph,H} &= S_{\rm ph,H}(T) = S_{\rm ph}(T,T_0)\ , \\ S_{\rm ph,D} &= S_{\rm ph,D}(T) = S_{\rm ph} - S_{\rm ph,H}\ , \end{aligned} \tag{9.12}$$

with $T_0 = 10$ K.

The total and ground state electronic entropy, $S_{\rm el,G}$ were found using Eq. 4.8 and the T_0=0 K electronic DOS calculated from first principles. The electronic entropy of dilation, $S_{\rm el,D}$, was taken to be the difference:

$$\begin{aligned} S_{\rm el} &= S_{\rm el}(T) = S_{\rm el}(T,T)\ , \\ S_{\rm el,G} &= S_{\rm el,G}(T) = S_{\rm el}(T,T_0)\ , \\ S_{\rm el,D} &= S_{\rm el,D}(T) = S_{\rm el} - S_{\rm el,G}\ , \end{aligned} \tag{9.13}$$

The electron-phonon entropy, described briefly in Chapter 4, was determined from the adia-

batic and non-adiabatic electron-phonon free energies calculated by Bock *et al.* [26, 33], using the thermodynamic relationship:

$$S = -\frac{\partial F}{\partial T} \ . \tag{9.14}$$

We expect the only configurational entropy to be from vacancies, thus we set $S_{\rm cf} = S_{\rm vac}$. Forsblom *et al.* [128] have found the entropy and enthalpy of formation of a vacancy in aluminum to be $\Delta S_{\rm vac,f} = 2.35\ k_{\rm B}$ and $\Delta H_{\rm vac,f} = 0.75$ eV, respectively. The configurational entropy $S_{\rm vac,c}$ and the formation entropy $S_{\rm vac,f}$ of sets of vacancies are given by:

$$\begin{aligned} c &= c(T) &&= \exp\left[-\beta(\Delta H_{\rm vac,f} - T\Delta S_{\rm vac,f})\right] \ , \\ S_{\rm vac,f} &= S_{\rm vac,f}(T) &&= c\Delta S_{\rm vac,f} \ , \\ S_{\rm vac,c} &= S_{\rm vac,c}(T) &&= -k_{\rm B}\left[c\ln(c) + (1-c)\ln(1-c)\right] \ , \end{aligned} \tag{9.15}$$

where c is the concentration of vacancies.

All contributions to the entropy are shown in Fig. 9.10. The total entropy of aluminum was obtained with Eq. 4.16. Values for the total entropy were taken from the NIST-JANAF thermochemical tables, [136] and agreement is excellent, with a root-mean-square deviation of 0.046 $k_{\rm B}$/atom. The root-mean-square deviations for the entropy as determined from the BvK models and from the damped BvK models were 0.066 and 0.039 $k_{\rm B}$/atom respectively. The differences between these three models are small; nevertheless, it may be that using a damped DOS (without resolution broadening) more accurately represents the phase space covered by the anharmonic oscillators. We also see excellent agreement between our (time-of-flight based) values for the phonon entropy and those derived using triple axis data at 80 and 300 K. (The data were taken from Stedman *et al.* [118] and used by Gilat *et al.* [122] to generate phonon DOS which we then used to find the phonon entropy.)

The harmonic phonon entropy accounts for most of the entropy of aluminum. The next largest contribution is from the phonon entropy of dilation, but this is already an order of magnitude smaller. The quasiharmonic model is a useful one for aluminum; nevertheless, the anharmonic phonon entropy is non-negligible, and comparable in magnitude to the the electronic entropy. The adiabatic electron-phonon interaction is another order of magnitude smaller, followed by the dilation correction to the electronic entropy. The vacancy contribution to the entropy is primarily configurational, and is very small.

Over the temperatures measured, the anharmonic phonon entropy, $S_{\rm ph,A}$, ranges from -0.10 to $+0.08\ k_{\rm B}$/atom (where we have incorporated errors of approximately $\pm 0.03\ k_{\rm B}$/atom). At our highest temperature of 775 K, we have $-0.10 < S_{\rm ph,A} < -0.04\ k_{\rm B}$/atom. The anharmonic entropy is positive up to around 625 K, after which it becomes negative and decreasing.

The anharmonic contribution to the entropy of aluminum is dominated by phonon-phonon inter-

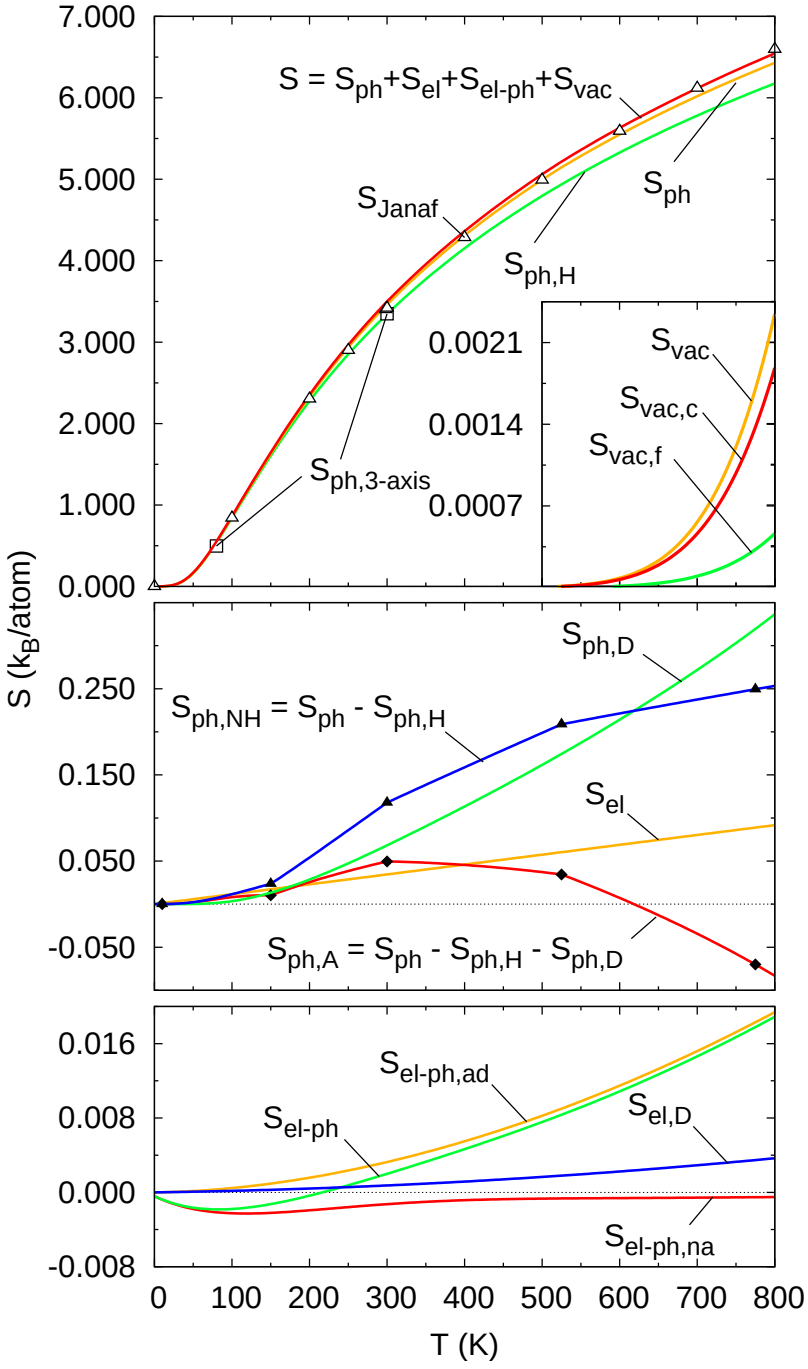

Figure 9.10: Contributions to the entropy of aluminum as a function of temperature. The temperature labels at the bottom of the plot apply to all panels and the inset. Open triangles are total entropy data taken from the NIST-JANAF thermochemical tables and open squares are phonon entropy derived from triple-axis data. Closed markers are data from the current experiment; lines are either calculations or interpolations.

actions over the much smaller contribution from electron-phonon interactions. [124] It is interesting that the shape of the anharmonic entropy curve is similar to that reported recently for the FCC nickel

[35] and the superlinear temperature dependence of $1/\mathcal{Q}$ is also similar. Aluminum is a simple metal, and nickel is a magnetic d-band metal with a complex electronic structure, so it would be surprising if their similar anharmonic behaviors originated from electron-phonon interactions. Phonon-phonon interactions are the probable source of the large increase in phonon linewidth with temperature in both metals. It is interesting that this increase in linewidth is approximately quadratic with temperature, as opposed to the linear effect predicted by the quasiharmonic approximation and perturbation theory. [38, 137, 138] The quasiharmonic approximation is expected to be most appropriate when the phonon frequency shifts are small and the phonon lifetimes are long. The latter condition may not apply well to aluminum or nickel.

9.6 Summary

Measurements of the inelastic scattering of neutrons by phonons in aluminum were made at temperatures of 10, 150, 300, 525, and 775 K. Phonon DOS were obtained from the reduced experimental data, and were used to determine the harmonic, nonharmonic and total phonon entropy of aluminum. The sum of the phonon, electronic and vacancy contributions to the entropy agree exceptionally well with accepted values for the total entropy over the entire range of temperatures studied. The anharmonic entropy obtained from the shifts of phonon frequencies was small, but the broadening of the phonon DOS was significant, and scaled superlinearly with temperature. The anharmonic behavior was attributed to phonon-phonon interactions. The experimental phonon DOS were fit to BvK models of the forces in the solid. A linear decrease with temperature was found for the the 1NN, 2NN and 3NN force constants, with the 1NN force constants decreasing by approximately 10% over the range of temperatures measured.

Chapter 10

Lead

10.1 Introduction

Lead has a melting temperature of $T_M = 600$ K, and a Debye temperature of $T_\mathrm{D} = 100$ K. Temperatures from near absolute zero to the melting point are easily accessible experimentally, and we expect to see signs of anharmonicity for all temperatures greater than T_D. As such, lead is nearly ideal for studies of phonon anharmonicity in metals, and its properties have been a common subject of interest for both experimentalists [57, 139–143] and theorists. [144–147]

Practically speaking, mining and processing of lead is inexpensive, and lead is highly malleable and resistant to corrosion. Consequently, the metal has myriad industrial uses, most notably in bullets, solder, radiation shielding, and lead-acid batteries. Perhaps less practically, the prospect of converting lead to gold has garnered the attention of some great scientific minds.[a] More recently, much of the scientific interest in lead has focused on the interactions between electrons and phonons. This over the entire temperature range of the solid phase.

At moderate and high temperatures, where lead is a nearly free electron metal, a great deal of attention has been paid to the presence of Kohn anomalies in the phonon dispersions. [148] Briefly, let $\mathbf{q}_1$ and $\mathbf{q}_2$ be electron wavevectors lying on the Fermi surface such that the planes tangent to the surface at these points are parallel. There may be many such points on the Fermi surface — for example, this would be the case for any pair of points directly opposite one another on the spherical Fermi surface of a free-electron metal. All such pairs contribute a logarithmic singularity to the electron screening at wavevector $\mathbf{Q} = \mathbf{q}_1 - \mathbf{q}_2$, and this may be seen as a kink in the phonon dispersions at wavevector $\mathbf{Q}$. As lead is a strong coherent scatterer of neutrons, and has a comparatively high superconducting transition temperature, it is a good candidate for a neutron scattering measurement of Kohn anomalies. Indeed, both Brockhouse *et al.* [149] and Stedman *et al.* [150] have made such measurements.

[a] For example, Roger Bacon, Tycho Brahe, and Isaac Newton, all expended significant effort on the study of alchemy.

Below the critical temperature, $T_S \approx 7.2$ K, the coupling of electrons and phonons in lead results in superconductivity. A number of measurements have been made investigating the changes in the energies and linewidths of the phonons around T_S. Mikhaĭlov *et al.* found that transverse phonons in the (111) direction in lead had energies that increased and linewidths that decreased as expected upon lowering the temperature from 300 to 20.4 K; however, they found these trends to be reversed upon lowering the temperature further, to 4.2 K.[151] Youngblood *et al.*, on the other hand, measured the same (111) transverse phonons and found no effect of the superconducting transition on their energies and lifetimes. [152] More recently, Habicht *et al.* found no anomalous changes in the phonon linewidths above and below T_S as measured with high resolution neutron-resonance spin-echo spectroscopy. [58] In a later measurement, however, they[b] did find changes in the phonon linewidths at T_S. [153] The later measurement had increased intensity, and this is the ostensible cause of the discrepancy. None of these measurements, however, cover enough of reciprocal space to give a phonon DOS.

Brockhouse *et al.* made triple-axis measurements of the phonon dispersions in lead in high symmetry directions at 100 K. [154, 155] They found that the forces in lead were exceptionally long range; nevertheless, Gilat used this data to find a Born–von Kármán model of the lattice dynamics in lead. [156] Subsequent triple-axis work by Stedman *et al.* [121, 157] covered a significantly larger fraction of reciprocal space and did not match the model very well, particularly in off-symmetry directions.[c] There is strong evidence that a measurement that samples a larger volume of reciprocal space is preferable for determination of the phonon spectrum of lead. [121, 158–162]

The superconducting state allows for determination of the phonon spectrum via measurements of electron tunneling [162–164] or of far-infrared reflectance. [165, 166] These measurements yield $\eta^2(E)g(E)$, where $\eta^2(E)$ is an effective electron-phonon coupling function for phonons with energy E. The factor $\eta^2(E)$ is fairly smooth as a function of energy [167] with the possible exception of a feature at roughly 1.6 meV. [161] This variation is insufficient to explain the differences between the phonon spectra derived from tunneling and those derived from neutron scattering seen in Fig. 10.1 The far-infrared reflectance measurements seen in Fig. 10.2 show more of the features seen in the neutron scattering results; however, there remain issues of the overall energy scale and of the precise energy dependence of $\eta(E)$. Moreover, these measurements may only be made at temperatures below the superconducting transition.

Here, we present measurements of the inelastic scattering of neutrons by phonons in lead at temperatures of 18, 38, 63, 88, 113, 137, 163, 188, 300, 390, and 500 K. The measurements were performed on a time-of-flight chopper spectrometer at a spallation neutron source so they sample all of reciprocal space. They represent a fairly direct determination of the phonon spectrum of lead,

[b] Only B. Keimer, T. Keller, and K. Habicht are authors on both Refs. [58] and [153]. T.Keller is actually the first author of the second reference.

[c] A more detailed comparison of our results with those of Stedman *et al.* is presented in § 10.4.

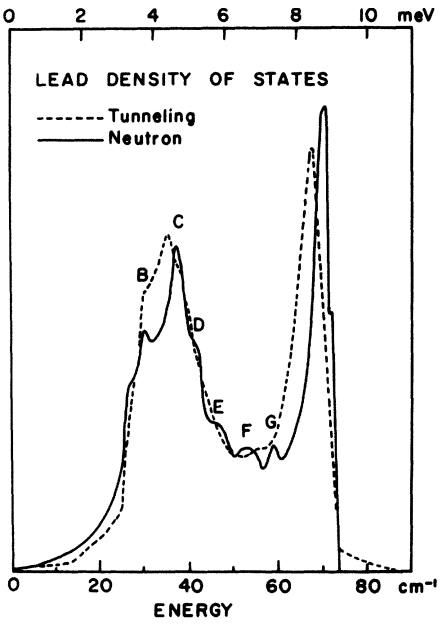

Figure 10.1: Phonon spectrum of lead derived from neutron scattering (solid line) and electron tunneling (dashed line) experiments. The spectrum from tunneling lacks all but the major features visible in the spectrum from neutron scattering. Figure taken from Ref. [165].

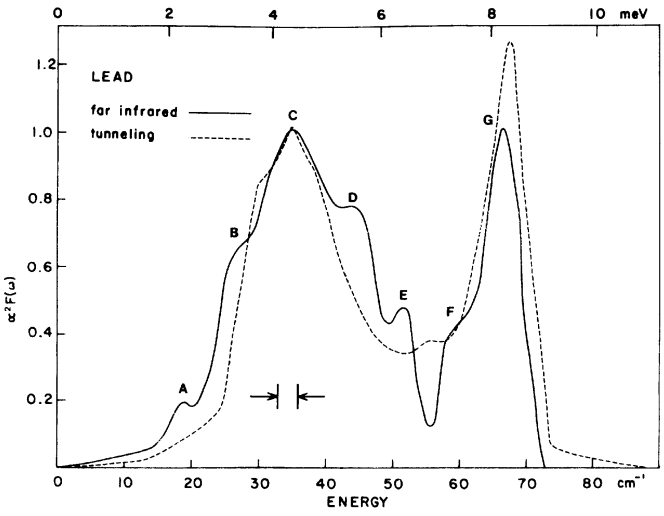

Figure 10.2: Electron-phonon coupling function weighted phonon spectrum of superconducting lead derived from far-infrared reflectance (solid line) and from electron tunneling (dashed line) experiments. The letters are meant to indicate common features in the reflectance and neutron derived spectra. The energy for the tunneling measurement been scaled so the spectra match at "C". Figure taken from Ref. [166].

which we use to determine the phonon contributions to the entropy of lead. We also assess the other entropic contributions, and compare to the total thermodynamic entropy. We find a purely anharmonic contribution to the phonon entropy, unaccounted for by the expansion of the lattice, of approximately $-0.23\ k_{\mathrm{B}}$/atom at 500 K. Additionally, we find a superlinear dependence of the phonon linewidths on temperature and discuss the measured shifts in phonon energy.

10.2 Experiment

10.2.1 Sample preparation

Clean sheets of lead foil of 99.998% purity were arranged in a thin-walled aluminum pan, whose height, width and depth were approximately 7.5, 5.0 and 0.1 cm, covering maximally the incident neutron beam The ratio of singly- to multiply-scattered neutrons was designed to be approximately 24:1.

10.2.2 Neutron scattering measurements

Inelastic neutron scattering measurements were performed on the ARCS spectrometer at the Spallation Neutron Source at Oak Ridge National Laboratory. The sample was mounted at 45° to the incident neutron beam, and measurements were made at 18, 300, 390, and 500 K. For the higher temperatures, 300, 390, and 500 K, the sample was mounted in a low background, electrical resistance furnace designed for vacuum applications. For the lower temperatures (including a second measurement at 300 K) the sample was mounted in a closed-cycle helium refrigerator (CCR). In both cases, temperature was monitored with several thermocouples, and is believed accurate to within 5 K over the bulk of the sample. As a measurement on ARCS takes roughly 20 minutes, and the CCR requires 4 hours to cool from room temperature to 21 K, measurements were also taken during the cooling process at median temperatures of 38, 63, 88, 113, 137, 163, and 188 K. All of these were used to determine lattice parameters, and the measurements at 88 and 163 K were given a complete analysis.[d] Due to a shortage of time, the only background measurement taken was of the empty CCR at room temperature (300 K).

The E0 chopper was set at 480 Hz giving a nominal energy of 30 meV for the incident neutrons. The counts from neutrons taking between 5500 and 8500 μs to reach the sample from the moderator were stored in bins of width 3 μs. Incident neutron energies for the different temperatures determined from the elastic peaks ranged from 29.63 to 29.70 meV (details in § 7.2.2). The experimentally determined full width at half maximum resolution in angle was approximately 0.1°. The measurements at 21, 300, 390, and 500 K were roughly 30 minutes in duration, and included approximately 20,000,000 counts. The 88 and 163 K measurements were shorter, with roughly 9,000,000 and 16,000,000 counts respectively.

10.3 Analysis and computation

Details of the data reduction procedures used here are given in Chapter 7, with rebinning described in § 7.4.1. The correction for multiple- and multiphonon scattering was described in § 8.1.2. For diffraction and determination of the quality factors see § 8.4 and § 8.2 respectively.

10.3.1 General data reduction

The raw data in time-of-flight and scattering angle Θ were first normalized using the integrated proton current. Bad detectors were identified and masked, and the data were corrected for detector efficiency using a measurement of vanadium, an incoherent scatterer. The data were then binned to get intensity, $I(\Theta, E)$, as a function of scattering angle, Θ, and energy, E, transferred to the sample.

[d] The measurements at 38 and 63 K were deemed to have insufficient counts for analysis. The 113, 137, and 188 K measurements will be analyzed in the future.

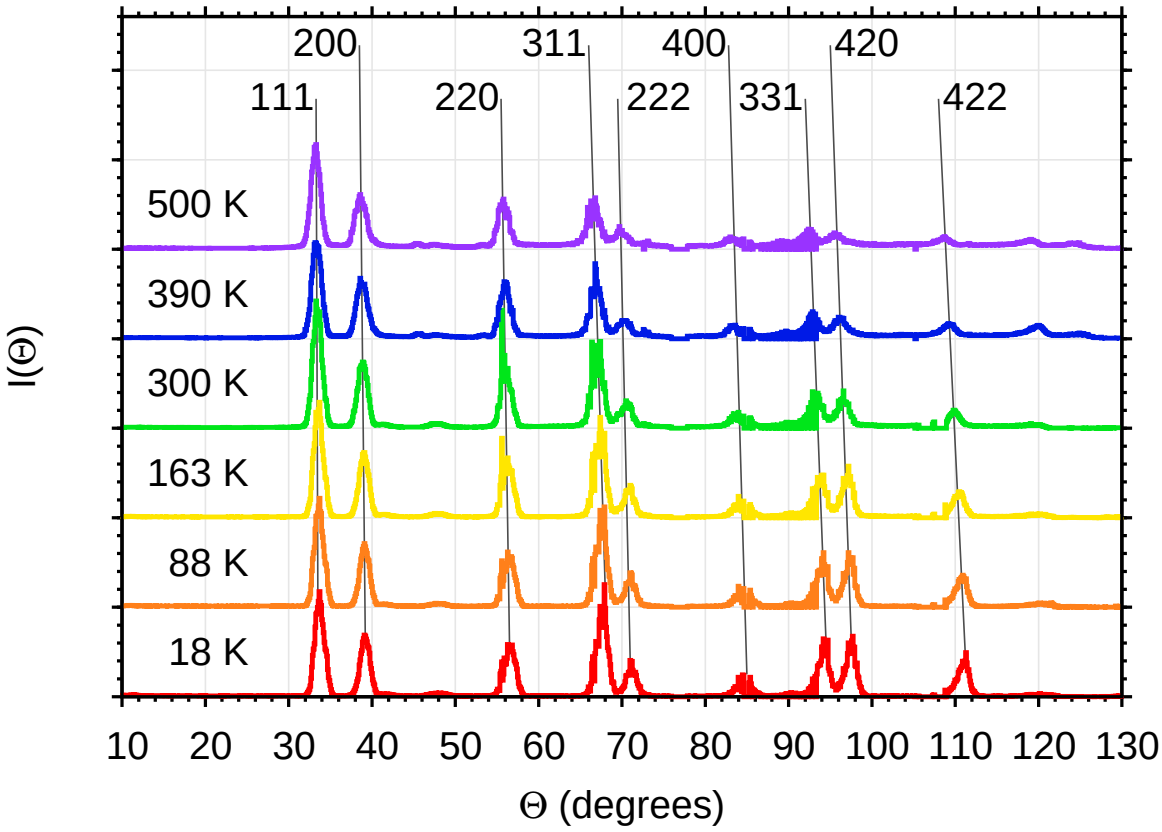

Figure 10.3: Diffraction patterns from lead at temperatures as indicated. These were used to determine the lattice parameters shown in Table 10.1.

Approximately, Θ ranged from 0° to 145° with a bin width of 0.1°, and E ranged from −30.0 to 30.0 meV with a bin width of 0.1 meV. The data, now reduced to, $I(\Theta, E)$ were then rebinned again into intensity, $I(Q, E)$, where Q is the momentum transferred to the sample. Values of Q ranged from 0.0 to 8 Å^{-1}, with a binwidth of about 0.025 Å^{-1}.

10.3.2 Elastic scattering: *in-situ* neutron diffraction

By summing $I(\Theta, E)$ from −2.1 to 2.1 meV, in-situ neutron diffraction patterns were obtained, and are shown in Fig. 10.3. Lattice parameters were determined using Nelson–Riley [104, 105] plots, and these are listed in Table 10.1. These are systematically larger than accepted values of the lattice parameter by roughly 0.02 Å; but the trends are consistent with thermal expansion data from Touloukian *et al.* [168]

Table 10.1: Experimentally determined lattice parameter, a, of lead and shifts of the lead phonon energies as a function of temperature. Fits of the 18 K DOS to the high temperature DOS by scaling of the energy and integral transformation with the damped oscillator function yield the relative frequency shifts Δ^{s} (Eq. 10.5). $\langle E\rangle_T/\langle E\rangle_{18}$ are ratios of the first moments of the DOS (Eq. 10.6).

T (K)	$a \pm 0.03$ (Å)	Δ^{s}	$\langle E\rangle_T/\langle E\rangle_{18}$	$S_{\mathrm{ph}} \pm 0.2$ (k_{B}/atom)
18	4.934	1.000	1.000	0.558
38	4.934	–	–	–
63	4.939	–	–	–
88	4.944	1.006	1.017	4.040
113	4.948	–	–	–
137	4.953	–	–	–
163	4.953	1.003	1.019	5.872
188	4.957	–	–	–
300	4.971	1.005	1.023	7.731
390	4.986	1.007	1.039	8.542
500	5.004	1.021	1.061	9.319

10.3.3 Background determination

As mentioned in the previous section, the only background measurement taken was of the empty CCR at room temperature (300 K). On LRMECS or Pharos, this might have been sufficient for all temperatures; however, ARCS is still in the process of acquiring shielding, a T0 chopper, and various other components. As such, the single background measurement was not even acceptable for the measurement of lead at room temperature in the CCR. Fig. 10.4 shows the measured scattering, $I_T^{\mathrm{Pb}}(E)$, from lead at $T = 18$, 88, 163, and 300 K, as well as the measured background, $I_{300}^{\mathrm{CCR}}(E)$.[e] The high energy cutoff of the phonon spectrum of lead is known from previous studies to be roughly 10 meV. [154–166] In order for us to have measured a similar cutoff, we would have needed to measure background scattering at 18 K with intensity similar to the curve marked I^{b} in Fig. 10.4; however, our measurement, I_{300}^{CCR}, has nowhere near this intensity.

Let I_{18}^{mph} be the multiphonon scattering from lead at 18 K. Then, in order to overcome the difficulties with the background, we have done the following (all energies are given in meV):

- Assume that the cutoff of the phonon spectrum is 10 meV at 18 K.
- Take:

$$I^{\mathrm{b}} + I_{18}^{\mathrm{mph}} \equiv \begin{cases} I_{18}^{\mathrm{Pb}} & E > 10 \\ I_{18}^{\mathrm{Pb}}(Q, 10) & \mathcal{E} < E < 10 \\ I_{300}^{\mathrm{CCR}} & E < \mathcal{E} \end{cases} , \tag{10.1}$$

[e] The intensities have been summed over Q. The functional dependence of the intensity on E and Q will be dropped whenever this can be done without causing confusion.

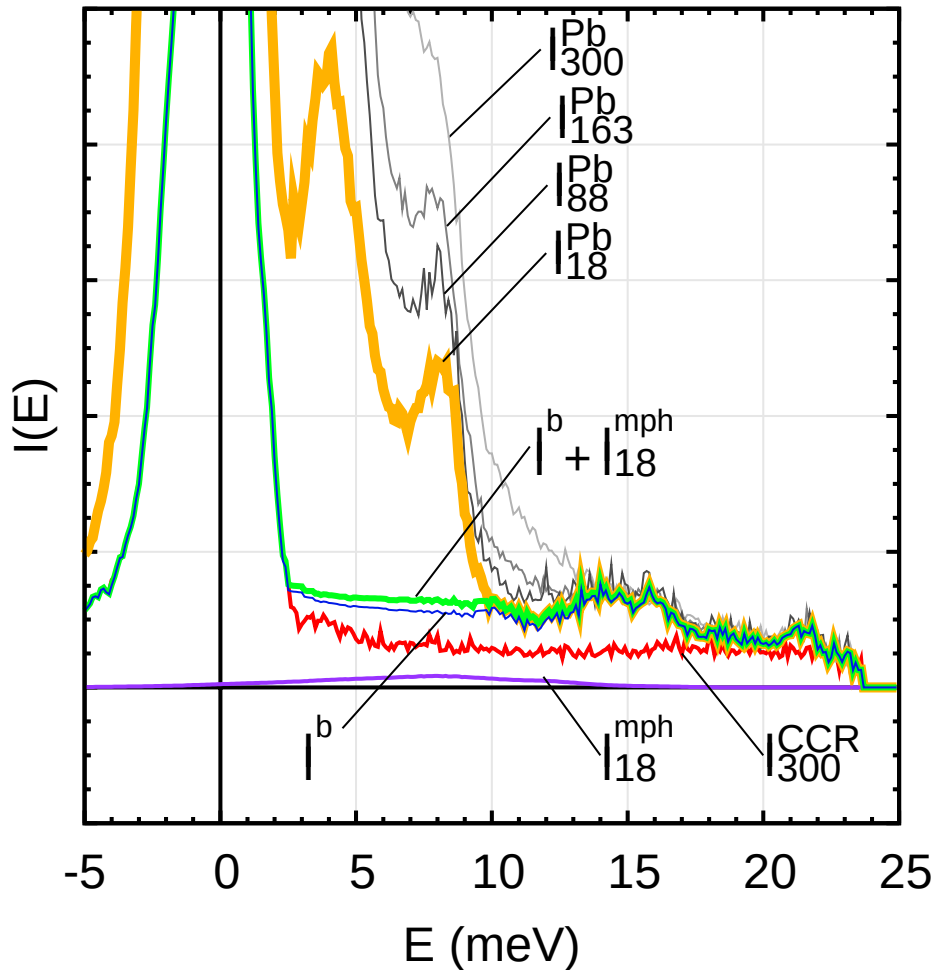

Figure 10.4: Determination of the background for lead measured at ARCS. $I_T^{\mathrm{Pb}}(E)$ is the scattering from lead at temperature T. I_{300}^{CCR} is the measured scattering from the empty CCR at 300 K. $I^{\mathrm{b}}+I_{18}^{\mathrm{mph}}$ is the assumed combination of background and multiphonon scattering at 18 K as described in § 10.3.3. I_{18}^{mph} is the multiphonon scattering determined using the phonon DOS found by taking $I^{\mathrm{b}} + I_{18}^{\mathrm{mph}}$ to be the background, and I^{b} is the background finally used in our analysis.

where $\mathcal{E} \sim 2.1$ is the point where a line of constant intensity emanating from $I_{18}^{\mathrm{Pb}}(Q, 10)$ and heading towards $E = 0$ crosses I_{300}^{CCR}. (The crossing is on the elastic peak.)

- Find a phonon DOS for lead at 18 K, g'_{18}, by taking I_{18}^{Pb} as the scattering and $I^{\mathrm{b}} + I_{18}^{\mathrm{mph}}$ as the background and using the iterative technique from § 8.1.2.

- Use g'_{18} to determine the multiphonon scattering, I_{18}^{mph}, and separate it from background scattering I^{b}.

The apparent deviations from linearity in the $2.1 \lesssim E < 10$ region are caused by the kinematical restrictions on Q and E. For measurements at or below 300 K, I^{b} was used as the background. For temperatures above 300 K, we took the background to be the sum of I^{b} and the difference of the

scattering from lead as measured in the furnace at 300 K and in the CCR at 300 K, $I^{\mathrm{b}} + \delta I$. These were then subtracted from I_T^{Pb}.

There is some justification for this procedure in that the intensity of inelastic scattering is temperature dependent. That the features at ~ 14 meV in the alleged background scattering appear to be constant as a function of temperature, and that they are completely absent from the measurement of the empty CCR, suggests that some neutrons are scattering elastically in the lead sample, hitting another object in the instrument, and then and then rescattering elastically into the detectors.

10.3.4 Inelastic scattering: S(Q,E) and the phonon DOS

To determine the inelastic scattering, the elastic peak was removed below 2.1 meV and replaced by a function of the form:

$$I(E) = \frac{\zeta_0 E}{1 - \exp\left(-\beta E\right)} \,, \tag{10.2}$$

where the constant ζ_0 was determined from the inelastic scattering just past the elastic peak. Here, we have assumed that the phonon DOS is proportional to E^2 in the low energy regime, as in a Debye model. The phonon DOS were then extracted from the scattering, making the thermal corrections and corrections for multiphonon and multiple scattering, as described previously. [35] These phonon DOS are shown by markers in Fig. 10.5.

10.3.5 Phonon shifts and broadening

With increasing temperature, the phonon peaks in a metallic solid typically broaden and undergo a shift to lower energies. These shifts were approximated as a constant multiplier, Δ^{s}, applied to all phonon energies E:

$$E \rightarrow \Delta^{\mathrm{s}} E \,. \tag{10.3}$$

The broadening of the phonons was assumed to take the form of a damped harmonic oscillator function, $B(\mathcal{Q}, E', E)$ centered about energy E': [84]

$$B(\mathcal{Q}, E', E) = \frac{1}{\pi \mathcal{Q} E'} \frac{1}{\left(\frac{E'}{E} - \frac{E}{E'}\right)^2 + \frac{1}{\mathcal{Q}^2}} \,. \tag{10.4}$$

Using Eqs. 10.3 and 10.4, the high temperature phonon DOS was approximated as a function of the low temperature DOS, with only two free parameters, Δ^{s} and $\mathcal{Q}$:

$$g_T(E) = B(\mathcal{Q}, E', E) \odot g_{18}(\Delta^{\mathrm{s}} E') \,, \tag{10.5}$$

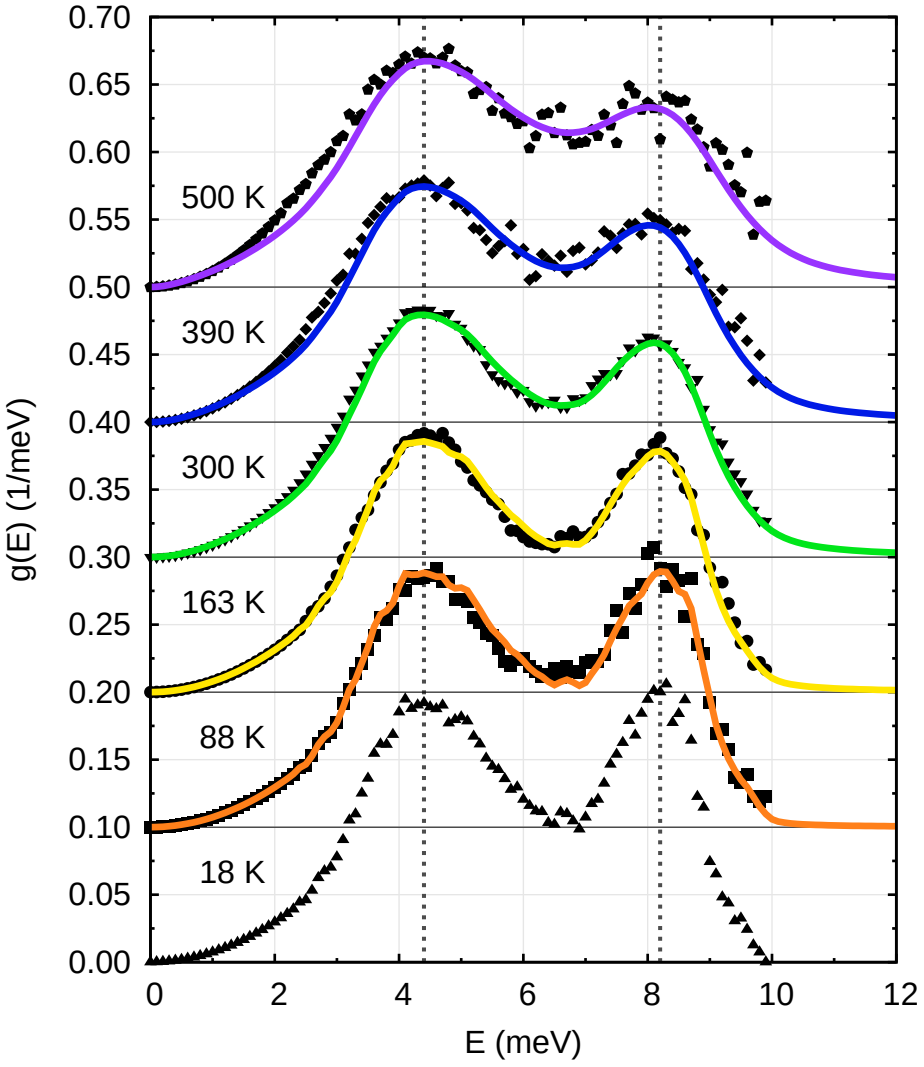

Figure 10.5: Phonon DOS of lead at temperatures as indicated, offset by integer multiples of 0.1 meV^{-1}. The markers show the experimentally determined DOS, and the lines the best fits of the 18 K DOS to the high temperature DOS by scaling of the energy and intrgral transform with the damped oscillator function as a kernel (Eq. 10.5). The two dotted-vertical lines serve to illustrate the fact that the positions of the longitudinal and transverse peaks are relatively constant as a function of temperature.

where g_T is the phonon DOS at temperature T, and $\odot$ denotes an integral transform that is similar to a convolution. (The subscript 18, as in 18 K, refers to the lowest temperature data from this experiment.)

At each temperature, the best $\mathcal{Q}$ and Δ^s for the experimental DOS were determined through a least squares algorithm. The $\mathcal{Q}$ so determined are shown in Fig. 10.6, and the fits to the phonon DOS are shown in Fig. 10.5. The shifts Δ^s are given in Table 10.1, along with the ratios of the mean

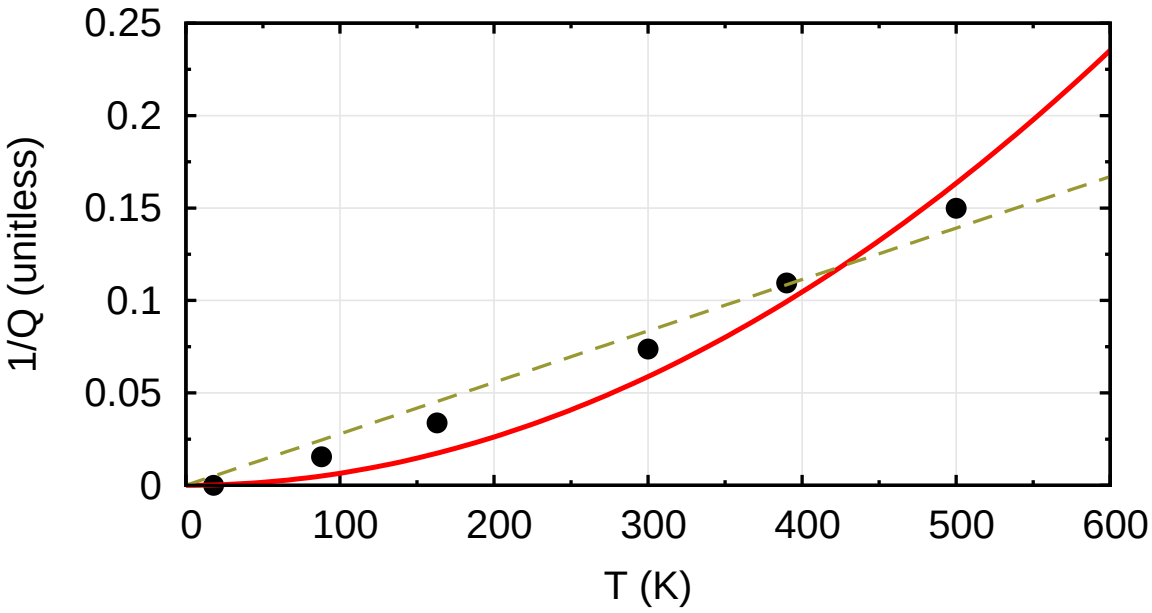

Figure 10.6: Markers show the inverse of the quality factor, $1/\mathcal{Q}$, as a function of temperature for lead phonons The dashed and solid lines are linear and parabolic fits, respectively. Neither of these seems to capture the temperature dependence of $1/\mathcal{Q}$.

phonon energies, $\langle E\rangle_T/\langle E\rangle_{18}$, as determined from the DOS:

$$\frac{\langle E\rangle_T}{\langle E\rangle_{18}} = \frac{\int E\; g_T(E)\; dE}{\int E\; g_{18}(E)\; dE}\;. \tag{10.6}$$

10.3.6 *Ab-initio* electronic structure calculations

We used the plane-wave code VASP [130, 131] to calculate the electronic DOS of lead as a function of unit cell volume. The calculations used projector augmented plane waves and the Perdew-Burke-Ernzerhof generalized gradient approximation. [133] A conventional FCC cell was used, and it was relaxed using the 'accurate' setting for the kinetic energy cutoff, with a $41 \times 41 \times 41$ Monckhorst-Pack q-point grid. [134] The relaxed volume (which matched the experimentally determined volume within 2.3%) was taken to be the 0 K volume of the unit cell, and the values of the linear coefficient of thermal expansion from Touloukian *et al.* [168] were used to determine the volumes at 0, 100, 200, 300, 400, 500, and 600 K. At each of these volumes, the electronic DOS was determined. The electronic DOS at 0 and 600 K are shown in Fig. 10.7.

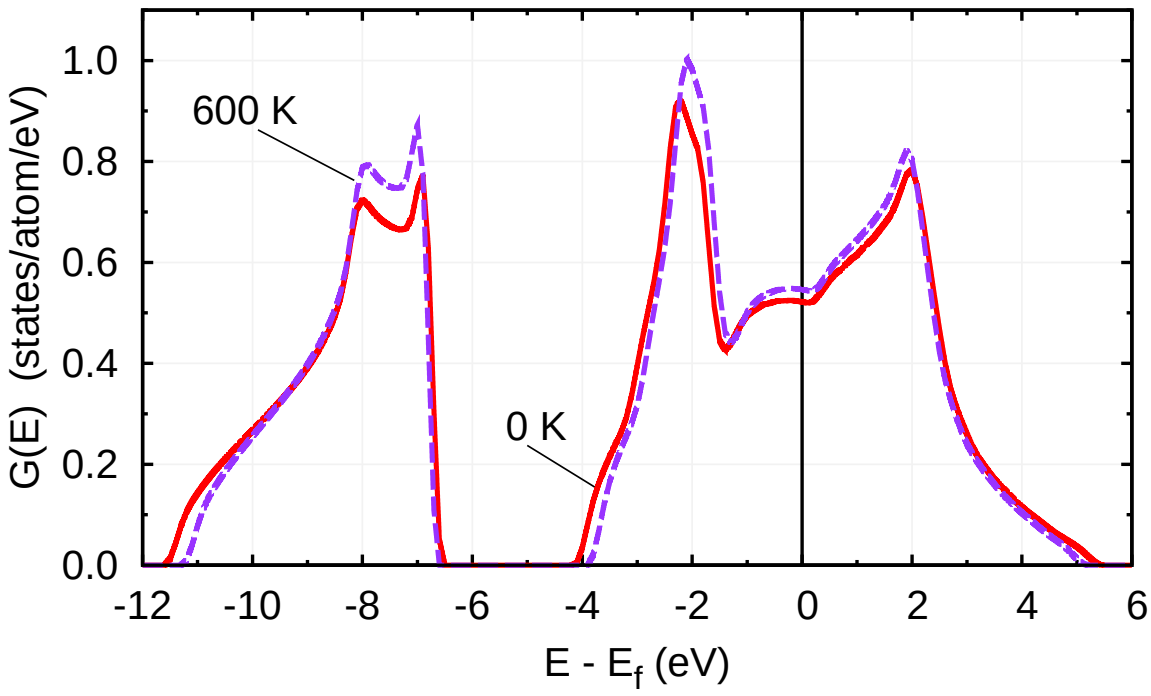

Figure 10.7: Electronic DOS of FCC lead at 0 K and 600 K, showing the effects of the expansion of the lattice with increasing temperature. E_{f} is the Fermi energy.

10.4 Results

Given the difficulties with the measurement of the background outlined in § 10.3.3, we will begin by comparing information culled from the current experiment with other experimental data.

Brockhouse *et al.* made extensive measurements of the phonons in lead at 100 K [154], and less extensive measurements at 213, 296, 425, and 570 K. [155] They found that the phonon energies in lead decreased with increasing temperature. This is at least somewhat at odds with the values of Δ^{s} or $\langle E\rangle_T/\langle E\rangle_{18}$ presented in Table 10.1, which seem to increase slowly, but steadily, with increasing temperatures. On the other hand, Brockhouse *et al.* find interplanar force constants for the 1NN planes that only decrease slightly as a function of temperature. These force constants are frequently most responsible for phonon softening in metals, as was the case in aluminum, and as we will see in nickel, iron, and many other metals. (See Chaps. 9, 11, 12 and 14.) More generally, they find that with increased temperature, the longitudinal modes decrease in frequency more slowly than the transverse modes. Looking at the fits in Fig. 10.5 we can see a similar effect at the highest temperatures.

Stedman *et al.* have measured phonons in lead at 80 and 300 K, [157], although the lower temperature measurement was much more extensive. To compare our measurements with theirs, we

Table 10.2: Characteristic temperatures from the phonon moments of lead, calculated using Eq. 10.7, Eq. 10.8, and the experimentally determined phonon spectra. Values are all given in degrees Kelvin. Wallace's values [37] are taken from the experimental data of Stedman *et al.* [121].

Characteristic temperature	Current work	Wallace & Stedman
$\overline{T}_0$	63.7	64.1
$\overline{T}_1$	91.3	91.3
$\overline{T}_2$	93.5	93.4

introduce moments and characteristic temperatures of the phonon spectrum:

$$\begin{aligned} \overline{\omega}_j &= \left[\tfrac{j+3}{3}\int_0^\infty \omega^j g(\omega)d\omega\right]^{\frac{1}{j}} , \qquad j > -3, j \neq 0 , \\ \overline{\omega}_0 &= \exp\left[\tfrac{1}{3}\int_0^\infty \ln(\omega) g(\omega)d\omega\right] , \end{aligned} \tag{10.7}$$

$$\begin{aligned} \overline{T}_j &= \tfrac{\hbar\overline{\omega}_j}{k_{\mathrm{B}}} , \qquad j > -3, j \neq 0 , \\ \overline{T}_0 &= \tfrac{\hbar\overline{\omega}_0}{k_{\mathrm{B}}} e^{-\frac{1}{3}} . \end{aligned} \tag{10.8}$$

Values of $\overline{T}_0$, $\overline{T}_1$, and $\overline{T}_2$ from the 88 K DOS of the current experiment and from the DOS determined by Stedman *et al.* at 80 K are shown in Table 10.2. The agreement is excellent. The difference in $\overline{T}_0$ is explained by the fact that both measurements are most error prone at low energies. In particular, the current measurements require removal of a large elastic peak to find the inelastic scattering at low energies. In a few specific directions, Stedman et al. found that the frequencies of the high Q (usually higher energy) modes tended to increase with temperature, whereas those at lower Q (usually lower energy) tended to decrease. This corresponds with what we see in Fig. 10.5, where the modes to the left of the first dashed vertical line appear to be moving to lower energies, and those to the right of the second dashed line are moving to higher energies.

On the other hand, agreement with the measurements of Furrer and Hälg [158] is not as good — at least with respect to the phonon shifts. They have measured phonons in lead over the entire (110) plane at 5, 80, and 290 K. We find ratios $\langle E\rangle_{88}/\langle E\rangle_{18} = 1.017$ and $\langle E\rangle_{300}/\langle E\rangle_{18} = 1.019$ as compared to $\langle E\rangle_{80}/\langle E\rangle_{5} = 0.982$ and $\langle E\rangle_{290}/\langle E\rangle_{5} = 0.940$ found by found by Furrer and Hälg. It should be noted that the measurements of Furrer and Hälg covered only a single plane in reciprocal space, whereas ours cover its entirety. Further, since our 88 K DOS is in excellent agreement with that of Stedman *et al.*, and our estimate of the background is probably best at 18 K, it seems that the ratio of the mean phonon energies for these temperatures is probably not off by the 3% required for agreement with Furrer and Hälg.

In the same experiment, Furrer and Hälg also measured phonon linewidths. Additionally, Habicht *et al.* made neutron spin-echo measurements of linewidths of a few low energy modes at 5, 10, 15,

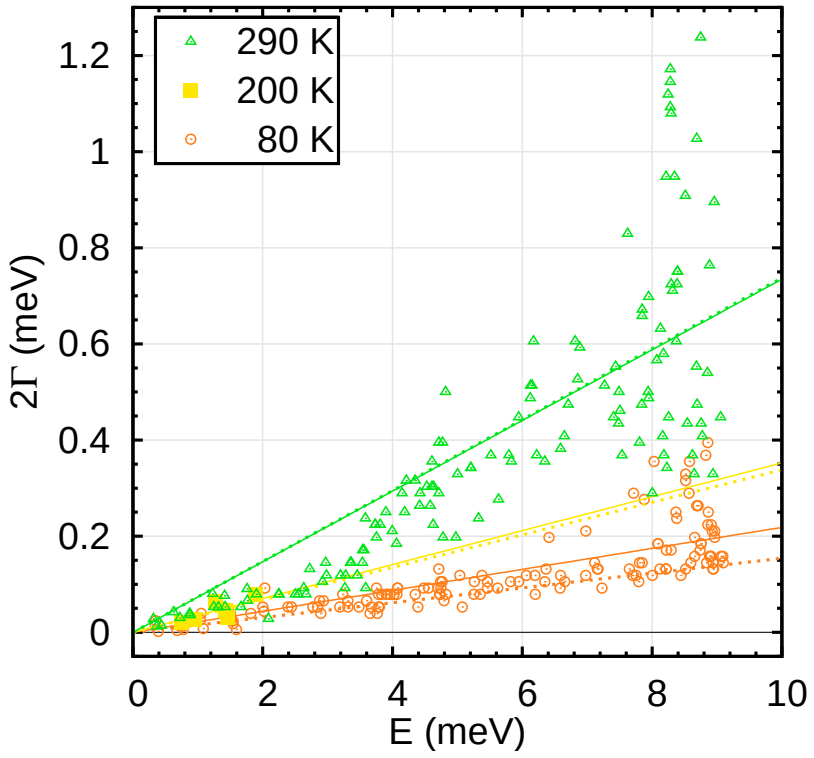

Figure 10.8: Markers show phonon full width at half maximum, 2Γ as a function of phonon energy, at temperatures as given in the key, taken from the triple axis and neutron spin echo measurements of Furrer and Hälg and of Habicht *et al.* [58, 158] The solid lines are linear fits to the (combined) data, the slope of which give $1/\mathcal{Q}$. The dotted lines have slopes $1/\mathcal{Q}$ taken from fits of the data from the current experiment at 88, 163, and 300 K using Eqs. 10.3, 10.4 and 10.5.

Table 10.3: Quality factors for lead from the linear fits in Fig. 10.8

Current work		Furrer & Hälg, Habicht *et al.*	
T (K)	$\mathcal{Q}$	T (K)	$\mathcal{Q}$
88	64.9	80	45.8
163	29.6	200	28.4
300	13.6	290	13.6

50, 100, 150, 200, and 300 K. [58] We have combined the measurements from the two sources at 80 and 100 K, and at 290 and 300 K. These and the linewidths at 200 K are plotted as a function of phonon energy in Fig. 10.8, as are linear fits to the data. These fits give the quality factors, $\mathcal{Q}$, via the relationship:

$$\frac{1}{\mathcal{Q}} = \frac{2\Gamma}{E} \,. \tag{10.9}$$

The values of $\mathcal{Q}$ for 88, 163, and 300 K are shown in Table 10.3 At the lowest temperature, the

agreement is fair. This is mainly because the triple axis and neutron spin echo measurements are sensitive to the intrinsic phonon linewidths, whereas ours are not. At higher temperatures, the intrinsic contributions to the phonon linewidths become negligible, and the agreement is excellent. On the other hand, at temperatures above 300 K we have no data with which to compare ours. Further, our high temperature measurements were made in the furnace rather than the CCR, and the assumed background is even more problematic.

Zoli has performed a theoretical investigation of the shifts and widths of phonons in lead at a few temperatures. [63] He finds shifts between 5 and 80 K that are even larger than those found by Furrer and Hälg; i.e., in even greater disagreement with our measurements. At room temperature, he finds $2\Gamma/E \approx 0.2$, which is almost 3 times the value we find, 0.074. Additionally, he finds a linear temperature dependence of the phonon linewidths between 80 and 300 K; whereas we find a temperature dependence of $1/\mathcal{Q}$ that is somewhere between linear and quadratic. This can be seen in Fig. 10.6. The temperature dependence here is not nearly as strong as that seen in aluminum in Chapter 9.

10.5 Discussion

Fig. 10.9 shows the various contributions to the entropy of lead. In increasing order of magnitude, we have contributions of monovacancies and divacancies, negative contributions from electron-phonon interactions, contributions from noninteracting electrons and anharmonic phonons, the contribution of harmonic phonons, and the sum total of all these.

As expected, the largest contribution to the total comes from the phonons, and this is shown in the top panel of Fig. 10.9. This contribution was calculated by interpolating between the spectra measured at 18, 88, 163, 300, 390, and 500 K and then using the interpolated g_T in the quasiharmonic formula for the phonon entropy:

$$S_{\mathrm{ph}} = 3k_{\mathrm{B}} \int g_T \left[(n_T + 1) \ln(n_T + 1) - n_T \ln(n_T) \right] dE \,, \tag{10.10}$$

where $n_T = \frac{1}{e^{\beta E} - 1}$ is the mean occupation number for bosons. The vast majority of this entropy comes from the harmonic oscillations of the lead atoms about their equilibria, and this contribution can be calculated by using the DOS from 18 K, g_{18}, instead of g_T in Eq. 10.10 This is also shown in Fig. 10.9, and it makes up more than 98% of the total phonon entropy at melting.

The next largest contributions to the entropy are the phonon entropy of dilation and the non-harmonic phonon entropy, $S_{\mathrm{ph,D}}$ and $S_{\mathrm{ph,NH}}$, respectively. Both are shown in the center panel of

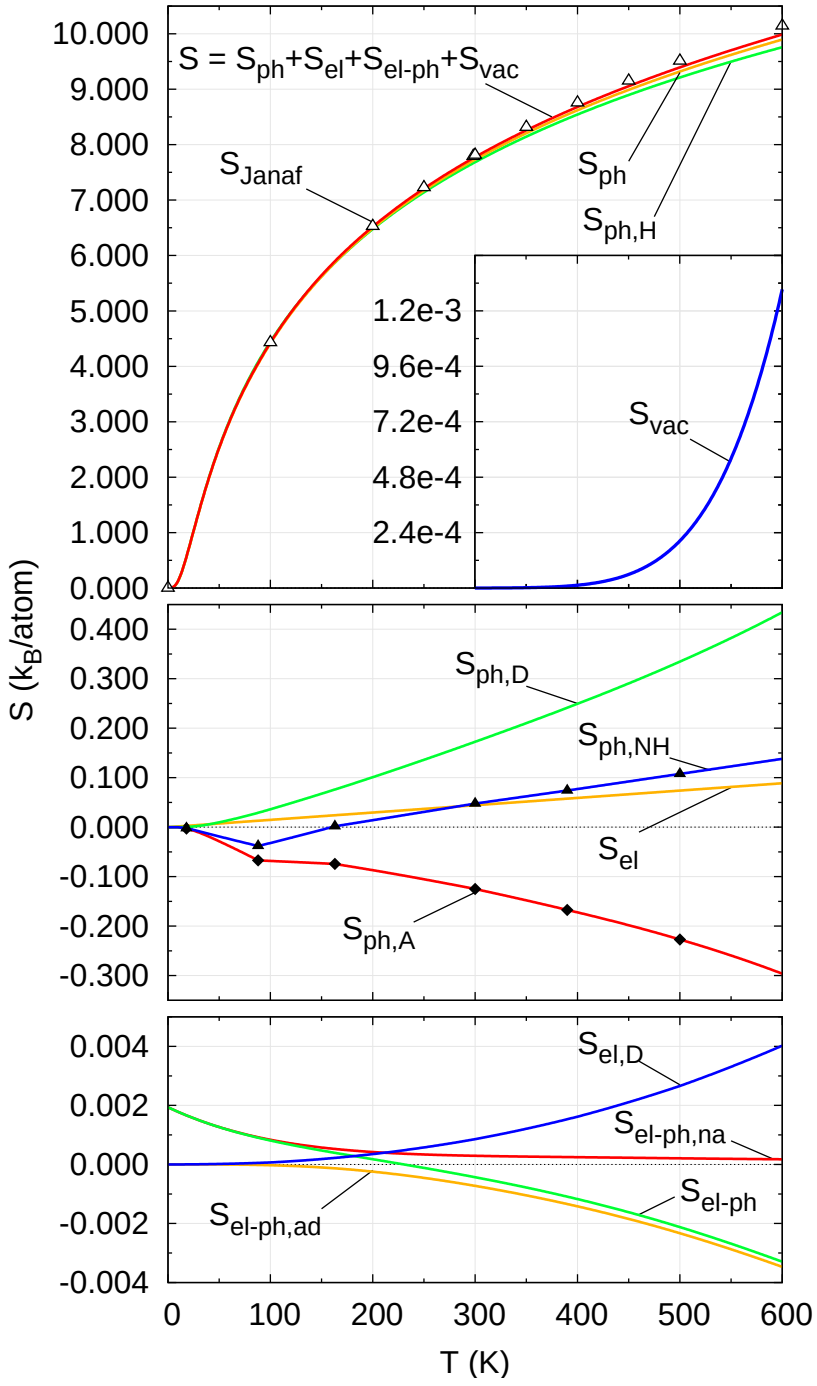

Figure 10.9: Contributions to the entropy of lead as a function of temperature. The temperature labels at the bottom of the plot apply to all panels and the inset. Open triangles are total entropy data taken from the NIST-JANAF thermochemical tables. Closed markers are data from the current experiment; lines are either calculations or interpolations.

Fig. 10.9. We have determined the former using the thermodynamic relationship:

$$S_{\mathrm{ph,D}} = \int_0^T \frac{9K_T\alpha^2}{\rho_N} dT' \,, \tag{10.11}$$

with values for the thermal expansion, α, of lead from Touloukian *et al.* [168] and the isothermal bulk modulus, K_T, from Cordoba and Brooks. [169] The latter is determined by taking the difference of the total phonon and harmonic phonon entropies, $S_{\mathrm{ph,NH}} = S_{\mathrm{ph}} - S_{\mathrm{ph,H}}$. If the only effects of anharmonicity are the expansion of the lattice against the bulk modulus, these two contributions should be equal. This is clearly not the case in lead, as can be seen by looking at the difference between these two, the anharmonic phonon entropy $S_{\mathrm{ph,A}} = S_{\mathrm{ph,NH}} - S_{\mathrm{ph,D}}$. We find the anharmonic entropy to be negative at all temperatures. At higher temperatures, it is of moderate magnitude, reaching $-0.23 k_{\mathrm{B}}$/atom at 500 K. Through an analysis of heat capacity measurements and other bulk thermodynamic properties, Leadbetter finds values of the anharmonic entropy of roughly -0.06 or -0.15 k_{B}/atom depending on whether he uses the 0- or ∞-temperature values for the electron-phonon enhancement factor. [34] Either of these is smaller than our value; however, the latter is of the same order of magnitude, and both have the same sign. Cordoba and Brooks get $S_{\mathrm{ph,A}} \approx -0.2$ k_{B}/atom at 500 K, which is in closer agreement with our measurement. [170] Both of these papers find a decrease in the magnitude of the anharmonic entropy between 500 K and melting; therefore, the extrapolations between 500 and 600 K in Fig. 10.9 should be regarded with some suspicion. That said, it seems likely that the anharmonic entropy at melting found by Wallace, $S_{\mathrm{ph,A}} = -0.04$ k_{B}/atom, is too small in magnitude. [37]

At roughly the same order of magnitude, we have the entropy for non-interacting electrons, which can be determined using the electron DOS shown in Fig. 10.7 and the following formula:

$$S_{\mathrm{el}} = -k_{\mathrm{B}} \int G_T \left[f_T \ln(f_T) + (1 - f_T) \ln(1 - f_T) \right] dE \,, \tag{10.12}$$

where $f_T = \frac{1}{e^{\beta(E-\mu)}+1}$ is the mean occupation number for bosons, and the chemical potential μ was determined using $N_{\mathrm{el}} = \int G_T(E) f_T(E) dE$. This contribution is also shown in the central panel of Fig. 10.9. As expected in a nearly free electron metal, this contribution to the entropy is approximately a linear function of temperature.

Nearly an order of magnitude smaller are the contributions to the entropy from the interactions of the electrons and phonons, and these are shown in the bottom panel of Fig. 10.9. These were found using the free energies for non-adiabatic and adiabatic electron-phonon interactions calculated by Bock *et al.* and the identity $S = -\frac{\partial F}{\partial T}$. [26, 28] The non-adiabatic contribution, $S_{\mathrm{el-ph,na}}$, accounts for the effects of the finite velocities of the nuclei, and is dominant at the lowest temperatures. This is a positive contribution to the entropy, and is frequently quantified as a multiplier on the electronic heat capacity at low temperatures. The adiabatic contribution, $S_{\mathrm{el-ph,ad}}$, accounts for the displacements of the nuclei from their equilibria, and dominates at higher temperatures. This provides a negative contribution to the entropy. The total contribution of electron-phonon interactions is their sum, $S_{\mathrm{el-ph}} = S_{\mathrm{el-ph,na}} + S_{\mathrm{el-ph,ad}}$, and this is also shown in the bottom panel Fig. 10.9, along with

Table 10.4: Formation energies and entropies for monovacancies and divacancies in lead after Cordoba and Brooks. [170]

Defect	$\Delta H_{\mathrm{vac,f}}$ (eV)	$\Delta S_{\mathrm{vac,f}}$ (k_{B})
monovacancy	0.52	1.0
divacancy	0.96	1.5

the contributions of the expansion of the lattice to the electronic entropy, $S_{\mathrm{el,D}}$. Given that lead is a superconductor up to 7.2 K, it is perhaps surprising that these contributions are so small, and further work verifying the size of this contribution is desirable.

The smallest contribution to the entropy comes from vacancies, and this is shown in the inset of Fig. 10.9. This contribution was determined using the values of the formation energies and entropies for monovacancies and divacancies from Cordoba and Brooks which are shown in Table 10.4. [170] Equations for the heat capacities of these defects are also given by Cordoba and Brooks, [171] and these were integrated to get the following expressions for the entropy:

$$S_{\mathrm{vac},1} = k_{\mathrm{B}} \left(\beta \Delta H_{\mathrm{vac,f},1} + 1\right) \exp\left(\frac{\Delta S_{\mathrm{vac,f},1}}{k_{\mathrm{B}}}\right) \exp\left(-\beta \Delta H_{\mathrm{vac,f},1}\right) , \tag{10.13}$$

$$S_{\mathrm{vac},2} = 6k_{\mathrm{B}} \left(\beta \Delta H_{\mathrm{vac,f},2} + 1\right) \exp\left(\frac{\Delta S_{\mathrm{vac,f},2}}{k_{\mathrm{B}}}\right) \exp\left(-\beta \Delta H_{\mathrm{vac,f},2}\right) , \tag{10.14}$$

where the value 6 in the second equation is half the coordination number for FCC lead. The value shown in the figure, S_{vac}, is the sum of these two contributions. We note that the contribution from divacancies is negligible at all temperatures.

Finally, we discuss the total entropy of lead. The values of the total entropy shown as triangles in the top panel of Fig. 10.9 are taken from the NIST-JANAF thermochemical tables. [136] Also plotted is the sum of the phonon, electron, electron-phonon, and vacancy contributions to the entropy as determined in the current work, $S = S_{\mathrm{ph}} + S_{\mathrm{el}} + S_{\mathrm{el-ph}} + S_{\mathrm{vac}}$. The agreement is excellent up to 300 K, and is quite good all the way to melting, with a maximum deviation of -1.6% at melting. Here we will consider currently the discrepancy at 500 K to avoid extrapolation. The anharmonic entropy at 500 K is $S_{\mathrm{ph,A}} = -0.23\ k_{\mathrm{B}}$/atom, and the difference between our total entropy and that given by NIST-JANAF is $\Delta S = -0.12 k_{\mathrm{B}}$/atom. This suggests that if our determination of the anharmonic entropy is off by a roughly factor of two, the discrepancy in the total entropy vanishes. It is difficult to rule out this possibility, given the difficulties with the background outlined in § 10.3.3. Another possible source of error is the electron-phonon interaction at high temperatures. This is plausible, as lead has a fairly high critical temperature for an elemental superconductor, and is thus known to have reasonably strong electron-phonon interactions at low temperatures. In particular, it is only recently that large, adiabatic electron-phonon effects at high temperatures have been seen experimentally in vanadium and its alloys. [40, 41] In these studies, the electron-phonon interactions

were expressed as a smearing of the electron DOS at the Fermi level; however, looking at Fig. 10.7 its clear that the smearing would have to be very large in order to have a significant impact.[f]

10.6 Summary

Measurements of the inelastic scattering of neutrons by phonons in lead were made at temperatures of 18, 38, 63, 88, 113, 137, 163, 188, 300, 390, and 500 K, and detailed comparisons to previous measurements were made. Phonon DOS were obtained from the reduced experimental data, and were used to determine the harmonic, nonharmonic and total phonon entropy of lead. The sum of the phonon, electronic and vacancy contributions to the entropy agree well with accepted values for the total entropy up to half the melting temperature, and there is fair agreement for the rest of the range of temperatures studied. The anharmonic entropy obtained from the shifts of phonon frequencies, $S_{\mathrm{ph,A}} = -0.23 k_{\mathrm{B}}/\mathrm{atom}$, was negative and larger than expected. Finally, the broadening of the phonon DOS was significant, scaling superlinearly with temperature.

[f]The formalism used in the cited papers applies a Lorentzian broadening to the electron DOS. In order for this to have a significant effect, the full width at half max for the Lorentzian would have to be larger than an electron-volt.

Chapter 11

Nickel

11.1 Introduction

Nickel is a ferromagnetic 3d transition metal commonly used in industrial and consumer products including stainless steels, corrosion resistant alloys, magnets, coins, and batteries. In addition to general scientific interest in nickel, [67, 172–179], its magnetic properties have been the subject of a large number of experimental [27, 180–187] and theoretical [45, 188–192] studies; particularly because the nature of magnetism in nickel is only partially explained by either localized or itinerant electrons models; [193–200] At low temperatures, observations of the d-electron Fermi surfaces in nickel show that the magnetic electrons are itinerant in nature. [193] The behavior at high temperatures, however, is not easily understood in an itinerant electron model. Specifically, it is well known that spin excitations persist well above the Curie temperature of nickel, $T_C = 631\ K$, [201–205] and that they make significant contributions to the entropy and heat capacity at high temperatures. [31, 36, 37]

In their studies of the entropy of nickel at high temperatures, Wallace [37] and Eriksson *et al.* [36] divided the electronic entropy into a contribution from the non-interacting, non-magnetic electrons, $S_{\mathrm{el,NM}}$, and a contribution from magnetism, $S_{\mathrm{el,M}}$,[a] such that:

$$S_{\mathrm{el}} = S_{\mathrm{el,NM}} + S_{\mathrm{el,M}} \ . \tag{11.1}$$

They determined $S_{\mathrm{el,G}}$ through an ab-initio electronic structure calculation, and used it to make an estimate of the sum of the anharmonic phonon and the magnetic entropies:

$$S_{\mathrm{ph,A}} + S_{\mathrm{el,M}} = S - S_{\mathrm{ph,H}} - S_{\mathrm{ph,D}} - S_{\mathrm{el,NM}} \ . \tag{11.2}$$

They are, however, unable to separate the two terms on the left hand side of this equation. Meschter, *et al.*, have performed a similar analysis of the heat capacity of nickel, also estimating the anharmonic

[a] They call these S_{el} or S_{EP} and δS_M, respectively.

contributions to the entropy.[31]

By measuring the phonon DOS at high temperatures, we are able to determine precisely the anharmonic contribution to the total entropy of nickel. Previous measurements of the phonon dispersions in nickel were reported by Birgeneau, Cordes, Dolling and Woods; Hautecler and Van Dingenen; and de Wit and Brockhouse;[206–208] but all these studies were confined to temperatures between 296 K and 676 K. The purpose of de Wit and Brockhouse's measurements was not specifically to investigate phonon thermodynamics, but rather to look for changes in the phonon modes as the metal went through the Curie transition at $T_C = 631$ K. They reported little change in the phonons through the magnetic transition, and shifts in the phonon energies that were largely consistent with a quasiharmonic model. They also reported significant broadening of the phonon peaks with increasing temperature, which they suggested may be due to interactions of magnetism with the lattice.[208]

Zoli, *et al.*, investigated the broadening of phonons in face-centered cubic (FCC) noble metals and aluminum.[64] Using force constants from Born–von Kármán fits to neutron data and third-order elastic constants, they calculated the full width at half maximum, 2Γ, of the phonon peaks. For aluminum and the noble metals, broadening of the phonon peaks is of course not caused by magnetism, but by phonon-phonon interactions that shorten phonon lifetimes. The coupling of phonon modes is also responsible for the expansion of the lattice; however, the quasiharmonic model does not necessarily offer a method of rationalizing the observed decrease in phonon lifetimes.

In the present research we measured the inelastic scattering of neutrons from elemental nickel from 10 K to 1275 K, which is about 75% of the melting temperature. We discuss the modest shifts of the phonon energies as well the large broadening of phonon peaks at elevated temperatures. The phonon DOS are used to calculate the anharmonic contribution to the entropy, and this is used to bound the value of the magnetic entropy at high temperature. Finally, we evaluate other phonon and electron contributions to the entropy.

11.2 Experiment

11.2.1 Sample preparation

Ingots of 99.98% pure nickel were cold-rolled to a thickness of 0.45 mm. At this thickness, 10% of the incident neutrons are scattered by the sample. The cold-rolled pieces were then cut into strips, and annealed at 1075 K in evacuated quartz tubes for 16 hours to relieve stress and induce recrystallization. There were no signs of oxidation on the annealed strips.

11.2.2 Neutron scattering measurements

Inelastic neutron scattering measurements were performed with the Pharos time-of-flight direct-geometry chopper spectrometer at the Los Alamos Neutron Science Center at temperatures of 10 K, 300 K, 575 K, 875 K, and 1275 K. For the 10 K and 300 K measurements, the strips of nickel were laid flat in a thin-walled aluminum pan, which was then mounted on a closed-cycle refrigerator. For higher temperatures a niobium pan was used, and the sample was mounted in a vacuum furnace built by A.S. Scientific. Several thermocouples were used to monitor the temperature of the sample, and it is estimated that the temperature deviations in the sample were no more than 5 K. Measurements of the empty sample pans were also performed at all temperatures.

Details about the Pharos spectrometer at Los Alamos have been given in § 6.4. At the time of the experiment, the 6 atm pressure detectors were located at the lower, and the 10 atm at the higher scattering angles. The time bins were spaced every 2.5 μs from 5500 μs to 9000 μs. Data were collected for a minimum of four hours at each temperature, giving on the order of one million counts. The nominal incident energy was 70 meV, and the incident energies calculated from the data ranged from 69.3 meV to 69.6 meV. The experimentally determined resolution of the instrument (full width at half maximum) was approximately 2.5 meV at the elastic line, and 1.0 meV at the high energy cutoff of the phonon DOS ($\sim$40 meV).

11.3 Data analysis and computation

Details of the data reduction procedures used here are given in Chapter 7, with rebinning described in § 7.4.1. The correction for multiple- and multiphonon scattering was described in § 8.1.2. For diffraction, determination of the quality factors, and fitting of BvK models, see § 8.4, § 8.2, and § 8.3.1.2, respectively.

11.3.1 General data reduction

The measured spectra, in time of flight, detector number, and pixel were first corrected for the efficiencies of the detectors. This was done using a room temperature measurement of pure vanadium, a fully incoherent scatterer, for calibration. Next, the time of flight independent background was estimated as an average over a region in time of flight having no appreciable scattering from the the sample or the environment and subtracted. The corrected data were normalized by the integrated proton current and converted to intensity, $I(\Theta, E)$, by rebinning into scattering angles, Θ, ranging from 5° to 145° with a binwidth of 0.5° and energy transfers, E, from -65 meV to 65 meV with a bin width of 0.5 meV. The scattering from the empty pans was subtracted from the data, scaled by 90% to account for the self-shielding of the sample.

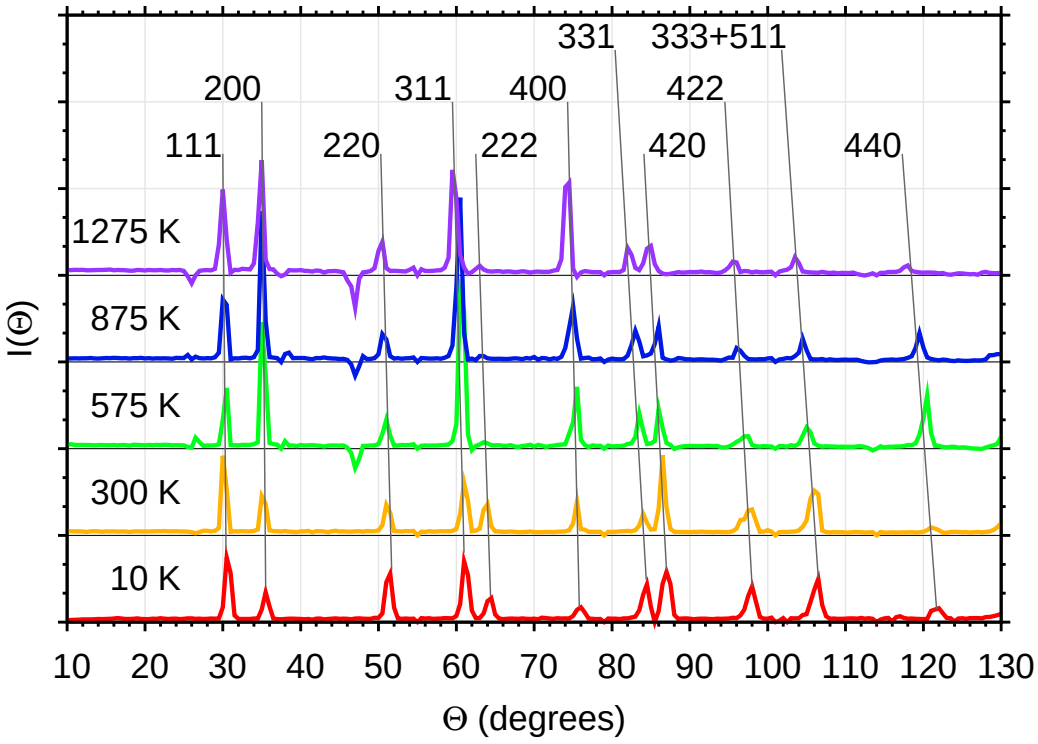

Figure 11.1: Diffraction patterns from nickel, taken in-situ at temperatures as labeled. The quality of the patterns taken above room temperature is reduced due to the increased background of the furnace.

11.3.2 Elastic scattering: in-situ neutron diffraction

The scattering with energy transfers between −2.5 meV and 2.5 meV was used to obtain diffraction patterns from nickel, as shown in Fig. 11.1. Using the Nelson–Riley plots [104, 105] shown in Fig. 8.9, the lattice parameter, a, was found at all measured temperatures. These are listed in Table 11.1, and agree with values of the lattice parameter calculated using the accepted temperature dependent linear coefficient of thermal expansion[168] and room temperature lattice parameter.[209]

In addition to those shown in Fig. 11.1, diffraction patterns were obtained without the furnace at incident neutron energies of 30 meV, 50 meV, and 70 meV, with the 222 peak at 108°, 78°, and

Table 11.1: Experimentally determined lattice parameter, a, of nickel and shifts of the nickel phonon energies as a function of temperature. Fits using a damped oscillator function and Eq. 11.4 yield Δ^s, $\langle E_T\rangle/\langle E_{10}\rangle$ was calculated with Eq. 11.6.

T (K)	$a \pm 0.005$ (Å)	Δ^s	$\langle E\rangle_T/\langle E\rangle_{10}$
10	3.513	1.000	1.000
300	3.521	0.988	0.985
575	3.540	0.970	0.963
875	3.559	0.947	0.945
1275	3.585	0.920	0.913

64° in 2θ respectively. These are shown in Fig. 8.8. The ratios of peak intensities remained largely unchanged, showing that the sample did not have substantial crystallographic texture. Sample texture should not affect lattice parameters as determined with Nelson-Riley plots. Regardless, effects of the texture are addressed briefly in Sec. 11.3.5.

11.3.3 Inelastic scattering: S(Q,E) and the density of states

The data were rebinned again to obtain the intensity, $I(Q, E)$, with momentum transfer Q ranging from 0.0 Å^{-1} to 13.5 Å^{-1} with a binwidth of 0.0675 Å^{-1}. Since nickel is ferromagnetic up to the Curie temperature, we excluded scattering at lower momentum transfers, where magnetic scattering is present, to ensure that the scattering from the phonons was dominant. The elastic peak was removed below ∼5 meV, and replaced with a straight line, corresponding to the continuum limit at low energies. The data were then corrected for multiple and multiphonon scattering simultaneously as described in § 8.1.2. The resulting DOS at all temperatures are shown in Fig. 11.2.

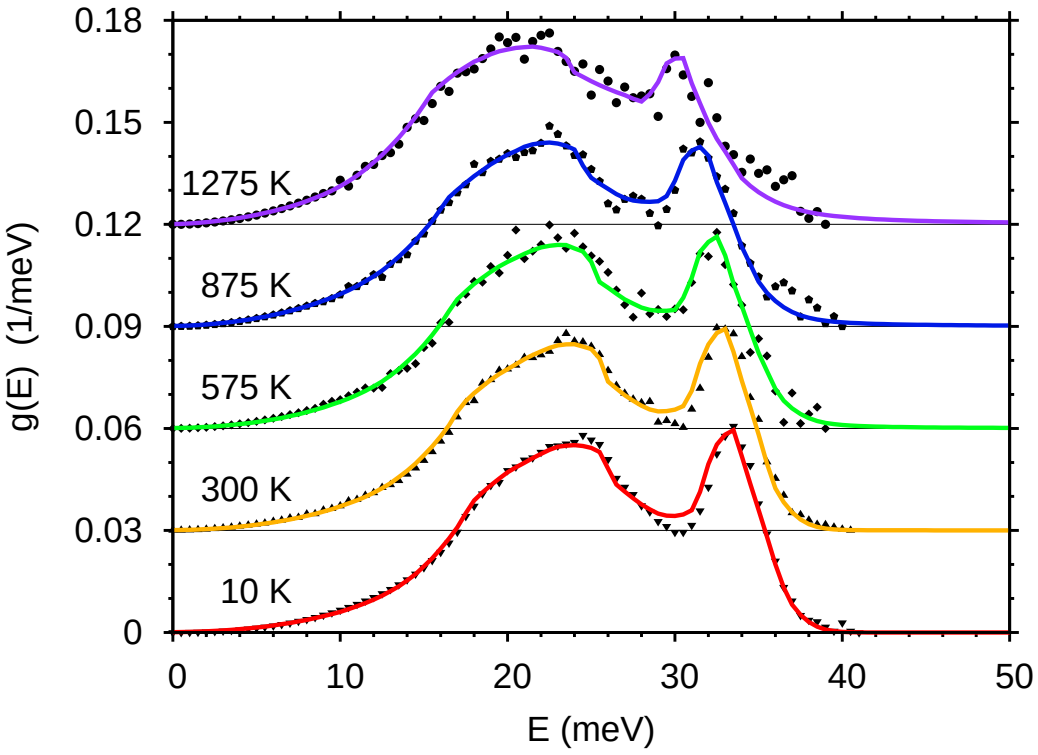

Figure 11.2: Phonon DOS for nickel at temperatures indicated. Markers are experimental data, lines are Born–von Kármán fits. The increase in phonon lifetime broadening and the shifting of modes to lower energies with increasing temperature is evident. The DOS are offset by integer multiples of 0.03 meV^{-1}.

11.3.4 Phonon shifts and broadening

We expect the broadening of the phonons to take the form of a damped harmonic oscillator function,[16, 113, 114] $B(\mathcal{Q}, E', E)$, with central energy E' and width proportional to the phonon energy E:[54]

$$B(\mathcal{Q}, E', E) = \frac{1}{\pi \mathcal{Q} E'} \frac{1}{\left(\frac{E'}{E} - \frac{E}{E'}\right)^2 + \frac{1}{\mathcal{Q}^2}} \,. \tag{11.3}$$

The quality factors, $\mathcal{Q}$, were determined by a least-squares fit. First, the energies of the 10 K DOS were scaled by a factor Δ^{s}. Candidate fits of the hight temperature DOS were then found using:

$$g_T(E) \approx B(\mathcal{Q}, E', E) \odot g_{10}(\Delta^{\mathrm{s}} E') \,, \tag{11.4}$$

where g_{10} is the phonon DOS at the temperature of 10 K, and $\odot$ denotes an integral transform similar to a convolution. The $\mathcal{Q}$ so determined at all temperatures are shown in Fig. 11.3, and the fits to the DOS are shown in Fig. 11.4. Approximately, we find:

$$\frac{1}{\mathcal{Q}} \approx \frac{2\Gamma}{E} \approx 6.816 \times 10^{-8} T^2 \,, \tag{11.5}$$

where T is in Kelvin. The shifts Δ^{s} and the ratios of the mean phonon energies:

$$\frac{\langle E \rangle_T}{\langle E \rangle_{T_0}} \equiv \frac{\int E \; g_T(E) \; \mathrm{d}E}{\int E \; g_{T_0}(E) \; \mathrm{d}E} \,, \tag{11.6}$$

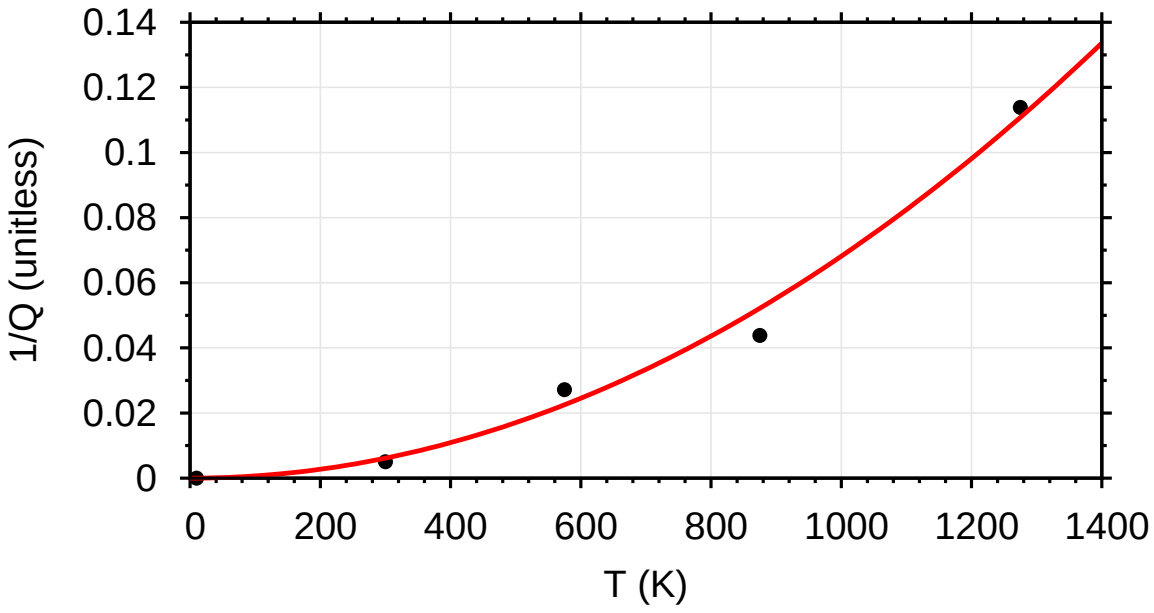

Figure 11.3: Markers show the inverse of the quality factor, $1/\mathcal{Q}$, as a function of temperature for nickel phonons. The line is a fit from Eq. 11.5.

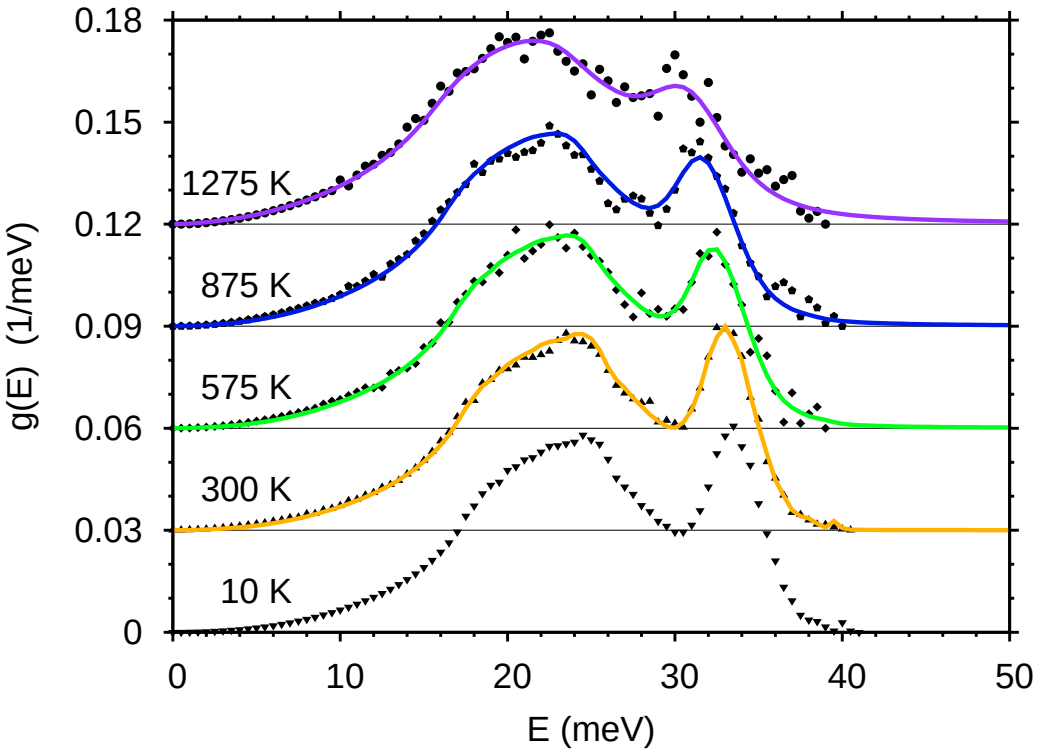

Figure 11.4: Phonon DOS of nickel at temperatures as indicated. Markers are experimental data. The lines are fits to the experimental data, acquired by shifting the 10 K DOS and performing an integral transform the damped oscillator function as a kernel, as described by Eqs. 11.3 and 11.4. The shifts are listed in Table 11.1. The DOS are offset by integer multiples of 0.02 meV^{-1}.

are presented in Table 11.1.

11.3.5 Born–von Kármán models of lattice dynamics

The DOS were fit with a Born–von Kármán model of the lattice dynamics.[71, 72] Force constants out to fifth-nearest-neighbors were optimized using a gradient search method. The fits at all temperatures, after integral transforms with the damped oscillator and the Gaussian instrument resolution functions as kernels, are shown in Fig. 11.2. The optimized force constants are listed in Table 11.2.

As a check on our calculated force constants, and on the effects of sample texture on our determination of the DOS, comparisons were made to the dispersions measured by de Wit and Brockhouse.[208] These are plotted in Fig. 11.5 Our 300 and 575 K models are in reasonable agreement with their 295 and 673 K models, respectively, as are trends in the dispersions with respect to temperature.

11.3.6 *Ab-initio* calculations

In order to investigate electronic contributions to the entropy of FCC nickel, we used the plane-wave code VASP [130, 131] to calculate the electronic DOS as a function of unit cell volume in the non-magnetic state, and as a function of unit cell volume and magnetization in the magnetic state. The non-magnetic and spin-polarized (magnetic) calculations both used projector augmented plane waves and the Perdew-Burke-Ernzerhof generalized gradient approximation. [133] A conventional FCC cell was used, and it was relaxed using the 'accurate' setting for the kinetic energy cutoff, with a $51 \times 51 \times 51$ Monckhorst-Pack q-point grid. [134]

For the non-magnetic case, the relaxed lattice parameter was within 0.05% of the experimentally determined lattice parameter, and was taken to be the 0 K lattice parameter of the unit cell. The values of the linear coefficient of thermal expansion from Touloukian *et al.* [168] were used to determine the corresponding volumes at 631 and 1500 K. The electronic DOS in the non-magnetic state were determined at these two volumes, and are shown in Fig. 11.6.

For the spin polarized case, a ferromagnetic ground state was found. The relaxed lattice parameter was within 0.25% and the magnetic moment was within 1.3% of the experimentally determined values. These were taken to be the 0 K lattice parameter and magnetic moment, and the values of the linear coefficient of thermal expansion from Touloukian *et al.* [168] and of the relative magnetization from Crangle *et al.* [210] were used to fix the corresponding volumes and magnetizations at 0, 480, 556, 594, 618, 625, 628, 630, 631, 1200, and, 1500 K.[b] The electronic DOS of the majority

[b]For example, our values for the lattice parameter and magnetic moment of a conventional FCC Ni unit cell at 0 K were $a_0 = 3.52415$ Å and $\mu_0 = 2.4948$ Bohr magnetons, respectively. At 480 K, we are at 76% of $T_C = 631$ K.

Table 11.2: Optimized tensor force constants in N/m as a function of temperature for FCC nickel. A Cartesian basis is used, where $\langle xyz \rangle$ is the bond vector for the given tensor components.

	$\langle xyz \rangle$	10 K	300 K	575 K	875 K	1275 K
$[\mathbf{K}_1]_{xx}$	$\langle 110 \rangle$	17.584	17.545	16.584	15.910	13.975
$[\mathbf{K}_1]_{xy}$		18.976	18.253	18.822	17.670	16.915
$[\mathbf{K}_1]_{zz}$		−0.391	−0.274	−0.384	−0.316	−0.345
$[\mathbf{K}_2]_{xx}$	$\langle 200 \rangle$	0.975	0.885	1.235	0.920	1.009
$[\mathbf{K}_2]_{yy}$		−0.610	−0.993	−0.551	−0.559	−0.644
$[\mathbf{K}_3]_{xx}$	$\langle 211 \rangle$	0.593	0.442	0.518	0.440	0.850
$[\mathbf{K}_3]_{xy}$		0.378	0.340	0.368	0.441	0.357
$[\mathbf{K}_3]_{yy}$		0.302	0.133	0.220	0.157	0.325
$[\mathbf{K}_3]_{yz}$		−0.120	−0.128	−0.105	−0.092	−0.106
$[\mathbf{K}_4]_{xx}$	$\langle 220 \rangle$	0.386	0.331	0.314	0.262	0.400
$[\mathbf{K}_4]_{xy}$		0.517	0.412	0.502	0.444	0.466
$[\mathbf{K}_4]_{zz}$		−0.218	−0.167	−0.127	−0.153	−0.217
$[\mathbf{K}_5]_{xx}$	$\langle 310 \rangle$	−0.085	−0.065	−0.093	−0.078	−0.092
$[\mathbf{K}_5]_{xy}$		−0.039	−0.047	−0.031	−0.035	−0.028
$[\mathbf{K}_5]_{yy}$		0.006	0.003	0.007	0.004	0.006
$[\mathbf{K}_5]_{zz}$		0.014	0.014	0.014	0.016	0.021

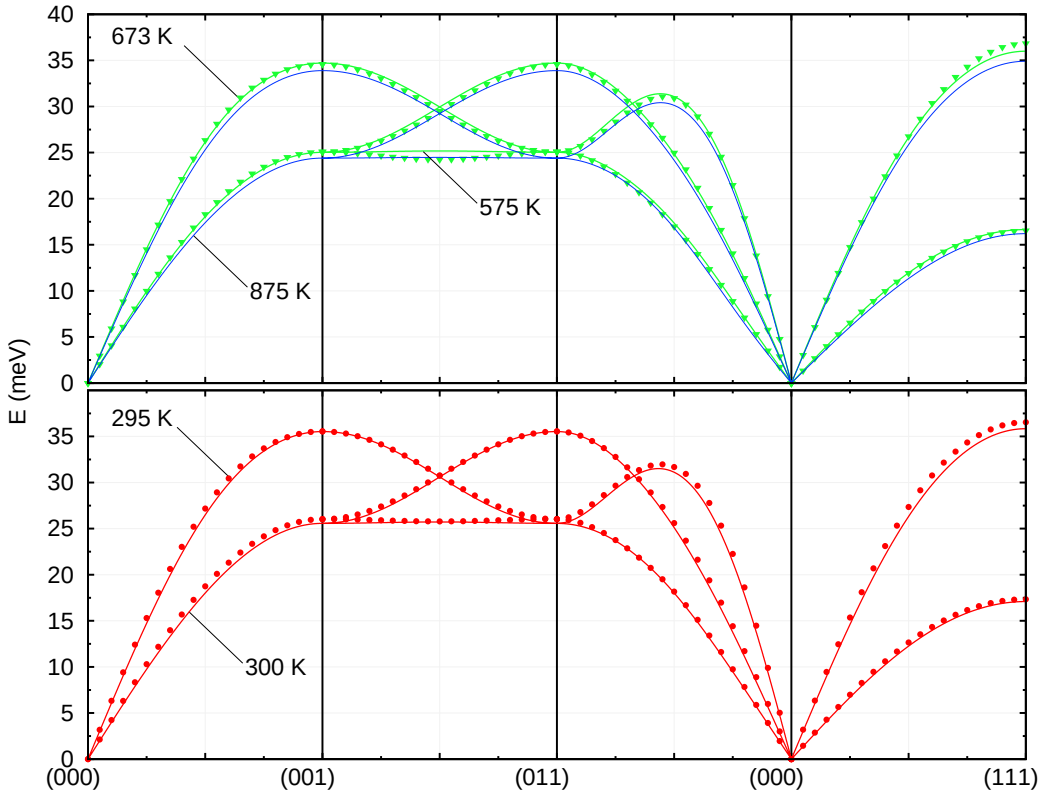

Figure 11.5: Phonon dispersions for nickel from BvK models. Along the bottom of the figure, points ($\mathbf{q}_x\mathbf{q}_y\mathbf{q}_z$) are marked such that zero corresponds to the zone center and 1 to a zone boundary. Paths between these points are linear. Markers show the models of de Wit and Brockhouse[208] at 295 and 673 K, and lines show our models at 300, 575, and 875 K. At the lower temperature, the agreement is quite good with the exception of the phonons near (111). This improves at higher temperatures; however, the phonons between (001) and (011) develop some discrepancies.

and minority spin electrons[c] were determined at these volumes and magnetizations, and those at 0, 625, and 1500 K are shown in Fig. 11.7.

It should be noted that our assumption that the size of the magnetic moments are changing with temperature is wrong. Actually, the size of the magnetic moments is largely temperature-independent, and it is solely their orientations that change with temperature. Nevertheless, this greatly simplified model may help guide our thoughts about the magnetic and non-magnetic contributions of the electrons to the entropy.

Crangle *et al.* report that the magnetization should be 0.7938 μ_0 and Touloukian that the lattice parameter should be 1.005 a_0, so the 480 K simulation was run with the lattice parameter fixed to be 3.5418 Å and the magnetic moment fixed to be 1.9804 Bohr magnetons.

[c] "Majority" or "minority" indicate the spin (up or down) that is carried by the majority or minority of the electrons.

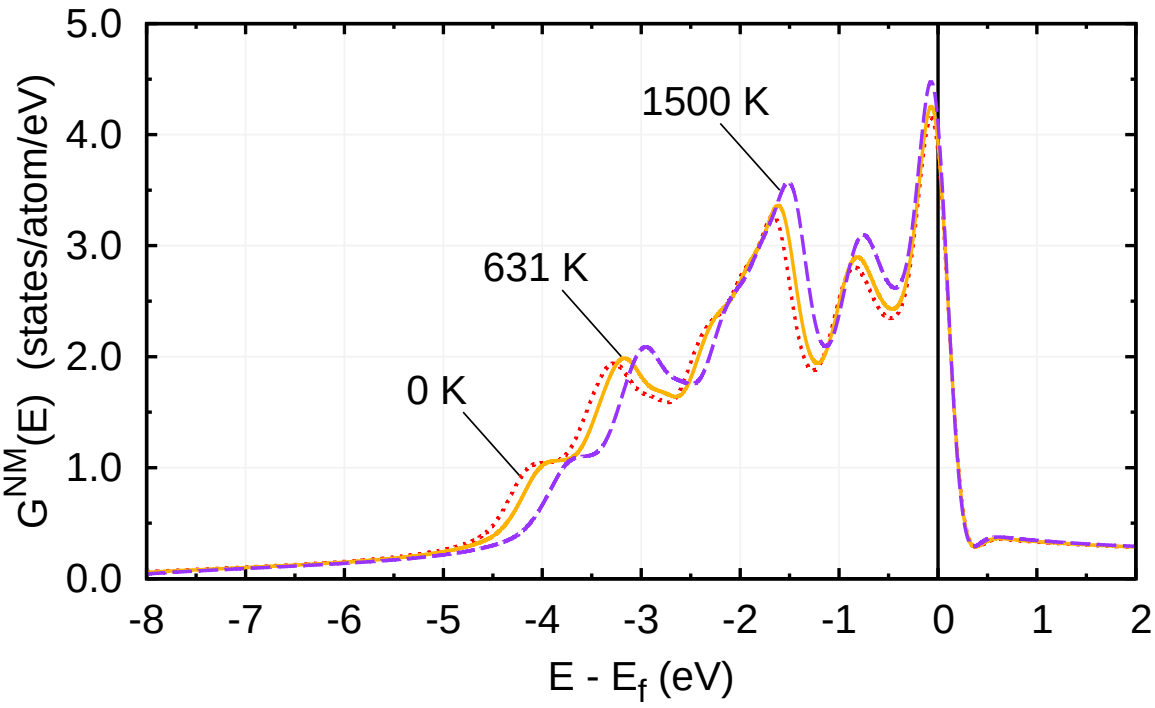

Figure 11.6: Non-magnetic electronic DOS of nickel at temperatures as indicated, calculated as described in the text.

11.4 Results and discussion

At all temperatures, both the longitudinal and the transverse force constants decrease rapidly with nearest-neighbor distance. (These constants were found by diagonalizing the force constant tensors $[\mathbf{K}_X]$, where X corresponds to the XNN shell. The longitudinal force constant was determined by comparison to the projection of $[\mathbf{K}_X]$ onto the bond vector $\langle xyz \rangle$, and the transverse modes were taken to be the remaining two eigenvalues.) Only the first-nearest-neighbor (1NN) longitudinal force constants show a monotonic decrease with temperature, and are almost solely responsible for the shift of the DOS to lower energies with increasing temperature. All longitudinal force constants are plotted in Fig. 11.8.

The softening of the measured phonon DOS is consistent with that found by de Wit and Brockhouse. They found $\langle E \rangle_{573}/\langle E \rangle_{295} = 0.976$,[208] and we find $\langle E \rangle_{575}/\langle E \rangle_{300} = 0.978$. The values of $\mathcal{Q}$ shown in Fig. 11.3 are related to the full widths at half maximum, 2Γ, of the phonon peaks, through the equation $1/\mathcal{Q} \approx 2\Gamma/E$. Values of a similar magnitude were found experimentally for BCC titanium, zirconium, and hafnium,[16, 113, 114] and our 2Γ values are also comparable in magnitude to the values found by Zoli, *et al.*, for phonon-phonon interactions in aluminum and the noble FCC metals.[64] The quadratic form of $1/\mathcal{Q}$ seen in Fig. 11.3 is also consistent with phonon-phonon interactions, if we assume that the damping is proportional to the number of phonons, and that the

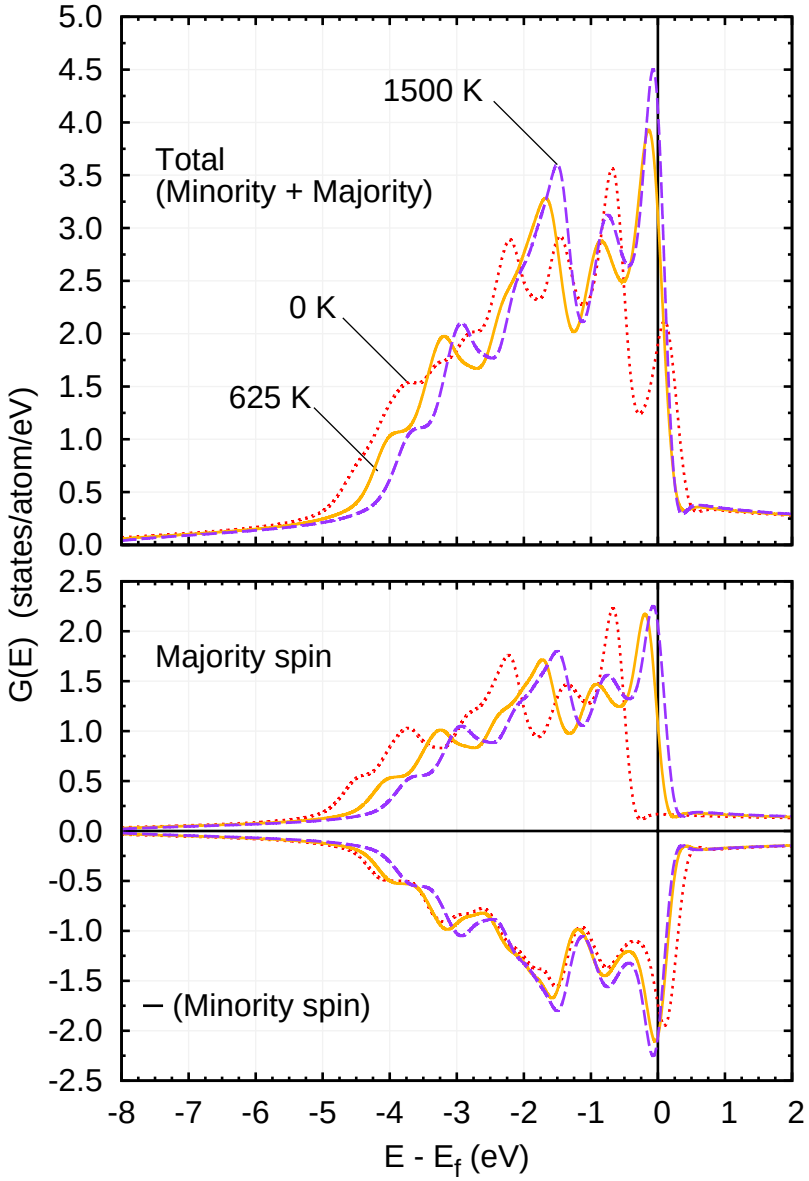

Figure 11.7: Spin-polarized and non-magnetic electronic DOS of nickel calculated as described in the text. In both the top and bottom panels, the red-dotted, yellow, and purple-dashed lines correspond to 0, 625, and 1500 K respectively. The bottom panel shows the DOS for majority and minority spin electrons. As the temperature and volume increase and the magnetization decreases, electronic density accumulates at the Fermi energy. This can be seen in the top panel, where the total density of states at the Fermi level rises by a factor of 2 going from 0 to 1500 K. (Actually, this occurs going from 0 to 631 K, the Curie temperature, as can be seen by comparing the 1500 K DOS shown here with the very similar 631 K DOS shown in Fig. 11.6).

number of phonons is linear in T.

To find the entropy from the softening of the DOS, we use the following expression:

$$S_{\rm ph}(T,T') = 3k_{\rm B}\int_0^\infty g_{T'}\left[(n_T+1)\ln(n_T+1) - n_T\ln(n_T)\right]\,{\rm d}E\,, \tag{11.7}$$

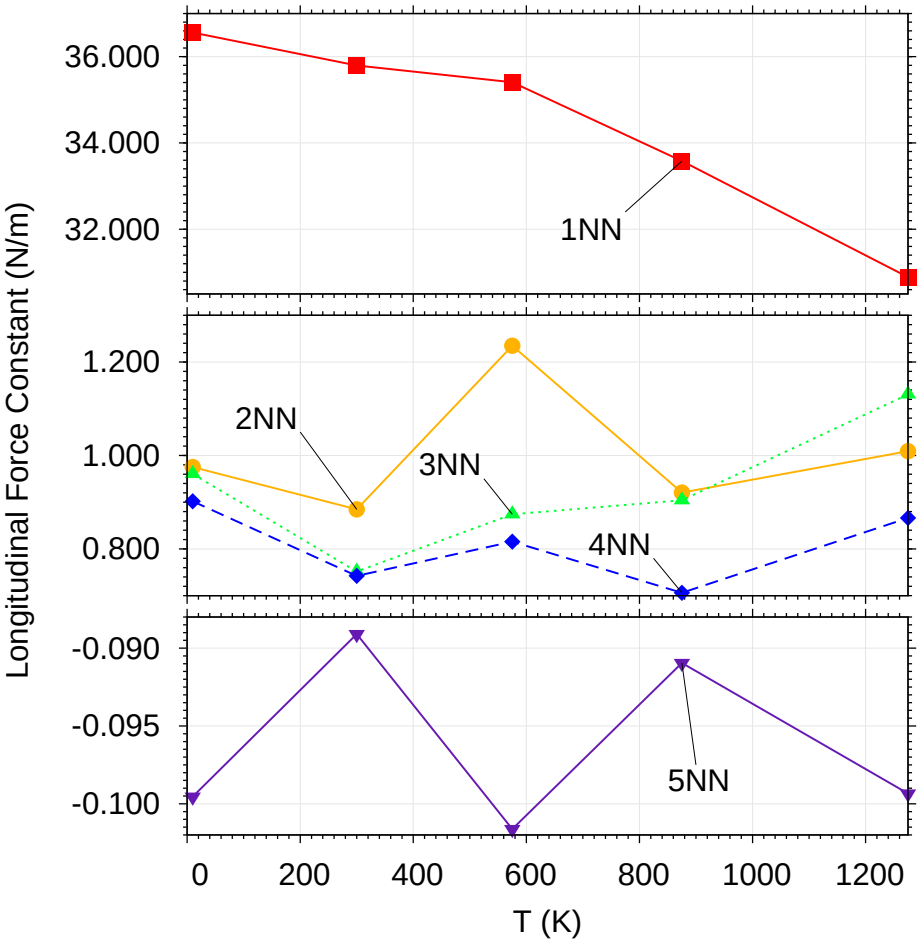

Figure 11.8: Longitudinal force constants for first through fifth-nearest neighbors as indicated.

where $g_{T'}$ is the phonon DOS at temperature T' and n_T is the mean occupancy for bosons at temperature T (both $g_{T'}$ and n_T are functions of E). We seek the change in entropy due to changes in the phonon states, not due to changes in phonon occupancy. We calculate the difference between the total phonon entropy and the harmonic phonon entropy as:

$$S_{\rm ph} - S_{\rm H} = S_{\rm ph}(T,T) - S_{\rm ph}(T,T_0)\ . \tag{11.8}$$

We now compare the entropy of phonon softening to the entropy of dilation. With tabulated data for the elastic constants of nickel,[211] we use:

$$S_{\rm ph,D} = S_{\rm ph,D}(T) = \int_0^T \frac{C_P - C_V}{T'} dT' = \int_0^T \frac{9K_T\alpha^2}{\rho_N} dT'\ , \tag{11.9}$$

with T_0 =10 K, to calculate, $S_{\rm ph,D}$, the entropy of dilation. The center panel of Fig. 11.10 shows

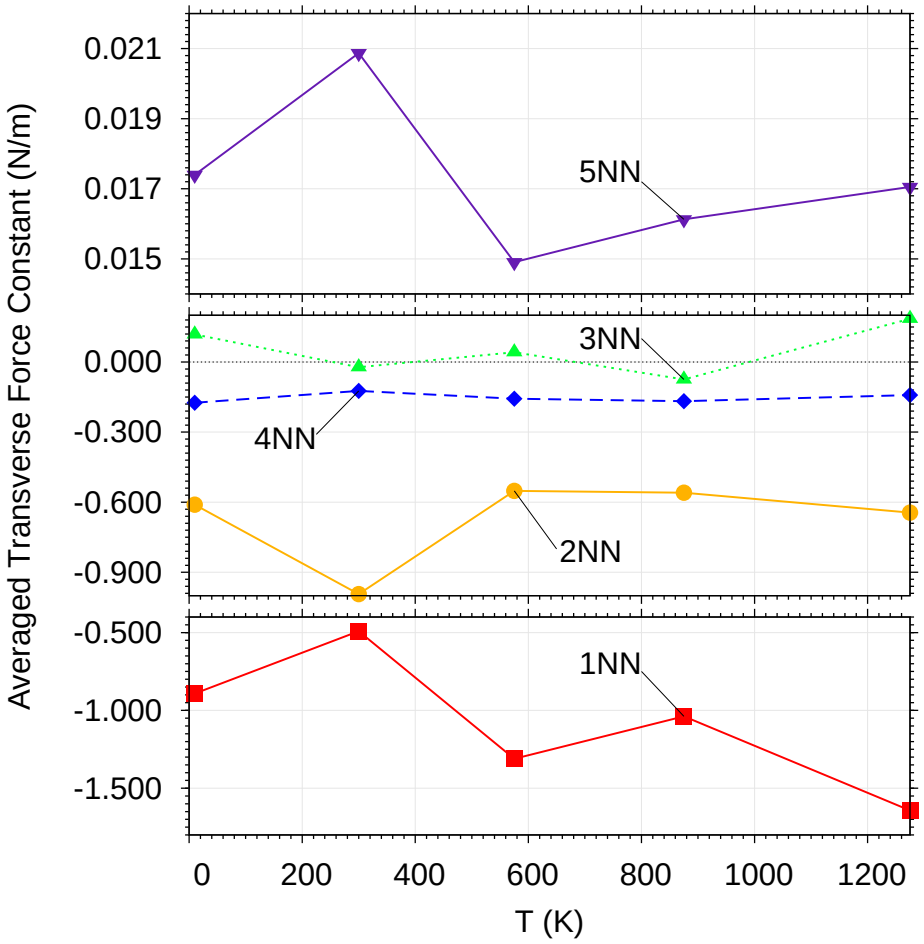

Figure 11.9: Averaged transverse force constants for first through fifth-nearest neighbors as indicated.

the entropy of dilation and $S_{\rm ph} - S_{\rm ph,H}$ as determined with Eqs. 11.7 and 11.8. The agreement is generally good. The anharmonic entropy, shown as a solid line, is the difference between these two contributions. Over the entire temperature range, the anharmonic entropy is bounded by $-0.08 < S_{\rm ph,A} < 0.05$ $k_{\rm B}$/atom, where we have already incorporated our errors of ± 0.02 $k_{\rm B}$/atom. Negative values indicate phonons that are slightly stiffer than they would be if their energies were determined by lattice expansion against the bulk modulus alone. This is nominally the case above 700 K where we have $-0.08 < S_{\rm ph,A} < 0.03$ $k_{\rm B}$/atom. The crossover from positive to negative appears to occur somewhere in the vicinity of the Curie temperature, and the trends in the sign of $S_{\rm ph} - S_{\rm ph,H}$ appear to be consistent over either the ferromagnetic or the paramagnetic regions.

We will now consider the high temperature contributions of the magnetism to the entropy: First, by using values for $S - S_{\rm ph}$ and for $S_{\rm el}$ taken from Wallace [37] and second by using the NIST-JANAF values for the total entropy, our measurements of the phonon entropy, and the electronic entropy as determined from the electronic structure calculations described in § 11.3.6.

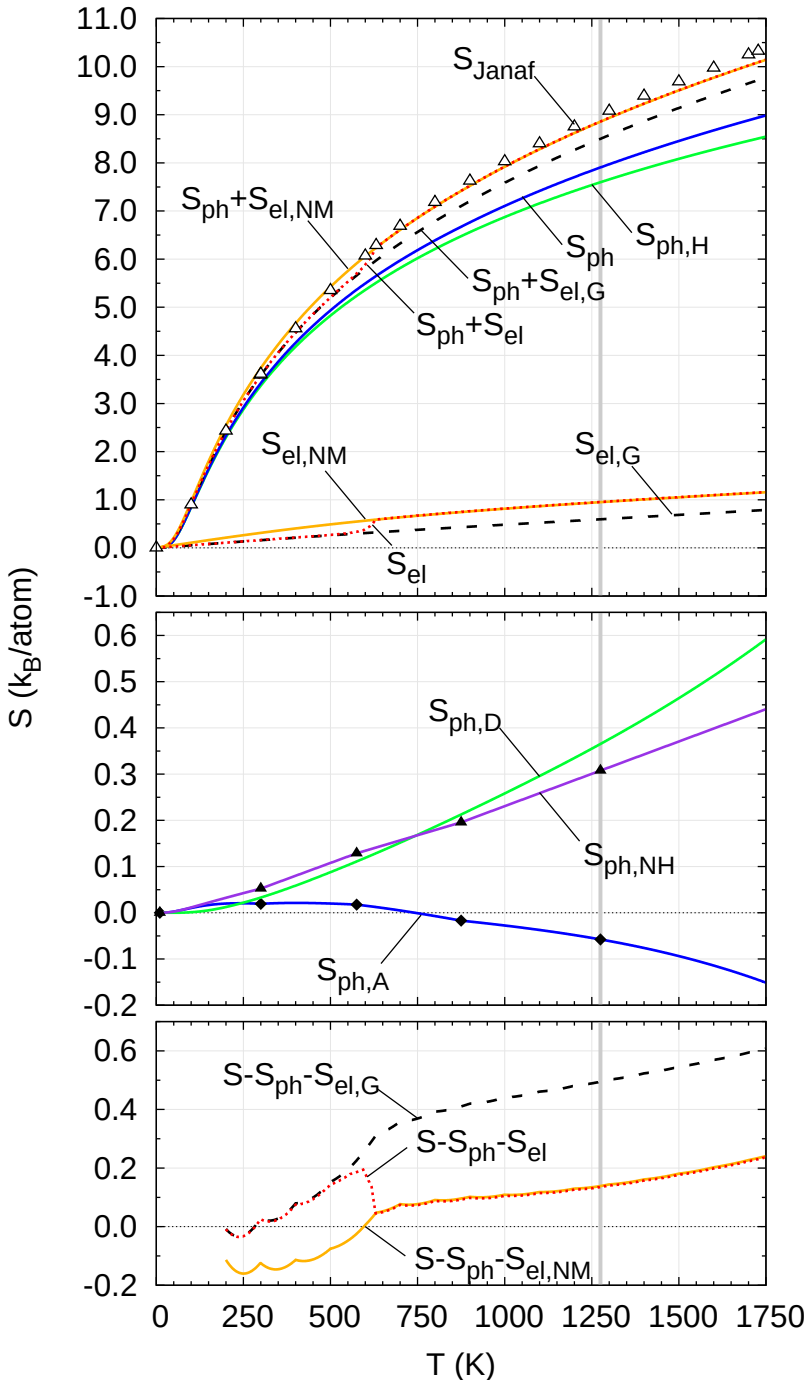

Figure 11.10: Contributions to the entropy of nickel, as labeled in the plot. The vertical gray line denotes the highest temperature at which the phonon spectrum was measured. Values for the total entropy, S_{Janaf}, were taken from the NIST-JANAF thermochemical tables[136] and are shown as open triangles. Closed markers are data from the current experiment; lines are either calculations or interpolations. Calculation of the various contributions is described in the text.

From Wallace's plots of S_{el} and $S - S_{\mathrm{ph}}$,[37] we find the sum of the magnetic and anharmonic contributions to the entropy to be approximately 0.23 k_{B}/atom at 1275 K. Wallace found

that the sum of the magnetic and anharmonic entropies at the melting temperature, 1728 K, was 0.31 $k_{\rm B}$/atom. Wallace assumes that the anharmonic contribution is zero, and attributes the entire quantity to magnetic entropy. It appears that the magnetic entropy is slightly larger. At 1275 K, we find $-0.08 < S_{\rm ph,A} < -0.04$ $k_{\rm B}$/atom, subtracting these values from $S_{\rm ph,A} + S_{\rm ph,M}$, we obtain $0.27 < S_{\rm el,M} < 0.31$ $k_{\rm B}$/atom. If we take this to be the value at melting, we get $0.35 < S_{\rm el,M} < 0.39$ $k_{\rm B}$/atom. The center panel of Fig. 11.10 suggests that the anharmonic entropy will decrease linearly with temperature above 1273 K, so the magnetic entropy at melting may be larger than was previously suggested. If we assume that this trend continues out to 1728 K, we get $S_{\rm ph,A}(1728) \approx -0.11$ $k_{\rm B}$/atom, and $S_{\rm el,M}(1728) \approx 0.42$ $k_{\rm B}$/atom.

Using the electronic DOS shown in Figs. 11.6 and 11.7, we may determine various electronic entropies as follows: First, with $N_{\rm el}$ the number of electrons and $f_T(E)$ the mean occupancy for fermions at temperature T, we use:

$$N_{\rm el} = \int G_T(E) f_T(E) dE \; , \tag{11.10}$$

to find the chemical potential, μ. Then we have:

$$S_{\rm el} = -k_{\rm B} \int dE G_T \left[(1 - f_T) \ln (1 - f_T) + f_T \ln (f_T) \right] , \tag{11.11}$$

$$S_{\rm el,G} = -k_{\rm B} \int dE G_0 \left[(1 - f_T) \ln (1 - f_T) + f_T \ln (f_T) \right] , \tag{11.12}$$

$$S_{\rm el,NM} = -k_{\rm B} \int dE G_T^{\rm NM} \left[(1 - f_T) \ln (1 - f_T) + f_T \ln (f_T) \right] . \tag{11.13}$$

The values of the electronic entropy used by Wallace [37] are derived from a non-magnetic determination of the electron DOS. This should be analogous to our $S_{\rm el,NM}$, determined with the electronic DOS in Fig. 11.6. Using this, the experimentally determined phonon entropy $S_{\rm ph}$, the values of the total entropy from the NIST-JANAF, $S_{\rm Janaf}$ — all of which are shown in the top panel of Fig. 11.10 — we may determine the unaccounted for entropy. Assuming that all unaccounted for entropy is magnetic in origin, we find $S_{\rm el,M} = 0.14$ $k_{\rm B}$/atom at 1275 K. Extrapolating to the melting temperature, $T_M = 1728$ K, we get $S_{\rm el,M} = 0.23$ $k_{\rm B}$/atom. This is considerably smaller than the value found using plots from Wallace [37] and our value for the anharmonic phonon entropy.

Part of this discrepancy stems from our differing estimates of $S_{\rm el,NM}$. Again, looking at plots from Wallace [37], we see that at 1275 K, he has $S_{\rm el,NM} \approx 0.88$ $k_{\rm B}$/atom, whereas we get 0.95 $k_{\rm B}$/atom. The difference, $\delta S_{\rm el,NM} \approx 0.07$ $k_{\rm B}$/atom, is only about half of the difference in the estimates of the magnetic entropy, $\delta S_{\rm el,M} = 0.14 k_{\rm B}$/atom at 1275 K. Given the information presented by Wallace, the rest of the difference is much more difficult to sort out; however, it seems likely that it stems more from values of the total entropy and of the phonon entropy of dilation than from values of the phonon entropy, $S_{\rm ph}$. Specifically, values of the total entropy at 1275 K from Meschter *et al.* [31] or

from NIST-JANAF [136] vary by roughly 0.3 k_B/atom. Measurements of temperature dependence of the thermal expansion coefficient and the bulk modulus are also subject to variation, and this will impact the fraction of the nonharmonic entropy, $S_{ph,NH} = S_{ph,D} + S_{ph,A}$ that goes into the dilation contribution as opposed to the anharmonic contribution to the phonon entropy.

11.5 Summary

Phonon spectra of FCC nickel were measured by time-of-flight neutron spectrometry over a wide range of temperatures spanning from 10 K to 1275 K. The softening of the DOS was generally consistent with the softening expected from expansion of the lattice against the bulk modulus, but the softening is less than expected at high temperatures. We are able to bound the entropic contribution from phonon anharmonicity to $-0.08 < S_{ph,A} < -0.04$ k_B/atom at 1275 K. Taking values of $S_{ph,A} + S_{el,M}$ from Wallace, [37] this bounds the contribution of the magnetic entropy to $0.27 < S_{el,M} < 0.31$ k_B/atom at 1275 K. Additionally, we found there to be significant broadening of the phonons with increased temperature, which we tentatively attribute to phonon-phonon interactions.

Part IV

Phonons in BCC Metals at Elevated Temperatures

Nuclear resonant inelastic x-ray scattering (NRIXS) measurements of polycrystalline iron are presented in detail here, and inelastic neutron scattering measurements of polycrystalline chromium and vanadium are briefly summarized. With the exception of § 12.4.1, the analyses and computations for iron are quite similar to the corresponding ones for nickel described in § 11.3.

Chapter 12

Iron

12.1 Introduction

Due to its abundance, technological value, importance to geology, myriad solid-solid phase transitions, and itinerant electron magnetism, the fundamental physics of iron and its phase diagram is and has been the focus of a great deal of theoretical [17–20, 46, 212–229] and experimental [230–241] research.

Iron comprises roughly 5% of the Earth's crust, and its use in steel alone makes it one of the most widely used metals in industry. Additionally, due to its low cost and relatively strong magnetism, it is frequently used in magnetic components. [242] Much of our understanding of geodynamics comes from studying seismic waves. Accurate values of the sound velocity of iron at high temperatures and pressures are critical to refining our understanding of the composition and dynamics of Earth's iron core. At 0 K and ambient pressures, iron is a ferromagnet which takes the body-centered-cubic (BCC) structure. It undergoes a transition from ferromagnet to paramagnet at $T_{\mathrm{C}} = 1043$ K, transforms to a face-centered-cubic (FCC) structure at 1185 K, and then transforms back to a BCC structure at 1667 K. At room temperature, iron undergoes a phase transition to a hexagonal-close-packed (HCP) structure somewhere between 10 and 16 GPa.[243] Understanding these phase transitions requires detailed knowledge of the electronic structure of iron — including its magnetism — as well as its vibrational dynamics.

According to Moriya and Takahashi, [193] the debate over whether magnetism in iron is due to localized or itinerant electrons has spanned nearly half a century. [194–200] Briefly, we paraphrase their summary of the situation: A purely localized electron magnet has magnetic excitations that are localized in real space; whereas those of a purely itinerant electron magnet are localized in reciprocal space. For magnetic 3d transition metals, the former fails to explain nonintegral values (in Bohr magnetons) of the saturization magnetization and predicts values of the low temperature cohesive energy and specific heat that are too small. The latter, on the other hand, predicts Curie temperatures, T_{C}, that are too high, and fails to predict the Curie-Weiss behavior of the magnetic

susceptibility at high temperatures. Thus, it is clear that neither of these extremes offers a satisfactory explanation of the magnetism in iron; rather, spin excitations in iron are somewhat localized (and somewhat delocalized) in both real and reciprocal space. The summary is from 1984; however, despite great progress, our understanding of the electronic structure of magnetic transition metals — particularly in their high temperature paramagnetic states — is still less than satisfactory. [32, 45, 47] For example, spin-polarized electronic structure calculations including adiabatic spin-dynamics only successfully predict the magnetization of iron to roughly $\frac{T_C}{2}$. [191, 192]

Iron is a strong, coherent scatterer of neutrons; therefore, its phonon dispersions have been measured using triple-axis neutron spectrometry, [244–247] including studies of the temperature dependence [59, 248–250] and the pressure dependence. [251, 252] Many of these studies are targeted at determining whether or not the phonons play a role in the various solid-solid phase transitions. There have also been a number of neutron measurements of the critical scattering [253, 254] and of the magnetic scattering including its temperature dependence. [255–258] Most of these experiments explored the nature of the magnetic excitations in iron, as well as to determine their role in the solid-solid phase transitions. Finally, there is a good deal of theoretical interest in the interactions between the vibrational and magnetic excitations. [45, 259–261]

From measurements of magnetic scattering, we know that only the lowest energy magnetic excitations contribute to the thermodynamics of iron. [191, 192] At low energies, the spin dispersions of iron are expected to be isotropic in $\mathbf{q}$; [258] therefore, a measurement in a single direction in $\mathbf{q}$-space may yield a picture of the spin dynamics that is sufficient for thermodynamic use. Phonons, on the other hand, may vary significantly with $\mathbf{q}$. Born–von Kármán models provide a means of interpolating data from a few high-symmetry directions over the whole Brillouin zone; however, the phonon spectra from these models often differ slightly from the spectra found by experiments that sample a larger portion of the Brillouin zone. As such, a measurement of the phonons over the entire Brillouin zone is desirable, as it answers directly any questions about the phonon contributions to the thermodynamics.[a]

Iron is a Mössbauer isotope, and with the advent of synchotron x-ray sources, it has become a test material for nuclear forward and resonant inelastic x-ray scattering instruments. [262–275] As the requirements on sample size are smaller i for x-ray scattering than for neutron scattering, practitioners of NRIXS have paid particular attention to iron under pressure. [274–282] NRIXS provides a direct measurement of the phonon spectrum, and analysis of NRIXS data typically requires only the assumption of harmonic phonons, and has no need of BvK models.[b] Additionally, NRIXS is an

[a] Most determinations of phonon spectra are made under the assumption of harmonicity. This might also lead to inaccuracies in our interpretations of the vibrational thermodynamics; perhaps of the same order of magnitude as using BvK models for the vibrational dynamics.

[b] Analysis of data from neutron time-of-flight chopper spectrometers is also frequently done without BvK models; however, this involves the incoherent approximation. Quite generally, the analysis of data from neutron time-of-flight chopper spectrometers is significantly more involved than for NRIXS, and a brief description of this is given towards the end of § 12.2.

extremely low noise measurement; therefore, the phonon spectra determined by this technique are likely of the highest quality currently available.

Here, we present NRIXS measurements of the phonon spectrum for the BCC phase from near absolute zero to near the Curie point. We find that there is a large differential softening between the first and second transverse modes. Specifically, the former soften dramatically upon approaching the Curie temperature; whereas the latter seem to soften largely in proportion to the longitudinal modes. We also consider the phonon contributions to the entropy of iron, and find that the phonons in iron are highly anharmonic. Finally, we will comment on the electronic and magnetic contributions to the entropy.

12.2 Background

Nuclear resonant inelastic x-ray scattering (NRIXS), also known as the phonon-assisted Mössbauer effect, has previously been described in great detail. [270–275, 283–286] Here we present only a brief summary. Additionally, many of the principles are similar to those for the scattering of neutrons by phonons, which were presented in Chapter 5.

A free nucleus may enter an excited state when a photon of the right energy is incident upon it. After some time, the nucleus relaxes back to the lower energy state and emits a γ-ray. In both cases, conservation of momentum forces the nucleus to recoil, and the recoil energy E_R is given by:

$$E_R = \frac{E_t^2}{2Mc^2} \ , \tag{12.1}$$

where M is the mass of the nucleus, c is the speed of light, and E_t is the energy of the nuclear transition. For a free nucleus, the recoil energy can be a significant fraction of the linewidth of the nuclear excited state; causing the emitted photon to lack the energy required to excite another (similar) nucleus. If the nucleus is in a crystal, however, the recoil energy may be taken up by the entire lattice. The mass in Eq. 12.1, then, becomes the mass of the crystal, and the recoil energy becomes negligible relative to the linewidth. The emitted photon thus retains the energy required to excite another nucleus, and a *resonance* occurs. Rudolph Mössbauer discovered this process, for which he won the 1961 Nobel prize.

In a NRIXS experiment, the incident x-rays are detuned from resonance by energies that may be made up for by the creation or annihilation of phonons (or other excitations coupled to the nuclei) in the sample. The resulting counts are proportional to the excitation probability density for the resonant nuclei in the sample, $S_r(E)$. This is precisely $\frac{1}{\hbar}\sum_{\mathcal{P}} S_{\mathcal{P}}(\omega)$ as defined around Eqs. 5.48, and 5.50, and thus gives access to the partial phonon spectrum for the resonant nucleus.

With inelastic neutron scattering, a lack of incident neutron flux, insufficient energy resolution,

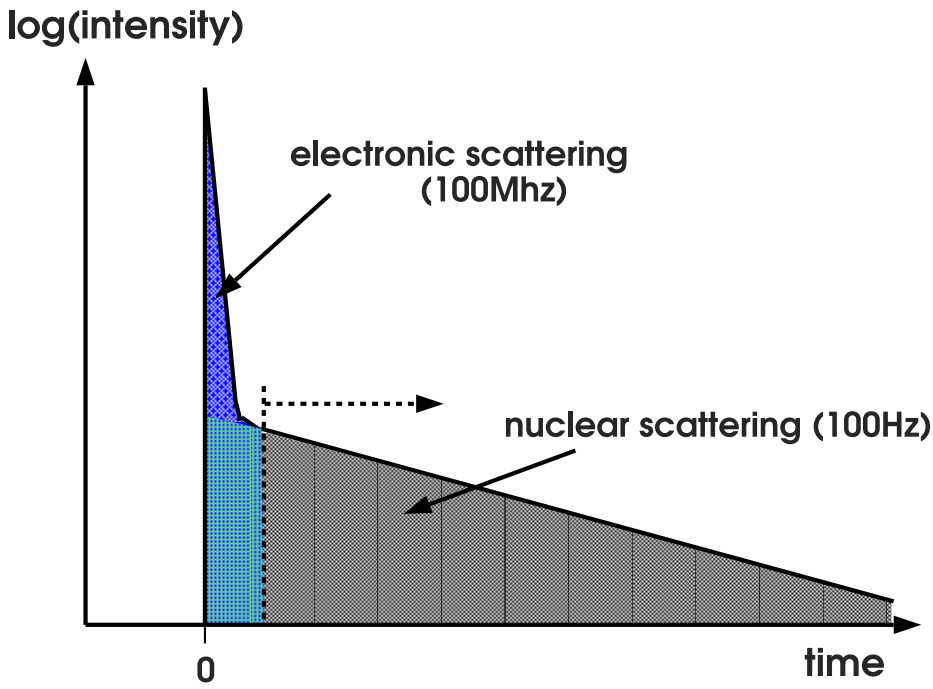

Figure 12.1: A schematic of the importance of timing in a nuclear resonant inelastic x-ray scattering experiment. The x-ray pulse arrives at time $t = 0$, and is followed by a huge amount of electronic scattering. After a few picoseconds this has subsided, and after a few nanoseconds the counts from the nuclear resonant scattering may be collected without background. Figure taken from "Nuclear resonant spectroscopy" by W. Sturhahn. [284]

and a wide variety of unwanted scattering create challenges for the experimentalist. For NRIXS, none of these problems exist provided that an appropriate resonant nucleus is used. Synchotron sources generate huge numbers of x-rays, and the tuning of the incident x-ray beam may be accomplished with modern high resolution monochromators. [287–291] The background may be suppressed entirely using what is sometimes called the *time discrimination trick*. When a pulse of x-rays hits the sample, a huge intensity of electronic scattering occurs on a picosecond timescale. If the linewidth of the excited state of the resonant nucleus is sufficiently small, the γ-rays emitted by the nuclei upon relaxation may be delayed significantly. This is shown schematically in Fig.12.1. The disadvantage of NRIXS, then, is that it is only feasible for nuclei that have excited states at accessible energies with appropriate lifetimes.[c] Further, the technique is only sensitive to the properties of the resonant nuclei; therefore, it is only able to give a partial account of the vibrational dynamics for most materials.[d]

Fortunately, the first excited state of ^{57}Fe is at 14.413 keV, and its linewidth is 4.66 neV, which

[c] Neutron scattering is also not feasible for all elements, as some of them absorb too many neutrons. That said, the number of elements suitable for neutron scattering far exceeds the number of isotopes currently suitable for NRIXS.

[d] Conversely, neutrons generally give information about the vibrational dynamics of all the nuclei in the sample; albeit weighted by their scattering cross-sections. The varying neutron scattering cross-sections can make sorting out which vibrations come from which nuclei extremely difficult.

corresponds to a lifetime of 141 ns. Of these energies, the former is easily achievable with modern synchotrons and monochromators, and the latter is sufficiently small to allow for use of the time discrimination trick. This makes iron an ideal nucleus for NRIXS experiments.

12.3 Experiment

12.3.1 Sample preparation

Samples were made of 96.06% ^{57}Fe enriched ingot of 99.99% chemical purity rolled to a foil of 27 μm thickness. To remove strain and crystallographic texture, they were sealed in an evacuated quartz tube, heat treated at 1173 K for 30 minutes, and quenched in iced brine. The resulting samples showed no visible signs of texture, preferred orientation, or oxidation.

12.3.2 Nuclear resonant inelastic x-ray scattering at HP-CAT

The NRIXS experiment was performed at beam line 16-IDD of the High Pressure Collaborative Access Team at the Advanced Photon Source at Argonne National Laboratory. The synchotron ring was operated in top-up singlet mode with x-ray bunches separated by 153 ns. The crystal monochromator at this beamline was diamond 111, and the focused beam size was 20 μm$\times$ 50μm. The incident x-ray energy was tuned to 14.413 keV to match the ^{57}Fe resonance. Data were collected in scans of the incident energy from -120 to 120 meV with a monochromator resolution of 2 meV.

A room temperature (295 K) measurement was made with the sample placed at a grazing angle with respect to the incident photon beam, and the delayed signal was detected by two avalanche photodiode (APD) detectors. These were positioned opposite each other, avoiding the forward beam, with a separation of approximately 5 mm. For measurements at high temperatures, the sample was mounted in a custom furnace as described below. The ^{57}Fe foil was cylindrically wrapped around a single resistive heating element as the primary radiation shield. Several other niobium and copper radiation shields were utilized, each with a small slit allowing passage of the incident and scattered photons. The temperature was monitored with a single thermocouple attached to the ^{57}Fe foil, and was maintained using a temperature controller and DC power supply. The entire assembly was held under vacuum in an aluminum tube with a Kapton window giving access to the sample. Two APDs were positioned approximately 2 cm from the sample. Measurements were taken at 523, 773, 923, and 1023 K, after which the sample was allowed to cool. No visible oxidation was present after the heating. Finally, the sample was remounted in a He-flow cryostat equipped with a Be dome, with a single APD positioned several centimeters ($\sim$ 4 cm) from the sample for a measurement at 21 K. The normalized spectra are shown in Fig. 12.2.

12.4 Analysis and computation

Details of the determination of the quality factors and fitting of BvK models are given in § 8.4, § 8.2, and § 8.3.1.2, respectively.

12.4.1 $S(E)$ and the phonon density of states

The phonon DOS were extracted from the scattering using PHOENIX. [292] The program performs all the necessary corrections including removal of the elastic peak and multiphonon scattering using

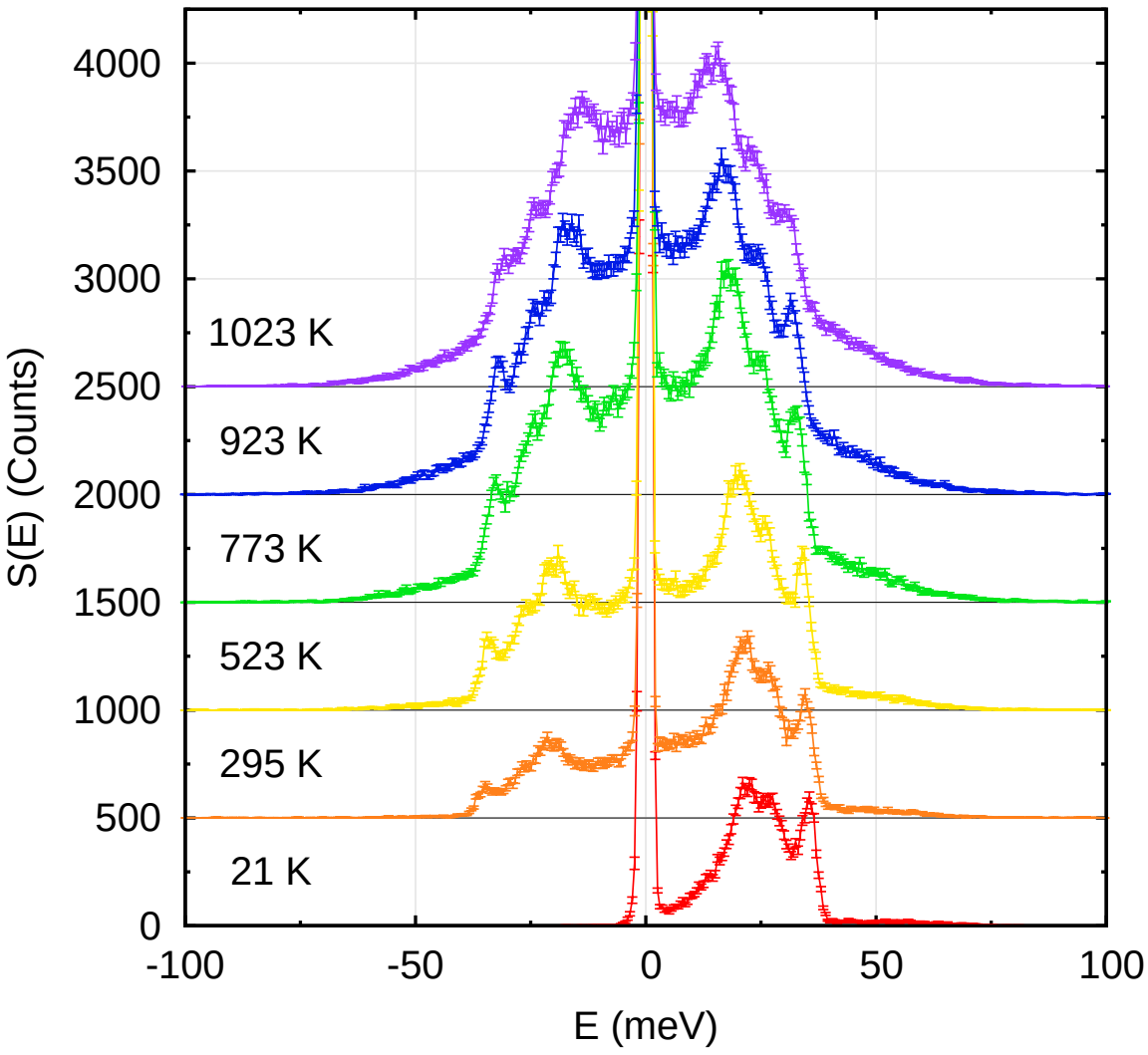

Figure 12.2: Phonon probability densities, $S(E)$ of iron at temperatures as indicated. The elastic peaks extend well above the figure. The absence of all background scattering is particularly evident at 21 K. As the temperature increases, the phonon annihilation (left) side of the spectrum increases relative to the phonon creation (right) side as dictated by detailed balance. The multiphonon scattering — above ∼35 meV also becomes more significant with increasing temperature.

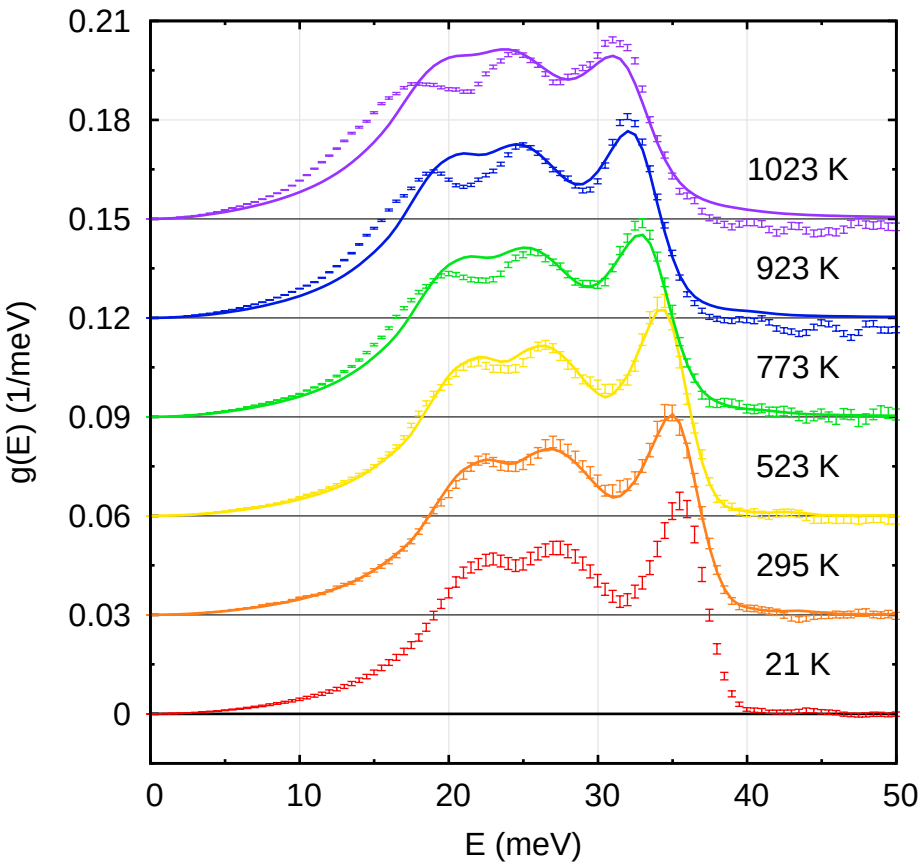

Figure 12.3: Phonon DOS of iron at temperatures as indicated. The markers show the experimentally determined DOS, and the lines the best fits of the 21 K DOS to the high temperature DOS by scaling of the energy and integral transform with the damped oscillator function as a kernel. (Eq. 12.3).

the Fourier-log technique described in § 8.1.1. The phonon spectra thus determined are shown by markers in Figs. 12.3 and 12.4.

12.4.2 Phonon shifts and broadening

Fits of the quality factor $\mathcal{Q}$ were performed as described in § 8.2, and are shown in Fig. 12.3. Briefly, the phonon broadening was assumed to take the form:

$$B(\mathcal{Q}, E', E) = \frac{1}{\pi \mathcal{Q} E'} \frac{1}{\left(\frac{E'}{E} - \frac{E}{E'}\right)^2 + \frac{1}{\mathcal{Q}^2}} \,. \tag{12.2}$$

The high temperature phonon DOS was then approximated as a function of the low temperature DOS with only two free parameters, Δ^s and $\mathcal{Q}$:

$$g_T(E) = B(\mathcal{Q}, E', E) \odot g_{21}(\Delta^s E') \,, \tag{12.3}$$

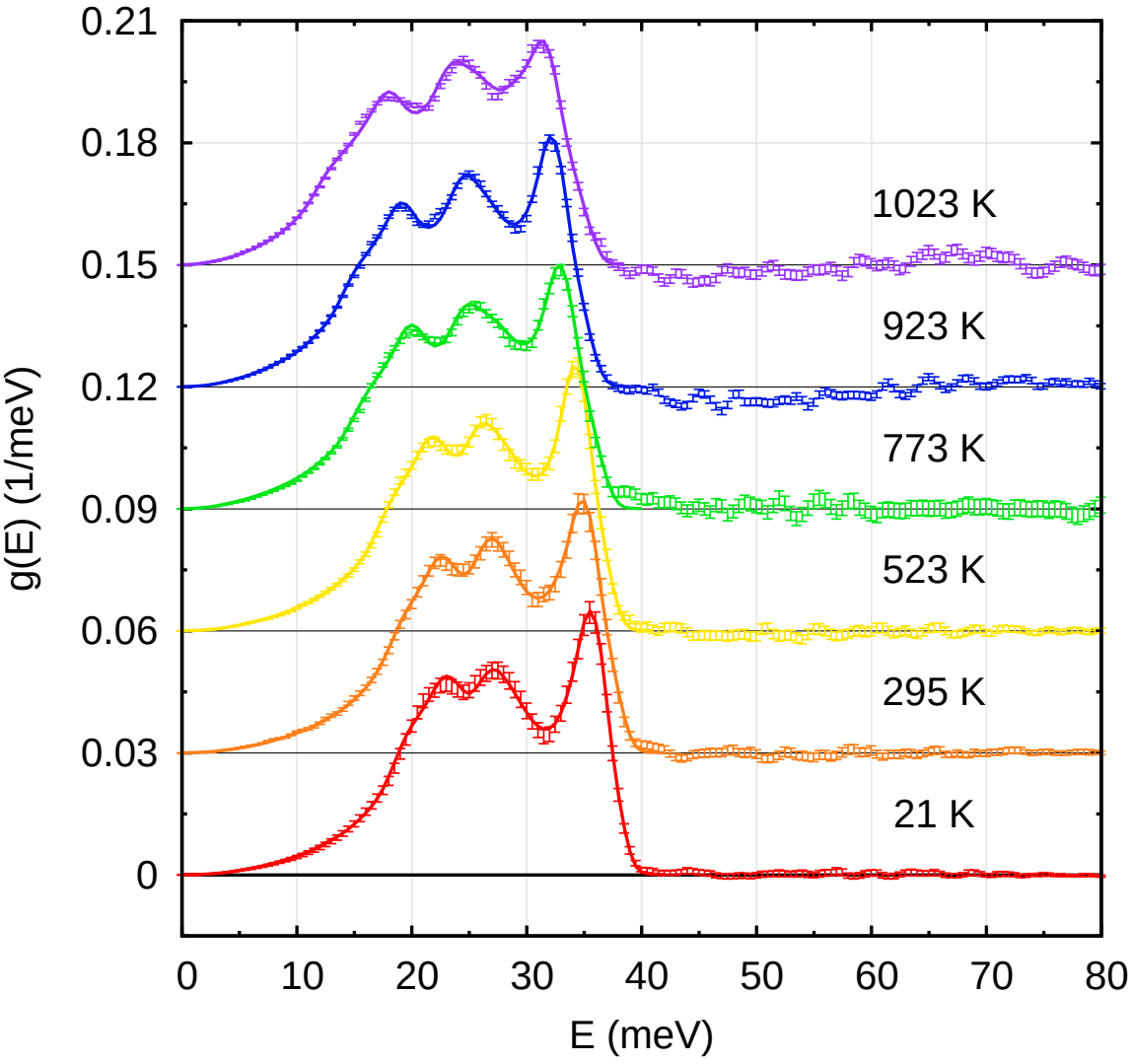

Figure 12.4: Phonon DOS for iron at temperatures as indicated. Markers show experimental data, lines show Born–von Kármán fits. There is a large overall shift of the modes to lower frequencies, and the changes in the shapes of the first and second transverse peaks and the longitudinal peak are strong indications of anharmonicity. The DOS are offset by integer multiples of 0.03 meV^{-1}.

where $\odot$ denotes an integral transform over the variable E', Δ^{s} rescales the phonon energy, g_T is the phonon DOS at temperature T, and g_{21} is the phonon DOS at 21 K — the lowest temperature for which we have a measurement. At 923 and 1023 K, the $\mathcal{Q}$ are of order 100. As such, the transformation with the damped harmonic oscillator function had a negligible effect on the DOS, and it is mainly the effects of the shift, Δ^{s}, that is seen in the solid lines in Fig. 12.3. Because of this, and because of the failure of this model at high T, we will subsequently take $B = \mathbf{1}$ — i.e., we assume oscillators of infinite quality.

Table 12.1: Optimized tensor force constants in N/m as a function of temperature for BCC iron. A Cartesian basis is used, where $\langle xyz \rangle$ is the bond vector for the given tensor components.

	$\langle xyz \rangle$	21 K	295 K	523 K	773 K	923 K	1023 K
$[\mathbf{K}_1]_{xx}$	$\langle 111 \rangle$	17.263	16.213	15.641	13.887	14.020	13.336
$[\mathbf{K}_1]_{xy}$		14.910	14.941	14.489	14.354	13.729	13.652
$[\mathbf{K}_2]_{xx}$	$\langle 200 \rangle$	15.314	14.568	15.103	15.289	12.726	12.829
$[\mathbf{K}_2]_{yy}$		0.115	0.311	0.652	0.943	1.128	0.943
$[\mathbf{K}_3]_{xx}$	$\langle 220 \rangle$	1.020	1.289	0.961	0.843	0.528	0.352
$[\mathbf{K}_3]_{xy}$		0.273	0.329	0.054	−0.749	−0.812	−1.847
$[\mathbf{K}_3]_{zz}$		−0.393	0.450	−0.385	−0.320	−0.256	−0.077
$[\mathbf{K}_4]_{xx}$	$\langle 311 \rangle$	−0.286	−0.191	−0.340	−0.426	−0.600	−0.362
$[\mathbf{K}_4]_{xy}$		−0.067	0.016	−0.101	−0.179	−0.331	−0.398
$[\mathbf{K}_4]_{yy}$		0.048	−0.001	0.033	0.002	0.050	−0.167
$[\mathbf{K}_4]_{yz}$		0.566	0.891	0.654	1.006	0.700	1.332
$[\mathbf{K}_4]_{zz}$		0.048	−0.001	0.033	0.002	0.050	−0.167
$[\mathbf{K}_5]_{xx}$	$\langle 222 \rangle$	−0.382	−0.411	−0.316	−0.201	−0.485	−0.419
$[\mathbf{K}_5]_{xy}$		0.090	0.465	0.575	1.166	0.674	1.053

12.4.3 Born–von Kármán models of lattice dynamics

The phonon spectra were then fit with Born–von Kármán models of the lattice dynamics. Tensorial force constants out to the 5NN shell were determined using a Nelder-Mead simplex algorithm as implemented in SciPy [293] as per the technique discussed briefly in § 8.3.1.1. The experimentally determined resolution function was used for Z, and we assumed $B = \mathbf{1}$ as explained above. The force constants so determined are listed in Table 12.1, and the best fits to the DOS at all temperatures are shown in Fig. 12.4.

The longitudinal and average transverse force constants were determined in the manner described in § 8.3.2. Briefly, the longitudinal force constants were found by projecting the tensor onto the bond vectors $\langle xyz \rangle$. The 3×3 force constant tensors were then diagonalized. The longitudinal force constant was matched to one of the eigenvalues and the average transverse constant was taken to be the mean of the two remaining eigenvalues. Longitudinal force constants to 3NN are shown in Fig. 12.5, and the averaged transverse force constants out to 3NN are shown in Fig. 12.6. The 1NN longitudinal force constants, $\mathcal{K}_1(T)$, decrease with increasing temperature approximately as:

$$\mathcal{K}_1(T) = 47.689 - 6.640 \times 10^{-3}\ T\ , \tag{12.4}$$

where T is in degrees Kelvin and $\mathcal{K}_1(T)$ is in N/m. The fit is also shown in Fig. 12.5.

12.4.4 *Ab-initio* calculations

To investigate electronic contributions to the entropy of BCC iron, we used the plane-wave code VASP [130, 131] to calculate the electronic DOS of iron as a function of unit cell volume in the

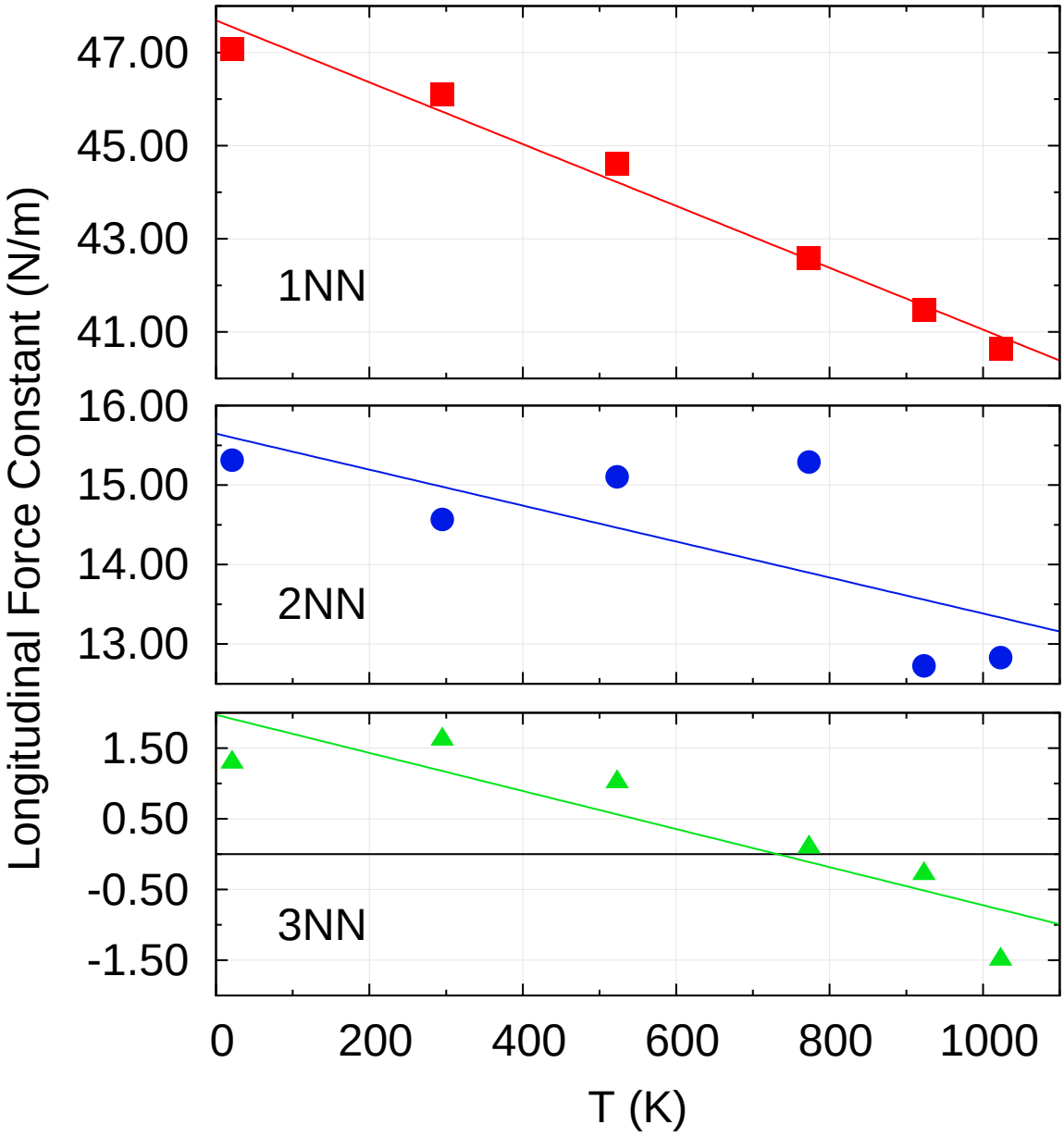

Figure 12.5: Markers show longitudinal force constants of iron for first through third nearest neighbors as indicated. The lines show linear fits, which appear to match reasonably well only for the 1NN shell.

non-magnetic state, and as a function of unit cell volume and magnetization in the magnetic state. The non-magnetic and spin-polarized (magnetic) calculations both used projector augmented plane waves and the Perdew-Burke-Ernzerhof generalized gradient approximation. [133] A conventional BCC cell was used, and it was relaxed using the 'accurate' setting for the kinetic energy cutoff, with a $31 \times 31 \times 31$ Monckhorst-Pack q-point grid. [134]

For the non-magnetic case, the relaxed lattice parameter was within 4% of the experimentally

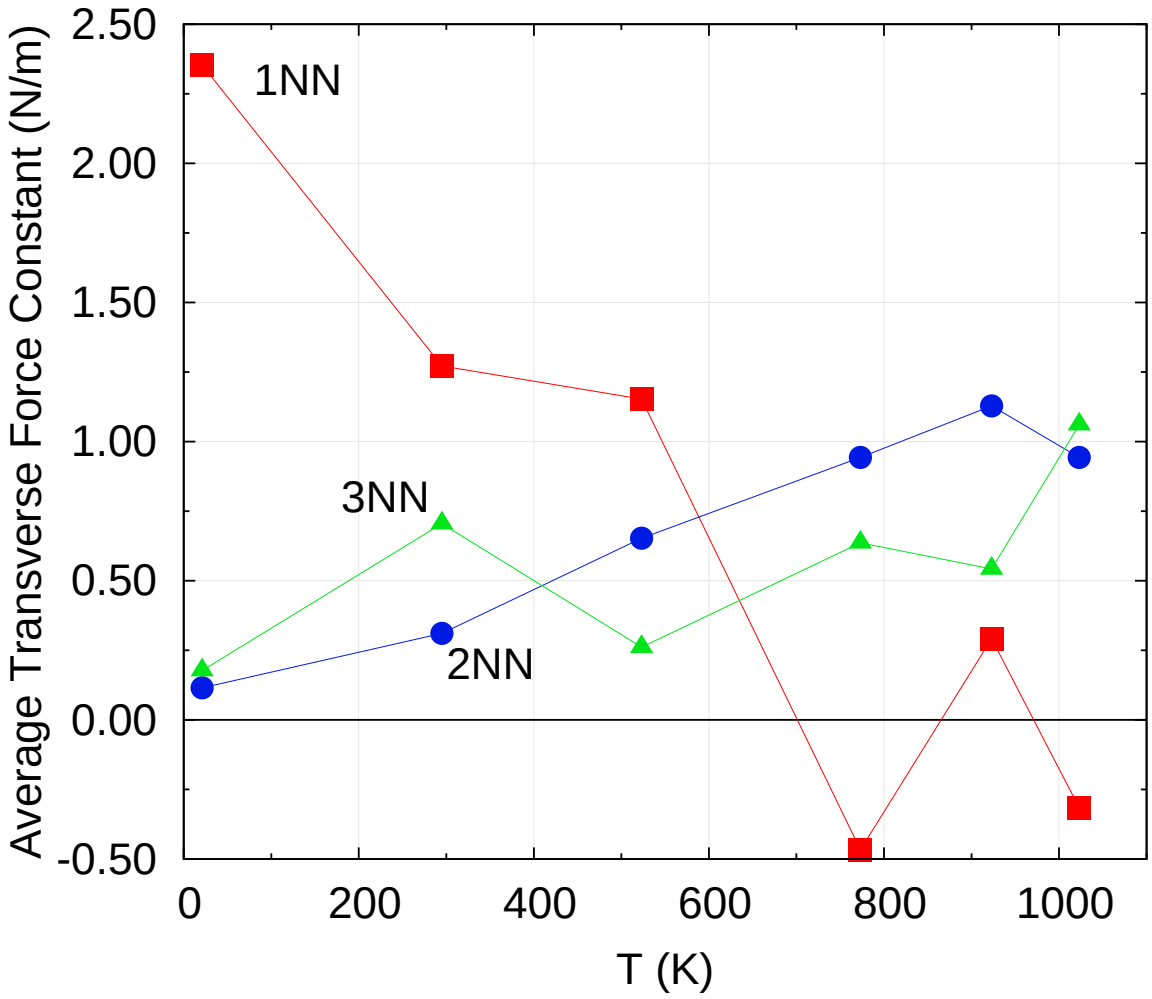

Figure 12.6: The markers and lines show averaged transverse force constants of iron. In the 1NN shell, the transverse forces appear to go rapidly to zero by roughly 750 K. The transverse forces for the second and third neighbor shells, on the other hand, appear to increase with increasing temperature.

determined lattice parameter, and was taken to be the 0 K lattice parameter of the unit cell. The values of the linear coefficient of thermal expansion from Touloukian *et al.* [168] were used to determine the corresponding volume at 1043 K. The electronic DOS in the non-magnetic state were determined at these two volumes, and are shown in Fig. 12.7.

For the spin polarized case, a ferromagnetic ground state was found. The relaxed lattice parameter was within 1% and the magnetic moment was within 0.5% of the experimentally determined values. These were taken to be the 0 K lattice parameter and magnetic moment, and the values of the linear coefficient of thermal expansion from Touloukian *et al.* [168] and of the relative magnetization from Crangle *et al.* [210] were used to fix the corresponding volumes and magnetizations at

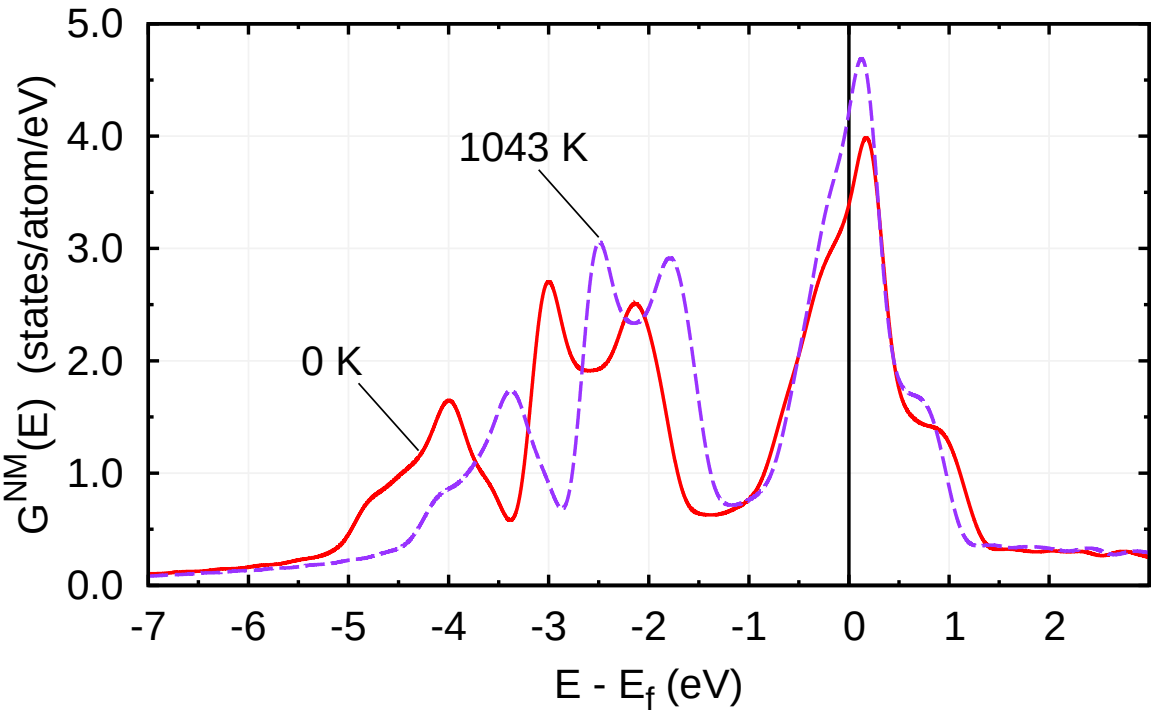

Figure 12.7: Non-magnetic electronic DOS of iron at temperatures as indicated, calculated as described in the text. The increased volume at 1043 K is accompanied by a modest increase of the density of states at the Fermi level.

522, 793, 918, 981, 1022, 1033, 1038, 1041, 1043, and 1150 K. [e] The electronic DOS of the majority and minority spin electrons[f] were determined at these volumes and magnetizations, and those at 0, 1038, and 1150 K are shown in Fig. 12.8.

As in Chapter 11, we point out that our tacit assumption that the size of the magnetic moments are changing with temperature is wrong. Rather it is the orientations of the spins that change with temperature. Regardless, this model can give us some guidance as we consider the magnetic and non-magnetic contributions of the electrons to the entropy.

12.5 Results and discussion

The best fits of the quality factor and shift as a function of temperature shown in Fig. 12.3 fail quite dramatically for temperatures 773 K and higher. Specifically, they are unable to capture the differential shifting of the two transverse peaks. Even at 523 K the deviations in the two transverse

[e] For example, our values for the lattice parameter and magnetic moment of a conventional BCC Fe unit cell at 0 K were $a_0 = 2.8346$ Å and $\mu_0 = 4.4153$ Bohr magnetons, respectively. At 522 K, we are at 50% of $T_C = 1043$ K. Crangle *et al.* report that the magnetization should be 0.9400 μ_0 and Touloukian that the lattice parameter should be $1.005a_0$, so the 522 K simulation was run with the lattice parameter fixed to be 2.8488 Å and the magnetic moment fixed to be 4.1504 Bohr magnetons.

[f] "Majority" or "minority" indicate the spin (up or down) that is carried by the majority or minority of the electrons.

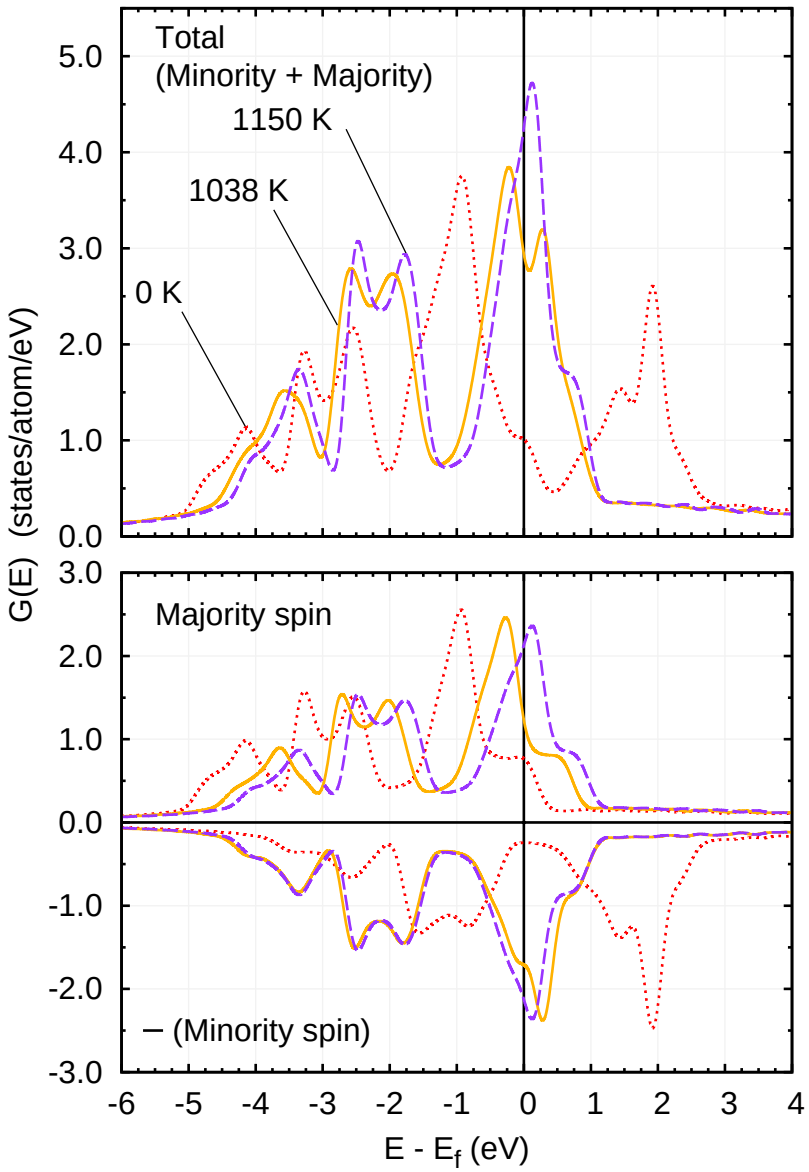

Figure 12.8: Spin-polarized and non-magnetic electronic DOS of iron calculated as described in the text. In both the top and bottom panels, the red-dotted, yellow, and purple-dashed lines correspond to 0, 1038, and 1150 K respectively. The bottom panel shows the DOS for majority and minority spin electrons. As the temperature and volume increase and the magnetization decreases, electronic density accumulates at the Fermi energy. This can be seen in the top panel, where the total density of states at the Fermi level rises by a factor of 4 going from 0 to 1150 K. (Actually, this occurs going from 0 to 1043 K, the Curie temperature, as can be seen by comparing the 1150 K DOS shown here with the nearly identical 1043 K DOS shown in Fig. 12.7).

peaks are noticeable in the fit; nevertheless, at 295 and 523 K the fits are much better than at the higher temperatures. The first transverse peak shifts to lower energies much more rapidly than the second transverse or the longitudinal peaks. This trend has been seen in triple-axis neutron

scattering measurements by Neuhaus *et al.* [248] and Satija *et al.*,[g] [261] as well as in elastic constants measured by Alves and Vâllera. [260] The effect can also been seen in theoretical calculations of the phonon spectrum of iron by Hasegawa *et al.* [214] These temperature effects are somewhat in contrast to measurements by Klotz and Braden [252] of the pressure dependence of the phonons, which show no differential shifting of the first transverse modes. Similarly for calculations of the pressure dependence by Sha and Cohen. [243] The longitudinal peak appears to broaden with temperature; however, it lacks the damped harmonic oscillator-like tails seen in the spectra of the FCC metals, Al, Pb, and Ni as seen in Chaps. 9, 10, and 11. [35, 42] At room temperature, Minkiewicz *et al.* found that the measured phonon linewidths could be attributed to their instrument resolution. [247] For the [110]T1 zone boundary phonon, Satija *et al.* report negligible linewidths at room temperature, and a linewidth on the order of 1 meV at T_{C}. [261] Our assumption for our BvK models that $B = \mathbf{1}$, then, is reasonable but not perfect. We note that the anharmonicties in the FCC metals are different, as the damping of the modes is far and away their most obvious manifestation. Here, the effects of anharmonicity on the phonon spectra are much more noticeable in the energy shifts, which are larger than expected.

The longitudinal constants for the first two shells of neighbors decrease with increasing temperature, and are thus largely responsible for the large softening of the phonon modes. The decrease in the 1NN longitudinal force constant is quite linear from room temperature up, and likely makes the largest contribution to the softening. The 3NN shell also contributes to the softening up to around 750 K, after which it becomes negative and begins increasing in magnitude. Room temperature force constants found by Brockhouse *et al.*, [245] Bergsma *et al.*, [246], and Minkiewicz *et al.* [247], as well as force constants found by Klotz and Braden [252] at room temperature and both ambient pressure and 9.8 GPa all agree with our finding that $[\mathbf{K}_1]_{xx} > [\mathbf{K}_1]_{xy}$ from 21-523 K, implying that at these temperatures the 1NN transverse forces are bonding rather than repulsive. Zaretsky and Stassis [250] find $[\mathbf{K}_1]_{xx} < [\mathbf{K}_1]_{xy}$ for the FCC phase, at 1428 K, indicating repulsive transverse forces. From 773 K up we find that $[\mathbf{K}_1]_{xx} - [\mathbf{K}_1]_{xy}$ is scattered about zero, which is at least consistent with the idea that the 1NN transverse forces go from bonding to repulsive with increasing temperature. Also around 750 K, the averaged transverse constant in the 1NN shell stops decreasing in magnitude and appears to be scattered about zero. The instability in the longitudinal forces in the 3NN shell, the switch from bonding to repulsive transverse forces in the 1NN shell, and the overall decrease in the 1NN transverse forces might be related to the strong anharmonicity seen in the transverse peaks of the phonon DOS, and may contribute to the BCC to FCC phase transition that occurs at 1185 K. Indeed, Neuhaus *et al.* cite the shifts in the transverse branches as an indication of a low potential energy barrier for displacements towards an FCC structure, and

[g] These authors speak of softening in the T2 or second transverse modes; however it is clear that they are actually referring to the same set of modes as we are.

thus can be thought of as a dynamical precursor to the phase transition. [248]

Looking at the spectra from 923 and 1023 K in Fig.12.4, the slow oscillation of the background — with trough at ∼45 and crest at ∼65 meV — is another indication of anharmonicity. Specifically, it seems that the harmonic model fails to correctly predict the multiphonon scattering seen experimentally. As the crest is at approximately twice the energy of the longitudinal peak, it seems likely that the 2-phonon processes are sampling anharmonic parts of the potential. Interference effects between 1-phonon and multiphonon scattering are known to exist for sufficiently anharmonic solids, [294] and this seems a possibility here.

Perhaps the clearest indicator of anharmonicity in iron is the deviation of its phonon entropy from that predicted by the quasiharmonic model of a solid. As discussed in Chapter 4, in a quasiharmonic solid, the entropy of dilation, $S_{\rm ph,D}$, is determined by the expansion of the lattice against the bulk modulus:

$$S_{\rm ph,D} = \int_0^T \frac{9K_T\alpha^2}{\rho_N} dT' \,, \tag{12.5}$$

where we have used the coefficients of thermal expansion, α, from Touloukian *et al.*, [168] and the temperature dependent isothermal bulk modulus, K_T from Rayne and Chandasekhar [295] and Fukuhara and Sanpei. [296] We may compare this to the nonharmonic entropy, $S_{\rm ph,NH}$, which may be determined directly from the phonon spectra:

$$S_{\rm ph} = 3k_{\rm B}\int dE g_T \left[(n_T+1)\ln(n_T+1) - n_T\ln(n_T)\right] , \tag{12.6}$$

$$S_{\rm ph,H} = 3k_{\rm B}\int dE g_{T_0} \left[(n_T+1)\ln(n_T+1) - n_T\ln(n_T)\right] , \tag{12.7}$$

$$S_{\rm ph,NH} = S_{\rm ph} - S_{\rm ph,H} \,. \tag{12.8}$$

The difference between these two is the anharmonic entropy, $S_{\rm ph,A}$:

$$S_{\rm ph,A} = S_{\rm ph,NH} - S_{\rm ph,D} \,. \tag{12.9}$$

All of these are shown in the center panel of Fig. 12.9. The anharmonic entropy is quite large, comprising over 3.5% of the total entropy of iron at 1023 K. If the measured trends hold, it would be close to 5% at the BCC to FCC phase transition — typical values for other solids *at melting* are less than 1%. [37]

Given the electronic DOS as a function of temperature, we may determine the various electronic entropies as follows: First, with $N_{\rm el}$ the number of electrons, we use:

$$N_{\rm el} = \int G_T(E) f_T(E) dE \,, \tag{12.10}$$

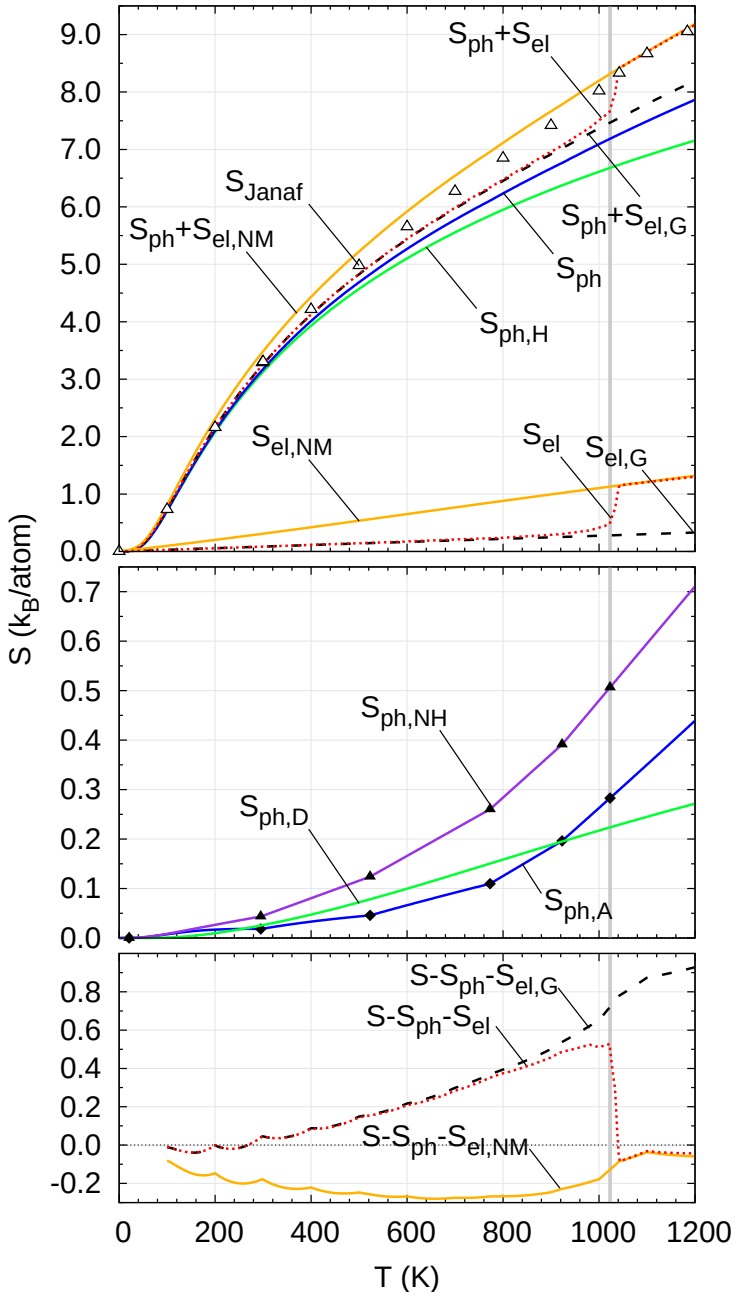

Figure 12.9: Contributions to the entropy of iron. The vertical gray line denotes the highest temperature at which the phonon spectrum was measured. The open markers show accepted values of the total entropy taken from the NIST-JANAF thermochemical tables, [136] filled markers show experimental data points. The various contributions are discussed in the text.

to find the chemical potential, μ. Then:

$$S_{\rm el} = -k_{\rm B} \int dE G_T \left[(1-f_T) \ln (1-f_T) + f_T \ln (f_T) \right] , \tag{12.11}$$

$$S_{\rm el,G} = -k_{\rm B} \int dE G_0 \left[(1-f_T) \ln (1-f_T) + f_T \ln (f_T) \right] , \tag{12.12}$$

$$S_{\rm el,NM} = -k_{\rm B} \int dE G_T^{\rm NM} \left[(1-f_T) \ln (1-f_T) + f_T \ln (f_T) \right] . \tag{12.13}$$

Our best estimate of the electronic entropy, $S_{\rm el}$, is found using the temperature dependent electronic DOS including the scaled magnetization. We get the ground state electronic entropy, $S_{\rm el,G}$, by using the 0 K ferromagnetic electron DOS, $G_0(E)$. This is in reasonable agreement with values found by Weiss and Tauer [297] and Grimvall, [199]. Alternatively, we get $S_{\rm el,NM}$ by using the temperature dependent non-magnetic electron DOS, $G_T^{\rm NM}(E)$. The three corresponding curves are shown in the top panel of Fig. 12.9. The phonon and harmonic phonon entropy, $S_{\rm ph}$ and $S_{\rm ph,H}$ determined with the phonon DOS, $g_T(E)$ and $g_{21}(E)$ from experiment are also shown, where the subscript 21 is for 21 K, our lowest temperature measurement.

If contributions from spin dynamics, electron-phonon interactions, and defects are negligible, the sum of the electronic and phonon entropies should give the total entropy.[h] The top panel of Fig. 12.9 shows values for the total entropy, $S_{\rm Janaf}$, taken from the NIST-JANAF thermochemical tables [136] (as markers) as well as the sums of the phonon entropy and the ground state and non-magnetic electronic entropies. For all temperatures the former underestimates the total entropy and the latter overestimates:

$$S_{\rm ph} + S_{\rm el,G} < S < S_{\rm ph} + S_{\rm el,NM} \; . \tag{12.14}$$

This is particularly noticeable below the Curie point, where spin excitations are actually playing a large role in the entropy.

The bottom panel of Fig. 12.9 shows the differences between $S_{\rm Janaf}$ and the three sums $S_{\rm ph} + S_{\rm el,G}$, $S_{\rm ph} + S_{\rm el}$, and $S_{\rm ph} + S_{\rm el,NM}$. The solid-yellow curve in the bottom panel of Fig. 12.9 comes from assuming a non-magnetic electronic DOS at all temperatures. The negative values at low temperatures show that the electron DOS at the Fermi level for the non-magnetic state is significantly higher than it is in the (actual) ferromagnetic state. Starting around $T \approx 800$ K, the curve begins to increase, finally leveling off at the Curie temperature. The Fermi level is almost certainly increasing as iron passes through the Curie point; however, some of the increase seen here is due to short range magnetic excitations.

At low temperatures, the black-dashed curve, $S - (S_{\rm ph} + S_{\rm el,G})$, is approximately zero. That is, the contributions from the phonons and electrons are probably well understood here, and other contributions to the entropy are negligible. As the temperature increases, a variety of effects begin to contribute to the entropy. There are adiabatic electron-phonon and defect contributions to the entropy; however, we will assume that these are negligible at these temperatures. What remains are changes in the electronic DOS at the Fermi level, and increasing magnon entropy. Looking at Fig. 12.8, it appears that the electronic DOS at the Fermi level is indeed increasing as we approach the Curie point. The black-dashed curve, however, continues increasing past the Curie temperature.

[h] It is well established that spin dynamics *do* contribute to the entropy of iron, and we will discuss this further; however, the other two contributions are likely to be quite small.

One interpretation would be that the ferromagnet to paramagnet transition comes about when spin excitations have disrupted the long range order; however, some short range order persists above the Curie temperature. The continued increase in the black-dashed curve above the Curie temperature, then, corresponds to the increasing disorder at short ranges.

Using the electronic DOS calculated by fixing both the volume and magnetization, we get the entropy shown by the red-dotted curve in Fig. 12.9. This curve is nearly identical to the black-dashed one up to about 750 K, after which it levels off, followed by a precipitous drop at the Curie temperature. In this case, the changes in the electronic states at the Fermi level have been incorporated into the electronic entropy, and the only contribution to the red-dotted curve is the dynamics of the spins. As we expect the disorder in the magnetic degrees of freedom as measured by the entropy to be a monotonically increasing function of the temperature, the shape of the red-dotted curve cannot be correct. It is clear, then, that the changes in the electronic DOS at the Fermi level have been overestimated by our simple model of the electronic structure.

12.6 Summary

Nuclear resonant inelastic x-ray scattering measurements of the phonon spectrum of BCC iron were made at temperatures of 21, 295, 523, 773, 923, and 1023 K. We found little broadening of the phonons at increased temperature but large shifts in phonon energies at increased temperatures. Further, a large differential shifting of the transverse modes was apparent. BvK models of the lattice dynamics showed a fairly linear decrease in the 1NN longitudinal force constant as a function of temperature which likely dominated the softening of the phonons. Additionally, we found a transition from bonding to repulsive transverse forces in the 1NN shell at roughly 750 K. Combining this with an instability of the longitudinal forces in the 3NN shell and decreases in magnitude of the 1NN transverse forces also occurring around 750 K, we have found strong evidence for dynamical precursors to the BCC-FCC phase transition at 1185 K. The phonon DOS were also used to determine the various components of the phonon entropy of iron as a function of temperature up to T_{C}. The anharmonic entropy obtained from the shifts of phonon frequencies was quite large, approaching 4% of the total entropy at the Curie point. Electronic contributions to the entropy were also calculated, and by comparison to the total entropy we concur that the magnetic contributions to the entropy must continue to increase above T_{C}, indicating some persistent short range order.

Chapter 13

Chromium and Vanadium

Here we consider inelastic neutron scattering measurements of the phonons in BCC chromium and vanadium. The treatment is significantly less detailed than those of Chapters 9–12. The information presented here will be used in subsequent discussion of trends in the phonons of cubic metals.

Extensive high temperature measurements of the phonon spectra of chromium have been made by Trampenau *et al.* [39] and of vanadium by Bogdanoff *et al.* [54] and Delaire *et al.* [41]; however, as we have made our own measurements of the former and have direct access to the data for the latter, we will very briefly present these data here. We will only consider the anharmonic phonon entropy, and fits of the high temperature phonon spectra using the low temperature DOS. Briefly, these fits consist of shifting the energy $E \rightarrow \Delta^s E$ of the low temperature spectrum and then performing an integral transform using the damped harmonic oscillator function as a kernel:

$$B(\mathcal{Q}, E', E) = \frac{1}{\pi \mathcal{Q} E'} \frac{1}{\left(\frac{E'}{E} - \frac{E}{E'}\right)^2 + \frac{1}{\mathcal{Q}^2}} , \tag{13.1}$$

where $\mathcal{Q}$ is a quality factor. That is:

$$g_T(E) = B(\mathcal{Q}, E', E) \odot g_{10}(\Delta^s E') , \tag{13.2}$$

with Δ^s and $\mathcal{Q}$ determined through least squares analysis. The subscript 10 refers to 10 K, the lowest temperature measurement of the phonon spectra for vanadium and chromium. Unless noted otherwise, *all* experimental and data analysis procedures are the same as those detailed in Chapter 9 and its references.

For both the chromium and the vanadium, a difference that should be pointed out between the fits shown here and those in Chapters 9, 10, and 11 is that these fits rely on data from two different instruments. That is, the 10 K measurements from LRMECS were used to fit high temperature data from Pharos. Presumably, the latter instrument is higher resolution; and this may have an impact on the optimized values of $\mathcal{Q}$. At 300 K, we have measurements from both instruments, and

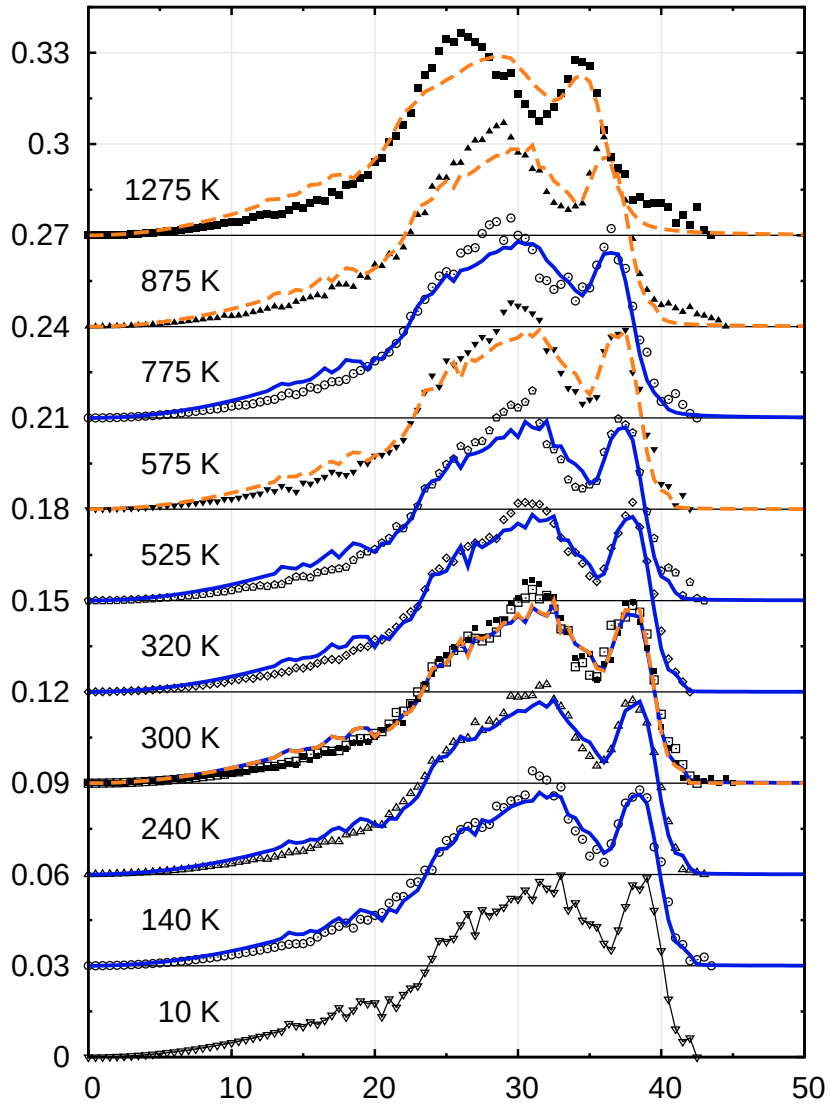

Figure 13.1: Phonon DOS of chromium at temperatures as indicated. Unfilled markers are from LRMECS measurements, solid markers from Pharos. The solid black line at 10 K simply connects the experimental data points. Solid blue lines and dashed orange lines are respectively fits to LRMECS or Pharos data using Eqs. 13.1 and 13.2.

these are shown in Figs. 13.1 and 13.2. At least for chromium, the phonon DOS from LRMECS appears to be a very slightly broadened version of the Pharos measurement. For vanadium, the LRMECS spectrum actually appears to be sharper. Regardless, fits to both 300 K measurements are also shown in Figs. 13.1 and 13.2, and the differences are negligible. We take this as an indication that the fitting procedure gives reasonable results for $\mathcal{Q}$ and Δ^s, despite the differences in the two instruments.

Chromium samples were prepared by crushing 99.995% pure chromium ingot into a coarse powder powder. The powder was then sealed in quartz tubes and annealed at 1200 K for 24 hours to remove

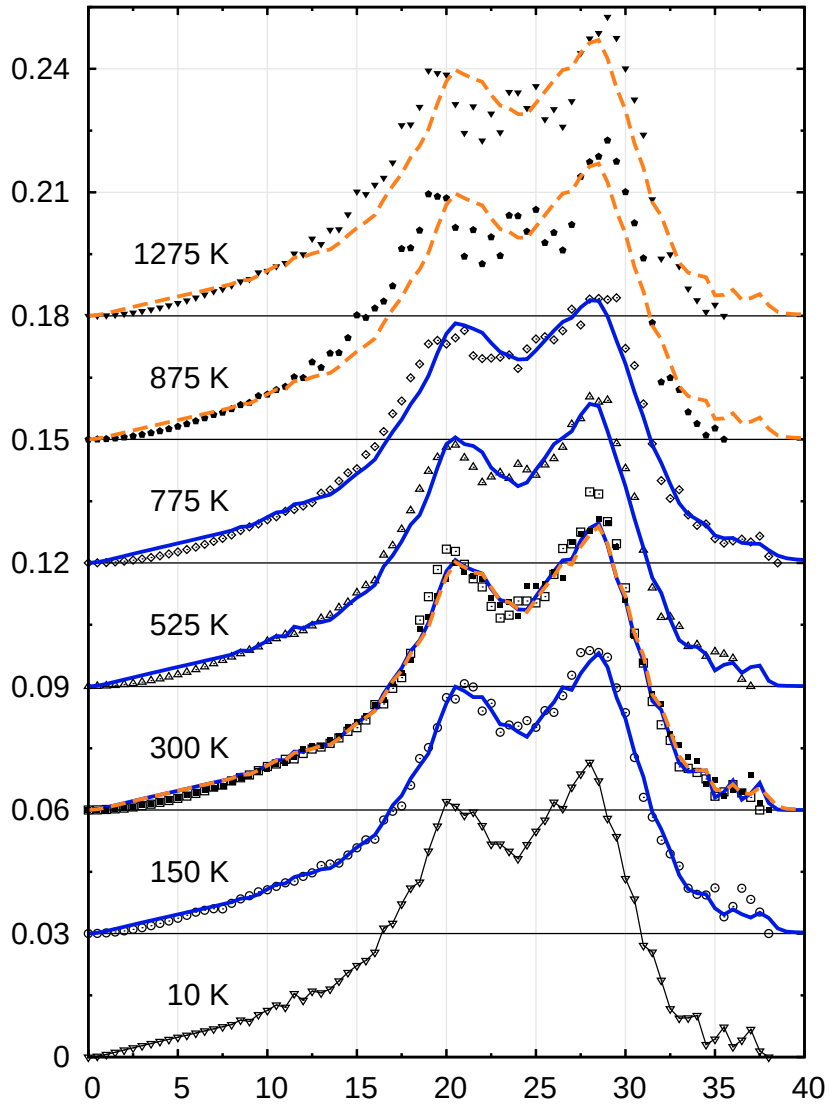

Figure 13.2: Phonon DOS of vanadium at temperatures as indicated. Unfilled markers are from LRMECS measurements, solid markers from Pharos. The solid black line at 10 K simply connects the experimental data points. Solid blue lines and dashed orange lines are respectively fits to LRMECS or Pharos data using Eqs. 13.1 and 13.2.

strain and induce recrystallization. There were minimal signs of oxidation on the sample surface; however x-ray and in-situ neutron diffraction patterns indicated that the bulk samples were largely free of oxidation. Vanadium samples were made by cutting and rolling a vanadium slab of 99.998% purity.[a] The rolled vanadium strips were then sealed in quartz tubes and annealed at 1200 K for 24 hours to remove strain and induce recrystallization. There were no visible signs of oxidation.

The inelastic scattering of neutrons from chromium was measured in experiments at LRMECS at 10, 140, 240, 300, 320, 575, and 775 K, and at Pharos at 300, 575, 875, and 1275 K. For vanadium,

[a]Just for kicks, we point out that the slab was purchased on E-bay.

measurements were made at 10, 150, 300, 525, and 775 K on LRMECS and at 300, 875, and 1275 K on Pharos. At all temperatures, the measured scattering was reduced to a phonon spectrum, and these are shown as markers in Figs. 13.1 and 13.2, and the lines are fits using Eqs. 13.1 and 13.2.

For chromium, the fits have failed noticeably by the time the temperature reaches 1275 K, and there is evidence of the failure already at 525 K. Specifically, the low transverse modes appear to move to lower energies at a higher rate than the high transverse or longitudinal modes. More generally, Trampenau *et al.* found chromium to be highly anharmonic, and our measurements agree. Using the data from Trampenau *et al.*, Eriksson *et al.* [36] find $S_{\mathrm{ph,A}} \approx 0.83$ at melting. Finally, we note that the melting temperature of chromium is 2180 K, thus the failure at our model is apparent by $T/T_M \approx 0.24$

Similar to chromium, the low transverse modes in vanadium shift faster than the high transverse or longitudinal modes. The first clear signs of our model failing appear at about 525 K, and it is still worse by 1275 K. As the melting temperature of vanadium is 2183 K, we see the model failing by $T/T_M \approx 0.24$. The anharmonic entropy of vanadium is bit odd, with a minimum of $S_{\mathrm{ph,A}} \approx -0.13 k_{\mathrm{B}}$/atom at roughly 1200 K, rising to a maximum of $S_{\mathrm{ph,A}} \approx 0.17 k_{\mathrm{B}}$/atom at melting. [36]

In summary, phonons in chromium and vanadium appear to broaden less than the FCC metals. At sufficiently high temperatures — $\frac{T}{T_M} \gtrsim 0.3$ — characterizing the phonon linewdiths becomes somewhat problematic because of the differential motion of the longitudinal, low transverse, and high transverse modes.

Part V

Phonon Trends in Cubic Metals

Chapter 14

Anharmonicity and the Shape of the Phonon DOS

Here we will outline similarities and differences in the phonon spectra of BCC and FCC transition metals, as well as of the nearly free electron (NFE) metals lead and aluminum. Specifically, we consider the phonon entropy and the force constants from BvK models, and we will argue that there are greater similarities amongst the FCC metals than amongst the BCC.

To get a quick sense of the temperature dependencies of the phonons in these materials, we first consider anharmonic contributions to the phonon entropy at melting. Table 14.1 shows $S_{\mathrm{ph,A}}$ at melting for BCC and FCC transition metals and the NFE FCC metals aluminum and lead. The difference in the range of values is remarkable, with the BCC metals spanning -0.09 to 0.72 k_{B}/atom, whereas the FCC metals span only -0.15 to 0.00 k_{B}/atom.[a] The FCC metals are largely quasi-harmonic, with expansion against the bulk modulus accounting for nearly all of the nonharmonic phonon entropy. This is also true for the BCC metals niobium and tantalum and to some extent vanadium; however, for iron, chromium, tungsten, and molybdenum, the anharmonic entropy is quite significant.

Looking now at the forces, for any BvK model, we may determine the longitudinal and transverse force constants for a given shell of neighbors using the procedure described in § 8.3.2. The longitudinal force constants for first- and second-nearest neighbor (1NN and 2NN) and the transverse force constants for 1NN so determined are shown for FCC metals in Table 14.2 and for BCC metals in Table 14.3. There are some rather striking trends in these data. For all of the FCC metals, the 1NN longitudinal force constants are at least 3.8 times larger than the 2NN longitudinal force constants. If we discard iridium — this is the metal with the least available experimental data — then the 1NN longitudinal forces are at least 5.8 times as large as the 2NN ones. For the BCC metals, on the other hand, only the 1NN forces in tantalum are this large relative to the 2NN ones. In fact, the 2NN forces are larger than their 1NN counterparts in molybdenum and in chromium at

[a] We have taken our adjusted value for aluminum to be reliable, but not so our value for lead.

Table 14.1: Anharmonic entropies at melting from Wallace [37] and from the present work. For the latter, we give the value at the highest measured temperature, and assume that the trend at that temperature will continue to melting. This is probably quite reasonable for aluminum, lead, and nickel. For iron, however, there remains one magnetic and two structural phase transitions before melting, making an estimate of $S_{\mathrm{ph,A}}$ more difficult.

Structure	Element	$S_{\mathrm{ph,A}}$ at $T = T_M$ (k_B/atom)	
		Wallace	Present Work
FCC	Ni	0.00	$\leq$ -0.06
	Al	0.01	$\leq$ -0.07
	Cu	0.00	–
	Pb	-0.04	$\leq$ -0.20
	Ag	-0.07	–
	Au	-0.09	–
	Pd	-0.03	–
	Pt	-0.15	–
	Rh	–	–
	Ir	–	–
BCC	W	0.59	–
	Nb	-0.09	–
	Mo	0.72	–
	V	0.16	–
	Ta	-0.07	–
	Cr	0.58	–
	Fe	–	$\gg$ 0.28

all but the highest temperature.

Another trend can be seen in the signs of the 1NN transverse force constants. The average of these constants is negative for *all* of the FCC metals. With the exceptions of aluminum at 525 and 775 K this is true also of the unaveraged transverse force constants. The BvK models for aluminum at high temperatures were perhaps overly simplified, as they included forces only to the 3NN shell despite the fact that the forces in NFE aluminum are known to be fairly long range. This could very well explain why these two models are an exception to the rule. For the BCC metals, with the exceptions of chromium at 1773 K, and of Fe at 773 and 1023 K, all of the transverse constants are positive. For chromium, the negative values are likely not statistically different from zero, or from small positive values, and we believe that the negative values in iron above 773 K are precursors to the BCC to FCC transition at 1185 K. Physically, this means that whereas the FCC metals have repulsive forces in the transverse directions, the BCC transition metals appear to have attractive ones. *Very* closely related is the trend found by Brockhouse *et al.* [245] that $[\mathbf{K}_1]_{xx} < [\mathbf{K}_1]_{xy}$ for FCC transition metals and $[\mathbf{K}_1]_{xx} > [\mathbf{K}_1]_{xy}$ for BCC transition metals. For non-transition BCC metals, such as sodium and potassium, they find the opposite inequality.[b] They concluded that this suggests that the d-electrons are involved in some sort of covalent bonding in the BCC transition

[b] Roughly, these trends are the same, and are related through the Gershgorin circle theorem. [298]

Table 14.2: 1NN and 2NN Longitudinal force constants, $\mathcal{K}_1$ and $\mathcal{K}_2$, as well as 1NN transverse force constants, $\mathcal{K}_1^{\mathrm{T}1}$ and $\mathcal{K}_1^{\mathrm{T}2}$, from Born–von Kármán models for FCC metals. The ratio of the longitudinal force constants in the 2NN and 1NN shell, $\mathcal{K}_2/\mathcal{K}_1$, and the mean value of the transverse force constants in the 1NN shell, $\langle\mathcal{K}_1^{\mathrm{T}j}\rangle$, are also shown. All force constants given in N/m.

Symbol	T (K)	$\mathcal{K}_1$	$\mathcal{K}_2$	$\mathcal{K}_2/\mathcal{K}_1$	$\mathcal{K}_1^{\mathrm{T}1}$	$\mathcal{K}_1^{\mathrm{T}2}$	$\langle\mathcal{K}_1^{\mathrm{T}j}\rangle$
Al	10	21.26	2.45	0.12	-1.36	-1.04	-1.20
	150	20.41	2.41	0.12	-1.20	-0.99	-1.09
	300	20.09	2.22	0.11	-2.06	-0.67	-1.36
	525	19.77	1.97	0.10	-3.37	1.31	-1.03
	775	19.08	1.96	0.10	-3.46	1.14	-1.16
Ni	10	36.56	0.97	0.03	-1.39	-0.39	-0.89
	300	35.80	0.89	0.02	-0.71	-0.27	-0.49
	575	35.41	1.24	0.03	-2.24	-0.38	-1.31
	875	33.58	0.92	0.03	-1.76	-0.32	-1.04
	1275	30.89	1.01	0.03	-2.94	-0.34	-1.64
Cu	49	27.91	-0.04	-0.00	-1.35	-1.35	-1.35
	295	27.92	0.36	0.01	-1.72	-1.42	-1.57
	296	28.37	0.29	0.01	-1.81	-1.25	-1.53
	298	27.75	0.53	0.02	-1.50	-1.50	-1.50
	673	26.34	0.70	0.03	-1.79	-1.32	-1.55
	973	26.07	1.55	0.06	-2.70	-1.42	-2.06
	1336	25.37	0.24	0.01	-1.94	-1.79	-1.86
Rh	297	40.89	6.96	0.17	-4.03	-0.69	-2.36
Pd	120	42.95	0.92	0.02	-3.43	-2.51	-2.97
	296	41.76	1.42	0.03	-3.09	-2.83	-2.96
	673	38.95	1.39	0.04	-3.75	-2.41	-3.08
	853	38.15	2.00	0.05	-3.38	-2.88	-3.13
Ag	296	23.03	0.06	0.00	-1.75	-1.61	-1.68
Ir	0	46.89	12.15	0.26	-2.53	-2.04	-2.29
Pt	90	55.62	3.94	0.07	-6.92	-3.95	-5.44
Au	296	36.36	4.04	0.11	-6.54	-3.50	-5.02
Pb	80	9.00	1.41	0.16	-2.49	-0.35	-1.42

metals.

There has been some theoretical work on determining the shape of phonon spectra based on the space group symmetries of a crystal. [72, 299–302] In particular, Rosenstock [300] determined the locations of the critical points of the phonon spectra for simple-, body-centered-, and face-centered-cubic lattices, given forces that went out to only 2NN. This is an underestimate of the range of the forces in typical metals; in particular, the forces in aluminum and lead are known to be very long range. Regardless, in this model, the ratio of the 2NN to 1NN force constants determines the shape of the phonon spectrum. For FCC metals, the phonon spectrum has different shapes for the

Table 14.3: 1NN and 2NN Longitudinal force constants, $\mathcal{K}_1$ and $\mathcal{K}_2$, as well as 1NN transverse force constants, $\mathcal{K}_1^{\mathrm{T}1}$ and $\mathcal{K}_1^{\mathrm{T}2}$, from Born–von Kármán models for BCC metals. The ratio of the longitudinal force constants in the 2NN and 1NN shell, $\mathcal{K}_2/\mathcal{K}_1$, and the mean value of the transverse force constants in the 1NN shell, $\langle\mathcal{K}_1^{\mathrm{T}j}\rangle$, are also shown. All force constants given in N/m.

Symbol	T (K)	$\mathcal{K}_1$	$\mathcal{K}_2$	$\mathcal{K}_2/\mathcal{K}_1$	$\mathcal{K}_1^{\mathrm{T}1}$	$\mathcal{K}_1^{\mathrm{T}2}$	$\langle\mathcal{K}_1^{\mathrm{T}j}\rangle$
Cr	293	28.21	37.70	1.34	7.42	7.42	7.42
	673	32.38	27.52	0.85	2.41	2.41	2.41
	1073	30.20	27.44	0.91	1.85	1.85	1.85
	1473	30.22	23.16	0.77	1.42	1.42	1.42
	1773	29.41	19.10	0.65	-0.05	-0.05	-0.05
Fe	21	47.08	15.31	0.33	2.35	2.35	2.35
	295	46.09	14.57	0.32	1.27	1.27	1.27
	523	44.62	15.10	0.34	1.15	1.15	1.15
	773	42.59	15.29	0.36	-0.47	-0.47	-0.47
	923	41.48	12.73	0.31	0.29	0.29	0.29
	1023	40.64	12.83	0.32	-0.32	-0.32	-0.32
Nb	293	33.08	13.33	0.40	3.23	3.23	3.23
	773	32.70	13.32	0.41	3.62	3.62	3.62
	1773	32.82	12.11	0.37	2.74	2.74	2.74
	2223	31.84	12.46	0.39	1.63	1.63	1.63
Mo	296	40.07	44.57	1.11	4.73	4.73	4.73
Ta	296	39.38	1.42	0.04	5.78	5.78	5.78
W	298	59.90	45.70	0.76	3.20	3.20	3.20

following cases:

$$\begin{gathered}\mathcal{K}_2/\mathcal{K}_1 < -0.067\\ \mathcal{K}_2/\mathcal{K}_1 = -0.067\\ -0.067 < \mathcal{K}_2/\mathcal{K}_1 < 0.0\\ \mathcal{K}_2/\mathcal{K}_1 = 0.0\\ 0.0 < \mathcal{K}_2/\mathcal{K}_1\end{gathered} \tag{14.1}$$

For BCC metals, we have the following cases:

$$\begin{gathered}\mathcal{K}_2/\mathcal{K}_1 < 0.0\\ \mathcal{K}_2/\mathcal{K}_1 = 0.0\\ 0.0 < \mathcal{K}_2/\mathcal{K}_1\end{gathered} \tag{14.2}$$

Taking the longitudinal force constants to be most representative, and ignoring forces past the 2NN shell, we may calculate these ratios from the force constants for the BvK models shown in Fig. 14.1. The ratios for the FCC metals are given in Table 14.2 and for BCC metals in Table 14.3. Despite the variety of shapes available, particularly for FCC metals, the values all indicate the same shape

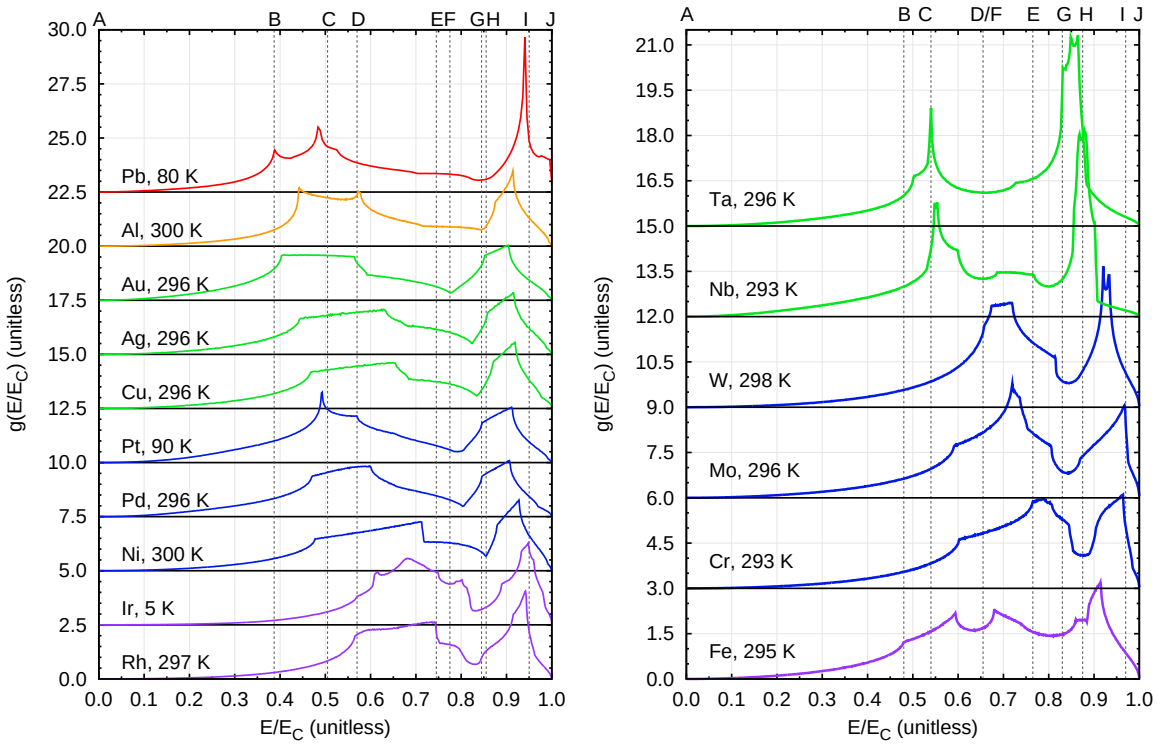

Figure 14.1: Phonon DOS near room temperature from BvK models for FCC and BCC metals in the left and right hand panels, respectively. Note that the cutoff energy, E_C, is temperature dependent. The spectra for the FCC metals appear to have much more in common than those for the BCC metals. The meanings of the vertical lines (marked by letters) are described in Table 14.4 and in the text.

for either FCC or BCC metals.[c] The values for the FCC metals are distributed over a small range, from 0.003 to 0.259, whereas the BCC metals range from 0.030 up to 1.112.

Looking at Fig. 14.1 and the associated Table 14.4, we may identify some trends in the shapes of the phonon spectra for the cubic metals. First, consider a general description of these phonon spectra, where we have renormalized the energy using the cutoff energy, E_C. Starting at $E/E_C = 0$, the spectra rise monotonically to a critical point (CP). For sufficiently small E/E_C, the rise is quadratic as in a Debye model of a crystal. For larger E/E_C, higher order polynomial terms are required. The first transverse modes dominate between this first CP and another CP, after which the second transverse modes begin to dominate. The second transverse modes then decline in density until a local minimum is reached. After the minimum, the longitudinal modes begin to dominate until, finally, the density of longitudinal modes drops off rather sharply and the spectrum goes to zero at $E/E_C = 1$.

The biggest difference between the shapes of the spectra for the FCC and BCC metals concerns

[c]The model of the 49 K copper DOS actually gives $\frac{\mathcal{K}_2}{\mathcal{K}_1} = -0.001$, which would indicate a different shape of the DOS. This value, however, is *very* small, relative to the errors.

Table 14.4: Shapes of phonon spectra from BvK models for FCC and BCC metals. E_C is the cutoff energy, CP1 stands for first critical point, L for longitudinal, T for transverse, and TX for X^{th} transverse, X$\in \{1, 2\}$. "First" and "Last" refer respectively the lowest and highest energy occurrences of some feature for the set of phonon DOS in question.

		E/E_C		
Label	Description	FCC	BCC	Comments
A		0.000	0.000	
B	First CP1	0.385	0.480	
C	First T1 peak to "end"	0.505	0.540	Unclear for FCC Pb
D	Last CP1	0.570	0.655	
E	Last T1 peak to "end"	0.745	0.765	
F	First minimum between T and L peaks	0.775	0.655	Unclear for BCC Ta
G	First CP starting L peak	0.845	0.830	
H	Last minimum between T and L peaks	0.855	0.875	
I	Last CP ending L peak	0.950	0.970	Unclear for FCC Ir
J		1.000	1.000	

the existence of a single local minimum between the transverse and longitudinal peaks. For the FCC metals, shown in the left hand panel of Fig. 14.1, this minimum is easy to find, is the only local minimum after the first transverse peak has died out, and lies between 77 and 86% of the cutoff energy, as marked by the letters F and H. Further, the longitudinal peaks for *all* of the FCC spectra are concentrated between the lines marked G and I, at energies higher than *all* of these minima.[d] For the BCC metal tantalum, shown in the right hand panel of Fig. 14.1 it is not even clear where this minimum lies, or if it exists at all. The letter F marks the only obvious local minimum after the first transverse peak in tantalum; however, it seem likely that this is before the second transverse peak, rather than after it. The density in the longitudinal modes for tantalum is almost gone by the point H at which the minimum appears in the chromium spectrum. There are no obvious minima between the first and second transverse modes for the FCC metals; however, the BCC metals sometimes show such minima and sometimes do not. At lower energies, the spread in the starting points for the the first transverse modes in the FCC metals is larger than for the BCC metals, as marked by the letters B and D in the left and right hand panels of Fig. 14.1. Similarly for the ends of the first transverse modes, as marked by the letters C and E. Overall, the FCC metals appear to have more similarities in the shape of their spectra than do the BCC metals — certainly at medium and high energies.

A similar trend is visible as a function of temperature, as shown in Fig. 14.2. Once normalized for the cutoff energy, E_C, the changes in the phonon spectra with temperature for the FCC metals aluminum, nickel, copper, and palladium is much less noticeable than the changes for the BCC metals chromium iron and niobium.[e] In particular, the transverse modes in the BCC metals —

[d] There is a tiny overlap between the first CP of the longitudinal peak in palladium at G and the minimum between the peaks in gold at H.

[e] There appear to be more changes in aluminum than in the other FCC metals; however, some of this may be do

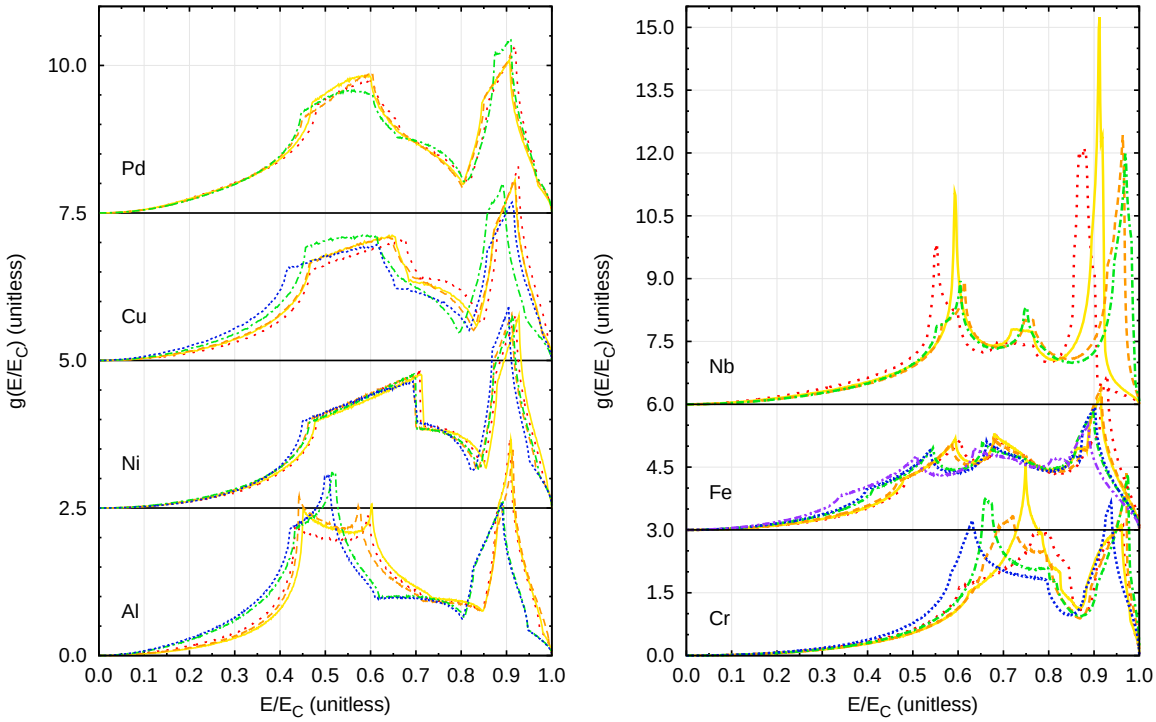

Figure 14.2: Temperature dependence of phonon DOS for BCC and FCC metals from BvK models are shown in the left and right hand panels, respectively. Note that the cutoff energy, E_C, is a function of temperature. The shape of the phonon spectra for the FCC metals are much more consistent than those of the BCC metals. (From cold to hot, the curves are sparsely-dotted red, dashed orange, solid yellow, dash-dotted green, densely-dotted blue, and dash-double-dotted purple; and the relevant temperatures for the FCC and BCC metals are listed in Tables 14.2 and 14.3, respectively.)

especially for chromium and niobium — appear to change much more with temperature than do those in the FCC metals. For niobium, there also appear to be significant shifts in the longitudinal modes.

In so much as differences between the phonon spectra of the FCC and BCC metals may be attributed to differences in the transverse modes (as opposed to the longitudinal ones), we may understand their differences in terms of the structural stability of the two crystal lattices. [303, 304] Fig. 14.3 shows a central atom and its nearest neighbors in the simple cubic (SC), BCC, and FCC lattices. Assuming that only there are only central forces between 1NN, for all three lattices, we may not move an atom towards its 1NN without inducing a force on those atoms. For the case of the SC lattice, consider the 1NN that are not on the pictured plane. For any small rotation of these atoms about the central atom, there is no restoring force.[f] The SC lattice, then, has some structural

to shorter range of the forces in the models for the highest temperature. For example, this also seems to have had an effect on the transverse force constants as seen in Table 14.2 and discussed in the text.

[f]Consider planes parallel to the one pictured, that pass through the out-of-plane atoms. If these planes pivot so as to remain parallel while the out-of-plane atoms undergo their rotation, then there is no restoring force throughout the entire lattice.

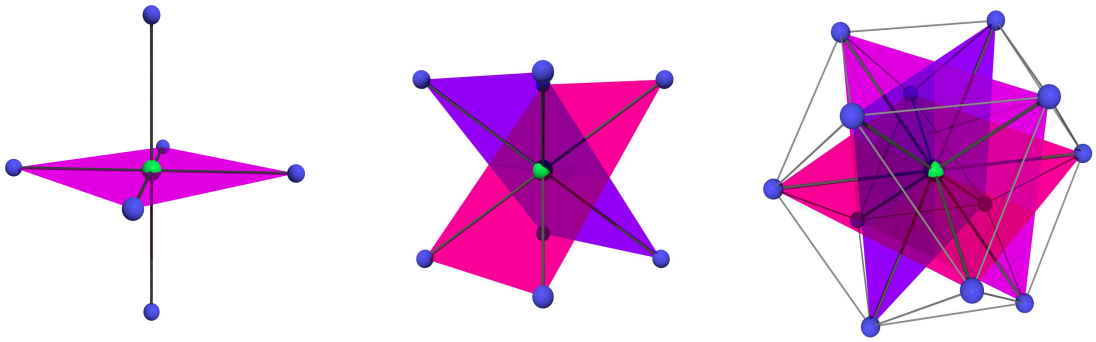

Figure 14.3: First nearest neighbors for SC, BCC, and FCC lattices are shown in the left, center, and right panels, respectively. The 1NN bonds are given by thin cylinders connecting the atoms. The planes pass through the central atom and as many 1NN atoms as possible. For the SC and BCC lattices, the only 1NN bonds visible are those connecting to the central atom; however, for the FCC lattice some of the 1NN are also 1NN of each other.

instability in transverse directions. There are fewer degrees of freedom for the BCC lattice; however, we may still rotate one plane about the line where the planes intersect without inducing a restoring force. In the FCC lattice, there are no such degrees of freedom. That is, structurally, the FCC lattice is stable to all displacements, longitudinal or transverse. This is directly related to the trends we see in the non-central, 1NN force constants for the FCC and BCC metals. Specifically, the 1NN transverse forces in the BCC metals are necessarily bonding in nature to compensate for the structural instability, whereas those force in the FCC metals can be repulsive. Structural differences are also responsible for the trend of 2NN force constants being more significant in BCC than in FCC metals, simply because the ratio of 1NN to 2NN distances is 0.87 as opposed to 0.71. That is, the 2NN in a BCC lattice are not significantly farther away than the 1NN, which is not the case for FCC lattices.

Finally, we consider the phonon linewidths as a function of temperature. Looking at Figs. 9.3, 10.5, and 11.4, we see that for the FCC metals aluminum, lead, and nickel, our simple model of the phonon linewidths begins showing the first signs of failure at roughly $T/T_M = 525/933 = 0.56$, $T/T_M = 390/600 = 0.65$, and $T/T_M > 1275/1728 = 0.74$, respectively. From Figs. 12.3, 13.1, and 13.2, we see the first signs of failure at roughly $T/T_M = 775/1811 = 0.43$, $T/T_M = 525/2180 = 0.24$, and $T/T_M = 525/2183 = 0.24$ respectively for the BCC metals iron, chromium, and vanadium. In short, this simplified model of the phonon broadening appears to be much more robust in the FCC metals than in the BCC metals. As such, we consider phonon linewidths in the FCC metals in greater detail.

Chapter 15

Mean Phonon Linewidths in FCC metals

15.1 Introduction

Anharmonic effects in solids cause non-zero phonon linewidths in addition to more widely known phenomena such as shifts in phonon energies, thermal expansion, and temperature-dependent elastic constants. [50–52] Phonon broadening can be a prominent feature in inelastic scattering experiments, as seen in the plots of $S(Q, E)$ for aluminum, lead, and nickel in Fig. 15.1, and in the plots of the phonon densities of states (DOS) in Figs. 9.3, 10.5, and 11.4. The shifts in phonon energy can sometimes be predicted by a quasiharmonic model [36–38] in terms of the bulk modulus and the temperature-dependent lattice parameter; however, to our knowledge, a simple model to predict phonon linewidths doesn't exist, despite a number of systems that appear to have simple trends (see, for example, Chaps. 9, 10, and 11).

In Chapter 14, we saw that a wide variety of behaviors exists for phonons in BCC metals; whereas there is greater uniformity in the phonons in the elemental FCC metals. Table 14.1, shows similarities in their anharmonic entropies, which may be understood in terms of the shifts of phonon energies. [36–38] There are further likenesses in the shape of their phonon spectra, and in their near-neighbor force constants. Because of these similarities, we have focused our study on FCC metals, and we hypothesize and explore a simple model for predicting phonon linewidths in FCC metals based on damped harmonic oscillators.

In this chapter, we give a brief review of damped, driven harmonic oscillators and the relationship between quality factors, linewidths and lifetimes. Also a brief review of molecular dynamics is given. A simple molecular dynamics simulation of a linear chain is used to illustrate the possible meaning of quality factors in conservative systems. We then examine our simple model for predicting the phonon linewidths in FCC metals in light of the results of a series of simulations and experiments. Namely, we consider molecular dynamics simulations — including determinations of phonon spectra

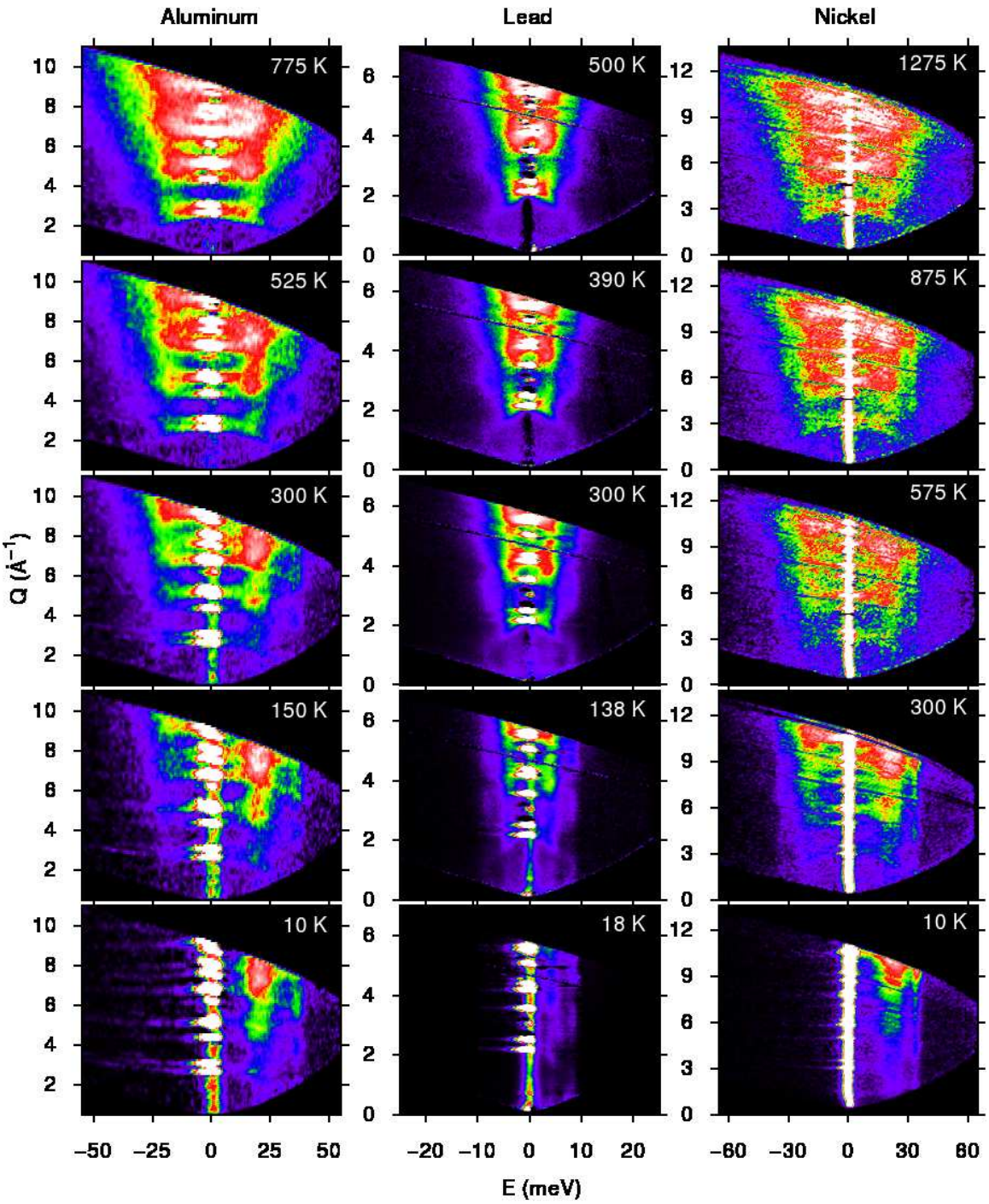

Figure 15.1: $S(Q, E)$ for aluminum, lead, and nickel at temperatures as marked. At low temperatures, dispersive information is visible on the phonon creation side of the spectrum. As the temperature rises, in addition to increased scattering, the dispersive features broaden significantly.

and associated quality factors — for the FCC transition metals nickel, copper, rhodium, palladium, silver, iridium, platinum, and gold, and the nearly free electron (NFE) metals aluminum and lead.

We also consider experimental data for FCC aluminum, lead, and nickel that was presented in Part III, and experimental data for FCC copper taken from triple-axis measurements by Larose and Brockhouse. [60, 305] We find that our simple model is remarkably successful in accounting for the phonon qualities as a function of temperature, and it suggests a deep commonality in the interatomic potentials of the FCC metals.

15.2 Background

15.2.1 Quality factors

We use the notion of a quality factor for oscillatory motion extensively in this chapter, so we review it briefly with respect to some features of the damped harmonic oscillator. More detailed treatments are widely available. [53, 306]

15.2.1.1 Damped driven harmonic oscillators

We have considered the harmonic oscillator and coupled harmonic oscillators in § 3.3 and 3.4. We now add a dissipative term, $C\dot{u}$, to the 1D harmonic oscillator, giving the following equation of motion:

$$0 \;=\; M\ddot{u} + C\dot{u} + Ku \;=\; \ddot{u} + \frac{\omega'}{\mathcal{Q}}\dot{u} + \omega'^2 u \;, \tag{15.1}$$

where u is the displacement of the mass M, K is a spring constant, and C a damping constant. We have also defined the undamped frequency $\omega' = \sqrt{\frac{K}{M}}$ and the quality factor $\mathcal{Q} = \frac{\sqrt{MK}}{C}$. For $\mathcal{Q} > \frac{1}{2}$, a solution to the equation is:

$$u \;=\; \exp\left(-\frac{\omega'}{2\mathcal{Q}}t\right)\cos(\omega t) \;, \tag{15.2}$$

$$\dot{u} \;=\; -\frac{\omega'}{2\mathcal{Q}}\exp\left(-\frac{\omega'}{2\mathcal{Q}}t\right)\cos(\omega t) - \omega\exp\left(-\frac{\omega'}{2\mathcal{Q}}t\right)\sin(\omega t) \;, \tag{15.3}$$

$$\ddot{u} \;=\; \left[\frac{\omega'^2}{4\mathcal{Q}^2} - \omega^2\right]\exp\left(-\frac{\omega'}{\mathcal{Q}}t\right)\cos(\omega t) + \frac{\omega\omega'}{\mathcal{Q}}\exp\left(-\frac{\omega'}{2\mathcal{Q}}t\right)\sin(\omega t) \;, \tag{15.4}$$

where we have defined:

$$\omega^2 \equiv \left(1 - \frac{1}{4\mathcal{Q}^2}\right)\omega'^2 \;. \tag{15.5}$$

The oscillatory solutions to this equation are modulated by an exponential decay as is illustrated in Fig. 15.2.

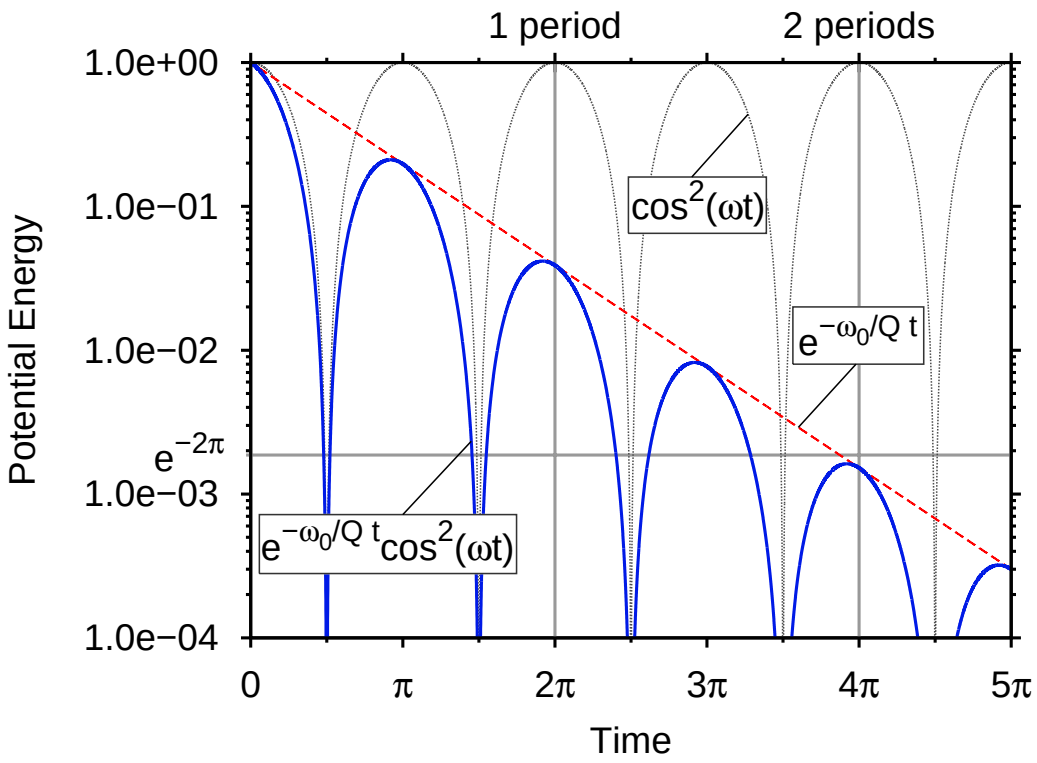

Figure 15.2: The potential energy of a damped harmonic oscillator with $\omega = 1$ and $\mathcal{Q} = 2$. The dense-dotted gray line shows the potential energy for the oscillations in the absence of damping ($Q = \infty$) with $\omega' = \omega$. The dashed red line shows decay envelope, and the solid blue line shows the potential energy for the damped oscillator. After approximately $\mathcal{Q} = 2$ periods, the potential energy in the oscillations has decreased by a factor of $e^{2\pi}$.

15.2.1.2 Effects of damping: shifts, quality factors, linewidths, and lifetimes

To compare with anharmonic phonons, we consider the frequency shift, $\Delta\omega \equiv \omega - \omega'$, caused by the damping term in the equation of motion:

$$\frac{\Delta\omega}{\omega'} \quad = \quad \frac{\omega - \omega'}{\omega'} = \sqrt{1 - \frac{1}{4\mathcal{Q}^2}} - 1 \approx -\frac{1}{8\mathcal{Q}^2} \; . \tag{15.6}$$

In this model, the frequency shift and the quality factor are inversely related.[a]

The quality factor is unitless, and approximately equals the number of oscillations before the energy in the oscillations decays by a factor of $e^{2\pi}$. Systems for which $\mathcal{Q} > \frac{1}{2}$ are called *underdamped*, and this classification applies to all of the oscillations considered here. If $\mathcal{Q} < \frac{1}{2}$ the system does not oscillate at all, and such systems are called *overdamped*. Finally, if $\mathcal{Q} = \frac{1}{2}$ the system is said to be *critically damped*.

The quality factor is related to the linewidth of the damped harmonic oscillator as measured in

[a] $\Delta\omega$ should not be confused with a linewidth, an equation for which we will derive shortly.

a scattering experiment. We demonstrate this by considering a driving force $F = F(t)$:

$$\frac{F}{M} = \ddot{u} + \frac{\omega'}{\mathcal{Q}}\dot{u} + \omega'^2 u \ . \tag{15.7}$$

We now take the Fourier transform:

$$\frac{1}{M}\mathcal{FT}\{F\} = -\omega^2\mathcal{FT}\{u\} + i\omega\frac{\omega'}{\mathcal{Q}}\mathcal{FT}\{u\} + \omega'^2\mathcal{FT}\{u\} \ , \tag{15.8}$$

which yields the transfer function:

$$\begin{aligned}
\frac{\mathcal{FT}\{u\}}{\mathcal{FT}\{F\}} &= \frac{1}{M}\frac{1}{-\omega^2 + \omega'^2 + \frac{i\omega\omega'}{\mathcal{Q}}} \\
&= \frac{1}{M}\left(\frac{1}{-\omega^2 + \omega'^2 + \frac{i\omega\omega'}{\mathcal{Q}}}\right)\left(\frac{-\omega^2 + \omega'^2 - \frac{i\omega\omega'}{\mathcal{Q}}}{-\omega^2 + \omega'^2 - \frac{i\omega\omega'}{\mathcal{Q}}}\right) \\
&= \frac{1}{M\omega'^2\omega^2}\frac{\omega'^2 - \omega^2}{\left[\frac{\omega'}{\omega} - \frac{\omega}{\omega'}\right]^2 + \frac{1}{\mathcal{Q}^2}} + i\frac{1}{M\omega'^2\omega^2}\frac{\frac{\omega'\omega}{\mathcal{Q}}}{\left[\frac{\omega'}{\omega} - \frac{\omega}{\omega'}\right]^2 + \frac{1}{\mathcal{Q}^2}} \ .
\end{aligned} \tag{15.9}$$

The fluctuation-dissipation theorem [307–312] relates the spectrum of fluctuations (related, in turn, to the incoherent inelastic scattering) to the imaginary (or dissipative) part of the transfer function, and we consider this here:

$$\Im\left(\frac{\mathcal{FT}\{u\}}{\mathcal{FT}\{F\}}\right) = \frac{1}{M\mathcal{Q}\omega\omega'}\frac{1}{\left[\frac{\omega'}{\omega} - \frac{\omega}{\omega'}\right]^2 + \frac{1}{\mathcal{Q}^2}} \ . \tag{15.10}$$

For large $\mathcal{Q}$, we have $\omega \approx \omega'$, and we may write:[b]

$$\frac{\omega'}{\omega} - \frac{\omega}{\omega'} = \frac{1}{\omega'\omega}\left(\omega' - \omega\right)\left(\omega' + \omega\right) \approx \frac{2\left(\omega' - \omega\right)}{\omega'} \ . \tag{15.11}$$

Substituting this into Eq. 15.10, we have:

$$\Im\left(\frac{\mathcal{FT}\{u\}}{\mathcal{FT}\{F\}}\right) \approx \frac{1}{M\mathcal{Q}\omega'^2}\frac{1}{\left[\frac{2(\omega' - \omega)}{\omega'}\right]^2 + \frac{1}{\mathcal{Q}^2}} = \frac{\hbar^2}{4M\mathcal{Q}}\frac{1}{\left(E' - E\right)^2 + \left(\frac{E'}{2\mathcal{Q}}\right)^2} \ . \tag{15.12}$$

This is a Lorentzian with full width at half maximum given by $2\Gamma \approx \frac{E'}{\mathcal{Q}}$. 2Γ, then, is the linewidth measured in a measurement of the spectrum of the oscillator.

The Heisenberg uncertainty principle for time and energy is $2\Gamma\Delta t \geq \frac{\hbar}{2}$; therefore, we expect the lifetime of a quantum mechanical state associated with the driven damped harmonic oscillator to be

[b] Though somewhat disconcerting, this partial substitution of ω' for ω is commonplace, and leads to the expected Lorentzian behavior for high quality resonances.

related to its linewidth and quality factor:

$$2\Gamma = \frac{E'}{\mathcal{Q}} \geq \frac{\hbar}{2\Delta t} \; . \tag{15.13}$$

That is, a phonon with a large linewidth (relative to its energy) also has a short lifetime and a low quality factor.

15.2.2 Molecular dynamics

Molecular dynamics (MD) is a computational technique that takes as input a set of particles and an analytical description of their interactions and produces as output the particle trajectories through configuration space. Generally, the interactions are given as potential energies or force-fields. The work of the simulation consists of evaluating the forces on the particles and integrating the classical equations of motion, and the interest to the scientist is in calculating various physical properties from the trajectories. Here, we give a very brief description of some of the key components of an MD engine. There are many texts that provide more detail. [313–315]

15.2.2.1 Equations of motion and numerical integration

We have, to some extent, already discussed equations of motions for atoms in a crystal in § 3.4.2; however, we limited ourselves to a harmonic potential. One of the great advantages of molecular dynamics, and of simulations in general, is that any potential is amenable.

The positions of all the atoms in the crystal are given by $\mathbf{r} = \mathbf{r}(t)$, then the potential energy is some function of the positions, $\mathcal{V}(\mathbf{r})$. The force on the j^{th} atom in the c^{th} direction, then, is given by:

$$\left[\mathbf{F}_j\right]_c = \left[\mathbf{M}_{jj}\right]_{cc} \left[\ddot{\mathbf{r}}_j\right]_c = -\frac{\partial \mathcal{V}(\mathbf{r})}{\partial \left[\mathbf{r}_j\right]_c} \; . \tag{15.14}$$

We may rewrite the second order differential equations as pairs of coupled first order ones:

$$\left[\dot{\mathbf{r}}_j\right]_c = \left[\mathbf{v}_j\right]_c \; , \tag{15.15}$$

$$\left[\dot{\mathbf{v}}_j\right]_c = -\left[{\mathbf{M}^{-1}}_{jj}\right]_{cc} \frac{\partial \mathcal{V}(\mathbf{r})}{\partial \left[\mathbf{r}_j\right]_c} \; . \tag{15.16}$$

Given the positions and velocities, $\mathbf{r}(t_0)$ and $\mathbf{v}(t_0)$ at some time t_0, we may integrate the equations of motion numerically. The simplest technique for doing this is the forward Euler method. We choose a discrete step in time, Δt, and let $t_m = t_0 + m\Delta t$, which allows us to write:

$$\mathbf{r}(t_m) = \mathbf{r}(t_{m-1}) + \Delta t \left.\frac{\partial \mathbf{r}}{\partial t}\right|_{t=t_{m-1}} = \mathbf{r}(t_{m-1}) + \Delta t \; \mathbf{v}(t_{m-1}) \; . \tag{15.17}$$

This particular integration technique does not enforce conservation of energy. Here, as for most algorithms, the rate of error accumulation is largely dependent on the size of the time step relative to the magnitudes of the velocities of the particles being simulated. For the purpose of molecular dynamics, the Verlet integrators [315–317] are enormously popular because they are time reversible and conserve volume in phase space.[c] These properties, in turn, are related to conservation of energy.

15.2.2.2 Thermostats and barostats

At best, the integration procedures discussed in the previous section conserve energy and particle number. Volume can be conserved through appropriate boundary conditions — for example, periodic boundary conditions are typically used for studies of crystals. These conserved quantities correspond to the microcanonical or NVE ensemble. Experiments, however, are typically conducted at constant temperature and constant pressure, corresponding to the isothermal isobaric or NPT ensemble.

By adding fictitious particles to the equations of motion, we may dynamically reproduce trajectories consistent with an NPT ensemble. [318–322] One possible set of equations is given below:

$$\left[\dot{\mathbf{r}}_j\right]_c = \left[\mathbf{v}_j\right]_c + \mathrm{v}_P \left[\mathbf{r}_j\right]_c \ , \tag{15.18}$$

$$\left[\dot{\mathbf{v}}_j\right]_c = -\left[\mathbf{M}^{-1}{}_{jj}\right]_{cc} \frac{\partial \mathcal{V}(\mathbf{r})}{\partial \left[\mathbf{r}_j\right]_c} - \left\{\left(1 + \frac{\mathcal{D}}{\mathcal{N}}\right)\mathrm{v}_P + \mathrm{v}_T\right\}\left[\mathbf{v}_j\right]_c \ , \tag{15.19}$$

$$\dot{\mathrm{v}}_T = \frac{1}{M_T}\left\{\sum_j \sum_c \left[\mathbf{M}_{jj}\right]_{cc} \left[\mathbf{v}_j\right]_c^2 + M_P \mathrm{v}_P^2 - \left(\mathcal{N}+1\right) k_\mathrm{B} T\right\} \ , \tag{15.20}$$

$$\dot{V} = \mathcal{D} V \mathrm{v}_P \ , \tag{15.21}$$

$$\dot{\mathrm{v}}_P = \frac{\mathcal{D}V}{M_P}\left(P_\mathrm{I} - P\right) + \frac{\mathcal{D}}{\mathcal{N} M_P}\sum_j \sum_c \left[\mathbf{v}_j\right]_c - \mathrm{v}_P \mathrm{v}_T \ , \tag{15.22}$$

$$P_\mathrm{I} = \frac{1}{\mathcal{D}V}\left\{\sum_j \sum_c \left[\mathbf{v}_j\right]_c - \sum_j \sum_c \left[\mathbf{r}_j\right]_c \cdot \frac{\partial \mathcal{V}(\mathbf{r})}{\partial \left[\mathbf{r}_j\right]_c} - \mathcal{D} V \frac{\partial \mathcal{V}(\mathbf{r})}{\partial V}\right\} \ . \tag{15.23}$$

The desired temperature and pressure are given by T and P, the dimension of the problem by $\mathcal{D}$, and the number of degrees of freedom by $\mathcal{N} = \mathcal{D}\mathcal{A}$, where $\mathcal{A}$ is the number of atoms (particles) in the simulation. The internal or instantaneous pressure is given by P_I. The velocity and mass of the fictitious particle responsible for pressure regulation are v_P and M_P, and v_T and M_T are those for the particle involved in temperature regulation. These masses are constants that impact, for example, the frequencies and amplitudes of the volume and temperature fluctuations experienced by the particles in the simulation, and choosing optimal values for a particular simulation is somewhat of a black art.

Simulation in the canonical or NVT ensemble is also possible, and the so-called Nosé–Hoover

[c] They are only time reversible in theory. In practice, numerical error will cause differences in the forward and reverse trajectories.

thermostat[320–325] represents the most common set of equations used to these ends:

$$\begin{aligned}
\left[\dot{\mathbf{r}}_j\right]_c &= \left[\mathbf{v}_j\right]_c \ , & (15.24)\\
\left[\dot{\mathbf{v}}_j\right]_c &= -\left[\mathbf{M}^{-1}{}_{jj}\right]_{cc} \frac{\partial \mathcal{V}(\mathbf{r})}{\partial \left[\mathbf{r}_j\right]_c} - \mathrm{v}_T \left[\mathbf{v}_j\right]_c \ , & (15.25)\\
\dot{\mathrm{v}}_T &= \frac{1}{M_T} \left\{ \sum_j \sum_c \left[\mathbf{M}_{jj}\right]_{cc} \left[\mathbf{v}_j\right]_c^2 - \mathcal{N} k_{\mathrm{B}} T \right\} \ . & (15.26)
\end{aligned}$$

These are the same as Eqs. 15.18–15.20 above, with $\mathrm{v}_P \equiv 0$ and $(\mathcal{N}+1) \rightarrow \mathcal{N}$.

15.2.2.3 Projections onto normal modes

At the end of a molecular dynamics simulation, we know the trajectory for each particle as a function of time, $\mathbf{r}(t)$. In a crystal, we likely know the equilibrium positions of the atoms, $\mathbf{x}$, and we may therefore calculate the displacements:

$$\mathbf{u} = \mathbf{u}(t) = \mathbf{r}(t) - \mathbf{x} \ . \tag{15.27}$$

In general, finding the normal modes of a crystal is rather involved (as seen in § 3.4.2); however, frequently some modes may be found by inspection. Given the displacement pattern for some normal mode, $\boldsymbol{\epsilon}$ we may *project* the particle displacements onto that pattern and look at the amplitude in that mode as a function of time, $A_{\boldsymbol{\epsilon}} = A_{\boldsymbol{\epsilon}}(t)$:

$$A_{\boldsymbol{\epsilon}} = \frac{\mathbf{u}(t) \cdot \boldsymbol{\epsilon}}{|\mathbf{u}(t)|\,|\boldsymbol{\epsilon}(t)|} \ . \tag{15.28}$$

By taking the Fourier transform of the amplitude with respect to time, we may see the frequency response in the particular mode, $\boldsymbol{\epsilon}$.

15.2.2.4 Phonon DOS

The phonon density of states of a simulated material may be found by looking at the Fourier transform of the velocity autocorrelation function: [83, 315, 326–330]

$$\begin{aligned}
\langle \mathbf{v}(0) \cdot \mathbf{v}(t) \rangle &\equiv \frac{1}{\mathcal{M}\mathcal{D}\mathcal{A}} \sum_m^{\mathcal{M}} \sum_j^{\mathcal{A}} \left[\mathbf{v}_j(m\Delta t + t)\right] \cdot \left[\mathbf{v}_j(m\Delta t)\right] \ , & (15.29)\\
g(E) &= \frac{1}{\hbar} \mathcal{FT}\left\{ \frac{\langle \mathbf{v}(0) \cdot \mathbf{v}(t) \rangle}{\langle \mathbf{v}(0) \cdot \mathbf{v}(0) \rangle} \right\} = \frac{1}{2\pi\hbar} \int dt e^{i\omega t} \frac{\langle \mathbf{v}(0) \cdot \mathbf{v}(t) \rangle}{\langle \mathbf{v}(0) \cdot \mathbf{v}(0) \rangle} \ , & (15.30)
\end{aligned}$$

where $\mathcal{M}$ gives the total number of time steps in the simulation.

15.3 Simulation

15.3.1 Qualities in conservative systems: The Fermi-Pasta-Ulam problem

In the 1950s, Fermi *et al.* performed a numerical study of a linear chain of oscillators subject to non-linear forces. [331] Their goal was to witness the rate of approach to equipartition of energy amongst the degrees of freedom in the chain; however, they found instead long-term oscillatory behavior. Here, we have performed the same style of numerical study but with a much shorter chain, and with the intent of looking at behavior that could be considered analogous to dissipation.

Clearly, an anharmonic crystal is a conservative system, and conservative systems do not have dissipative terms. Here, we justify our use of a quality factor in conservative systems by investigating a simple anharmonic system that displays behavior that looks like damping. Specifically, the system we investigated is depicted in Fig. 15.3 and consisted of three atoms, all with mass M, connected to one another by non-linear springs. This simple calculation shows basic effects of anharmonicity.

The initial positions and velocities of the atoms were selected at random, subject to the constraint that the center of mass for the system be stationary. With the definition $u_{jk} \equiv u_j - u_k$, we used the following equations of motion:

$$\begin{aligned} M\ddot{u}_0 &= -K(u_{01}+u_{02}) - K_2(u_{01}^2+u_{02}^2) - K_3(u_{01}^3+u_{02}^3)\,, \\ M\ddot{u}_1 &= -K(u_{12}+u_{10}) - K_2(u_{12}^2+u_{10}^2) - K_3(u_{12}^3+u_{10}^3)\,, \\ M\ddot{u}_2 &= -K(u_{20}+u_{21}) - K_2(u_{20}^2+u_{21}^2) - K_3(u_{20}^3+u_{21}^3)\,. \end{aligned} \tag{15.31}$$

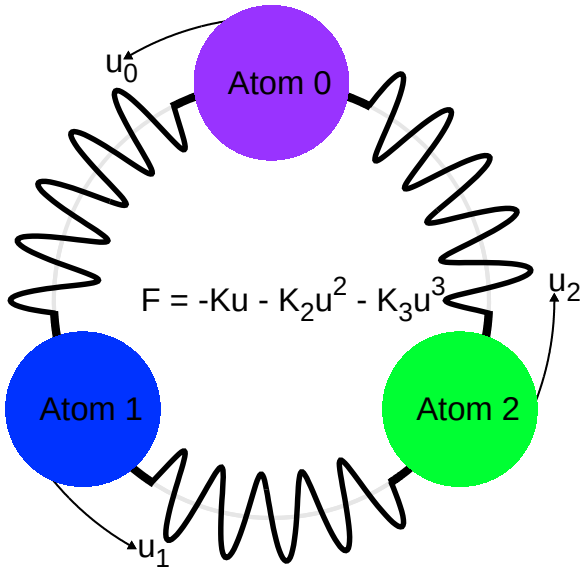

Figure 15.3: Periodic linear chain of 3 atoms connected by non-linear springs used in the simple simulations as described in the text.

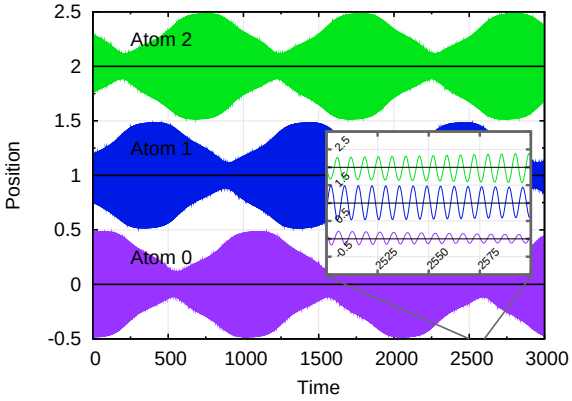

Figure 15.4: Displacement amplitude for the three atoms in the chain. The inset shows the behavior on a much smaller time scale, where the atoms appear to be undergoing a normal sort of harmonic motion. On the larger time scale of the figure, however, it is clear that energy is being passed back and forth from atom to atom. The curves for the three atoms are offset by 1.

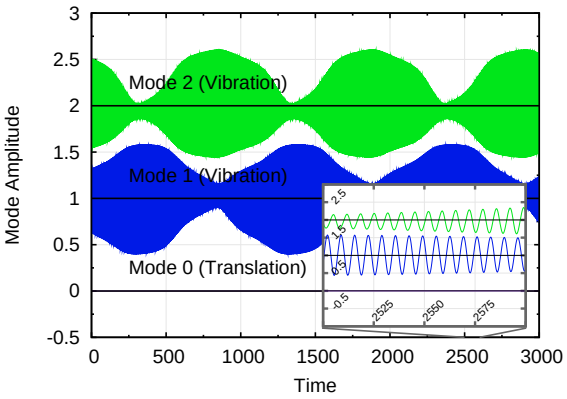

Figure 15.5: Displacement amplitude projected onto normal modes of the harmonic system. By construction, there is no displacement in the translational mode. As in Fig. 15.4, the inset shows that the behavior on a smaller time scale might be mistaken for regular harmonic motion. Again, on the larger time scale of the figure it is clear that energy is being passed back and forth from mode to mode. They are thus, not *normal* modes at all. The curves for the three modes are offset by 1.

These were integrated numerically using the forward Euler method described in § 15.2.2.1, and the displacements of the masses as a function of time are shown in Fig. 15.4.

In the harmonic case, the equations of motion reduce to:

$$\begin{aligned} M\ddot{u}_0 &= -K(u_{01}) - K(u_{02}) = -K(2u_0 - u_1 - u_2) \,, \\ M\ddot{u}_1 &= -K(u_{12}) - K(u_{10}) = -K(2u_1 - u_2 - u_0) \,, \\ M\ddot{u}_2 &= -K(u_{20}) - K(u_{21}) = -K(2u_2 - u_0 - u_1) \,. \end{aligned} \tag{15.32}$$

Or:

$$\mathbf{M}\ddot{\mathbf{u}} = -\mathbf{K}\mathbf{u} \,, \tag{15.33}$$

where we have:

$$\mathbf{M} = \begin{pmatrix} 1 & 0 & 0 \\ 0 & 1 & 0 \\ 0 & 0 & 1 \end{pmatrix} M \,, \qquad \mathbf{K} = \begin{pmatrix} 2 & -1 & -1 \\ -1 & 2 & -1 \\ -1 & -1 & 2 \end{pmatrix} K \,. \tag{15.34}$$

This system has three modes: the first is translational, with frequency 0, and the remaining two are degenerate and vibrational, with frequency $3\omega'$. So long as we choose orthogonal eigenvectors that

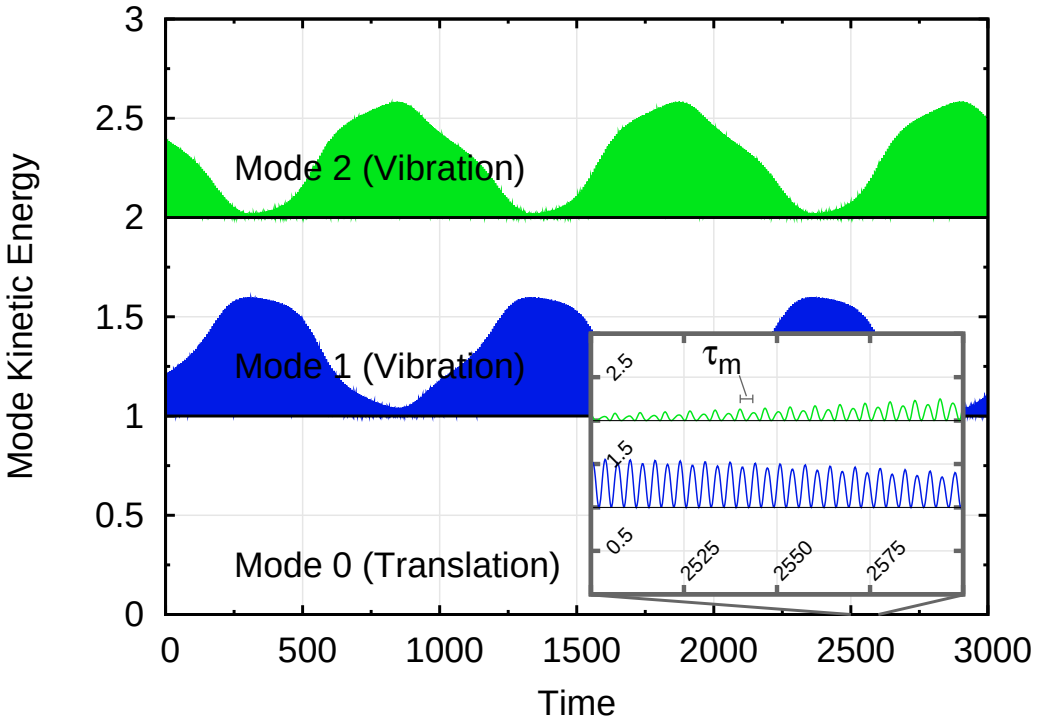

Figure 15.6: Kinetic energy projected onto the normal modes of the three atom chain. By construction and conservation laws, there is no energy in the translational mode. The inset shows behavior on a smaller time scale, with a sort of periodicity, τ_m. Here, fluctuations in the local maxima and minima of the kinetic energy are clearly visible, and the motion cannot be mistaken for regular harmonic motion. This is even more clear on the larger time scale, where almost all of the energy is quite visibly being passed back and forth from mode 1 to mode 2. The curves for the three modes are offset by 1.

span the degenerate subspace, we find that the energy in a particular mode is constant.

In either the harmonic or anharmonic case, we may project the trajectories onto the eigenvectors of the harmonic system, as described in § 15.2.2.3. These projections are shown in Fig. 15.5. With the non-linear springs, it is clear that energy moves in and out of the eigenmodes of the harmonic system. Figs. 15.6 and 15.7 show the kinetic energy for the two vibrational modes,[d] the former showing the short time scale behavior and the latter showing the autocorrelation function over large time scales. The energy starts out roughly split between the two degenerate modes. As time passes, nearly all of the energy passes from one mode to the other, and the time scale upon which this occurs is given clearly by the first maximum after the first minimum in the autocorrelation, marked as τ_C in Fig. 15.7. Also marked are the minimum and maximum kinetic energy in each mode, $\mathcal{T}_{\min}$ and $\mathcal{T}_{\max}$. Finally, we note that the frequency, ω', for displacement in the modes may be found by looking at the distance between subsequent local minima (or maxima) in the kinetic energy. This is

[d] For an anharmonic oscillator, there is no way of breaking the potential energy up amongst the different modes as can be done in the harmonic case.

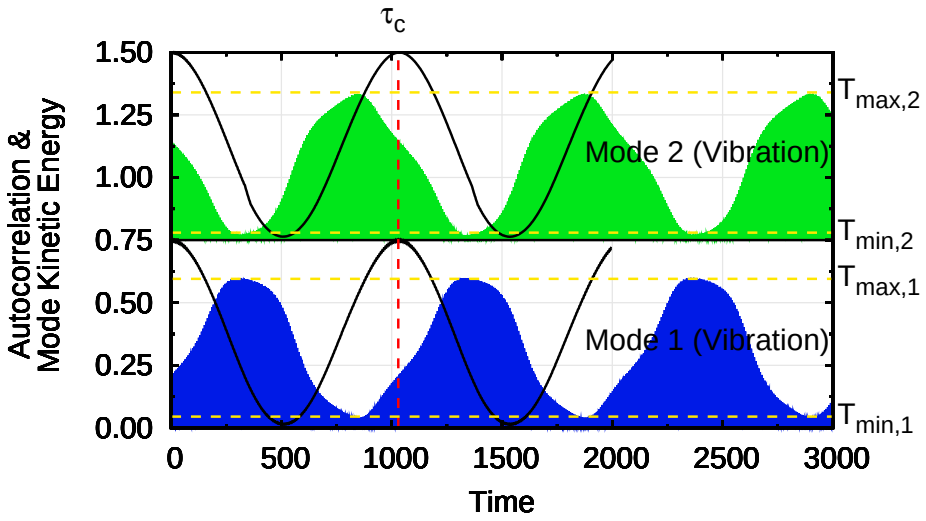

Figure 15.7: Kinetic energy in the vibrational modes of a periodic linear chain of 3 atoms connected by non-linear springs. The black curves are the autocorrelation functions for the two modes, and they show that the overall periodicity in the energy transfer is roughly τ_C, which is marked with the vertical, red dashed line. The maximum and minimum kinetic energy, $\mathcal{T}_{\rm max}$ and $\mathcal{T}_{\rm min}$ are shown by the horizontal, dashed yellow lines.

shown as τ_m in the inset of Fig. 15.6.

Using these sorts of parameters, we may define a quality factor for the anharmonic linear chain. For example, we might be motivated by the decay of the kinetic energy in a damped harmonic oscillator to propose the following relationship:

$$\mathcal{T}_{\rm max} \exp\left(-\frac{\omega'}{\mathcal{Q}}\frac{\tau_c}{2}\right) \quad = \quad \mathcal{T}_{\rm min} \; . \tag{15.35}$$

Taking $\omega' = \frac{2\pi}{\tau_m}$, this yields:

$$\frac{1}{\mathcal{Q}} \quad = \quad \pi\frac{\tau_c}{\tau_m}\ln\left(\frac{\mathcal{T}_{\rm max}}{\mathcal{T}_{\rm min}}\right) \; . \tag{15.36}$$

The point of this discussion is *not* whether or not Eq. 15.36 is in any sense *right* — in fact, Fig. 15.7 does not appear to have an exponential decay at all. Rather, the point is that there are any number of ways to define an effective quality factor for the vibrations in a crystal — a system that is conservative but not harmonic — and that the quality somehow quantifies the rate of energy transfer in and out of the vibrational modes.

15.3.2 Molecular dynamics with GULP

Here we provide a description of the molecular dynamics simulations performed as a part of the current study. Specifically, using the program GULP [332–335] as our molecular dynamics engine we

have simulated FCC aluminum, nickel, copper, rhodium, palladium, silver, iridium, platinum, gold, and lead using published interatomic potentials as well as our own, modified ones. The trajectories were analyzed with the program nMoldyn [314, 336, 337], allowing us to find simulated phonon spectra for the metals as a function of temperature. Figures showing the results for the ten metals are given in a more systematic fashion in Appendix F. Only a representative fraction of the results are shown here.

15.3.2.1 Optimizing the potential

As a starting point for our simulations, we adopted embedded atom potentials for FCC metals from Cleri and Rosato: [338]

$$\mathcal{V}_j^{\mathrm{B}} = -\left\{\sum_k K_0^2 \exp\left[-2K_1\left(\frac{r_{jk}}{r_0}-1\right)\right]\right\}^{\frac{1}{2}}, \tag{15.37}$$

$$\mathcal{V}_j^{\mathrm{R}} = -\sum_k K_2 \exp\left[-K_3\left(\frac{r_{jk}}{r_0}-1\right)\right], \tag{15.38}$$

$$\mathcal{V} = \sum_j \mathcal{V}_j^{\mathrm{B}} + \mathcal{V}_j^{\mathrm{R}}, \tag{15.39}$$

where $\mathcal{V}_j^{\mathrm{B}}$ gives the bonding and $\mathcal{V}^{\mathrm{R}}$ the repulsive contribution to the potential energy for the j^{th} atom. The equilibrium 1NN distance is r_0, and the distance between the j^{th} and k^{th} atoms is r_{jk}:

$$r_{jk} = \sqrt{|[\mathbf{r}_j]-[\mathbf{r}_k]|^2}. \tag{15.40}$$

The parameters K_0, K_1, K_2, K_3, and r_0 may be determined by fits to experimental data.

Cleri and Rosato optimized their potentials to reproduce experimental values for the enthalpy, bulk modulus, elastic constants, and lattice parameters of the FCC metals. As such, the potentials were reasonably well suited to calculations of low temperature properties of the pure metals, and succeeded in reproducing some high temperature properties as well. Further, the fit to the enthalpy allowed for use of the potentials in simulations of alloys. The authors indicate that the potentials tend to overestimate both thermal expansion and the Grüeisen parameter; therefore, they tend to overestimate the anharmonicity in these metals.

To obtain potentials better suited to our studies of anharmonicities, we optimized the parameters K_0, K_1, K_2, K_3, and r_0 to reproduce experimental values for the elastic constants, and for the temperature dependent lattice parameter. We did not try to match experimental values of the enthalpy as they are not relevant to studies of phonon dynamics in pure metals. As a result, our potentials may reproduce anharmonic effects in the pure metals better than the originals; however, they are not currently suitable for use in models of alloys. We describe our fitting procedure in slightly greater detail here.

Table 15.1: Optimized parameters for embedded atom potentials for FCC metals. The parameters for nickel, rhodium, and iridium are separated from the others due to the problems described in the text in § 15.3.2.1.

Symbol	K_0 (eV)	K_1	K_2 (eV)	K_3
Al	1.464	2.378	0.142	7.494
Cu	1.346	1.983	0.085	10.377
Pd	2.564	2.894	0.192	8.449
Ag	1.399	2.732	0.098	9.790
Pt	3.872	3.223	0.341	8.224
Au	2.305	3.282	0.180	8.484
Pb	1.729	2.273	0.159	6.614
Ni	0.905	0.326	0.074	11.817
Rh	1.340	0.370	0.109	15.033
Ir	2.307	0.259	0.058	14.486

The potentials from Cleri and Rosato were used as initial guesses at the parameters of the embedded atom potential, and the values for the elastic constants and isothermal bulk modulus, C_{11}, C_{12}, C_{44} and K_T, were taken from Simmons and Wang.[338, 339] Values for the temperature dependent thermal expansion were taken from Touloukian *et al.* [168], except for aluminum, which was taken from Wang and Reeber. [107] Values of the lattice parameter at room temperature were taken from various sources [340–348] and used in conjunction with the thermal expansion to produce experimental values for the lattice parameter as a function of temperature. In particular, lattice parameters at $\frac{1}{6}$, $\frac{2}{6}$, $\frac{3}{6}$, $\frac{4}{6}$, and $\frac{5}{6}$ of the highest temperature for which values of the thermal expansion coefficient were available were used in the optimization. As the molecular dynamics simulations are classical in nature, the lowest temperatures were not included in the optimization to avoid quantum effects impacting the lattice expansion.

For each function evaluation in our optimization, the low temperature elastic constants and bulk modulus were determined analytically by GULP. At each temperature, a 1 ps molecular dynamics simulation was run in the NPT ensemble at a pressure of 1 atmosphere. The first 0.49 ps were used for equilibration and the last 0.51 ps were used to determine the lattice parameter at pressure and temperature. These values were then compared to the experimental ones, and a weighted least squares penalty was minimized using the program "fmin" from the SciPy python package.[293] A convergence study showed that a $3 \times 3 \times 3$ conventional FCC unit cell gave a sufficiently accurate lattice parameter, so this cell size was used for our potential optimizations. The potentials were cut off after 12.0 Å, which is the default setting for the Cleri-Rosato potentials in GULP. Roughly, this captures interactions out to 5NN in nickel and copper; 4NN in aluminum, rhodium, palladium, silver, iridium, platinum, and gold; and 3NN in lead. The optimized parameters for the potentials are shown in Table 15.1 and the values of the bulk modulus and elastic constants from experiment, the Cleri-Rosato potential, and our optimized potentials are shown in Table 15.2. The top panels of Fig. 15.8

Table 15.2: Elastic constants of FCC metals from experiment (Exp.), [339] the potentials of Cleri and Rosato (Clr.), [338] and from our optimized potentials (Opt.) — % errors relative to the experimental values are given in parentheses. The parameters for nickel, rhodium, and iridium are separated from the others due to the problems described in the text in § 15.3.2.1.

		K_T		C_{11}		C_{12}		C_{44}	
Al	Exp.	74.7		84.4		69.8		30.2	
	Clr.	81.3	(-8.9)	95.0	(-12.5)	74.5	(-6.8)	37.0	(-22.7)
	Opt.	76.0	(-1.8)	107.0	(-26.7)	61.0	(12.6)	29.0	(3.8)
Cu	Exp.	141.7		174.2		125.5		84.3	
	Clr.	142.4	(-0.5)	176.7	(-1.4)	125.2	(0.2)	82.2	(2.4)
	Opt.	142.0	(-0.2)	176.0	(-1.0)	125.0	(0.4)	82.0	(2.7)
Pd	Exp.	195.7		221.6		182.8		71.9	
	Clr.	196.3	(-0.3)	231.9	(-4.6)	178.5	(2.3)	72.6	(-1.0)
	Opt.	195.0	(0.4)	234.0	(-5.6)	176.0	(3.7)	71.0	(1.2)
Ag	Exp.	108.4		129.1		98.0		51.9	
	Clr.	108.3	(0.0)	131.7	(-2.0)	96.6	(1.4)	50.6	(2.4)
	Opt.	108.0	(0.3)	131.0	(-1.5)	97.0	(1.0)	51.0	(1.7)
Pt	Exp.	288.6		317.9		273.9		78.4	
	Clr.	296.0	(-2.6)	341.1	(-7.3)	273.4	(0.2)	90.6	(-15.6)
	Opt.	288.0	(0.2)	358.0	(-12.6)	254.0	(7.3)	77.0	(1.7)
Au	Exp.	166.3		184.0		157.5		47.0	
	Clr.	165.4	(0.6)	187.4	(-1.8)	154.4	(2.0)	44.7	(4.8)
	Opt.	166.0	(0.2)	187.0	(-1.6)	155.0	(1.6)	45.0	(4.2)
Pb	Exp.	40.9		44.8		38.9		13.9	
	Clr.	42.6	(-4.4)	48.4	(-8.1)	39.7	(-2.2)	12.8	(8.5)
	Opt.	41.0	(-0.3)	46.0	(-2.7)	38.0	(2.3)	14.0	(-0.4)
Ni	Exp.	186.5		256.4		151.6		134.7	
	Clr.	222.1	(-19.1)	298.2	(-16.3)	184.1	(-21.5)	157.2	(-16.7)
	Opt.	188.0	(-0.8)	261.0	(-1.8)	151.0	(0.4)	132.0	(2.0)
Rh	Exp.	268.7		374.2		216.0		196.4	
	Clr.	294.5	(-9.6)	399.0	(-6.6)	242.3	(-12.2)	202.0	(-2.8)
	Opt.	269.0	(-0.1)	422.0	(-12.8)	192.0	(11.1)	194.0	(1.2)
Ir	Exp.	369.5		524.4		292.0		271.3	
	Clr.	415.4	(-12.4)	554.5	(-5.7)	345.8	(-18.4)	261.4	(3.6)
	Opt.	370.0	(-0.1)	599.0	(-14.2)	256.0	(12.3)	269.0	(0.8)

show the experimental, Cleri and Rosato, and our optimized lattice parameters for aluminum and lead. In both cases, our optimized potential reproduces the experimental data significantly better than does the original Cleri-Rosato potential. The discrepancy in the lattice parameter for aluminum at the highest temperature is due to its having melted, and the optimized potential quite consistently underestimates the thermal expansion for lead.

15.3.2.2 Generating trajectories

Using GULP with both the original potentials from Cleri and Rosato and the optimized potentials, we ran 70 ps simulations of aluminum, nickel, copper, rhodium, palladium, silver, iridium, platinum, gold, lead using 864-atom supercells ($6 \times 6 \times 6$ conventional FCC cells). For each combination of

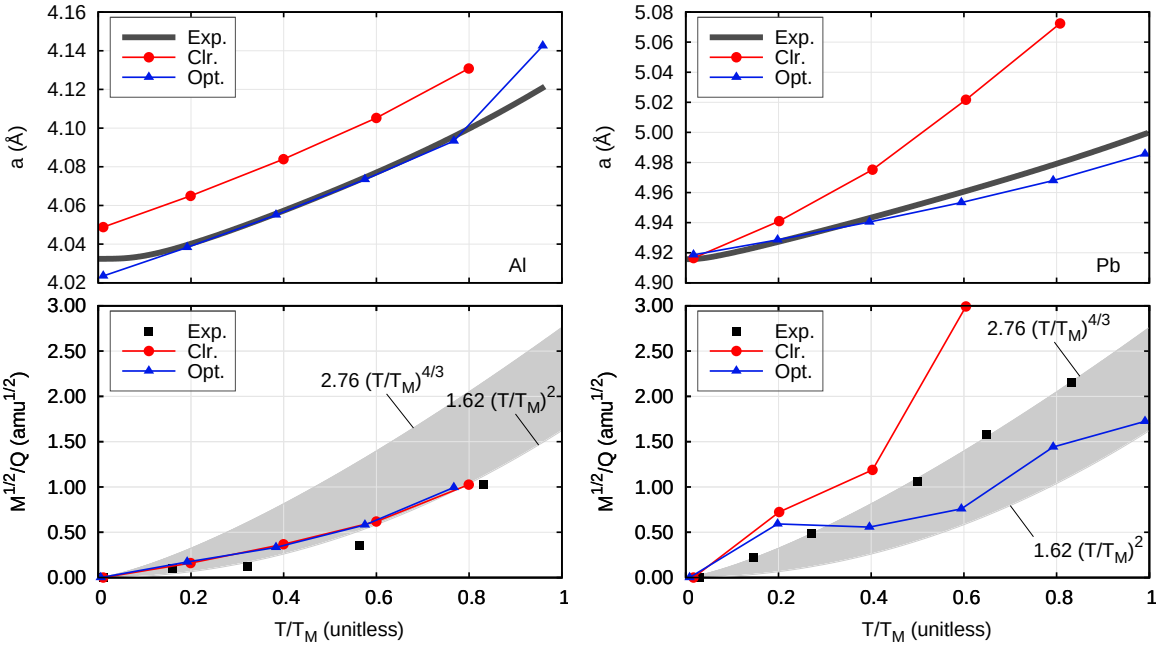

Figure 15.8: Lattice parameters and inverse qualities for aluminum (left) and lead (right). In the top panels, the thick gray line shows the experimental values for the lattice parameter, the red line with circular points the values from the potential of Cleri and Rosato, and the blue line with triangular points the values from the optimized potential. The bottom panels show the inverse quality scaled by the square root of the mass. The gray region corresponds roughly to the region in which lie our experimental data, the red lines with circular points are from the potential of Cleri and Rosato, and the blue lines with triangular points are from the optimized potential. The qualities were found from fits of the phonon spectra as described in § 15.3.2.4. In the bottom panel of the right hand plot for lead, the black points are the experimental data from Chapter 10 — these points were used to find the upper boundary of the gray region.

potential, metal, and temperature, we performed a 1 ps simulation at NPT at a pressure of one atmosphere with the 864-atom cell to find the temperature dependent lattice parameter.[e] This was, in turn, used to fix the size of the supercell, and the simulations were then run at constant temperature and volume (NVT). For the longer simulations, the use of an NVT ensemble rather than NPT was necessary because the most effective operating frequencies for the barostats significantly overlapped with the frequencies of the phonon spectrum (perhaps this is not surprising).

15.3.2.3 Projections onto normal modes

The normal modes of an 864 atom crystal are fairly complicated; however, we may pick out some simple ones and investigate some of their properties. Fig. 15.9 shows cross sections of the supercell in equilibrium, displaced in a low energy mode, and displaced in a high energy mode. We may project the trajectories of the atoms in our crystal onto these displacement patterns as described

[e]Cross checks with the temperature dependent lattice parameters from the optimizations showed solid agreement for all the metals despite change in cell size, including nickel, rhodium and iridium with their problematic potentials.

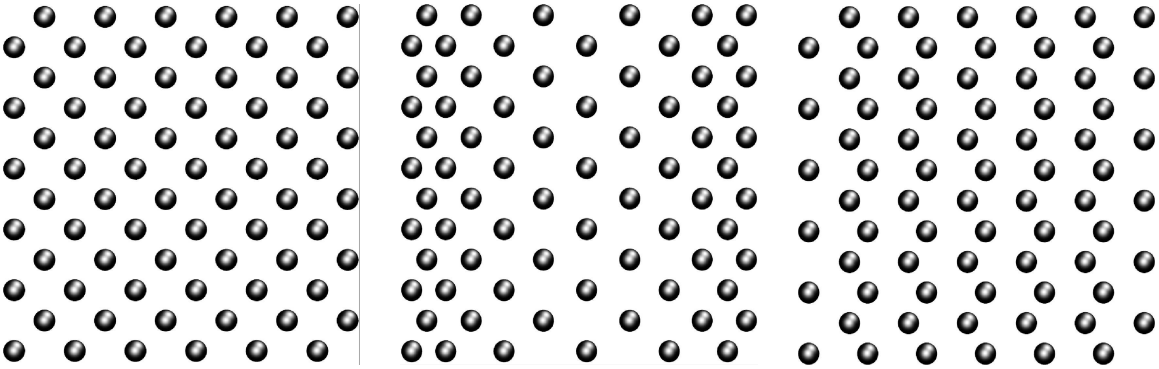

Figure 15.9: Cross-sections of the super-cell used for the molecular dynamics simulations. The left panel shows the cell in equilibrium, the center displaced in a low energy mode, and the right displaced in a high energy mode. The low energy mode has a wavelength of one cell width (twelve planes with different displacements), and the high energy mode a wavelength one sixth that (displacements in pairs of planes).

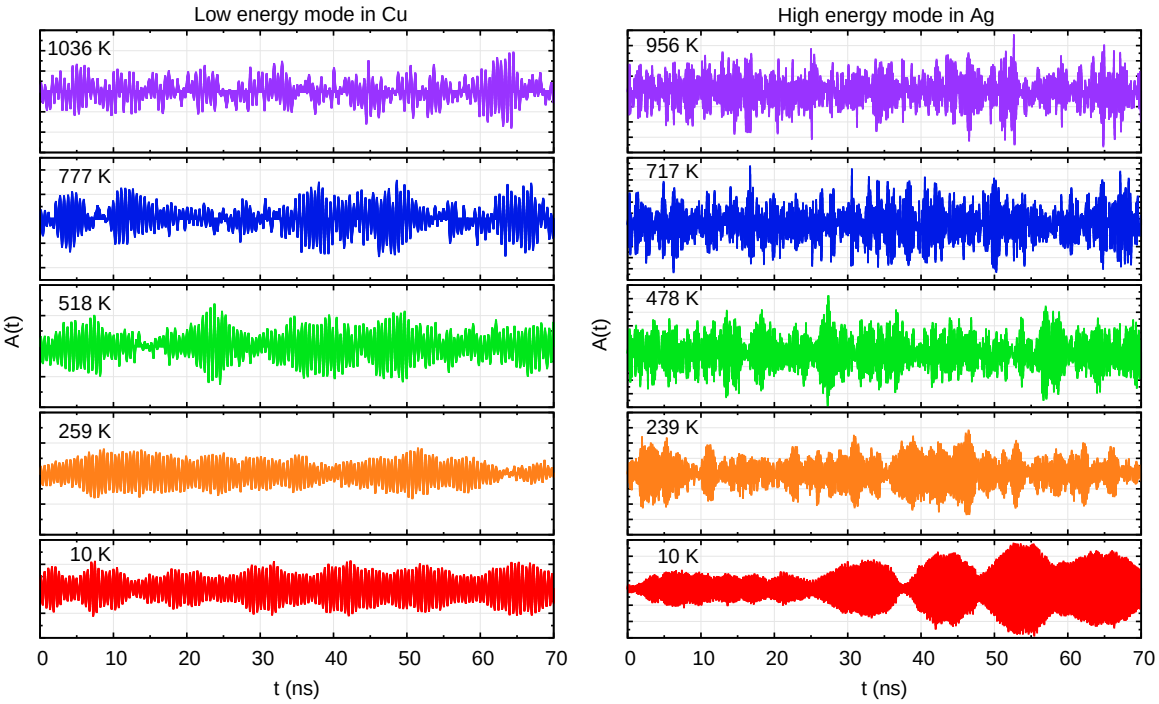

Figure 15.10: Amplitude as a function of time and temperature of a low energy mode in copper (left) and of a high energy mode in silver (right). The local minima and maxima are visible on the right, but not on the left, consistent with their differing frequencies. In both panels, the reduction in quality with increased temperature is visible in the progression from smoother to more jagged curves.

in § 15.2.2.3, and examples of these projections for the low energy mode in Cu and the high energy mode in Ag are shown in Fig. 15.10. The difference in frequency of the modes is visible in the relative density (in time) of the amplitude curves for the two modes. In both cases, there appears

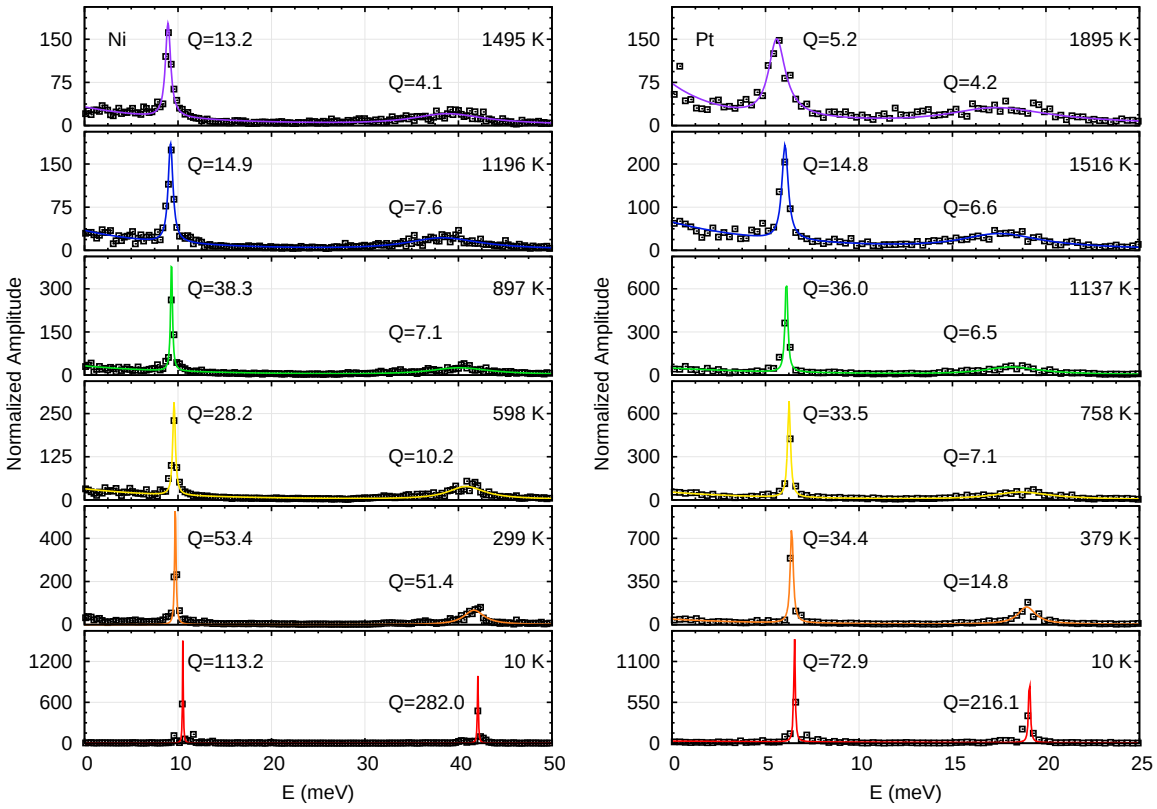

Figure 15.11: Energy response for the lower and higher energy modes in nickel (left) and platinum (right). The points in the plot are a downsampling of the Fourier transformed trajectories, and the lines are fits to the data using the damped harmonic oscillator function of Eq. 15.10. The quality factors, $\mathcal{Q}$, are displayed in the plot, and they generally decrease with increasing temperature. Linewidths for the high energy mode tend to be larger than for the low energy one, as would be the case with constant $\mathcal{Q}$. The plots look very similar, despite difficulties with the optimized potential in nickel.

to be longer time-scale structure at lower temperatures that is largely broken up into random fits and spurts at higher temperatures.

The energy response in the two modes may be assessed more directly by taking the Fourier transform of the amplitude. Fig. 15.11 show the energy response for the lower and higher energy modes in nickel[f] and platinum, respectively. The points in the plot are a downsampling of the Fourier transformed trajectories, and the lines are fits to the data using the damped harmonic oscillator function of Eq. 15.10 where the fit parameters were ω' and $\mathcal{Q}$, the latter of which are displayed in the plot. Generally, the quality factors decrease with increasing temperature. Also, the linewidths tend to be larger for the high energy mode than for the low energy ones. This would also be the case if $\mathcal{Q}$ was constant at a given temperature.

[f]Note that these look very similar, despite the aforementioned difficulties with the optimized potential in nickel.

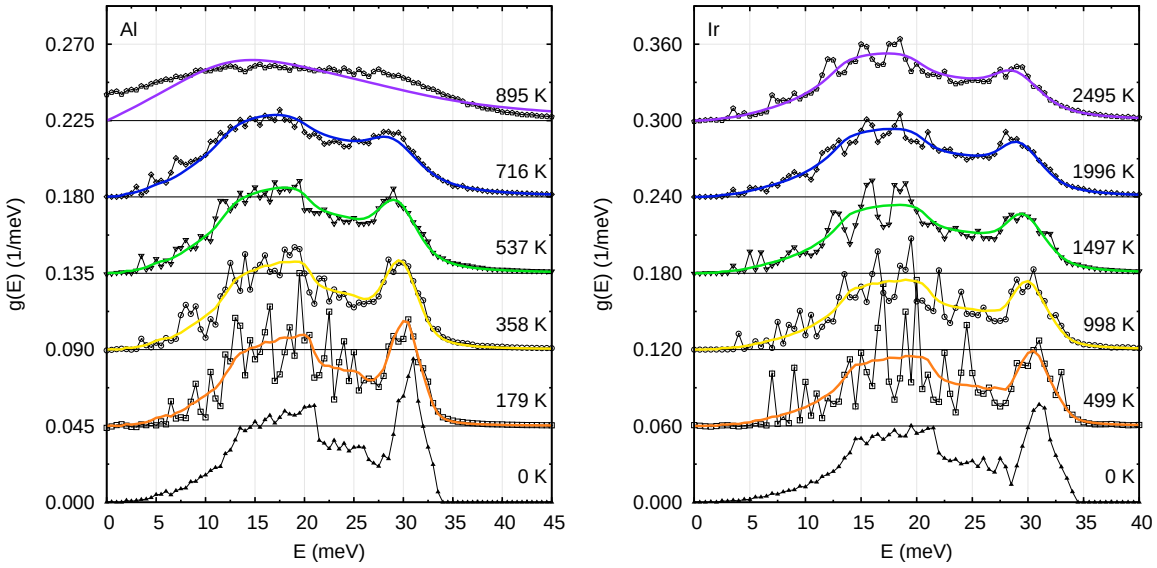

Figure 15.12: Phonon DOS of aluminum (left) and iridium (right) from molecular dynamics. The black lines with points were found using nMoldyn as described in the text, the colored solid lines are fits using Eqs. 15.41 and 15.42. In the simulation, aluminum has melted at 895 K, as is visible by the non-zero value of the DOS at $E = 0$. (This is related to the diffusion constant.) The noise in the spectra at low temperatures is largely due to the reduced thermal motion, which reduces the sampling of vibrational states. At higher temperatures, the persistent small peaks are largely due to finite-size effects. Note that the spectra for the two metals are similar, despite problems with the optimized potential for iridium.

.

15.3.2.4 Phonon spectra and quality factors

Once the simulations were completed, the program nMoldyn was used to obtain the velocity autocorrelation function and the phonon DOS from the particle velocities as described in § 15.2.2.4. Phonon DOS of aluminum and iridium from molecular dynamics are shown in Fig. 15.12. As seen in Chapters 9–13 , we may describe the damping in terms of a damped harmonic oscillator response function:

$$B(\mathcal{Q}, E', E) = \frac{1}{\pi \mathcal{Q} E'} \frac{1}{\left(\frac{E'}{E} - \frac{E}{E'}\right)^2 + \frac{1}{\mathcal{Q}^2}} \ , \tag{15.41}$$

where $\mathcal{Q}$ is an average quality for the phonons. We then model the temperature dependent energy shifts and broadening of the DOS with:

$$g_T(E) = B(\mathcal{Q}, E', E) \odot g_{T_0}(\Delta^s E') \ , \tag{15.42}$$

where $\mathcal{Q}$ and Δ^s are parameters to be determined, and $g_T(E)$ and $g_{T_0}(E)$ are the phonon DOS at high and low temperatures, respectively. Fits of this variety are shown as solid colored lines in

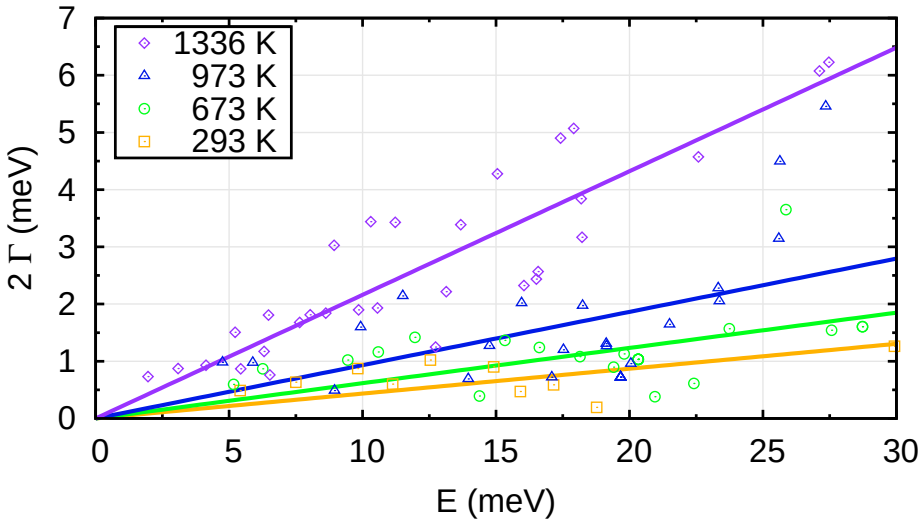

Figure 15.13: Markers show phonon full width at half maximum, 2Γ as a function of phonon energy, at temperatures as given in the key. Data are from the triple axis neutron scattering measurements of copper taken by Larose and Brockhouse. [60, 305] The solid lines are linear fits to the data, the slope of which give $1/\mathcal{Q}$.

Fig. 15.12, and work quite well for all of the FCC metals studied here.

15.4 Experiment

Measurements of the inelastic scattering of neutrons by aluminum, lead and nickel were made over a wide range of temperatures, and these experiments are described in great detail in Chapters 9, 10, and 11 respectively. At each temperature, the phonon DOS was determined, and these were used to get quality factors as a function of temperature for each metal using Eqs. 15.41 and 15.42.

Using the same procedure as was outlined for the lead data on phonon linewidths taken from triple-axis measurements (see § 10.4), the quality factors for copper at elevated temperatures were also determined using triple-axis data from Larose and Brockhouse. [60, 305] The fits to the triple axis measurements are shown in Fig. 15.13.

15.5 Discussion

In § 15.2.1.2, we found a relationship between the shifts and the qualities for a damped harmonic oscillator, $\frac{\Delta\omega}{\omega'} = -\frac{1}{8\mathcal{Q}^2}$ (Eq. 15.6). This is shown for experimental data from aluminum, nickel, copper, and lead in Fig. 15.14. For lead, the dependence appears to be superlinear; however, we have discussed at length in Chapter 10 the fact that the values we have found for the shifts in lead do not agree with previous results, and are suspicious because of problems with the background. With

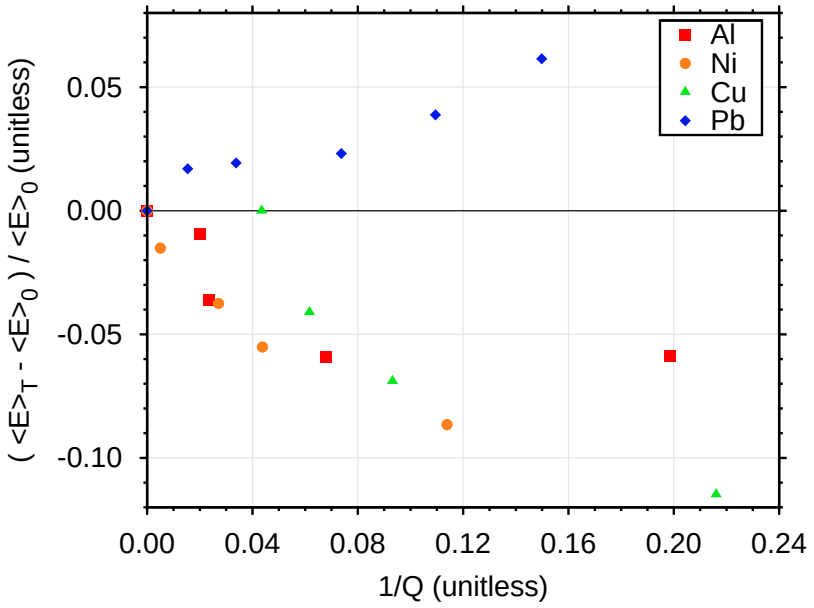

Figure 15.14: Experimental values for shifts plotted against quality factors for FCC metals aluminum, nickel, copper, and lead. For a given metal, points farther to the right are at higher temperatures. A damped harmonic oscillator should show a quadratic dependence of $\frac{\langle E\rangle_T - \langle E\rangle_0}{\langle E\rangle_0}$ on $\frac{1}{Q}$; however, the dependence appears to be more like a square root.

the possible exception of lead, the dependence of the scaled shift on the quality is not quadratic as suggested by Eq. 15.6. Rather, the dependence for aluminum, nickel, and copper appears to be more like a square root. Nevertheless, the sign of the relationship appears to be correct for these metals, and there does appear to be some structure in the relationship between the two anharmonic quantities.

Shifts in phonon energy with change in temperature are sometimes quantified through a mode Grüneisen parameter, $\gamma_b(\mathbf{q})$, which gives the frequency shift for a particular mode given a change in volume. (See Eq. 3.78) The thermodynamic Grüneisen parameter γ gives an average over all modes:

$$\gamma = \frac{\sum_{\mathbf{q}}\sum_b \gamma_b(\mathbf{q})\frac{\partial}{\partial T}n_{\omega_b(\mathbf{q})}(T)}{\sum_{\mathbf{q}}\sum_b \frac{\partial}{\partial T}n_{\omega_b(\mathbf{q})}(T)}\,, \tag{15.43}$$

where $n_{\omega_b(\mathbf{q})}$ is the mean occupancy for bosons with energy $E_b(\mathbf{q}) = \hbar\omega_b(\mathbf{q})$. Clearly, the collection of all mode Grüneisen parameters provides more information than the thermodynamic one; however, as the name implies, the latter provides valuable thermodynamic information. For example, in the quasiharmonic model, the Grüneisen relation gives the thermal expansion in terms of the volume, V, the heat capacity at constant volume, C_V, and the isothermal bulk modulus, K_T:

$$\alpha(T) = \frac{1}{3K_T V}\gamma C_V(T)\,. \tag{15.44}$$

Similarly, the quality factors for all modes are not the same; however, we may consider an average over the phonon spectrum. The mode dependence of the linewidths can be seen in a variety of experimental measurements. Figs. 15.13 and 10.8 show the varied values of the linewidths for specific phonons in copper and lead as determined by triple-axis neutron spectrometry. [58, 60, 152, 158, 349, 350] The phenomenon is also clearly visible in Raman spectra. [351–354] The molecular dynamics simulations presented here also display this property, with the qualities for the low and high energy modes in Ni and Pt shown in Fig. 15.11 having different quality factors even at a fixed temperature. That said, at fixed temperature the energy response appears to be resonance-like, and the linewidths of the individual modes do tend to be larger at larger energies, as seen in Fig. 15.11, and as would be the case if the quality factor were constant. Further, Figs. 15.13 and 10.8 show the approximation that the individual phonon linewidths have a linear dependence on energy is plausible. We suspect that average qualities may have thermodynamic importance[g] and we hope that the average quality may have a more structured temperature dependence than the qualities of individual modes. Thus, average quality factors are shown in Fig. 15.15 and are considered here.

In § 15.2.1 we defined the quality factor, $\mathcal{Q} \equiv \frac{\sqrt{KM}}{C}$, and in § 15.3.1 we showed how it might apply to a conservative system, such as phonons in a crystal. Here, we test far this analogy can take us. From the definition of the quality factor, we have:

$$\frac{\sqrt{M}}{\mathcal{Q}} = \frac{C}{\sqrt{K}} \, . \tag{15.45}$$

The scaled quality factors are shown as a function of scaled temperature, $\frac{T}{T_M}$, in Fig. 15.15. The experimental values of the melting temperatures, T_M, were used. The left hand side of Eq. 15.45 is known — the qualities from experiment or simulation, the mass from experiment. The right hand side is not known, and is some ratio of the damping coefficient to the harmonic force constant. Thus, in so much as the damping coefficient represents the anharmonic part of the potential, $\frac{\sqrt{M}}{\mathcal{Q}}$ gives the relative strengths of the harmonic and anharmonic forces. This ratio is strikingly similar for aluminum, nickel, copper, and lead as determined by experiment, and for all the FCC metals when using the optimized interatomic potential.

To aid comparison with experiment, we have fit the scaled quality factors from aluminum, nickel, and copper to a function $\frac{\sqrt{M}}{\mathcal{Q}} = c\left(\frac{T}{T_M}\right)^2$ and from lead to $\frac{\sqrt{M}}{\mathcal{Q}} = c\left(\frac{T}{T_M}\right)^{\frac{4}{3}}$. We find:

$$\begin{aligned} \text{Pb}: \quad \frac{\sqrt{M}}{\mathcal{Q}} &\approx 2.76\left(\frac{T}{T_M}\right)^{\frac{4}{3}} \, , \\ \text{Al, Ni, \& Cu}: \quad \frac{\sqrt{M}}{\mathcal{Q}} &\approx 1.62\left(\frac{T}{T_M}\right)^{2} \, , \end{aligned} \tag{15.46}$$

where the mass is given in AMU. These are shown as lines in the top panel of Fig. 15.15, and they

[g] See, for example, Chapter 9, where the entropy determined with phonon spectra that include anharmonic phonon broadening best reproduce the total entropy of aluminum.

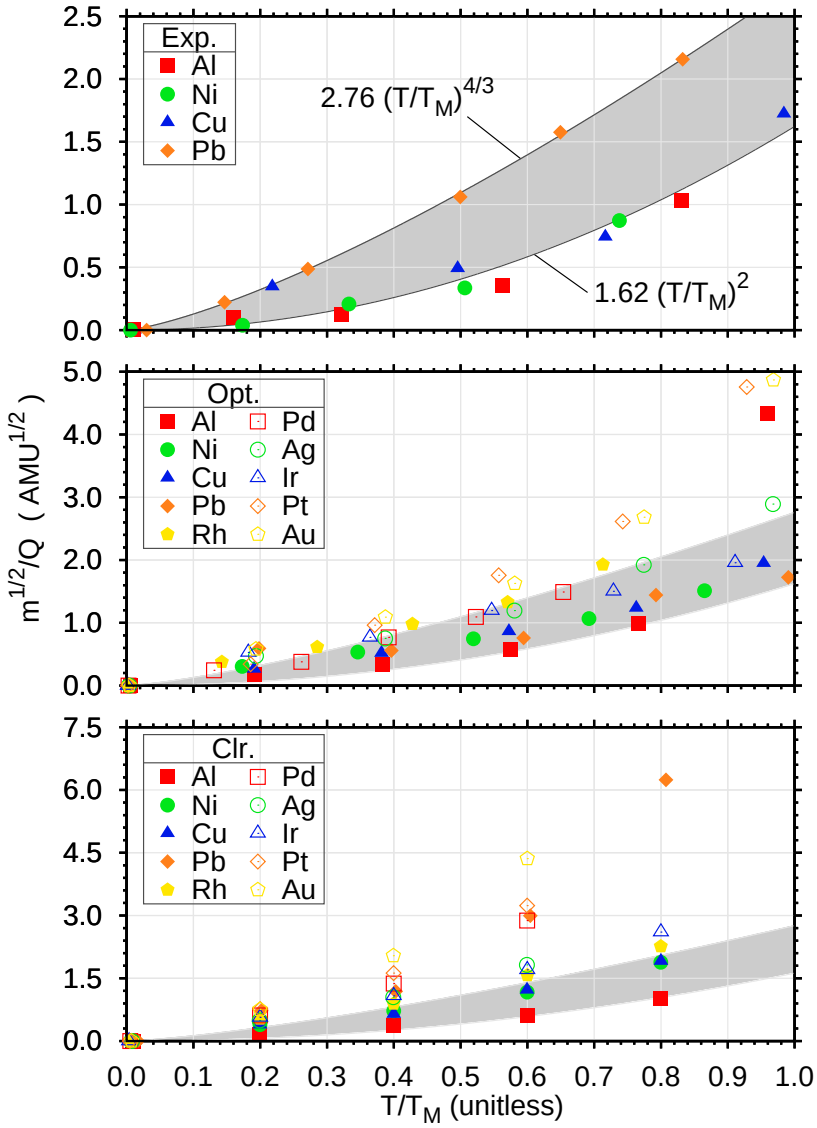

Figure 15.15: Scaled qualities, $\frac{\sqrt{M}}{\mathcal{Q}}$ as a function of scaled temperature $\frac{T}{T_M}$ for FCC metals from experiment (top) and molecular dynamics with potentials from Cleri and Rosato (bottom) and optimized potentials (center) as described in the text. In all three panels, the top of the gray region comes from a fit to the experimental lead data, and the bottom comes from a fit to the experimental data for aluminum, nickel, and copper. For aluminum with the optimized potential, the simulated crystal has actually melted at the highest temperature point, $\frac{T}{T_M} \approx 0.95$.

form the border of the light gray region in all three panels of the figure.

For the molecular dynamics simulations, we may investigate a sort of ratio of anharmonic to harmonic forces more directly. To do so, we have found the potential energy as a function of volume (lattice parameter). We fit this to a high order polynomial over a wide range, and to a second order polynomial close to the zero temperature lattice parameter, a_0. Taking the derivatives of these with respect to the lattice parameter gave a force $F(a)$ and a harmonic force $F_H(a)$. At each temperature,

the force was integrated over the region, $\mathcal{R}$, for which the potential energy was less than the energy at twice the root mean squared displacement:[h]

$$\mathcal{R} \equiv \left\{a|\mathcal{V}(a) \leq \mathcal{V}\left(a_0 + 2\sqrt{\langle u^2\rangle}\right)\right\} , \tag{15.47}$$

$$\mathcal{R}_H \equiv \left\{a|\mathcal{V}_H(a) \leq \mathcal{V}_H\left(a_0 + 2\sqrt{\langle u^2\rangle}\right)\right\} , \tag{15.48}$$

where the mean squared displacement was calculated from the phonon DOS in the harmonic approximation:

$$\left\langle u^2 \right\rangle = \frac{3\hbar}{2M}\int \frac{g(\omega)}{\omega}\langle 2n+1\rangle d\omega . \tag{15.49}$$

This was then used to determine root mean squared forces:

$$\mathrm{rms}(F) = \sqrt{\langle F^2\rangle} = \sqrt{\frac{\int_{\mathcal{R}} F^2(a)da}{\int_{\mathcal{R}} da}} , \tag{15.50}$$

$$\mathrm{rms}(F_H) = \sqrt{\langle F_H^2\rangle} = \sqrt{\frac{\int_{\mathcal{R}_H} F_H^2(a)da}{\int_{\mathcal{R}_H} da}} . \tag{15.51}$$

The ratio of the anharmonic to harmonic forces, then, is given by:

$$\frac{\mathrm{rms}(F) - \mathrm{rms}(F_H)}{\mathrm{rms}(F_H)} = \frac{\sqrt{\langle F^2\rangle} - \sqrt{\langle F_H^2\rangle}}{\sqrt{\langle F_H^2\rangle}} . \tag{15.52}$$

For both the Cleri and Rosato and optimized potentials, this ratio is plotted as a function of the scaled temperature, $\frac{T}{T_M}$ in Fig. 15.16 In both cases, the structure is rather remarkable, but this is particularly true for the optimized potentials where all but the lead data fall precisely on a line. A linear fit to the data from the optimized potential, excluding lead, gives:

$$\frac{\mathrm{rms}(F) - \mathrm{rms}(F_H)}{\mathrm{rms}(F_H)} = -0.046 - 0.225\left(\frac{T}{T_M}\right) . \tag{15.53}$$

The deviation for lead is at least partially explained by the inferior quality of the fit to its lattice parameter, as seen in the right panel of Fig. 15.8. The sign of the errors in the lead data is consistent with this explanation. Anecdotally, in optimizing the potential for lead, it seemed that improvements in the lattice parameter tended to come at a large cost in accuracy of the elastic constants.

The idea of universality in the forces in metals is by no means new. Perhaps the most famous work in this regard is that from Rose *et al.* [355–362] who propose a universal binding energy curve for metals and alloys. Their formulation requires knowledge of the Wigner-Seitz radius, $r_{\mathrm{WS}} \equiv \left(\frac{3}{16\pi}a_0^3\right)^{\frac{1}{3}}$, the equilibrium binding energy, and the bulk modulus. A correlation between the binding

[h] For the harmonic case, this is equivalent to $\mathcal{R} = \left\{a| - a_0 - 2\sqrt{\langle u^2\rangle} \leq a \leq a_0 + 2\sqrt{\langle u^2\rangle}\right\}$.

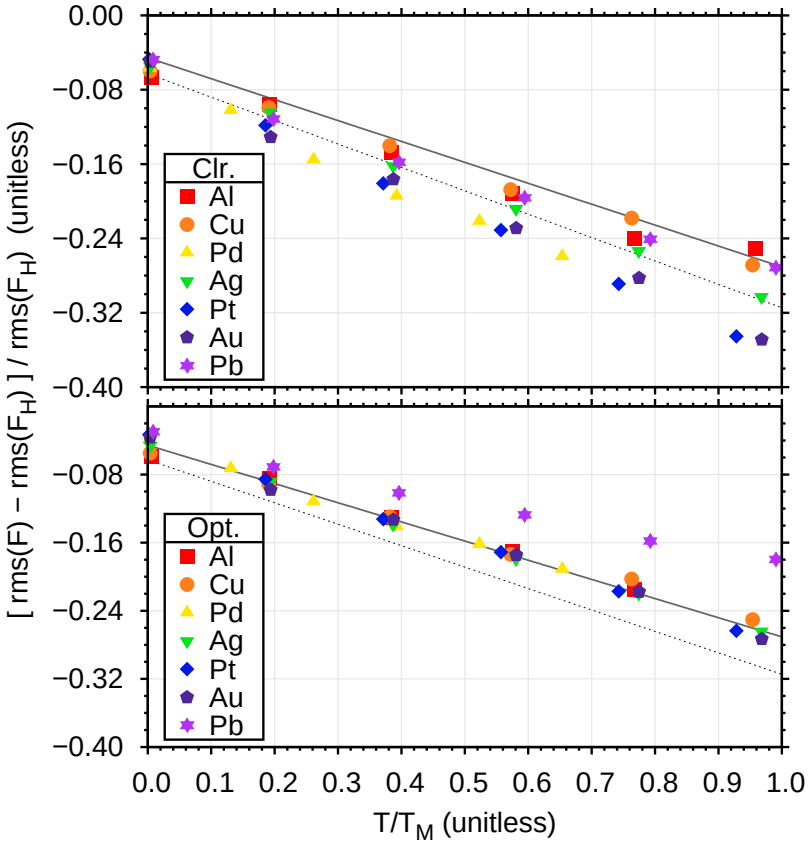

Figure 15.16: Ratios of anharmonic to harmonic forces in FCC metals from molecular dynamics simulations. For the potential from Cleri and Rosato (top), the simulated data show a good deal of spread about the linear fit (dotted gray line). The solid gray line is a linear fit to the simulated data from the optimized potential, and these data (bottom) are very near linear, with the exception of lead. The deviation of this metal may be explained by a relatively large underestimate of its thermal expansion, as seen in the top right hand panel of Fig. 15.8.

energy and the melting temperature is well known,[362] and somewhat intuitive, and this may explain its presence in Figs. 15.15 and 15.16. Another possible interpretation is that the melting temperature is related to the mean squared displacement, as suggested by Lindemann. [362, 363] Rose's universal equation of state is formulated in terms of a pressure-volume relationship, which would have implications primarily for the longitudinal modes. Here, we see that the transverse phonon modes are also showing universality.

Looking at Fig. 15.8 (and the similar figures in Appendix F), it is clear that the thermal expansion has an effect on the quality factors in the molecular dynamics simulations. The lattice parameters themselves are of little consequence, but their slope as a function of temperature (thermal expansion) is important. For $\frac{T}{T_M} < 0.8$ in aluminum, the lattice parameter has basically been shifted by a constant (~ -0.02 Å); however, the slope remains unchanged going from the potential of Cleri and Rosato to the optimized potential. The quality factors for aluminum are also unchanged. For lead,

the optimization reduced the slope significantly, and the quality factors are reduced as well.

It should be noted that the electronic structures of these FCC metals are quite varied: ranging from the nearly free electron metal aluminum, to the magnetic d-band metal nickel, to the non-magnetic d-band metal iridium. It would be surprising, then, if the similarities in the phonon damping arose from electron-phonon or magnon-phonon interactions. Rather, it seems that the similarities in the phonon linewidths arise from phonon-phonon interactions. The impact of the thermal expansion on the qualities and the strong similarities in the ratio of anharmonic to harmonic forces both lend further support to this thesis.

15.6 Summary

Inelastic neutron scattering measurements were made of the phonon spectra of FCC aluminum, lead, and nickel, and were used in conjunction with previous neutron measurements of copper to evaluated trends in phonon linewidths as a function of temperature. Additionally, we performed molecular dynamics simulations of FCC aluminum, nickel, copper, rhodium, palladium, silver, iridium, platinum, gold, and lead, finding simulated phonon spectra and phonon linewidths. Overall, we see strong trends in the linewidths when scaling the temperature by the melting temperature, and the linewidths by the square root of the mass, the latter being suggested by the equations for the damped harmonic oscillator. From experiment, we find:

$$1.62\left(\frac{T}{T_M}\right)^2 \lesssim \frac{\sqrt{M}}{\mathcal{Q}} \lesssim 2.76\left(\frac{T}{T_M}\right)^{\frac{4}{3}} , \tag{15.54}$$

where the mass is in AMU. We also find that this equation becomes increasingly accurate for the simulations as improvements are made to the interatomic potential. The relationship implies similarity in the ratio of anharmonic to harmonic forces of FCC metals, and we have found a strong linear trend in this ratio for the simulated FCC metals:

$$\frac{\mathrm{rms}(F) - \mathrm{rms}(F_H)}{\mathrm{rms}(F_H)} \quad = \quad -0.046 - 0.225\left(\frac{T}{T_M}\right) . \tag{15.55}$$

This may be thought of as an extension to the Grüneisen model of a solid. That is, we have developed a scheme that, taking a low temperature measurement of a phonon spectrum as input, allows a rough prediction of the phonon linewidths as a function of temperature. Combining this with a Grüneisen parameter, the overall change in the phonon spectrum may be approximated.

Finally, we conclude that the phonon broadening is likely related to the interatomic potentials because:

- The phonon linewidths are similar despite widely varying electronic structure in FCC metals

- Molecular dynamics simulations indicate that broadening is tied to thermal expansion, which is known to be related to the interatomic potential.
- Molecular dynamics simulations indicate trends in the ratio of anharmonic to harmonic forces.

That is, the broadening of the phonon spectra with increased temperature is due to phonon-phonon, not electron-phonon or magnon-phonon interactions.

Part VI

Summary and Future Work

Chapter 16

Summary

In Part II of this thesis, we considered the analysis of data from time-of-flight chopper spectrometers in some detail. The outline of a new technique for converting the raw data to $S(Q, E)$ was presented, as well as improved methods for automatically generating a mask and for finding the incident neutron energy for instruments lacking beam monitors. Given $S(Q, E)$, a new procedure for estimating the multiple scattering based on an analytical calculation of the multiphonon scattering was presented, as were updates to methods for fitting BvK models to phonon spectra, and quantifying the overall broadening of phonon spectra with temperature.

In Parts III and IV, we considered in great detail the various contributions to the total entropy of the FCC nearly free electron metals aluminum and lead from near absolute zero to near melting, and of the magnetic transition metals FCC nickel and BCC iron from near zero to temperatures well above, and just below, their Curie transitions. Specifically, we used time-of-flight chopper spectrometers to make measurements of the inelastic scattering of neutrons by phonons in aluminum, lead, and nickel from less than 3% to 83%, 73%, and 83% of their respective melting temperatures. For BCC iron, we used nuclear resonant inelastic x-ray scattering to measure the incoherent inelastic scattering at temperatures from less than 1% to 57% of its melting temperature. The reduced experimental data were used to obtain phonon spectra. Both neutron scattering with a time-of-flight chopper spectrometer and nuclear resonant inelastic x-ray scattering have great potential as methods for learning about anharmonic effects in solids in terms of the entire vibrational spectrum, rather than some limited set of modes. The experimentally determined phonon spectra were used to determine the harmonic, nonharmonic and total phonon entropy. Data for the temperature dependent thermal expansion and bulk modulus were then used to evaluate the purely anharmonic contributions to the phonon entropy. For the FCC metals aluminum and nickel, these contributions were small and negative, indicating that the phonons did not shift as much as expected, given the thermal expansion and bulk modulus. The anharmonic contributions for FCC lead were also negative, but slightly larger. For BCC iron, however, the anharmonic entropy was large and positive, even relatively far below the melting temperature. In all cases, anharmonicity made a larger contribution to the total

entropy than did vacancies or electron-phonon interactions, and the contributions were of the same order of magnitude as the electronic entropy. In iron and nickel, the anharmonic entropy was likely smaller than the magnetic contributions; however, they were by no means negligible. Overall, the anharmonic phonon entropy simply cannot be ignored in a serious evaluation of the contributions to the entropies of solids.

For aluminum in particular, we found that the sum of the various components of the entropy was in excellent agreement with the accepted value of the total entropy — particularly if the spectra broadened by phonon damping (but not by instrument resolution) were used. Very tentatively, we suggest that the quasiharmonic approximation, which states that the central frequencies are all that matters in determining the phonon entropy, may be less accurate than a model in which the entire, broadened spectrum is used.

In Part V, we have considered some trends in the forces in FCC and BCC transition metals, and the FCC nearly free electron metals aluminum and lead. (Henceforth referred to simply as "FCC metals" or "BCC metals".) The trends are:

- The 1NN longitudinal forces are dominant in FCC metals, but in BCC metals the 2NN longitudinal forces are also important.
- The transverse forces in the 1NN shell of the FCC metals are repulsive, whereas those in the BCC metals are attractive.
- The shapes of the phonon spectra for the FCC metals show less variation than those of the BCC metals, both across metals at fixed temperature, and for a particular metal as a function of temperature.
- The anharmonic entropy of the FCC metals tends to be small and negative, whereas there is a large variation for the BCC metals.

It seems that many of these differences can be attributed to the structures themselves. Specifically, the relative strength of 2NN longitudinal forces in BCC metals is likely related to the fact that the 2NN are not significantly further away than the 1NN, as they are in FCC metals. Also, the more *open* BCC structure may give more room for the constituent atoms to move about, providing increased possibilities for anharmonicity.

Given the similarities of the FCC metals, we were motivated to look for similarities in their phonon linewidths. Using experimental data and molecular dynamics simulations, we saw strong trends in the linewidths (when scaling the temperature by the melting temperature, and the linewidths by the square root of the mass). If we model the atoms in our solid as damped harmonic oscillators, this relationship implies similarity in the ratio of anharmonic to harmonic forces of FCC metals. We found a linear trend in this ratio for the simulated FCC metals. The simulations also indicated

that the broadening is related to the thermal expansion. Because of all of these similarities and the fact that the electronic structures of the FCC metals are quite varied, we have concluded that the phonon broadening in the FCC metals is likely related to the interatomic potentials. That is, the broadening of the phonon spectra with increased temperature is due to phonon-phonon interactions as opposed to interactions of phonons with electrons or magnons.

Chapter 17

Future Work

Here we present work that could improve upon the techniques and results presented in this thesis.

17.1 Data analysis

Procedures for converting the raw data — counts as a function of time-of-flight, detector, pixel — to the scattering function $S(Q, E)$ were discussed in § 7.4. In particular, the analytical reweighting and coordinate mapping technique has only been applied to LRMECS data because of the relative simplicity of the instrument. This technique should be generalized for use with instruments that have pixelated detectors and detectors at varying distances from the sample. Basically, the generalization would involve a method for ordering the pixels and time-channels such that given a (Q, E) pair it is not too difficult to find the neighboring points required for interpolation. A kD-tree might provide such a structure, for example.

When we analyze our neutron data, we do not take into account all of the information we have available. For example, we suspect that a neutron that appears at one time-of-flight cannot also appear at another. We also expect our data to be continuous and — with the possible exceptions of Bragg peaks and van Hove singularities — differentiable. A variety of methods exist for taking this sort of information into account when analyzing an experiment, perhaps the most popular being Bayesian techniques. [364–367] In fact, these methods have already been applied to neutron data, [368, 369] and even to data from time-of-flight chopper spectrometers; [255] though their use is not wide spread. In addition to offering solutions to the problems mentioned above, these sorts of methods also provide clean formalisms for handling instrument resolution, which would allow an experimentalist to make measurements using more than one incident neutron energy (thus with different resolutions) and later combine his data.

The procedures for obtaining a phonon spectrum from a measurement of $S(Q, E)$ are also in need of further improvement, particularly for measurements at elevated temperatures. The technique presented in § 8.1.2 does not account at all for instrument resolution, nor does it account for

anharmonic phonon broadening in so much as this should produce a Lorentzian style tail for the phonon DOS.

Recasting the problem as a constrained optimization may provide a solution to these difficulties. First, a representation of the instrument resolution is required. Specifically, given a *true* value of $S(Q, E)$, we need to be able to calculate the $S(Q, E)$ that we would measure with the instrument. Second, a quality factor might be estimated by a procedure similar to the one presented in § 8.2, but perhaps using the scattering $S(Q, E)$ or $S(E)$ instead of the phonon DOS. Third, the phonon spectrum should be parametrized in some economical fashion. For example, a polynomial spline with roughly 20 free parameters can frequently account for the detail in a phonon spectrum that requires 120 parameters when represented as a histogram.[a] A first guess at the DOS — and consequently, the parameters of the spline — may be obtained by assuming that there are no contributions from multiphonon or multiple scattering.

We may then perform an optimization in which the polynomial spline is constrained to be a phonon DOS — that is, to be positive and to integrate to 1. Given a phonon spectrum, the incoherent scattering $S^{\text{inc}}(Q, E)$ may be calculated, including multiphonon scattering and multiple scattering (in the approximation of § 8.1.2). We then account for the anharmonic phonon broadening by convolving[b] $S^{\text{inc}}(Q, E)$ with the damped harmonic oscillator function, using the estimated quality factor. We convolve this result with the instrument resolution, and compare to the experimental data. The parameters may then be adjusted according to some optimization algorithm. As with any optimization, the art and difficulty is in designing the appropriate penalty function. This sort of procedure should account for instrument resolution in so far as it is known, and can at least provide some guess at the anharmonic broadening.

More generally, undoing stuff is hard. Put more technically, matrix multiplication (or convolution) is more robust than matrix inversion (or deconvolution). If a model can be devised which — through a convolution with a resolution function — allows the data to be analyzed without deconvolution, the analysis will be much more robust. The optimization technique for finding a phonon spectrum given above is one example. Another might be to use Born–von-Kármán models to produce a phonon DOS or the scattering $S(Q, E)$, again convolving the model data with anharmonic and instrument broadening functions, rather than deconvolving the experimental data. Going even further, it may be that there are advantages to converting the model data to time-of-flight, detector, and pixel rather than performing the inverse operation on the experimental data. A Monte Carlo simulation of the entire instrument [370] and sample assembly would be one method by which counts

[a] A more physical picture might arise if the knots in the spline were aligned with the van Hove singularities in the phonon spectrum.

[b] For readability, we will use the terms *convolution* and *deconvolution* here, even though we are actually discussing integral transformations that are merely similar to convolutions.

in time-of-flight, detector, and pixel could be generated for comparison with experimental data.[c] [d]

17.2 Vibrations, magnetism, and superconductivity

For aluminum, we found exceptional agreement between the experimentally determined total entropy and the sum of many independent components. These sorts of analyses worked quite well for lead, nickel, and iron as well; however, in these cases there exists clear room for improvement.

For lead, the first step is to remeasure the phonon spectra as a function of temperature with accompanying measurements of the background. This experiment is already under way on the Pharos spectrometer at the Lujan center of Los Alamos National Lab for temperatures between 8 K and 550 K. Likely, this will explain the vast majority of the discrepancy between the total and componentized entropy for the metal. Further measurements above and below the superconducting phase transition at 7.2 K are of interest as well, as these may shed more light on the interaction of electrons and phonons in lead. If high temperature experiments do not yield a components of the entropy that sum to the accepted value of the total entropy, the entropy from electron-phonon coupling is the next most likely source of an explanation.

For nickel and iron, questions remain about the magnetic entropy, particularly above the Curie temperatures. Measurements of the phonon spectra directly above and below the Curie temperature would be of interest, even though previous such experiments on nickel concluded that there was not a significant effect on phonons in certain high symmetry directions. [208] The largest impacts for these metals, however, would be in a better assessment of their electronic structure, including their magnetism. Fixing the magnetization in order to account for the effects of temperature, as we did in Chapters 11 and 12 is not a good approximation. Modern first principles techniques allow for accurate determination of the magnetization to at least $\frac{T_C}{2}$, [192] and calculations with larger cells and more degrees of freedom may do even better. Further, modern first-principles techniques allow determinations of the magnon spectra, which might be used to find the magnon contributions to the entropy. Alternatively, a method might be devised for using the experimentally determined magnon dispersions to estimate the magnon entropy.

17.3 Mean phonon lifetimes in FCC Metals

We have collected or found experimental data on phonon lifetimes in the FCC metals aluminum, nickel, copper, and lead; however, there still remain rhodium, palladium, silver, iridium, platinum, and gold to measure. In particular, phonon spectra for rhodium and iridium have only been measured at room temperature. Time-of-flight chopper spectrometer measurements of these metals would be

[c] The buzzphrase for this general approach to data analysis is *generative modeling*.
[d] These last two procedures have the added advantage of using both coherent and incoherent scattering.

of the greatest use in refining and solidifying the model of the phonon linewidths presented in Chapter 15.

Triple-axis measurements are also of great interest, as they allow consideration of specific phonons; however, the amount of time required to get triple-axis measurements over a significant fraction of the Brillouin zone is prohibitive. A good compromise may be to take measurements using single crystals and time-of-flight chopper spectrometers. In this way, dispersions may be rapidly measured over large swaths of reciprocal space without the loss of directional information that accompanies measurements of polycrystals.

With respect to the molecular dynamics simulations, a great deal of work is left to be done. Perhaps the most obvious step is to redo the optimizations of nickel, rhodium, and iridium allowing for longer range interactions. Beyond this, the potentials developed in this thesis were the results of a very few number of optimizations with the parameters from Cleri and Rosato always taken as a starting point. A larger search with a greater number of randomized initial conditions might yield significantly better results.

Here, we fit to elastic constants and thermal expansion; however, there are many other relevant parameters to which the potentials might be optimized. In particular, fitting to experimental phonon spectra would be of interest; however this is almost certainly too time consuming. On the other hand, we might be able to use specific features of the spectra. For example, the high energy cutoff of the phonon DOS might be found by considering only a handful of carefully selected Q-points in a BvK style simulation, or possibly even by a very short molecular dynamics simulation. Similar procedures may be possible for finding van Hove singularities. Another exciting possibility is to use ab-initio molecular dynamics simulations. One advantage of this technique is that it should be able to capture quantum effects at low temperatures.

17.4 Vibrational entropy in the presence of damping

For all of the metals studied, the question of how to determine the entropy given a damped phonon spectrum is still open. Here, we have used the quasiharmonic approximation with the damped phonon spectrum. For aluminum, the damped phonon spectrum, first corrected for effects of instrument resolution, then used in the quasiharmonic approximation was found to give the better agreement with the total entropy than either the uncorrected or unbroadened spectra. Is this generally true? Are there still better techniques?

Molecular dynamics simulations may provide a way to get at an answer to these questions. Specifically, for a sufficiently long simulation with a sufficiently large supercell, the phonon entropy may be calculated directly from the trajectory, as well as from the phonon spectrum with and without damping. That is, we may compare the entropy as determined through a probability density

in configuration space with that found through the velocity correlation function. We may then see which phonon DOS — with or without anharmonic broadening — leads to the best agreement with the direct determination, and whether or not other approximations yield still better agreement.

Appendices

Appendix A

Table of Symbols

Symbol	Meaning
Operations, not quite variables:	
∂	Partial derivative
$\dot{x}$	Time derivative of x
$\ddot{x}$	Second time derivative of x
Δx	Increment or small change in x
$\langle x \rangle$	Mean value of x
$\lvert x \rvert$	Measure of x: magnitude, area, determinant, etc.
x^*	A particular value of x
x-vector	Vector with x elements
$\mathcal{FT}\{f(t)\}$	Fourier transform of $f(t)$
$*$	Convolution
$\odot$	Integral transform — similar to convolution

Symbol	Meaning
a	Lattice parameter
a_i	Scattering length
$\hat{\mathbf{a}}_+$	Creation operator
$\hat{\mathbf{a}}_-$	Annihilation operator
$\mathbf{a}$	Example atom vector
A	Amplitude of oscillation
$\mathcal{A}$	Number of atoms
b	Branch index
$B(\mathcal{Q}, E', E)$	Damped harmonic oscillator function
c	Speed of light (299,792,458 m/s)
$c, c_1, c_2, \cdots$	Index Cartesian directions
C_P	Heat capacity at constant pressure
C_V	Heat capacity at constant volume
d	Index for detectors
$\mathbf{D}$	Dynamical matrix (Various orders)
$\mathcal{D}$	Dimension (Number of dimensions)
e	2.7182818284590451
E	Energy, measured phonon energy (Energy transfer)
E_F	Final neutron energy (From sample to pixel)
E_I	Initial neutron energy (From moderator to sample)
$[E_\mathrm{e}]_{p^*}$	Energy for elastically scattered neutron as seen in a row of pixels
E_0	Ground State Energy
E_λ	Energy of the λ^{th} state
$\langle E \rangle_T$	Mean phonon energy at temperature T
E_f	Fermi energy
f	Fraction of background scattering to be removed
$f_T(E)$	Mean occupation for Fermions at temperature T
$\mathbf{F}$	Force
$\mathcal{F}$	Helmholtz free energy
$g(E) = g_T(E)$	Phonon density of states at temperature T
$G(E) = G_T(E)$	Electron density of states at temperature T
$\mathcal{G}$	Gibbs free energy
h	Planck's constant (6.626068×10^{-34} J·s)
h, k, l	Miller indices (only used together)
$\hbar$	Planck's constant over 2π
$\mathcal{H}$	Hamiltonian
$\mathcal{H}_\mathrm{ph}$	Nuclear Hamiltonian
i	Index ; Imaginary number, $\sqrt{-1}$
I''	Intensity before pressure- and energy- efficiency corrections
I'	Intensity before pressure- and after energy- efficiency correction
I	Intensity after pressure- and energy- efficiency corrections
I''^{van}	Intensity from vanadium (uncorrected)
I^{b}	Intensity from measurement of background
I^{s}	Intensity from measurement of sample
I^{el}	Intensity from elastic scattering
j	Index
$\mathbf{J}$	Jacobian matrix

Symbol	Meaning
k	General index, index for force constant matrices
k_{B}	Boltzmann's constant ($1.3806503 \times 10^{-23}$ J/K)
K	Force constant or force constant matrix
$\mathcal{K}$	Longitudinal force constant
K_T	Isothermal bulk modulus
l	Index
$\mathbf{l}$	Stack of all cell vectors
$[\mathbf{l}_i]$	Cell vector
L_{I}	Distance from moderator to the sample
L_{dp}	Distance from sample to pixel
L_d	Distance to a detector (used for un-pixelated detectors)
L_{p^*}	Distance to a row of pixels
L_{mon}	Distance between first and second monitors.
$\langle L_{\mathrm{det}} \rangle$	Mean distance traveled by a neutron while in a detector
$\mathcal{L}$	Number of cell vectors (number of q-points too)
$\mathcal{L}_i$	Number of cells along i^{th} direction.
m_{e}	Electron mass
m_{n}	Neutron mass
M	Nuclear mass
$\mathbf{M}$	Example matrix
$n_T(E)$	Mean occupancy for bosons at temperature T
N, N'	Normalization constants for multiphonon correction
$\mathbb{N}$	Counting numbers
p	Indexes pixels ; Momentum
$\mathcal{P}$	Number of phonons
$\mathcal{P}_E$	Number of phonons at energy E
$\mathbb{P}$	Principal value
$\mathbf{q}$	Reciprocal lattice vector
$\mathbf{Q}$	Wavevector transfer or phonon wavevector
$\mathbf{Q}_{\mathrm{I}}$	Initial neutron wavevector (from moderator to sample)
$\mathbf{Q}_{\mathrm{F}}$	Final neutron wavevector (from sample to pixel)
$\mathcal{Q}$	Quality factor
$\mathbf{r}$	Stack of all instantaneous position vectors
$[\mathbf{r}_i]$	Instantaneous position vector
R	Cube edge
$\mathcal{R}$	Region of integration (like a set)
$\lvert\mathcal{R}\rvert$	Area of region $\mathcal{R}$ (like the measure of the set)
$\mathbf{s}$	Stack of all site vectors
$[\mathbf{s}_i]$	Site vector

Symbol	Meaning
$S(Q,E)$	Angle averaged response function
$S^{\mathcal{P}}(Q,E)$	$\mathcal{P}$-phonon angle averaged response function
S^{inc}	Incoherent response function
S^{coh}	Coherent response function
S	Entropy
S_i	Component of the entropy
S_{cf}	Configurational entropy
S_{el}	Electronic entropy (non-magnetic)
$S_{\text{el,G}}$	Ground state electronic entropy
$S_{\text{el,D}}$	Dilation electronic entropy
$S_{\text{el,M}}$	Magnetic electronic entropy
S_{ph}	Phonon entropy
$S_{\text{ph,H}}$	Harmonic Phonon entropy
$S_{\text{ph,D}}$	Dilation Phonon entropy
$S_{\text{ph,Q}}$	Quasiharmonic Phonon entropy
$S_{\text{ph,A}}$	Anharmonic Phonon entropy
$S_{\text{ph,NH}}$	Nonharmonic Phonon entropy
$S_{\text{el}-\text{ph}}$	Electron-phonon entropy
$S_{\text{el}-\text{ph,ad}}$	Adiabatic electron-phonon entropy
$S_{\text{el}-\text{ph,na}}$	Non-adiabatic electron-phonon entropy
S_{Janaf}	Total entropy taken from NIST-Janaf
$\mathcal{S}$	Number of site vectors
t	Time ; Index for time-of-flight
T	Temperature
$\bar{T}_j$	Characteristic temperature of phonon spectrum
$\mathcal{T}_{\text{ph}}$	Nuclear kinetic energy
$\mathcal{T}_{\text{el}}$	Electronic kinetic energy
$\mathbf{u}$	Stack of all displacement vectors
$[\mathbf{u}_i]$	Displacement vector
$\mathbf{U}$	Normal mode vector
$\hat{\mathbf{U}}$	Displacement operator for neutron scattering (Squires p. 29)
$\mathcal{U}$	Number of primitive unit cells
v_{F}	Final neutron velocity
$\mathbf{v}_v$, v	Example vector and variable
V	Volume
$V_{\mathbf{q}}$	Reciprocal space volume
$\mathcal{V}$	Potential energy
$\mathcal{V}_{\text{ph}}$	Nuclear potential energy
$\mathcal{V}_{\text{el}}$	Electronic potential energy
$\mathcal{V}_{\text{el}-\text{ph}}$	Potential energy of electron-phonon interactions
$\hat{\mathbf{V}}$	Displacement operator for neutron scattering (Squires p. 29)
W	1/2 argument of Debye-Waller factor, $\exp(2W)$
$\mathbf{x}$	Stack of all equilibrium position vectors
$[\mathbf{x}_i]$	Equilibrium position vector
Y	Penalty function
$Z(Q,E)$	Instrument resolution function

Symbol	Meaning
α	Linear coefficient of thermal expansion
β	$\frac{1}{k_{\mathrm{B}}T}$
γ	Grüneisen parameter
Γ	Halfwidth of a phonon peak
δ_{ij}	Kronecker delta function
$\delta(v)$	Dirac delta function
Δ^i	Shift of type $i \in \{3, 4, \mathrm{Q}\}$
Δ^{s}	Shift from fit for quality factor
ϵ	Small number ...
ζ_0	Constant for removal of elastic peak
$\zeta_{\mathcal{P}}, \zeta'_{\mathrm{ms}}, \zeta_{\mathrm{ms}}$	Multiple scattering constants
η	Effective electron phonon coupling function
$\boldsymbol{\epsilon}_b(\mathbf{q})$	Polarization vector
θ	Index for scattering angles
Θ	Scattering angle
Θ_1	First scattering angle in array
λ	Energy level index
λ_{I}	Incident neutron wavelength
$\Lambda_b\mathbf{q}$	Eigenvalue of the dynamical matrix
μ	Chemical potential
$\xi = E - \mu$	Substitution variable, energy less chemical potential
Ξ	Grand canonical ensemble
π	3.1415926535897931
ρ_{He}	Number density of ^{3}He in a detector
$\rho_{\mathcal{A}}$	Atomic number density
σ^{inc}	Incoherent neutron cross-section (for vanadium, in Chapter 7)
σ^{coh}	Coherent neutron cross-section (for vanadium, in Chapter 7)
σ^{abs}	Absorption cross-section (for helium, in Chapter 7)
τ	Time-of-flight
τ_{I}	Time-of-flight at which neutrons arrive at the sample
τ_{e}	Time-of-flight at which elastically scattered neutrons arrive at a detector (or pixel)
τ_{dp}	Time-of-flight for neutron to travel from sample to pixel
τ_{mon}	Time-of-flight for neutron to go from first to second monitor.
$[\tau_{\mathrm{e}}]_{p^*}$	Time-of-flight for elastically scattered neutron as seen in a row of pixels
τ_1	First time-of-flight in array
Υ_{dt}	Probabilities of detecting a neutron
Υ_t	Energy-dependent probabilities of detecting a neutron
Υ_d	Pressure-dependent probabilities of detecting a neutron
$\Upsilon_{\mathcal{P}}(E)$	Probability of $\mathcal{P}$-phonon scattering with energy E
ϕ	Phase of oscillation
χ	parameters for potentials
ψ	Wavefunction
ψ_0	Ground state wavefunction
ψ_λ	Wavefunction for λ^{th} energy level
ω	Angular frequency
$\bar{\omega}_j$	Moment of phonon spectrum
Ω	Number of microstates corresponding to macrostate ; Solid angle
Ω_i	Number of microstates... for subsystem i

Appendix B

Entropy of Non-interacting Fermions and Bosons

In order to evaluate the entropy of systems of bosons or fermions, we place ourselves in the grand canonical ensemble. We have the following partition function, and expression for the entropy:

$$\Xi = \prod_{\lambda} \left[1 \pm e^{-\beta(E_\lambda - \mu)}\right]^{\pm 1} , \tag{B.1}$$

$$S = k_{\mathrm{B}} \ln \Xi + k_{\mathrm{B}} T \frac{\partial \ln \Xi}{\partial T} , \tag{B.2}$$

where μ is the chemical potential, E_λ is an energy, $\beta \equiv \frac{1}{k_{\mathrm{B}} T}$ and k_{B} is Boltzmann's constant. The plus signs correspond to fermions, and the minuses to bosons. The logarithm of a product may be rewritten as a sum of logs, so:

$$\ln \Xi = \sum_{\lambda} \ln \left\{ \left[1 \pm e^{-\beta(E_\lambda - \mu)}\right]^{\pm 1} \right\} = \pm \sum_{\lambda} \ln \left[1 \pm e^{-\beta(E_\lambda - \mu)}\right] . \tag{B.3}$$

Applying the chain rule, we have:

$$\frac{\partial \ln \Xi}{\partial T} = \frac{\beta}{T} \sum_{\lambda} \frac{E_\lambda - \mu}{e^{\beta(E_\lambda - \mu)} \pm 1} . \tag{B.4}$$

To simplify the development, we define $\xi_\lambda = E_\lambda - \mu$, so:

$$\begin{aligned}
\frac{S}{k_{\rm B}} &= \pm\sum_\lambda \ln\left(1 \pm e^{-\beta\xi_\lambda}\right) + \sum_\lambda \frac{\beta\xi_\lambda}{e^{\beta\xi_\lambda} \pm 1} \\
&= \mp\sum_\lambda \ln\left(\frac{1}{1 \pm e^{-\beta\xi_\lambda}}\right) + \sum_\lambda \frac{\beta\xi_\lambda}{e^{\beta\xi_\lambda} \pm 1} \\
&= \mp\sum_\lambda \ln\left(\frac{e^{\beta\xi_\lambda}}{e^{\beta\xi_\lambda} \pm 1}\right) + \sum_\lambda \frac{\beta\xi_\lambda}{e^{\beta\xi_\lambda} \pm 1} \\
&= \mp\sum_\lambda \ln\left(\frac{\mp 1 + e^{\beta\xi_\lambda} \pm 1}{e^{\beta\xi_\lambda} \pm 1}\right) + \sum_\lambda \frac{\beta\xi_\lambda}{e^{\beta\xi_\lambda} \pm 1} \\
&= \mp\sum_\lambda \ln\left(\frac{\mp 1}{e^{\beta\xi_\lambda} \pm 1} + 1\right) + \sum_\lambda \frac{\beta\xi_\lambda}{e^{\beta\xi_\lambda} \pm 1} \\
&= \mp\sum_\lambda \left[\ln\left(\frac{\mp 1}{e^{\beta\xi_\lambda} \pm 1} + 1\right) \mp \frac{\beta\xi_\lambda}{e^{\beta\xi_\lambda} \pm 1}\right] \\
&= \mp\sum_\lambda \left[\ln\left(1 \mp n_{\rm FB}\right) \mp n_{\rm FB}\beta\xi_\lambda\right] , \qquad \text{(B.5)}
\end{aligned}$$

where the $n_{\rm FB} = \frac{1}{e^{\beta\xi_\lambda} \pm 1}$ is either the mean fermion or boson occupation number, also denoted f_T and n_T, respectively. Continuing, we have:

$$\begin{aligned}
\frac{S}{k_{\rm B}} &= \mp\sum_\lambda \left[\ln\left(1 \mp n_{\rm FB}\right) \mp n_{\rm FB} \ln\left(e^{\beta\xi_\lambda}\right)\right] \\
&= \mp\sum_\lambda \left[\ln\left(1 \mp n_{\rm FB}\right) \mp n_{\rm FB} \ln\left(1 \mp n_{\rm FB}\right) \pm n_{\rm FB} \ln\left(1 \mp n_{\rm FB}\right) \mp n_{\rm FB} \ln\left(e^{\beta\xi_\lambda}\right)\right] \\
&= \mp\sum_\lambda \left[\left(1 \mp n_{\rm FB}\right) \ln\left(1 \mp n_{\rm FB}\right) \pm n_{\rm FB} \left\{\ln\left(1 \mp n_{\rm FB}\right) - \ln\left(e^{\beta\xi_\lambda}\right)\right\}\right] \\
&= \mp\sum_\lambda \left[\left(1 \mp n_{\rm FB}\right) \ln\left(1 \mp n_{\rm FB}\right) \pm n_{\rm FB} \left\{\ln\left(1 \mp \frac{1}{e^{\beta\xi_\lambda} \pm 1}\right) - \ln\left(e^{\beta\xi_\lambda}\right)\right\}\right] \\
&= \mp\sum_\lambda \left[\left(1 \mp n_{\rm FB}\right) \ln\left(1 \mp n_{\rm FB}\right) \pm n_{\rm FB} \left\{\ln\left(\frac{e^{\beta\xi_\lambda} \pm 1}{e^{\beta\xi_\lambda} \pm 1} \mp \frac{1}{e^{\beta\xi_\lambda} \pm 1}\right) - \ln\left(e^{\beta\xi_\lambda}\right)\right\}\right] \\
&= \mp\sum_\lambda \left[\left(1 \mp n_{\rm FB}\right) \ln\left(1 \mp n_{\rm FB}\right) \pm n_{\rm FB} \left\{\ln\left(\frac{e^{\beta\xi_\lambda}}{e^{\beta\xi_\lambda} \pm 1}\right) - \ln\left(e^{\beta\xi_\lambda}\right)\right\}\right] \\
&= \mp\sum_\lambda \left[\left(1 \mp n_{\rm FB}\right) \ln\left(1 \mp n_{\rm FB}\right) \pm n_{\rm FB} \left\{\ln\left(\frac{1}{e^{\beta\xi_\lambda} \pm 1}\right)\right\}\right] \\
&= \mp\sum_\lambda \left[\left(1 \mp n_{\rm FB}\right) \ln\left(1 \mp n_{\rm FB}\right) \pm n_{\rm FB} \ln\left(n_{\rm FB}\right)\right] . \qquad \text{(B.6)}
\end{aligned}$$

For fermions, we take the upper sign, and we have:

$$\frac{S}{k_{\rm B}} = -\sum_\lambda \left[\left(1 - f_T\right) \ln\left(1 - f_T\right) + f_T \ln\left(f_T\right)\right] . \qquad \text{(B.7)}$$

For bosons, we take the lower sign, and we have:

$$\frac{S}{k_{\mathrm{B}}} = \sum_{\lambda} \left[(1+n_T)\ln(1+n_T) - n_T \ln(n_T) \right] . \tag{B.8}$$

For phonons, we may use Eq.3.71, to convert the expression for the boson entropy into an integral using the density of states:

$$\frac{S_{\mathrm{ph}}}{N} = k_{\mathrm{B}}\mathcal{D} \int g(E) \left[(1+n_T)\ln(1+n_T) - n_T \ln(n_T) \right] dE . \tag{B.9}$$

Or, in 3D:

$$\frac{S_{\mathrm{ph}}}{N} = 3k_{\mathrm{B}} \int g(E) \left[(n_T+1)\ln(n_T+1) - n_T \ln(n_T) \right] dE . \tag{B.10}$$

Likewise, for electrons we may write:

$$\frac{S_{\mathrm{el}}}{N} = -k_{\mathrm{B}} \int G(E) \left[(1-f_T)\ln(1-f_T) + f_T \ln(f_T) \right] dE . \tag{B.11}$$

Appendix C

Analytical Reweighting — Algebra

In § 7.4.2 we came across the problem of finding the solution to the following integral:

$$|\mathcal{R}_{QE}| = \iint_{\mathcal{R}_{\Theta\tau}} |\mathbf{J}| d\Theta d\tau = \iint_{\mathcal{R}_{\Theta\tau}} \begin{vmatrix} \frac{dQ}{d\Theta} & \frac{dQ}{d\tau} \\ \frac{dE}{d\Theta} & \frac{dE}{d\tau} \end{vmatrix} d\Theta d\tau \ , \tag{C.1}$$

where $|\mathbf{J}|$ is the determinant of the *Jacobian matrix*, $\mathbf{J}$, and $\mathcal{R}_{\Theta\tau}$ is the region of integration in ϕ-T space, which is the rectangle formed by the points (Θ, τ), $(\Theta, \tau + \Delta\tau)$, $(\Theta + \Delta\Theta, \tau)$, and $(\Theta + \Delta\Theta, \tau + \Delta\tau)$.

The determinant is given by $|\mathbf{J}| = \mathbf{J}_{11}\mathbf{J}_{22} - \mathbf{J}_{12}\mathbf{J}_{21}$, and our first task is to find the components of $\mathbf{J}$. Since:

$$\mathbf{J}_{21} = \frac{dE}{d\Theta} = 0 \ , \tag{C.2}$$

we see that we don't need to find $\mathbf{J}_{12}$ in order to evaluate the integral.[a] From Fig.5.2, we see that:

$$\begin{aligned} \mathbf{J}_{11} = \frac{dQ}{d\Theta} &= \frac{d}{d\Theta}\sqrt{Q_{\mathrm{I}}^2 + Q_{\mathrm{F}}^2 - 2Q_{\mathrm{I}}Q_{\mathrm{F}}\cos(\Theta)} \\ &= \frac{-Q_{\mathrm{I}}Q_{\mathrm{F}}\sin(\Theta)}{\sqrt{Q_{\mathrm{I}}^2 + Q_{\mathrm{F}}^2 - 2Q_{\mathrm{I}}Q_{\mathrm{F}}\cos(\Theta)}} \ . \end{aligned} \tag{C.3}$$

Finally, we have:

$$\mathbf{J}_{22} = \frac{dE}{d\tau} = \frac{d}{d\tau}\left(E_{\mathrm{I}} - E_{\mathrm{F}}\right) = \frac{d}{d\tau}\left[E_{\mathrm{I}} - \frac{m_{\mathrm{n}}}{2}\left(\frac{L_d}{\tau - \tau_{\mathrm{I}}}\right)^2\right] = \frac{m_{\mathrm{n}}L_d^2}{\left(\tau - \tau_{\mathrm{I}}\right)^3} \ , \tag{C.4}$$

where L_d is the distance from the sample to the detector indexed by d.[b]

[a] Technically, the detectors at different angles might also be at different distances. As such $\mathbf{J}_{21}$ is not identically zero; however, our bins in Θ-τ space will never cross detector boundaries, and thus we will always have $\mathbf{J}_{21} = 0$ while we are evaluating Eq. C.1

[b] On a pixelated instrument, this distance should be L_{dp}.

We are thus trying to evaluate the following integral:

$$\begin{aligned} |\mathcal{R}_{QE}| &= \iint_{\mathcal{R}_{\Theta\tau}} \frac{m_{\rm n} L_d^2}{(\tau-\tau_{\rm I})^3} \frac{-Q_{\rm I}Q_{\rm F}\sin(\Theta)}{\sqrt{Q_{\rm I}^2+Q_{\rm F}^2-2Q_{\rm I}Q_{\rm F}\cos(\Theta)}} d\Theta d\tau \\ &= \int_{\mathcal{R}_\tau} \frac{m_{\rm n} L_d^2}{(\tau-\tau_{\rm I})^3} \left[\int_{\mathcal{R}_\Theta} \frac{-Q_{\rm I}Q_{\rm F}\sin(\Theta)}{\sqrt{Q_{\rm I}^2+Q_{\rm F}^2-2Q_{\rm I}Q_{\rm F}\cos(\Theta)}} d\Theta \right] d\tau \ . \end{aligned} \tag{C.5}$$

The integral over Θ may be evaluated immediately. In fact, it consists in simply undoing the derivative taken on the previous page:

$$|\mathcal{R}_{QE}| = \int_{\mathcal{R}_\tau} \frac{m_{\rm n} L_d^2}{(\tau-\tau_{\rm I})^3} \sqrt{Q_{\rm I}^2+Q_{\rm F}^2-2Q_{\rm I}Q_{\rm F}\cos(\Theta)}\ d\tau \ . \tag{C.6}$$

We note that:

$$Q_{\rm F} = \frac{m_{\rm n} L_d}{\hbar(\tau-\tau_{\rm I})} \ , \tag{C.7}$$

and rewrite Eq. C.6 in this form:

$$\begin{aligned} |\mathcal{R}_{QE}| &= \frac{\hbar^3}{m_{\rm n}^2 L_d} \int_{\mathcal{R}_\tau} Q_{\rm F}^3 \sqrt{Q_{\rm I}^2+Q_{\rm F}^2-2Q_{\rm I}Q_{\rm F}\cos(\Theta)}\ d\tau \\ &= \frac{\hbar^3}{m_{\rm n}^2 L_d} \int_{\mathcal{R}_\tau} Q_{\rm F}^4 \sqrt{\left(\frac{Q_{\rm I}}{Q_{\rm F}}\right)^2+1-2\frac{Q_{\rm I}}{Q_{\rm F}}\cos(\Theta)}\ d\tau \ . \end{aligned} \tag{C.8}$$

If we let $x = \frac{Q_{\rm I}}{Q_{\rm F}}$ and $z = \cos(\Theta)$, then $dx = \frac{\hbar Q_{\rm I}}{m_{\rm n} L_d} d\tau$, and we have:

$$\begin{aligned} |\mathcal{R}_{QE}| &= \frac{\hbar^2 Q_{\rm I}^3}{m_{\rm n}} \int_{\mathcal{R}_\tau} \frac{\sqrt{x^2+1-2xz}}{x^4}\ dx = \frac{\hbar^2 Q_{\rm I}^3}{m_{\rm n}} \int_{\mathcal{R}_\tau} \frac{\sqrt{1+\frac{1}{x^2}-\frac{2z}{x}}}{x^3}\ dx \\ &= \frac{\hbar^2 Q_{\rm I}^3}{m_{\rm n}} \sqrt{1-z^2} \int_{\mathcal{R}_\tau} \frac{\sqrt{1+\left(\frac{\frac{1}{x}-z}{\sqrt{1-z^2}}\right)^2}}{x^3}\ dx \ . \end{aligned} \tag{C.9}$$

Let:

$$y = \frac{\frac{1}{x}-z}{\sqrt{1-z^2}} \ , \tag{C.10}$$

which also gives:

$$dy = \frac{-1}{\sqrt{1-z^2}} \frac{dx}{x^2} \ . \tag{C.11}$$

Then:

$$\begin{aligned} |\mathcal{R}_{QE}| &= \frac{\hbar^2 Q_{\rm I}^3}{m_{\rm n}}\sqrt{1-z^2}\int_{\mathcal{R}_\tau}\frac{\sqrt{1+y^2}}{x^3}\,(-x^2\sqrt{1-z^2})dy \\ &= \frac{-\hbar^2 Q_{\rm I}^3}{m_{\rm n}}\left(1-z^2\right)\int_{\mathcal{R}_\tau}\frac{\sqrt{1+y^2}}{x}\,dy\;. \end{aligned} \tag{C.12}$$

We may solve Eq. C.10 for $\frac{1}{x}$, and substitute this into our integral:

$$\frac{1}{x} = y\sqrt{1-z^2}+z\;, \tag{C.13}$$

$$\begin{aligned} |\mathcal{R}_{QE}| &= \frac{-\hbar^2 Q_{\rm I}^3}{m_{\rm n}}\left(1-z^2\right)\int_{\mathcal{R}_\tau}\sqrt{1+y^2}\left(y\sqrt{1-z^2}+z\right)\,dy \\ &= \frac{-\hbar^2 Q_{\rm I}^3}{m_{\rm n}}\left(1-z^2\right)^{\frac{3}{2}}\int_{\mathcal{R}_\tau}\sqrt{1+y^2}\left(y+\frac{z}{\sqrt{1-z^2}}\right)\,dy \\ &= \frac{-\hbar^2 Q_{\rm I}^3}{m_{\rm n}}\left(1-z^2\right)^{\frac{3}{2}}\left[\int_{\mathcal{R}_\tau}y\sqrt{1+y^2}\,dy+\frac{z}{\sqrt{1-z^2}}\int_{\mathcal{R}_\tau}\sqrt{1+y^2}\,dy\right]\;. \end{aligned} \tag{C.14}$$

We may evaluate these two integrals with any standard software for symbolic manipulation (Maxima, Maple, Mathematica...); but, since we have come this far, we might as well do it the old-fashioned way.

For the first integral, we let $u = 1+y^2$, $du = 2ydy$, then:

$$\int_{\mathcal{R}_\tau}y\sqrt{1+y^2}\,dy = \frac{1}{2}\int_{\mathcal{R}_\tau}u^{\frac{1}{2}}\,du = \frac{1}{3}u^{\frac{3}{2}} = \frac{1}{3}\left(1+y^2\right)^{\frac{3}{2}}\;. \tag{C.15}$$

For the second integral, we let $y = \sinh(v)$, $dy = \cosh(v)dv$, then:

$$\begin{aligned} \int_{\mathcal{R}_\tau}\sqrt{1+y^2}\,dy &= \int_{\mathcal{R}_\tau}\sqrt{1+\sinh^2(v)}\,\cosh(v)dv = \int_{\mathcal{R}_\tau}\cosh^2(v)dv \\ &= \int_{\mathcal{R}_\tau}\frac{1}{4}\left[\exp(2v)+\exp(-2v)+2\right]dv \\ &= \frac{1}{4}\left[\frac{1}{2}\exp(2v)+\frac{1}{2}\exp(-2v)+2v\right] \\ &= \frac{1}{4}\left[2\cosh(v)\sinh(v)+2v\right] = \frac{1}{2}\left[y\sqrt{1+y^2}+\operatorname{arcsinh}(y)\right]\;. \end{aligned} \tag{C.16}$$

Putting this all together, we have:

$$\begin{aligned} |\mathcal{R}_{QE}| &= \frac{-\hbar^2 Q_{\rm I}^3}{m_{\rm n}}\left(1-z^2\right)^{\frac{3}{2}}\left\{\frac{1}{3}\left(1+y^2\right)^{\frac{3}{2}}+\frac{z}{\sqrt{1-z^2}}\frac{1}{2}\left[y\sqrt{1+y^2}+\operatorname{arcsinh}(y)\right]\right\} \\ &= \frac{-\hbar^2 Q_{\rm I}^3}{6m_{\rm n}}\left(1-z^2\right)^{\frac{3}{2}}\left\{2\left(1+y^2\right)^{\frac{3}{2}}+\frac{3z}{\sqrt{1-z^2}}\left[y\sqrt{1+y^2}+\operatorname{arcsinh}(y)\right]\right\}\;. \end{aligned} \tag{C.17}$$

We may now simplify and back-substitute:

$$\begin{aligned}
|\mathcal{R}_{QE}| &= \frac{-\hbar^2 Q_{\rm I}^3}{6m_{\rm n}}\left(1-z^2\right)^{\frac{3}{2}}\left\{2\left(1+y^2\right)^{\frac{3}{2}}+3zy\left(\frac{1+y^2}{1-z^2}\right)^{\frac{1}{2}}+\frac{3z}{\sqrt{1-z^2}}\text{arcsinh}(y)\right\} \\
&= \frac{-\hbar^2 Q_{\rm I}^3}{6m_{\rm n}}\left\{2\left[\left(1+y^2\right)\left(1-z^2\right)\right]^{\frac{3}{2}}\right. \\
&\qquad \left.+3yz\sqrt{1-z^2}\left[\left(1+y^2\right)\left(1-z^2\right)\right]^{\frac{1}{2}}+3z\left(1-z^2\right)\text{arcsinh}(y)\right\} \\
&= \frac{-\hbar^2 Q_{\rm I}^3}{6m_{\rm n}}\left\{\left[2\left(1+y^2\right)\left(1-z^2\right)+3yz\sqrt{1-z^2}\right]\sqrt{\left(1+y^2\right)\left(1-z^2\right)}\right. \\
&\qquad \left.+3z\left(1-z^2\right)\text{arcsinh}(y)\right\}\ . \qquad \text{(C.18)}
\end{aligned}$$

Finally, we use the following relationships:

$$\begin{aligned}
(1-z^2)(1+y^2) &= \frac{1}{x^2}-\frac{2z}{x}+1 \\
yz\sqrt{1-z^2} &= \frac{z}{x}-z^2\ , \qquad \text{(C.19)}
\end{aligned}$$

which yield:

$$\begin{aligned}
|\mathcal{R}_{QE}| &= \frac{-\hbar^2 Q_{\rm I}^3}{6m_{\rm n}}\left\{\left[\frac{2}{x^2}-\frac{4z}{x}+2+\frac{3z}{x}-3z^2\right]\left[\frac{1}{x^2}-\frac{2z}{x}+1\right]^{\frac{1}{2}}\right. \\
&\qquad \left.+3z\left(1-z^2\right)\text{arcsinh}\left(\frac{\frac{1}{x}-z}{\sqrt{1-z^2}}\right)\right\} \\
&= \frac{-\hbar^2 Q_{\rm I}^3}{6m_{\rm n}}\left\{\left[\frac{2}{x^2}-\frac{z}{x}+2-3z^2\right]\left[\frac{1}{x^2}-\frac{2z}{x}+1\right]^{\frac{1}{2}}\right. \\
&\qquad \left.+3z\left(1-z^2\right)\text{arcsinh}\left(\frac{\frac{1}{x}-z}{\sqrt{1-z^2}}\right)\right\} \\
&= \frac{-\hbar^2 Q_{\rm I}^3}{6m_{\rm n}}\left\{\left[2\frac{Q_{\rm F}^2}{Q_{\rm I}^2}-\frac{Q_{\rm F}}{Q_{\rm I}}\cos(\Theta)-3\cos^2(\Theta)+2\right]\left[\frac{Q_{\rm F}^2}{Q_{\rm I}^2}-2\frac{Q_{\rm F}}{Q_{\rm I}}\cos(\Theta)+1\right]^{\frac{1}{2}}\right. \\
&\qquad \left.+3\cos(\Theta)\sin^2(\Theta)\text{arcsinh}\left(\frac{\frac{Q_{\rm F}}{Q_{\rm I}}-\cos(\Theta)}{\sin(\Theta)}\right)\right\}\ . \qquad \text{(C.20)}
\end{aligned}$$

The last expression may be rewritten in terms of τ and $\tau_{\rm I}$, rather than $Q_{\rm I}$ and $Q_{\rm F}$; however, that is left as an exercise to the reader who is *truly* bored.

Appendix D

Summation Over Q

Inelastic neutron scattering data from a time-of-flight chopper spectrometer includes both coherent and incoherent scattering. As the phonon DOS is closely related to the incoherent scattering, and summing the coherent scattering over Q yields a good approximation of the incoherent scattering, we sum over Q to determine the phonon DOS. Fig. D.1 shows the region of the data used for integration.

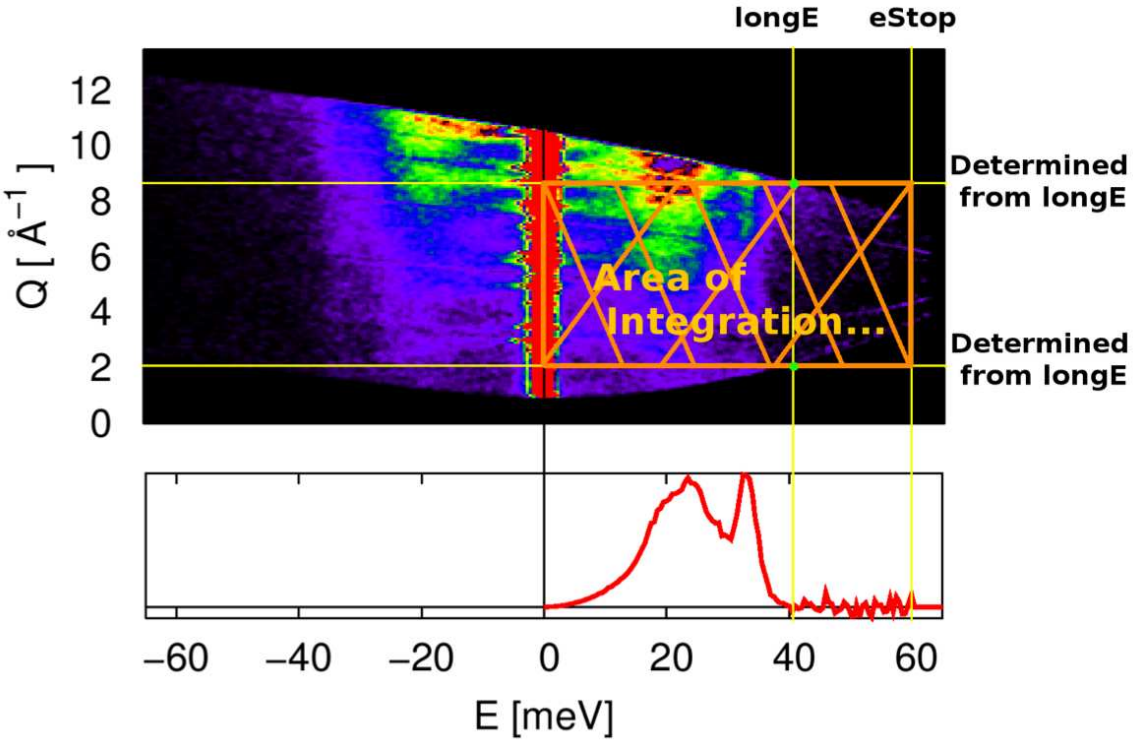

Figure D.1: Integration region for determination of the phonon DOS from inelastic neutron scattering data. Explanation given in the surrounding text.

The top panel shows the scattering, converted from time-of-flight and detector (and pixel) to

the scattering function, $S(Q, E)$. The energy, E, marked "longE" is an estimate of the highest single-phonon energy, and that marked "eStop" is the highest energy considered. From *longE*, a rectangular area of integration is found by looking along $E =$*longE* for the values of the momentum transfer, Q, at which the data starts and stops. The data above $E =$*eStop* is thrown away, as is the data below $E = 0$, the former because of issues with noise as the final velocity of the neutrons approaches zero, the latter because the resolution gets significantly worse as the final velocity of the neutrons increases. The bottom panel shows the phonon density of states as determined from the data, and it is clear that the chosen value of *longE* indeed corresponds to the highest phonon frequencies.

Appendix E

Constraints on Force Constants in BvK Models

Consider a pair of atoms in a crystal whose separation is given by some vector. The forces one atom experiences as the other is displaced may be represented with a force constant tensor. Assuming our crystal resides in three dimensions, we write:

$$F = \begin{pmatrix} F_{11} & F_{12} & F_{13} \\ F_{12} & F_{22} & F_{23} \\ F_{13} & F_{32} & F_{33} \end{pmatrix} . \tag{E.1}$$

Here, we have 9 degrees of freedom (DOF).

The point group symmetries of the crystal may be used to reduce the DOF. We take one of the 3×3 representations of the point group symmetries, S_s, and apply it to F, requiring that F remain unchanged:

$$S_s = \begin{pmatrix} S^s_{11} & S^s_{12} & S^s_{13} \\ S^s_{21} & S^s_{22} & S^s_{23} \\ S^s_{31} & S^s_{32} & S^s_{33} \end{pmatrix} . \tag{E.2}$$

Or:

$$S_s^{\mathrm{T}} F S_s = F \, . \tag{E.3}$$

We may rewrite this equation:

$$S_s^{\mathrm{T}} F - F S_s^{-1} = 0 \, . \tag{E.4}$$

This is a special case of the *Lyapunov equation*:

$$AX + XB = C \,, \tag{E.5}$$

where A, B, C and X are all square matrices of dimension N. It is clear that all the terms on the left-hand side of the equation are linear in the components of X, thus, their sum must be linear in the components of X. This means that we may rewrite the equation as follows:

$$Mx + b = 0 \,, \tag{E.6}$$

where M is a $N^2 \times N^2$ matrix, and y and b are N^2-vectors. The order in which we choose to map the components of the matrix X into the vector x is arbitrary; however, once we choose an order, we must be consistent. Let us work through an example. Let:

$$x = \begin{pmatrix} x_{11} \\ x_{12} \\ x_{13} \\ x_{21} \\ x_{22} \\ x_{23} \\ x_{31} \\ x_{32} \\ x_{33} \end{pmatrix} \,, \tag{E.7}$$

which would imply the same ordering for b, where the components would be given by $-C_{ij}$.

Let us construct the matrix $Z \equiv AX + XB$. For the 3x3 case, we have:

$$Z = \begin{pmatrix} A_{11}X_{11} + A_{12}X_{21} + A_{13}X_{31} & A_{11}X_{12} + A_{12}X_{22} + A_{13}X_{32} & A_{11}X_{13} + A_{12}X_{23} + A_{13}X_{33} \\ A_{21}X_{11} + A_{22}X_{21} + A_{23}X_{31} & A_{21}X_{12} + A_{22}X_{22} + A_{23}X_{32} & A_{21}X_{13} + A_{22}X_{23} + A_{23}X_{33} \\ A_{31}X_{11} + A_{32}X_{21} + A_{33}X_{31} & A_{31}X_{12} + A_{32}X_{22} + A_{33}X_{32} & A_{31}X_{13} + A_{32}X_{23} + A_{33}X_{33} \end{pmatrix}$$
$$+$$
$$\begin{pmatrix} X_{11}B_{11} + X_{12}B_{21} + X_{13}B_{31} & X_{11}B_{12} + X_{12}B_{22} + X_{13}B_{32} & X_{11}B_{13} + X_{12}B_{23} + X_{13}B_{33} \\ X_{21}B_{11} + X_{22}B_{21} + X_{23}B_{31} & X_{21}B_{12} + X_{22}B_{22} + X_{23}B_{32} & X_{21}B_{13} + X_{22}B_{23} + X_{23}B_{33} \\ X_{31}B_{11} + X_{32}B_{21} + X_{33}B_{31} & X_{31}B_{12} + X_{32}B_{22} + X_{33}B_{32} & X_{31}B_{13} + X_{32}B_{23} + X_{33}B_{33} \end{pmatrix} .$$

We see that Z_{12} depends on the 1$^{\text{st}}$ row of A, the 2$^{\text{nd}}$ column of X, the 1$^{\text{st}}$ row of X, and the 2$^{\text{nd}}$

column of B. More generally:

$$Z_{ij} = \sum_k A_{ik} X_{kj} + B_{kj} X_{ik} \ . \tag{E.8}$$

Because of our choice of mapping from X to x, the Z_{ij} tell us what row in M we are dealing with. The indices on the variables X_{kj} or X_{ik} tell us which column in M. All that is left is to add the A_{ik} and B_{kj} into the slots in M, so given. This is difficult to show explicily, but we will try anyways:

$$M = \begin{pmatrix} M_{11} & M_{12} & \dots & M_{19} \\ M_{21} & M_{22} & \dots & M_{29} \\ \vdots & \vdots & \ddots & \vdots \\ M_{91} & M_{92} & \dots & M_{99} \end{pmatrix} \leftarrow \begin{pmatrix} \{Z_{11}, X_{11}\} & \{Z_{11}, X_{12}\} & \dots & \{Z_{11}, X_{33}\} \\ \{Z_{21}, X_{11}\} & \{Z_{21}, X_{12}\} & \dots & \{Z_{21}, X_{33}\} \\ \vdots & \vdots & \ddots & \vdots \\ \{Z_{33}, X_{11}\} & \{Z_{33}, X_{12}\} & \dots & \{Z_{33}, X_{33}\} \end{pmatrix} . \tag{E.9}$$

The left and center of the equation are M and the components of M. The thing on the right is supposed to indicate that any time we have Z_{ij} on the left in Eq. E.8, and an X_{mn} next to one of the coefficients A_{pq} or B_{rt} on the right, we add that coefficient at the slot marked $\{Z_{ij} X_{mn}\}$ in M. The problem $AX + XB = C$ has now been reduced to $Mx + b = 0$, which linear algebra tells us how to solve.

For our particular case, we wish to find the constraints on the components of F. Simply take $A \to S_s^{\mathrm{T}}$, $B \to S_s^{-1}$, $X \to F$ in Eq. E.5, and $C = 0$ and then put M into reduced row echelon form. Reading off the rows gives us the constraints on the components of F. For example, we may end up with something that looks like this:

```
 xx  xy  xz  yx  yy  yz  zx  zy  zz
[ 0.  1.  0.  0.  0.  0.  0.  0.  0.]
[ 0.  0.  1.  0.  0.  0.  0.  0.  0.]
[ 0.  0.  0.  1.  0.  0.  0.  0.  0.]
[ 0.  0.  0.  0.  1.  0.  0.  0. -1.]
[ 0.  0.  0.  0.  0.  1.  0.  0.  0.]
[ 0.  0.  0.  0.  0.  0.  1.  0.  0.]
[ 0.  0.  0.  0.  0.  0.  0.  1.  0.] ,
```

which we can rewrite like so:

```
xy                          = 0
    xz                      = 0
        yx                  = 0
            yy          -zz = 0
                yz          = 0
                    zx      = 0
                        zy  = 0 .
```

We see, then, that there are two DOF. Both $yy = zz$, and xx may be varied independently This particular force constant tensor is axially symmetric.

If there are n symmetry elements, S_s, that can transform our bond vector back onto itself, we simply stack up the n M_s:

$$M = \begin{pmatrix} M_1 \\ M_2 \\ \vdots \\ M_n \end{pmatrix} , \tag{E.10}$$

find the reduced row echelon form of M, and read off the constraints on the force constants as above.

Appendix F

Supplementary Material for Chapter 15

Figs. F.1–F.10 show lattice parameters and quality factors for the FCC metals as a function of normalized temperature T/T_M. In the top panels, the thick gray line is the experimental data (sources are given in § 15.3.2.1). In all panels, the red circles and lines were calculated using the potentials from Cleri and Rosato [338], and the blue triangles and lines were calculated using our optimized potentials. The light gray region in the lower panels comes from fits to experimental data as described in § 15.5. The black squares in the bottom panel show the experimental data, when available.

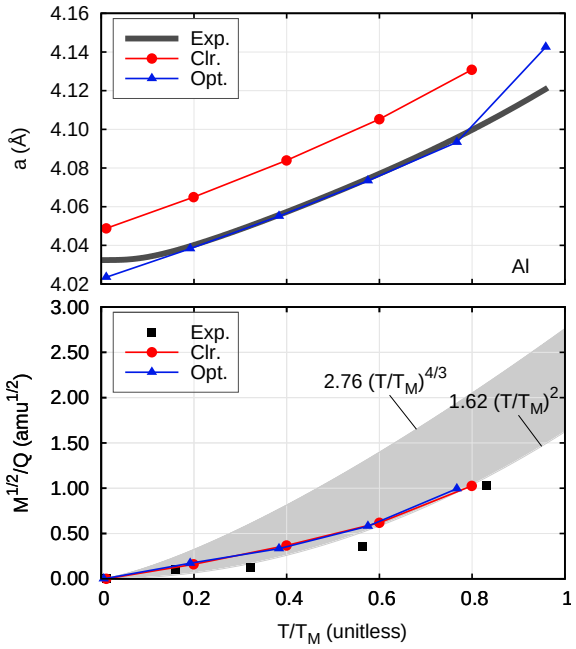

Figure F.1: Aluminum

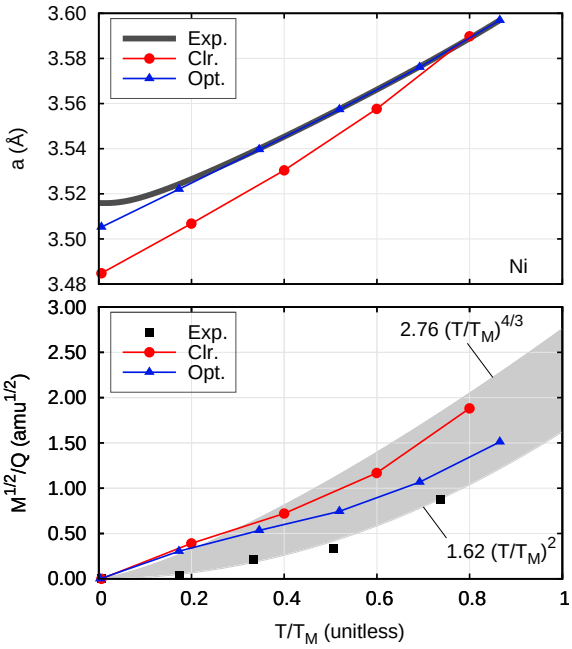

Figure F.2: Nickel

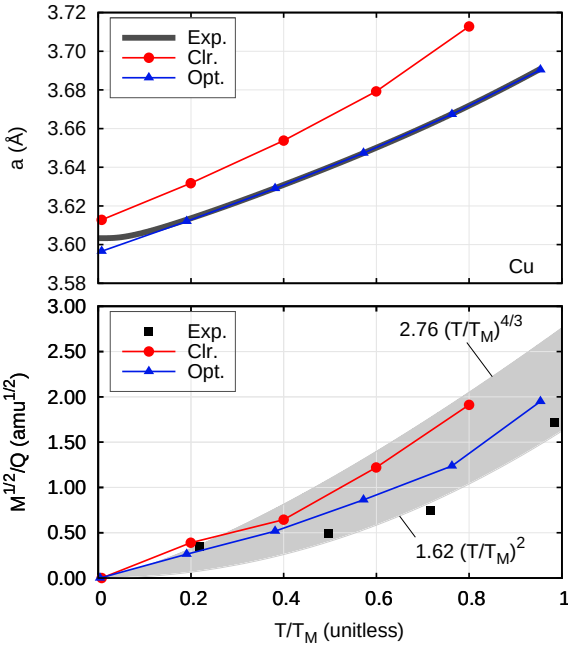

Figure F.3: Copper

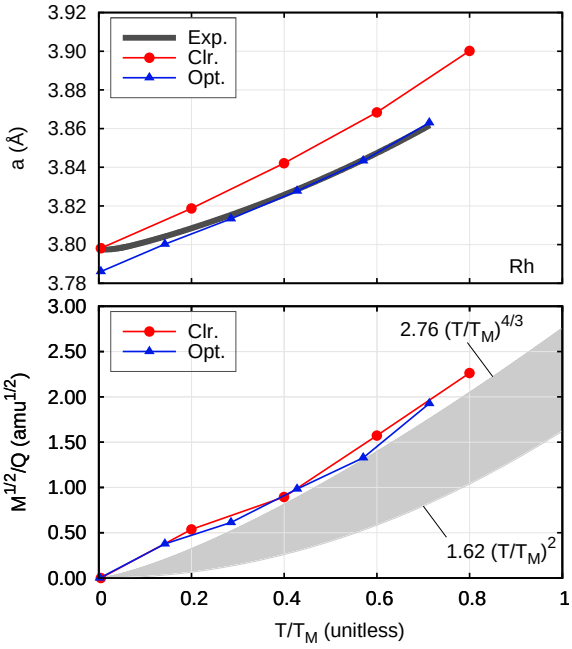

Figure F.4: Rhodium

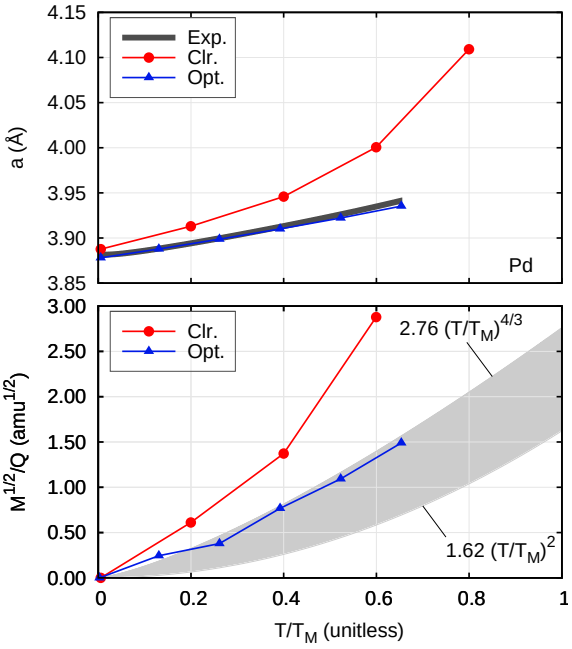

Figure F.5: Palladium

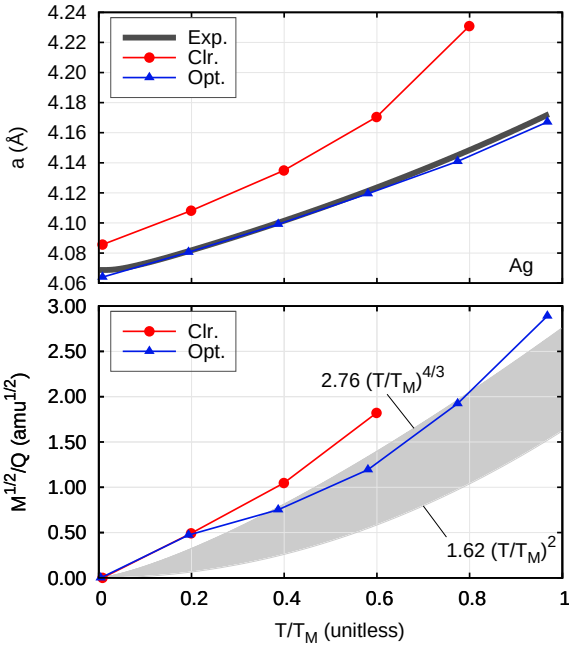

Figure F.6: Silver

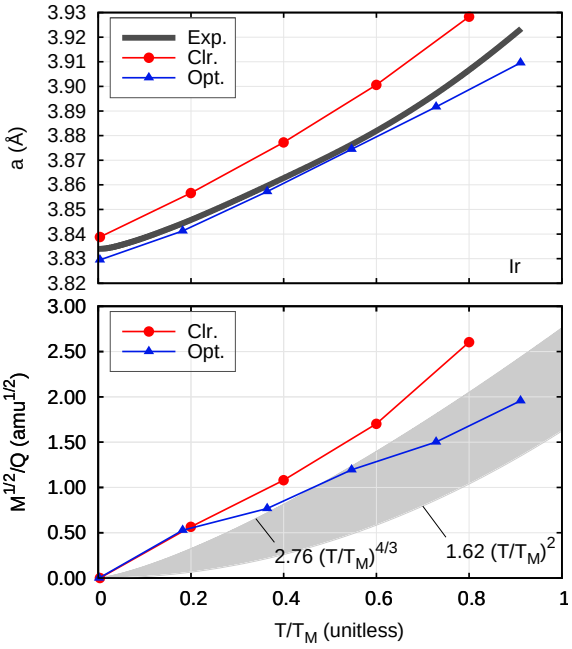

Figure F.7: Iridium

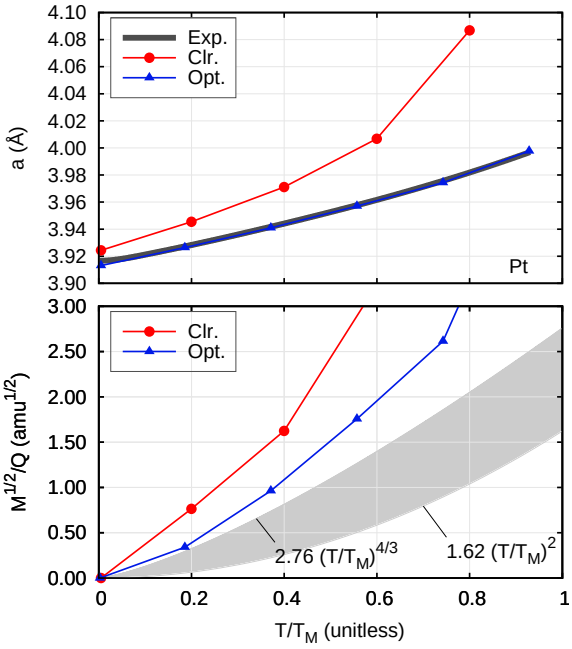

Figure F.8: Platinum

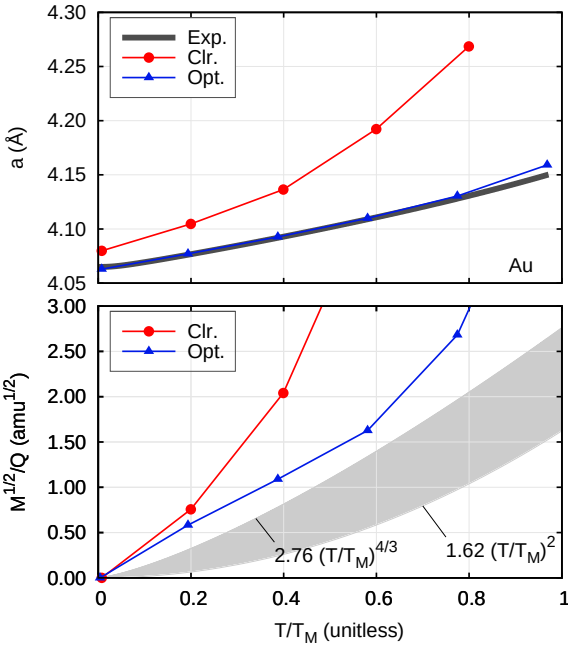

Figure F.9: Gold

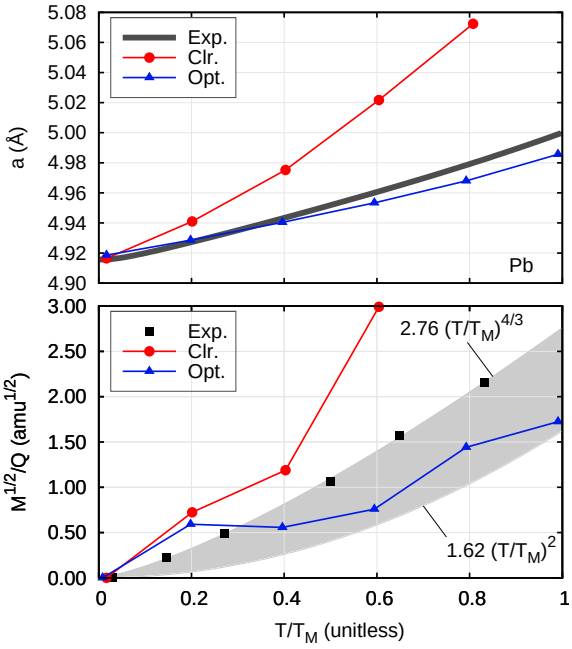

Figure F.10: Lead

Figs. F.11–F.20 show phonon spectra as a function of temperature (as marked) for the FCC metals as determined with molecular dynamics simulations using our optimized potentials in black lines and points. The colored, solid lines are fits to the data using Eqs. 15.41 and 15.42.

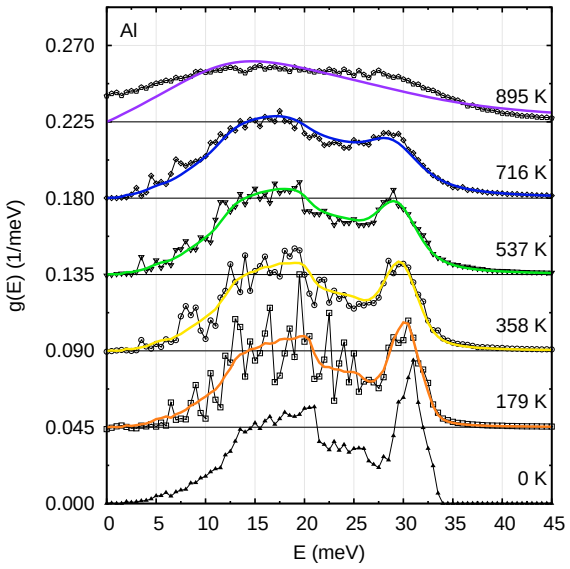

Figure F.11: Aluminum

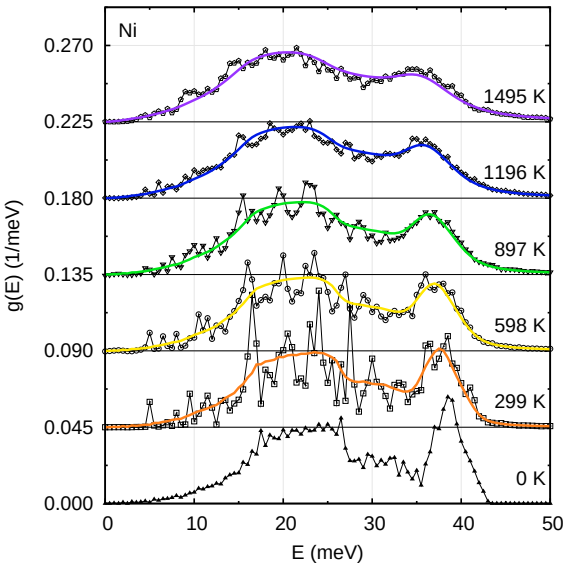

Figure F.12: Nickel

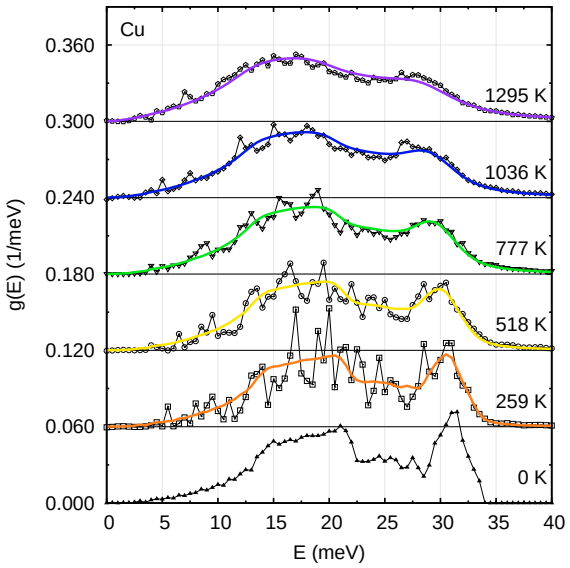

Figure F.13: Copper

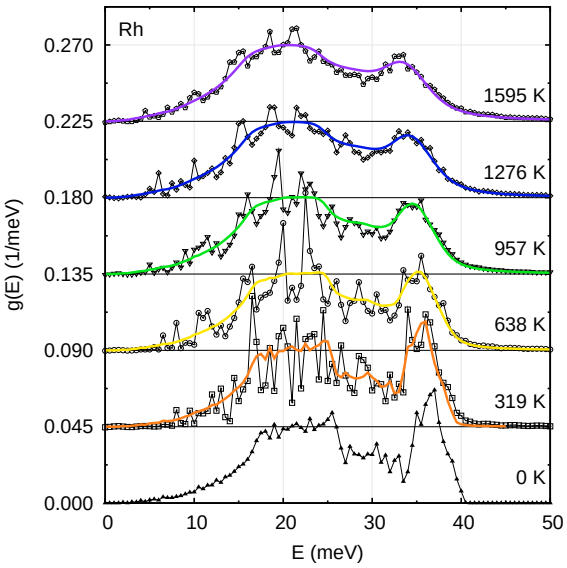

Figure F.14: Rhodium

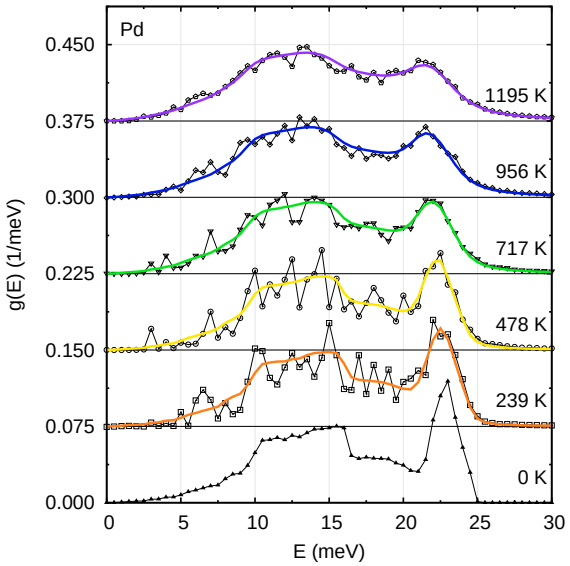

Figure F.15: Palladium

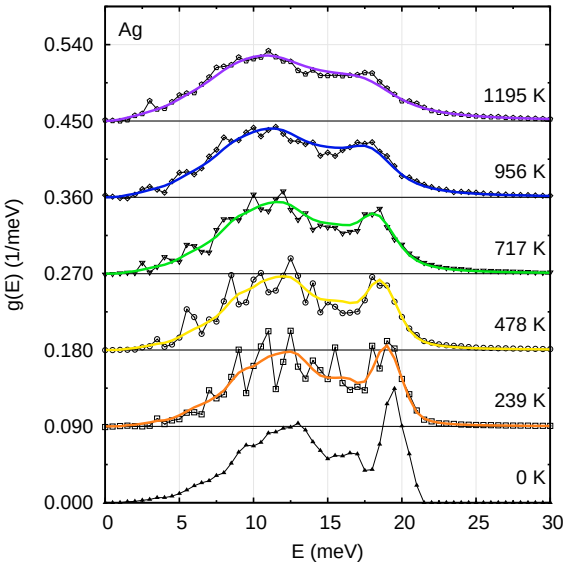

Figure F.16: Silver

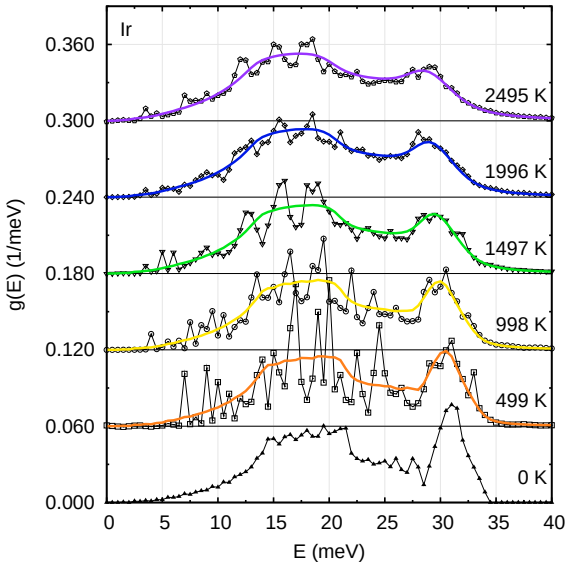

Figure F.17: Iridium

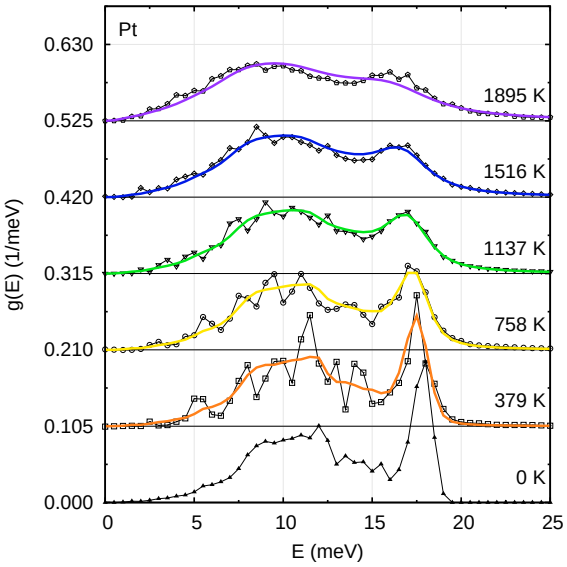

Figure F.18: Platinum

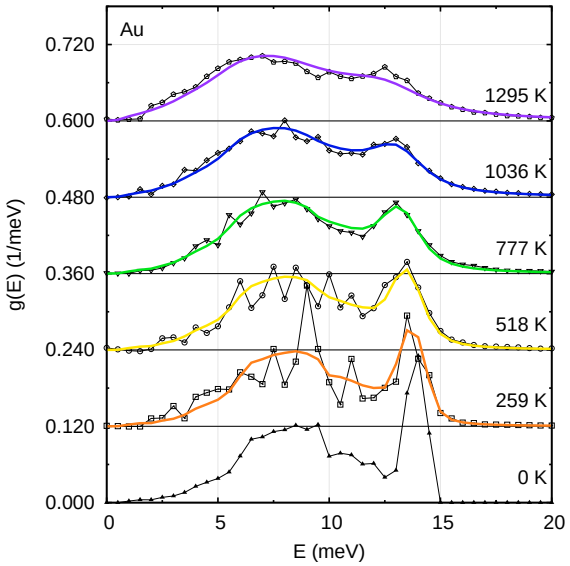

Figure F.19: Gold

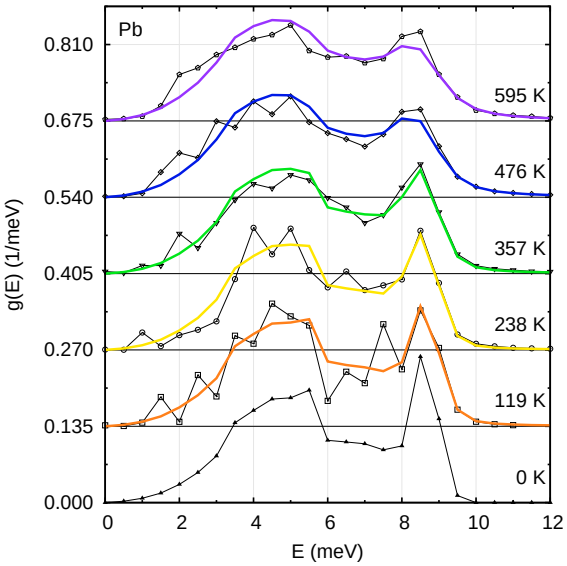

Figure F.20: Lead

Figs. F.21–F.30 show projections of molecular dynamics trajectories onto the high and low energy normal mode displacement patterns shown in Fig. 15.9. For each FCC metal, our optimized potential was used for the simulation, and the projections were performed as described in § 15.3.2.3 at temperatures as marked.

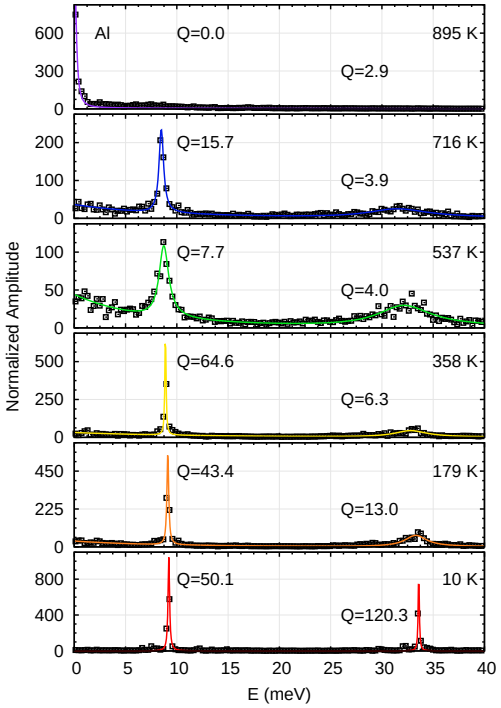

Figure F.21: Aluminum

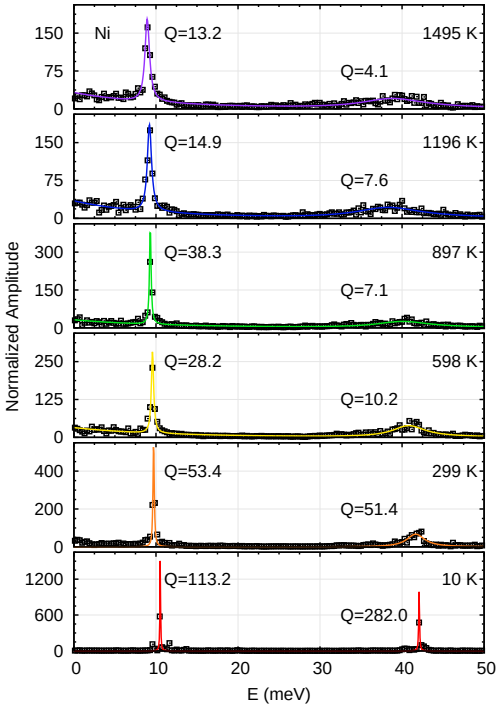

Figure F.22: Nickel

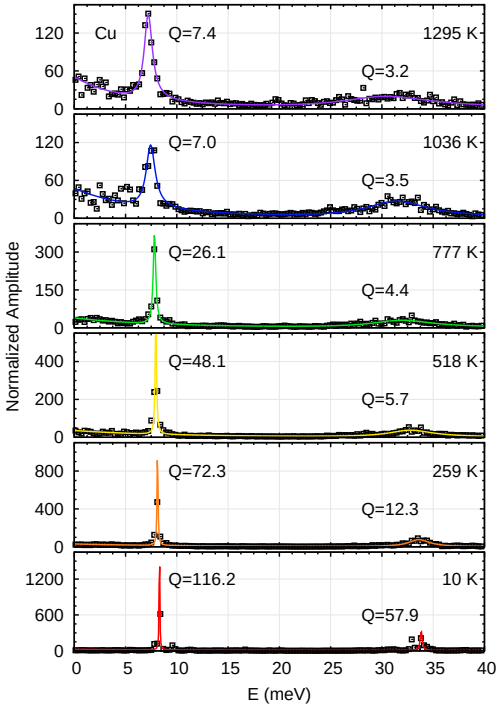

Figure F.23: Copper

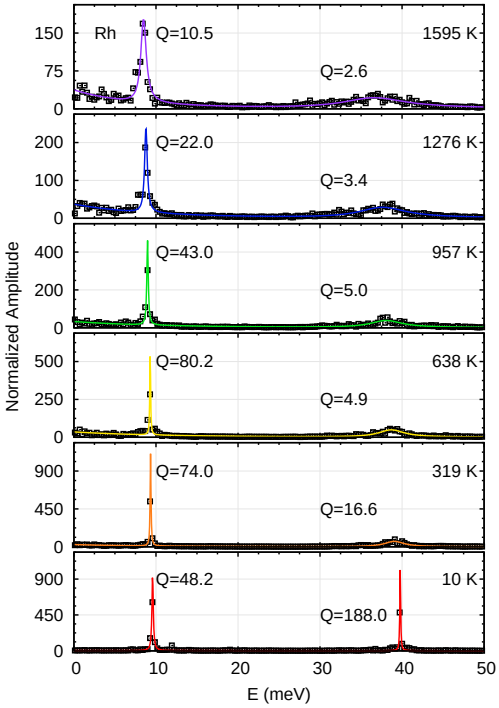

Figure F.24: Rhodium

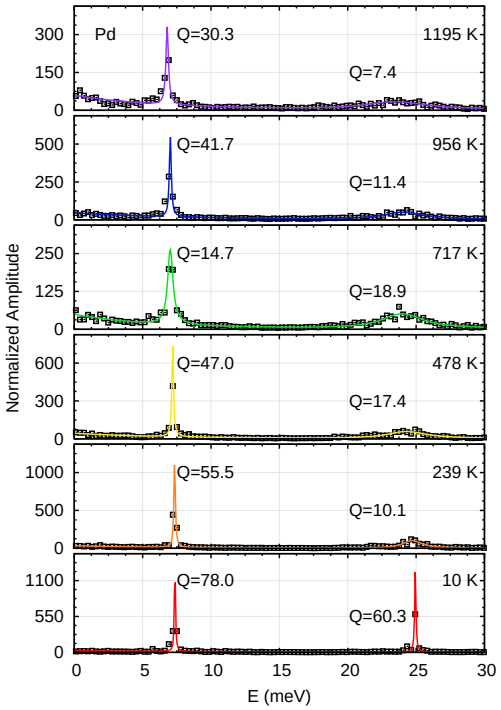

Figure F.25: Palladium

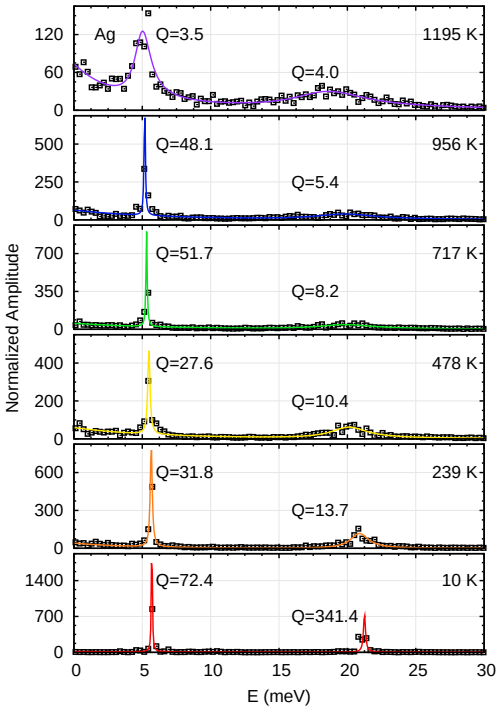

Figure F.26: Silver

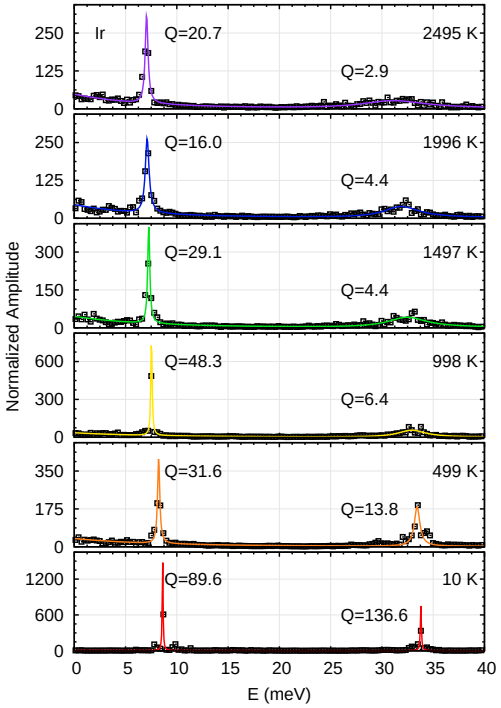

Figure F.27: Iridium

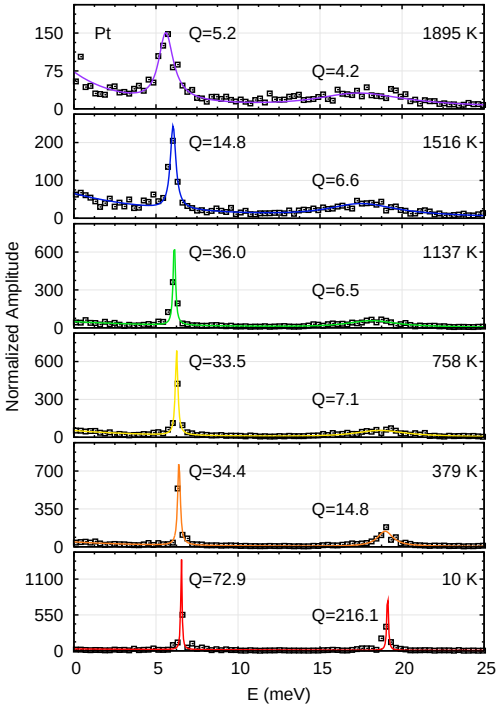

Figure F.28: Platinum

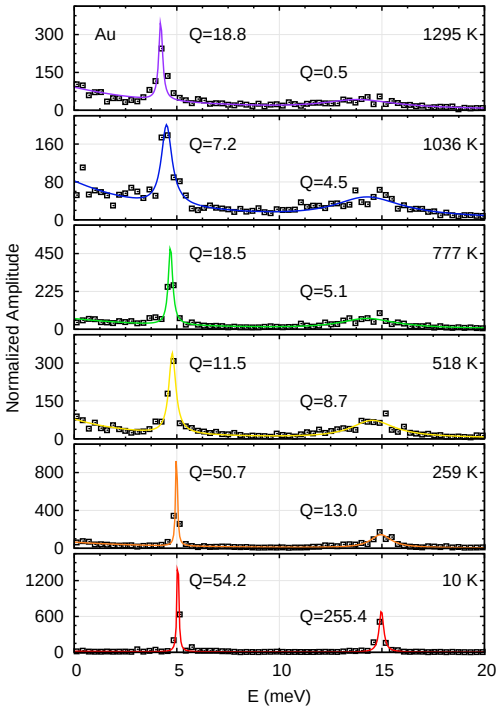

Figure F.29: Gold

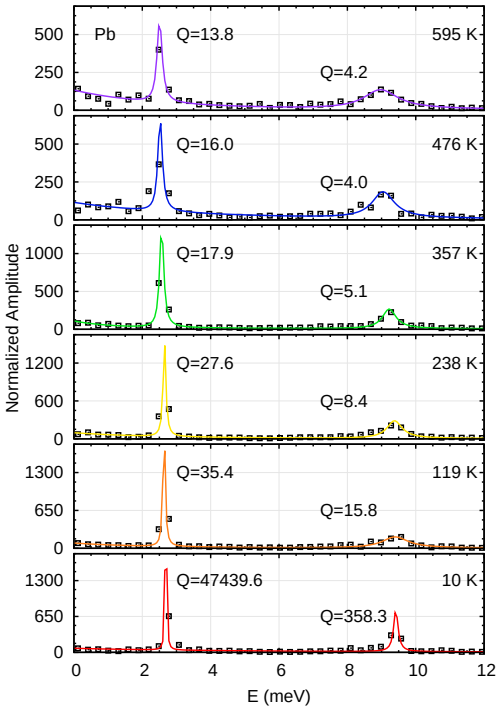

Figure F.30: Lead

Appendix G

Code

Some of the code that was produced for and used in this thesis is available on the web. None of it is complete, and in particular, much of it lacks decent documentation. It is here so that an extremely interested scientist may be able to more accurately reproduce my work.

The files are named *C.L.tbz2* where $C \in \{bvk,mph,qfit,gcon\}$ is a program "title" and $L \in \{gpl,bsd\}$ refers to the license. The programs are very briefly explained here:

- *bvk* — Refers to the BvK code (without the optimization components) that was used for fits to aluminum, nickel, and iron spectra in Chapters 9, 11, and 12.
- *mph* — Refers to the multiphonon correction code described in § 8.1.2 and used for the analysis of the aluminum, lead, nickel, chromium, and vanadium data in Chapters 9–11 and 13.
- *qfit* — Refers to the quality factor and shift finding code described in § 8.2 and used for the analysis of the quality factors for aluminum, lead, nickel, iron, chromium, and vanadium in Chapters 9–13; as well as for the quality factors for the spectra from molecular dynamics shown in Chapter 15.
- *gcon* — Refers to the code for numerically determining the constraints on force constants given point group symmetries.

The URLs for the BSD licensed programs are:

http://resolver.caltech.edu/CaltechETD:etd-12082008-130722/unrestricted/bvk.bsd.tbz2

http://resolver.caltech.edu/CaltechETD:etd-12082008-130722/unrestricted/mph.bsd.tbz2

http://resolver.caltech.edu/CaltechETD:etd-12082008-130722/unrestricted/qfit.bsd.tbz2

http://resolver.caltech.edu/CaltechETD:etd-12082008-130722/unrestricted/gcon.bsd.tbz2

The URLs for the GPLv3 licensed programs are:

http://resolver.caltech.edu/CaltechETD:etd-12082008-130722/unrestricted/bvk.gpl.tbz2

http://resolver.caltech.edu/CaltechETD:etd-12082008-130722/unrestricted/mph.gpl.tbz2

http://resolver.caltech.edu/CaltechETD:etd-12082008-130722/unrestricted/qfit.gpl.tbz2

http://resolver.caltech.edu/CaltechETD:etd-12082008-130722/unrestricted/gcon.gpl.tbz2

Bibliography

[1] *A theory of cooperative phenomena*, R. Kikuchi, Phys. Rev. **81**, 988 (1951).

[2] *Generalized cluster description of multicomponent systems*, J. M. Sanchez, F. Ducastelle, and D. Gratias, Physica A **128**, 334 (1984).

[3] Solid State Physics, D. de Fontaine, edited by H. Ehrenreich, F. Seitz and D. Turnbull, Academic Press, New York, 1979.

[4] Order and Phase Stability in Alloys, F. Ducastelle, North-Holland, Amsterdam, 1991.

[5] Statistics and Dynamics of Alloy Phase Transformations, A. Zunger, edited by P.E.A. Turchi and A. Gonis, Plenum, New York, 1994.

[6] *The effect of lattice vibrations on substitutional alloy thermodynamics*, A. van de Walle and G. Ceder, Revs. Modern Physics **74**, 11 (2002).

[7] *Large vibrational effects upon calculated phase boundaries in Al-Sc*, V. Ozolins and M. Asta, Phys. Rev. Lett. **86**, 448 (2001).

[8] *First-principles theory of vibrational effects on the phase stability of Cu-Au compounds and alloys*, V. Ozolins, C. Wolverton, and A. Zunger, Phys. Rev. B **58**, R5897 (1998).

[9] *Effect of lattice vibrations on the ordering tendencies in substitutional binary alloys*, G.D. Garbulsky and G. Ceder, Phys. Rev. B **49**, 6327 (1994).

[10] *Vibrational entropy of ordered and disordered Ni_3Al*, L. Anthony, J.K. Okamoto, and B. Fultz, Phys. Rev. Lett. **70**, 1128 (1993).

[11] *Superconductivity: iron under pressure*, K. Shimizu, T. Kimura, S. Furomoto, K. Takeda, K. Kontani, Y. Onuki, and K. Amaya, Nature **412**, 316 (2001).

[12] *Phonon-phonon coupling and the stability of the high-temperature BCC phase of Zr*, Y.Y. Ye, Y. Chen, K.M. Ho, B.N. Harmon, and P.A. Lindgard, Phys. Rev. Lett. **58**, 1769 (1987).

[13] *Vibrational and electronic entropy of beta-cerium and gamma-cerium measured by inelastic neutron scattering*, M.E. Manley, R.J. McQueeney, B. Fultz, R. Osborn, G.H. Kwei, P.D. Bogdanoff, Phys. Rev. B **65**, 144111-1 (2002).

[14] *No role for phonon entropy in the FCC→FCC volume collapse transition in* $Ce_{0.9}Th_{0.1}$ *at ambient pressure*, M.E. Manley, R.J. McQueeney, B. Fultz, T. Swan-Wood, O. Delaire, E. Goremychkin, J.C. Cooley, W.L. Hults, J.C. Lashley, R. Osborn, and J.L. Smith, Phys. Rev. B **67**, 014103-1 (2003).

[15] *Calculation of high-pressure phases of Al*, P.K. Lam and M.L. Cohen, Phys. Rev. B **27**, 5986 (1983).

[16] *Phonon dispersion of the BCC phase of group-IV metals. II. BCC zirconium, a model case of dynamical precursors of martensitic transitions*, A. Heiming, W. Petry, J. Trampenau, M. Alba, C. Herzig, H.R. Schober, and G. Vogl, Phys. Rev. B **43**, 10 948 (1991).

[17] *First-principles theory of iron up to earth-core pressures: structural, vibrational, and elastic properties*, P. Söderlind, J.A. Moriarty, and J.M. Wills, Phys. Rev. B **53**, 14063 (1996).

[18] *Ab initio study of the martensitic BCC-HCP transformation in iron*, M. Ekman, B. Sadigh, K. Einarsdotter, and P. Blaha, Phys. Rev. B **58**, 5296 (1998).

[19] *Ab initio free energy calculations on the polymorphs of iron at core conditions*, L. Vočadlo, J. Brodholt, D. Alfê, M.J. Gillan, and G.D. Price, Phys. Earth Planet. Inter. **117**, 123 (2000).

[20] *Magnetism in iron as a function of pressure*, G. Steinle-Neumann, R.E. Cohen, and L. Stixrude, J. Phys. Condens. Matter **16**, S1109 (2004).

[21] Binary alloy phase diagrams, M.F. Singleton, J.L. Murray, P. Nash, ASM International, Metals Park, 1991.

[22] *The role of phonons in the thermodynamics of the martensitic transformation in NiTi*, P.D. Bogdanoff and B. Fultz, Philos. Mag. **81**, 299 (2001).

[23] *Vibrational entropy of spinodal decomposition in FeCr*, T.L. Swan-Wood, O. Delaire, and B. Fultz, Phys. Rev. B **72**, 024305 (2005).

[24] *Vibrational entropy of the* γ*–*α *martensitic transformation in* $Fe_{71}Ni_{29}$, O. Delaire, M. Kresch, and B. Fultz, Philos. Mag. **85**, 3567 (2005).

[25] *Evaluation of thermodynamic functions of elemental crystals and liquids.*, D.C. Wallace, Phys. Rev. E **56**, 1981 (1997).

[26] *Nonadiabatic contributions to the free energy from the electron-phonon interaction in Na, K, Al, and Pb*, N. Bock, D. Coffey, and D.C. Wallace, Phys. Rev. B **72**, 155120-1 (2005).

[27] *Electron-magnetic, lattice, and magnon Grüneisen parameters of iron and nickel: results from thermal expansion measurements and model calculations*, G.D. Mukherjee, C. Bansal, and A. Chatterjee, Int. J. Mod. Phys. B **12**, 449 (1998).

[28] *Adiabatic and nonadiabatic contributions to the free energy from the electron-phonon interaction for Na, K, Al, and Pb*, N. Bock, D.C. Wallace, and D. Coffey, Phys. Rev. B **73**, 075114-1 (2006).

[29] *Thermodynamics of solids: corrections from electron-phonon interactions*, P.B. Allen and J.C.K. Hui, Z. Phys. B **37**, 33 (1980).

[30] *Corrections to the electronic heat capacity of metals due to the finite lifetimes of the conduction electrons*, M. Thiessen, Int. J. Thermophys. **7**, 1183 (1986).

[31] *Physical contributions to the heat capacity of nickel*, P.J. Meschter, J.W. Wright, C.R. Brooks, and T.G. Kollie, J. Phys. Chem. Solids **42**, 861 (1981).

[32] *Spin fluctuations in paramagnetic chromium determined from entropy considerations*, G. Grimvall, J. Häglund, and A. Fernandéz Guillermet, Phys. Rev. B **47**, 15 338 (1993).

[33] *Adiabatic and nonadiabatic contributions to the free energy from the electron-phonon interaction for Na, K, Al, and Pb*, N. Bock, D.C. Wallace, and D. Coffey, Phys. Rev. B **73**, 075114 (2006).

[34] *Anharmonic effects in the thermodynamic properties of solids II. analysis of data for lead and aluminum*, A.J. Leadbetter, J. Phys. C **1**, 1489 (1968).

[35] *Neutron scattering measurements of phonons in nickel at elevated temperatures*, M. Kresch, O. Delaire, R. Stevens, J.Y.Y. Lin, and B. Fultz, Phys. Rev. B **75**, 104301 (2007).

[36] *Electronic, quasiharmonic, and anharmonic entropies of transition metals*, O. Eriksson, J.M. Wills, and D. Wallace, Phys. Rev. B **46**, 5221 (1992).

[37] Statistical Physics of Crystals and Liquids: A Guide to Highly Accurate Equations of State, D.C. Wallace, World Scientific Publishing Co. Pte. Ltd., Singapore, 2002.

[38] Thermodynamics of Crystals, D.C. Wallace, Dover Publications, 1998.

[39] *Temperature dependence of the lattice dynamics of chromium*, J. Trampenau, W. Petry, and C. Herzig, Phys. Rev. B **47**, 3132 (1993).

[40] *Adiabatic electron-phonon interactions and high-temperature thermodynamics of the A15 compound V_3X,*, O. Delaire, M.S. Lucas, J. Munõz, M. Kresch, and B. Fultz, Phys. Rev. Lett. **101**, 105504 (2008).

[41] *Electron-phonon interactions and high-temperature thermodynamics of vanadium and its alloys,*, O. Delaire, M. Kresch, J. Munõz, M. Lucas, J.Y.Y. Lin, and B. Fultz, Phys. Rev. B **77**, 214112 (2008).

[42] *Phonons in aluminum at high temperatures studied by inelastic neutron scattering*, M. Kresch, M. Lucas, O. Delaire, J.Y.Y. Lin, and B. Fultz, Phys. Rev. B **77**, 024301 (2008).

[43] *Dependence of phonon frequencies on the pseudopotential form factor for aluminum*, D.C. Wallace, Phys. Rev. **187**, 991 (1969).

[44] *Ab initio calculation of phonon frequencies of Al*, P.K. Lam and M.L. Cohen, Phys. Rev. B **25**, 6139 (1982).

[45] *Magnetically induced variations in phonon frequencies*, J.H. Lee, Y.C. Hsue, and A.J. Freeman, Phys. Rev. B **73**, 172405 (2006).

[46] *Ab initio phonon dispersions of Fe and Ni*, A. Dal Corso and S. de Giaoncoli, Phys. Rev. B **62**, 273 (2000).

[47] *Influence of local electron interactions on phonon spectrum in iron*, J. Łażewski, P. Piekarz, A.M. Oleś, and K. Parlinski, Phys. Rev. B **74**, 174304 (2006).

[48] *Phonon dispersion relation in rhodium: ab initio calculations and neutron scattering investigations*, A. Eichler, K.-P. Bohnen, W. Reichardt, and J. Hafner, Phys. Rev. B **57**, 324 (1998).

[49] *Ab initio phonon dynamics of iridium*, R. Heid, K.-P. Bohnen, K. Felix, K.M. Ho, and W. Reichardt, J. Phys. Condens. Matter **10**, 7967 (1998).

[50] Solid State Physics, N.W. Ashcroft and N.D. Mermin, Saunders College, Philadelphia, 1976.

[51] Phonons: Theory and Experiments I, P. Brüesch, Springer-Verlag, Berlin, 1982.

[52] Introduction to Solid State Physics, C. Kittel, John Wiley & Sons, 1996.

[53] Vibrations and Waves, A.P. French, W.W. Norton & Company Inc., New York, 1971.

[54] *Temperature dependence of the phonon entropy of vanadium*, P.D. Bogdanoff, B. Fultz, J.L. Robertson, and L. Crow, Phys. Rev. B **65**, 014303 (2001).

[55] *Lattice dynamics and self-diffusion in niobium at elevated temperatures*, F. Güthoff, B. Hennion, C. Herzig, W. Petry, H.R. Schober, and J. Trampenau, J. Phys.: Condens. Matter **6**, 6211 (1994).

[56] *A study of some temperature effects on the phonons in aluminum by use of cold neutrons*, K.E. Larsson, U. Dahlborg, and S. Holmryd, Ark. Fys. **17**, 369 (1960).

[57] *Temperature dependence of lattice dynamics in lead*, F. Sacchetti, R. Caciuffo, C. Petrillo, and U. Steigenberger, J. Phys. Condens. Matter **3**, 8759 (1991).

[58] *Temperature-dependent phonon lifetimes in lead investigated with neutron-resonance spin-echo spectroscopy*, K. Habicht, R. Golub, F. Mezei, B. Keimer, and T. Keller, Phys. Rev. B **69**, 104301 (2004).

[59] *High temperature phonons in iron*, A.M. Vallêra, J. de Phys. **C6 suppl. 12**, 398 (1981).

[60] *Lattice vibrations in copper at elevated temperatures studied by neutron scattering*, A. Larose and B.N. Brockhouse, Can. J. Phys. **54**, 1990 (1976).

[61] *Anharmonic entropy of alkali metals*, D.C. Wallace, Phys. Rev. B **46**, 5242 (1992).

[62] *Anharmonic shifts in the phonon energies in aluminum*, M. Zoli, Phil. Mag. Lett. **62**, no. 3, 203-207 (1990).

[63] *Temperature-dependent frequency shifts and broadening of phonon linewidths in lead*, M. Zoli, J. Phys. Condens. Matter **3**, 6249 (1991).

[64] *Anharmonic damping of the phonon modes in the FCC metals*, M. Zoli, G. Santoro, V. Bortolani, A.A. Maradudin, and R.F. Wallis, Phys. Rev. B **41**, 7507 (1990).

[65] *Comparison of phenomenological and pseudopotential force constants for the lattice dynamics of al*, R.F. Wallis, A.A. Maradudin, V. Bortolani, A.G. Eguiluz, A.A. Quong, A. Franchini, and G. Santoro, Phys. Rev. B **48**, 6043 (1993).

[66] *Thermodynamic properties of FCC metals: Cu and Al*, M. Zoli and V. Bortolani, J. Phys.: Condens. Matter **2**, 525 (1990).

[67] *Many-body anharmonic interactions in Ag and Ni*, M. Zoli, Philos. Mag. A **62**, 377 (1990).

[68] Dynamics of Perfect Crystals, G. Venkataraman, L.A. Feldkamp, and V.C. Sahni, MIT Press, Cambridge, 1975.

[69] The Basics of Crystallography and Diffraction, C. Hammond, Oxford University Press, Oxford, 1997.

[70] http://commons.wikimedia.org/wiki/Image:Torus.png, March 18$^{\text{th}}$, 2008.

[71] Dynamical Theory of Crystal Lattices, M. Born, and K. Huang, Clarendon Press, Oxford, 1988.

[72] Solid State Physics, A. Maradudin, E. Montroll, G. Weiss, and I. Ipatova, edited by H. Ehrenreich, F. Seitz, and D. Turnbull, Academic Press, New-York, 1971, Suppl. 3, 2nd ed.

[73] Electrons and Phonons, J.M. Ziman, Oxford University Press, London, 1967.

[74] Introduction to Quantum Mechanics, D.J. Griffiths, Prentice Hall, Inc., Upper Saddle River, 1995.

[75] Quantum Mechanics, C. Cohen-Tannoudji, B. Diu, F. Laloë,, John Wiley & Sons, New York, 1977.

[76] States of Matter, D.L. Goodstein, Dover Publications, Inc., New York, 1975.

[77] *Scattering of neutrons by an anharmonic crystal*, A.A. Maradudin and A.E. Fein, Phys. Rev. **123**, no. 6, 2589 (1962).

[78] *Anharmonic crystals*, R.A. Cowley, Rep. Prog. Phys. **31**, pt. 1, 123 (1968).

[79] Complex Variables and Applications, J.W. Brown and R.V. Churchill, McGraw-Hill, Inc., New York, 1996.

[80] *Theory of anharmonic effects in crystals*, G. Leibfried and W. Ludwig, Solid State Phys. **12**, 275 (1961).

[81] Lattice Dynamics, T.H.K. Barron, edited by R.F. Wallis, Pergamon, Oxford, 1965.

[82] http://en.wikipedia.org/wiki/Relations_between_specific_heats, December 17$^{\text{th}}$, 2008.

[83] Introduction to the Theory of Thermal Neutron Scattering, G.L. Squires, Dover Publications, 1996.

[84] Theory of Neutron Scattering from Condensed Matter: Volume 1, S.W. Lovesey, Oxford University Press, 1984.

[85] Pulsed Neutron Scattering, C.G. Windso, Taylor & Francis, Ltd., 1982.

[86] *Interference effects in the total neutron scattering cross-section of crystals*, G. Placzek and L. Van Hove, Nuov. Cim. **1**, 233 (1955).

[87] Advanced Engineering Mathematics, E. Kreyszi, John Wiley & Sons, Inc., 1999.

[88] http://en.wikipedia.org/wiki/Nearest_neighbor_search, December 17$^{\text{th}}$, 2008.

[89] http://en.wikipedia.org/wiki/Kd_tree, December 17$^{\text{th}}$, 2008.

[90] http://en.wikipedia.org/wiki/R-tree, December 17$^{\text{th}}$, 2008.

[91] *Crystal dynamics and inelastic scattering of neutrons*, G. Placzek, and L. Van Hove, Phys. Rev. **93**, 1207 (1954).

[92] *Phonon density of states in vanadium*, V.F. Sears, E.C. Svensson, and B.M. Powell, Can. J. Phys. **73**, 726 (1995).

[93] *Slow-neutron multiple scattering*, V.F. Sears, Adv. Phys. **24**, 1 (1975).

[94] *Vibrational entropy contributions to the phase stability of iron- and aluminum-based binary alloys*, T.L. Swan-Wood, PhD. Thesis, California Institute of Technology (2005).

[95] *Vibrational entropy of $L1_2$ CuAu measured by inelastic neutron scattering*, P.D. Bogdanoff, B. Fultz, and S. Rosenkranz, Phys. Rev. B **60**, 3976 (1999).

[96] *Phonon entropy of alloying and ordering of Cu-Au*, P.D. Bogdanoff, T.L. Swan-Wood, and B. Fultz, Phys. Rev. B **68**, 014301 (2003).

[97] *Vibrations of micro-eV energies in nanocrystalline microstructures*, A.F. Yue, A.B. Papandrew, O. Delaire, B. Fultz, Z. Chowdhuri, R.M. Dimeo, and D.A. Neumann, Phys. Rev. Lett. **93**, 205501-1 (2004).

[98] *Negative entropy of mixing for vanadium-platinum solutions*, O. Delaire, T. Swan-Wood, and B. Fultz, Phys. Rev. Lett. **93**, 185704-1 (2004).

[99] *Charge redistribution and phonon entropy of vanadium alloys*, O. Delaire and B. Fultz, Phys. Rev. Lett. **97**, 245701 (2006).

[100] *Neutron multiple scattering and absorption factors*, E. Johnson, and L. Robinson, Rev. Sci. Instrum. **60**, 3447 (1989).

[101] *Phonon partial densities of states of Fe and Cr in BCC Fe-Cr from inelastic neutron scattering,*, M. Lucas, M. Kresch, R. Stevens, and B. Fultz, Phys. Rev. B 77, 184303 (2008).

[102] Matrix Differential Calculus with Applications in Statistics and Econometrics, J.R. Magnus, and H. Neudecker, John Wiley & Sons, 1999.

[103] *Solution of incorrectly formulated problems and regularization method.*, A.N. Tikhonov, Sov. Phys. Dokl. **151**, 501 (1963).

[104] Transmission Electron Microscopy and Diffractometry of Materials, Second Edition, B.T. Fultz, and J.M. Howe, Springer-Verlag, 2002.

[105] *An experimental investigation of extrapolation methods in the derivation of accurate unit-cell dimensions of crystals*, J.B. Nelson and D.P. Riley, Proc. Phys. Soc. **57**, 160 (1945).

[106] *A profile refinement method for nuclear and magnetic structures.*, H.M. Rietveld, J. Appl. Cryst. **2**, 65 (1969).

[107] *The perfect crystal, thermal vacancies and the thermal expansion coefficient of aluminum*, K. Wang and R.R. Reeber, Philos. Mag. **80**, 1629 (2000).

[108] *Lattice dynamical calculation of some thermodynamic properties for aluminum*, D.C. Wallace, Phys. Rev. B **1**, 3963 (1970).

[109] *Ab initio calculation of the static structural properties of Al*, P.K. Lam and M.L. Cohen, Phys. Rev. B **24**, 4224 (1981).

[110] *Ab initio calculation of melting and thermodynamic properties of crystal and liquid aluminum*, G.K. Straub, J.B. Aidun, J.M. Wills, C.R. Sanchez-Castro, and D.C. Wallace, Phys. Rev. B **50**, 5055 (1994).

[111] *First-principles equations of state and elastic properties of seven metals*, C. Bercegeay and S. Bernard, Phys. Rev. B **72**, 214101 (2005).

[112] *Correlation between lattice-strain energetics and melting properties: molecular dynamics and lattice dynamics using EAM models of Al*, K. Moriguchi and M. Igarashi, Phys. Rev. B **74**, 024111 (2006).

[113] *Phonon dispersion of the BCC phase of group-IV metals. I. BCC titanium*, W. Petry, A. Heiming, J. Trampenau, M. Alba, C. Herzig, H.R. Schober, and G. Vogl, Phys. Rev. B **43**, 10933 (1991).

[114] *Phonon dispersion of the BCC phase of group-IV metals. III. BCC hafnium*, J. Trampenau, A. Heiming, W. Petry, M. Alba, C. Herzig, W. Miekeley, and H.R. Schober, Phys. Rev. B **43**, 10 963 (1991)

[115] *Normal mode vibrations in nickel*, B.N. Brockhouse and A.T. Stewart, Phys. Rev. **100**, 756 (1955).

[116] *Inelastic scattering of slow neutrons by lattice vibrations in aluminum*, R.S. Carter, H. Palevsky, and D.J. Hughes, Phys. Rev. **106**, 1168 (1957).

[117] *Normal modes of aluminum by neutron spectrometry*, B.N. Brockhouse and A.T. Stewart, Rev. Mod. Phys. **30**, 236 (1958).

[118] *Dispersion relations for phonons in aluminum at 80 and 300 K*, R. Stedman and G. Nilsson, Phys. Rev. **145**, 492 (1966).

[119] *X-ray study of lattice vibrations in aluminum*, C.B. Walker, Phys. Rev. **103**, 547 (1956).

[120] *X-ray scattering by phonons in aluminum*, G.C. Peterson and T. Smith, J. Phys. F.: **2**, 7 (1972).

[121] *Phonon-frequency distributions and heat capacities of aluminum and lead*, R. Stedman, L. Almqvist, and G. Nilsson, Phys. Rev. **162**, 549 (1967).

[122] *Normal vibrations in aluminum and derived thermodynamic properties*, G. Gilat and R.M. Nicklow, Phys. Rev. **143**, 487 (1966).

[123] *Characteristic features of anharmonic effects in the lattice dynamics of FCC metals*, M.I. Katsnel'son, A.V. Trefilov, and K.Yu. Khromov, JETP Lett. **69**, 688 (1999).

[124] *Damping of phonons in aluminum*, G. Björkman, I. Lundqvist, and A. Sjölander, Phys. Rev. **159**, 551 (1967).

[125] *Theory of the anharmonic linewidths of surface phonons in aluminum*, A. Franchini, G. Santoro, V. Bortolani, A.A. Maradudin, and R.F. Wallis, Phys. Rev. B **45**, 11982 (1992).

[126] *Aluminum. I. Measurement of the relative enthalpy from 273 to 929 K and derivation of thermodynamic functions for Al from 0 K to its melting point*, D.A. Ditmars, C.A. Plint, and R.C. Shukla, Int. J. Thermophys. **6**, 499 (1985).

[127] *Aluminum. II. Derivation of C_{V0} from C_P and comparison to C_{V0} calculated from anharmonic models*, R.C. Shukla, C.A. Plint, and D.A. Ditmars, Int. J. Thermophys. **6**, 517 (1985).

[128] *Anharmonic effects in the heat capacity of Al*, M. Forsblom, N. Sandberg, and G. Grimvall, Phys. Rev. B **69**, 165106 (2004).

[129] *Mass effects on optical phonons in $L1_2$-ordered $Pt_3{}^{57}Fe$ and $Pd_3{}^{57}Fe$*, A.F. Yue, I. Halevy, A. Papandrew, P.D. Bogdanoff, B. Fultz, W. Sturhahn, E.E. Alp, and T. S. Toellner, Hyperfine Interact. **141**, 249 (2002).

[130] *Efficiency of ab-initio total energy calculations for metals and semiconductors using a plane-wave basis set*, G. Kresse and J. Furthmüller, Comput. Mater. Sci. **6**, 15 (1996).

[131] *From ultrasoft pseudopotentials to the projector augmented-wave method*, G. Kresse and D. Joubert, Phys. Rev. B **59**, 1758 (1999).

[132] D. Alfè, (1998). Program available at http://chianti.geol.ucl.ac.uk/∼dario

[133] *Generalized gradient approximation made simple*, J.P. Perdew, K. Burke, and M. Ernzerhof, Phys. Rev. Lett. **77**, 3865 (1996).

[134] *Special points for Brillouin-zone integrations*, H.J. Monkhorst and J.D. Pack, Phys. Rev. B **13**, 5188 (1976).

[135] *Thermoelastic and texture behavior of aluminum at high pressure and high temperature investigated by in situ neutron diffraction*, D. He, Y. Zhao, L.L. Daemen, J. Qian, K. Lokshin, T.D. Shen, J. Zhang, and A.C. Lawson, J. Appl. Phys. **95**, 4645 (2004).

[136] JANAF Thermochemical Tables, Fourth Edition, M.W. Chase, J. Phys. Chem. Ref. Data, Monograph 9, 1998.

[137] *Scattering of neutrons by an anharmonic crystal*, A.A. Maradudin and A.E. Fein, Phys. Rev. **128**, 2589 (1962).

[138] *The lattice dynamics of an anharmonic crystal*, R.A. Cowley Adv. Phys. **13** 421 (1963).

[139] *Temperature dependence of the Debye temperatures of aluminum, lead, and beta brass by an x-ray method*, D.R. Chipman, J. Appl. Phys. **31**, 2012 (1960).

[140] *Pressure-induced phonon frequency shifts in lead measured by inelastic neutron scattering*, R. Lechner and G. Quittner, Phys. Rev. Lett. **17**, 1259 (1966).

[141] *The heat capacity of lead from 300 to 850 K: experimental data*, G. Cordoba and C.R. Brooks, Phys. Stat. Sol. A **7**, 503 (1971).

[142] *The Debye-Waller factor of lead from 296 to 550 K*, E.J. Lisher, Acta Cryst. A **32**, 506 (1975).

[143] *Temperature dependence of the thermal vibrations in lead as determined from short-wavelength neutron diffraction data*, M. Merisalo, M.S. Lehmann, and F.K. Larsen, Acta Cryst. A **40**, 127 (1984).

[144] *New aspects on the electron-phonon system at finite temperature with an application on lead and mercury*, G. Grimvall, Phys. Kondens. Materie **9**, 283 (1969).

[145] *Anharmonic components of the heat capacity of copper, silver, gold, lead, and aluminum*, V.A. Korshunov, Fiz. Metal. Metalloved. **41**, 54 (1975).

[146] *Lattice dynamics of Al and Pb*, V.K. Thakur and T.N. Singh, Phys. Stat. Sol. B **142**, 401 (1987).

[147] *Calculations of optical conductivity in a two-band superconductor: Pb*, N. Bock and D. Coffey, Phys. Rev. B **76**, 174513-1 (2007).

[148] *Image of the Fermi surface in the vibrational spectrum of lead*, W. Kohn, Phys. Rev. Let. **2**, 393 (1959).

[149] *Image of the Fermi surface in the lattice vibrations of lead'*, B.N. Brockhouse, K.R. Rao, and A.D.B. Woods, Phys. Rev. Lett. **7**, 93 (1961).

[150] *Fermi surface of lead from Kohn anomalies*, R. Stedman, L. Almqvist, G. Nilsson, and G. Raunio, Phys. Rev. **163**, 567 (1967).

[151] *Phonons in lead at T = 4.2 K*, Yu.N. Mikhĭlov, V.I. Bobrovskiĭ, A.V. Mimel'shteĭn, and Yu.S. Ponosov, JETP Lett. **22**, 18 (1975).

[152] *Effect of the superconducting transition on phonon energies and lifetimes in lead*, R. Youngblood, Y. Noda, and G. Shirane, Solid State Commun. **27**, 1433 (1978).

[153] *Momentum-resolved electron-phonon interaction in lead determined by neutron resonance spin-echo spectroscopy*, T. Keller, P. Aynajian, K. Habicht, L. Boeri, S.K. Bose, and B. Keimer, Phys. Rev. Lett. **96**, 225501-1 (2006).

[154] *Crystal dynamics of lead I. dispersion curves at 100 K*, B.N. Brockhouse, T. Arase, G. Caglioti, K.R. Rao, and A.D.B. Woods, Phys. Rev. **128**, 1099 (1962).

[155] Inelastic Scattering of Neutrons in Solids and Liquids, B.N. Brockhouse, T. Arase, G. Caglioti, M. Sakamoto, R.N. Sinclair, and A.D.B. Woods, International Atomic Energy Agency, Vienna, 1960.

[156] *Phonon density states in lead*, G. Gilat, Solid State Commun. **3**, 101 (1965).

[157] *Dispersion relations for phonons in lead at 80 and 300 K*, R. Stedman, L. Almqvist, G. Nilsson, and G. Raunio, Phys. Rev. **162**, 545 (1967).

[158] *Experimental phonon frequencies and widths of lead at 5, 80, and 290 K*, A. Furrer and W. Hälg, Phys. Stat. Sol. **42**, 821 (1970).

[159] *Lattice frequency spectra of Pb and* $Pb_{40}Tl_{60}$ *by neutron spectrometry*, A.P. Roy and B.N. Brockhouse, Can. J. Phys. **48**, 1781 (1970).

[160] *A Born–von Kármán model for lead*, E.R. Cowley, Solid State Commun. **14**, 587 (1974).

[161] *Anisotropic superconducting energy gap in Pb*, P.G. Tomlinson and J.P. Carbotte, Phys. Rev. B **13**, 4738 (1975).

[162] *Phonon spectra in Pb and $Pb_{40}Tl_{60}$ determined by tunneling and neutron scattering*, J.M. Rowell, W.L. McMillan, and W.L. Feldmans, Phys. Rev. **178**, 897 (1969).

[163] *Lead phonon spectrum calculated from superconducting density of states*, W.L. McMillan and J.M. Rowell, Phys. Rev. Lett. **14**, 108 (1965).

[164] *Electron-phonon interaction in lead and lead-indium alloys under pressure*, V.M. Svistunov, O.I. Chernyak, M.A. Belogolovskii, and A.I. D'yachenko, Philos. Mag. **43**, 75 (1981).

[165] *Far-infrared measurements of the phonon density of states of superconducting lead*, B. Farnworth and T. Timusk, Phys. Rev. B **10**, 2799 (1974).

[166] *Phonon density of states of superconducting lead*, B. Farnworth and T. Timusk, Phys. Rev. B **14**, 5119 (1976).

[167] *Origin of discrepancy between tunneling and neutron-derived phonon densities of states in lead*, R.C. Dynes, J.P. Carbotte, and E.J. Woll Jr., Solid State Commun. **6**, 101 (1968).

[168] Thermophysical Properties of Matter, Y.S. Touloukian, R.K. Kirby, R.E. Taylor, and P.D. Desai, (IFI, New York, 1975), Vol 12.

[169] *The heat capacity of lead from 300 to 850 K: conversion of C_P to C_V for solid lead*, G. Cordoba and C.R. Brooks, Phys. Stat. Sol. A **11**, 749 (1972).

[170] *The heat capacity of lead from 300 to 850 K: contributions to the heat capacity of solid lead*, G. Cordoba and C.R. Brooks, Phys. Stat. Sol. A **13**, K 111 (1972).

[171] *The heat capacity of gold from 300 to 1200 K: experimental data and analysis of contributions*, G. Cordoba and C.R. Brooks, Phys. Stat. Sol. A **6**, 581 (1971).

[172] *The thermal expansion of pure metals: copper, gold, aluminum, nickel, and iron*, F.C. Nix and D. MacNair, Phys. Rev. B, 597 (1941).

[173] *Density of states curve for nickel*, G.F. Koster, Phys. Rev. **98**, 901 (1955).

[174] *Normal vibrations in nickel, palladium, and platinum*, O.P. Gupta, J. Chem. Phys. **82**, 927 (1985).

[175] *Bayesian deconvolution and analysis of photoelectron or any other spectra: Fermi-liquid versus marginal Fermi-liquid behavior of the 3d electrons in Ni*, U. Gerhardt, S. Marquardt, N. Schoeder, and S. Weiss, Phys. Rev. B **58**, 6877 (1998).

[176] *Interatomic potentials for monatomic metals from experimental data and ab initio calculations*, Y. Mishin, D. Farkas, M.J. Mehl, and D.A. Papaconstantopoulos, Phys. Rev. B **59**, 3393 (1999).

[177] *Thermodynamic properties of Al, Ni, NiAl, and Ni_3Al from first-principles calculations*, Y. Wang, Z.-K. Liu, and L.-Q. Chen, Acta Mater. **52**, 2665 (2004).

[178] *Physical properties of Ni FCC lattice in terms of the self-consistent phonon theory*, C. Malinowska-Adamska, P. Słoma, and J. Tomaszewski, J. Phys. Condens. Matter **18**, 751 (2006).

[179] *The elastic behavior in Ni monocrystal: nonlinear effects*, Y.-H. Wen, S.-Q. Wu, J.-H. Zhang, and Z.-Z. Zhu, Solid State Commun. **146**, 253 (2008).

[180] *Magnetic-moment distribution in nickel metal*, H.A. Mook and C.G. Shull, J. Appl. Phys. **37**, 1034 (1966).

[181] *Magnetic moment distribution of nickel metal*, H.A. Mook, Phys. Rev. **148**, 495 (1966).

[182] *Spin-wave spectrum of nickel metal*, H.A. Mook, R.M. Nicklow, E.D. Thompson, and M.K. Wilkinson, J. Appl. Phys. **40**, 1450 (1969).

[183] *Neutron-scattering measurements of the generalized susceptibility $\chi(q, E)$ for Ni*, H.A. Mook and D. Tocchetti, Phys. Rev. Lett. **43**, 2029 (1979).

[184] *Reconstruction of internal magnetization density distributions of iron and nickel by the maximum entropy method*, L. Dobrzyński, R.J. Papoular, and M. Sakata, J. Magn. Magn. Mater. **140-144**, 53 (1995).

[185] *Internal magnetization density distribution of iron and nickel by the maximum entropy method*, L. Dobrzyński, R.J. Papoular, and M. Sakata, J. Phys. Soc. Jpn. **65**, 255 (1995).

[186] *Temperature dependence of the magnetic moment and hyperfine constant of nickel*, R. Kaul and E.D. Thompson, J. Appl. Phys. **40**, 1383 (1969).

[187] *Neutron-scattering measurement of the spin-wave spectra for nickel*, H.A. Mook and D.McK. Paul, Phys. Rev. Lett. **54**, 227 (1985).

[188] *Magnetic excitations in nickel and iron*, J.C. Ododo and m.W. Anyakoha, J. Phys. F Met. Phys. **13**, 2335 (1983).

[189] *Wavevector-dependent spin susceptibility of nickel above the Curie temperature*, H. Hasegawa, J. Phys. F Met. Phys. **14**, 1235 (1984).

[190] *Ni magnetic anisotropy model*, A.I. Mitsek and V.A. Mitsek, Phys. Stat. Sol. B **199**, 549 (1997).

[191] *Magnon spectrum and related finite-temperature properties: a first-principle approach*, S.V. Halilov, A.Y. Perlov, P.M. Oppeneer, and H. Eschrig, Europhys. Lett. **39**, 91 (1997).

[192] *Adiabatic spin dynamics from spin-density-functional theory: application to Fe, Co, and Ni*, S.V. Halilov, H. Eschrig, A.Y. Perlov, and P.M. Oppeneer, Phys. Rev. B **58**, 293 (1998).

[193] *Itinerant electron magnetism*, T. Moriya and Y. Takahashi, Ann. Rev. Mater. Sci. **14**, 1 (1984).

[194] *Coarse-grained magnetic disorder above T_C in iron*, V. Heine and R. Joynt, Europhys. Lett. **5**, 81 (1988).

[195] *Wave vector-dependent spin susceptibility of iron above the Curie temperature*, H. Hasegawa, J. Phys. F: Met. Phys. **13**, 2655 (1983).

[196] *Magnetism of iron above the Curie temperature*, T. Oguchi, K. Terakura, and N. Hamada, J. Phys. F: Met. Phys **13**, 145 (1983).

[197] *Some current problems in itinerant electron magnetism*, D.M. Edwards, J. Magn. Magn. Mater. **15-18**, 262 (1980).

[198] *The magnetic entropy in paramagnetic iron phases*, G. Grimvall, Physica B **86-88**, 282 (1977).

[199] *Polymorphism of metals: III. theory of the temperature-pressure phase diagram of iron*, G. Grimvall, Physica Scripta **13**, 59 (1976).

[200] *Polymorphism of metals: II. electronic and magnetic free energy*, G. Grimvall, Physica Scripta **12**, 173 (1975).

[201] *Temperature dependence of the magnetic excitations in nickel*, H.A. Mook, J.W. Lynn, and R.M. Nicklow, Phys. Rev. Lett. **30**, 556 (1973).

[202] *Temperature dependence of the dynamic susceptibility of nickel*, J.W. Lynn and H.A. Mook, Phys. Rev. B **23**, 198 (1981).

[203] *Direct observation of spin waves above T_C for nickel*, H.A. Mook and J.W. Lynn, Phys. Rev. Lett. **57**, 150 (1986).

[204] *Temperature dependence of the high-energy magnetic excitations for Ni.*, H.A. Mook, D.McK. Paul, and S. Hayden, Phys. Rev. B **38**, 12058 (1988).

[205] *Comparison of the paramagnetic spin fluctuations in nickel with asymptotic renormalization-group theory*, P. Böni, H.A. Mook, J.L. Martĭnez, and G. Shirane, Phys. Rev. B **47**, 3171 (1993).

[206] *Normal modes of vibration in nickel*, R.J. Birgeneau, J. Cordes, G. Dolling, A.D.B. Woods, Phys. Rev. **136**, 1359 (1964).

[207] *Lattice dynamics of nickel*, S. Hautecler, and W. Van Dingenen, Physica **34**, 257 (1967).

[208] *The lattice dynamics of ferromagnetic and paramagnetic nickel*, G.A. de Wit, and B.N. Brockhouse, J. Appl. Phys. **39**, 451 (1968).

[209] *Time-of-flight neutron transmission diffraction*, J.R. Santisteban, L. Edwards, A. Steuwer, P.J. Withers, J. Appl. Crystallogr. **34**, 289 (2001).

[210] *The magnetization of pure iron and nickel*, J. Crangle and G.M. Goodman, Proc. R. Soc. A **321**, 477 (1971).

[211] Landolt-Börnstein: Elastische piezoelektriche, piezooptische und elektrooptische Konstanten von Kristallen, R. Bechmann, and R.F.S. Hearmon, (Springer-Verlag, Berlin, 1966), Vol. 3.

[212] *New aspects on the thermodynamic functions of iron*, G. Grimvall, Solid State Commun. **14**, 551 (1974).

[213] *Magnetic contributions to thermal expansion of transition metals: implications for local moments above* T_{C}, A.J. Holden, V. Heine, and J.H. Samson, J. Phys. F Met. Phys. **14**, 1005 (1984).

[214] *Phonon softening in ferromagnetic BCC iron*, H. Hasegawa, M.W. Finnis, and D.G. Pettifor, J. Phys. F Met. Phys. **17**, 2049 (1987).

[215] *Spin disorder in paramagnetic FCC iron*, G. Grimvall, Phys. Rev. B **39**, 12300 (1989).

[216] *Ab initio and empirical approaches to the thermodynamics of transition metals, with application to tungsten*, G. Grimvall, Physica B **159**, 39 (1989).

[217] *BCC and HCP phase competition in Fe*, E.G. Moroni and T. Jarlborg, Europhys. Lett. **33**, 223 (1996).

[218] *Applications of the NRL tight-binding method to magnetic systems*, M.J. Mehl, D.A. Papaconstantopoulos, I.I. Mazin, N.C. Bacalis, and W.E. Pickett, J. Appl. Phys. **89**, 6880 (2001).

[219] *Ferromagnetic and antiferromagnetic spin fluctuations and superconductivity in the HCP-phase of Fe*, T. Jarlborg, Phys. Lett. A **300**, 518 (2002).

[220] *Superconductivity in compressed iron: role of spin fluctuations*, I.I. Mazin, D.A. Papaconstantopoulos, and M.J. Mehl, Phys. Rev. B **65**, 100511(R) (2002).

[221] *Spin fluctuations, electron-phonon coupling and superconductivity in near magnetic elementary metals — Fe, Co, Ni, and Pd*, T. Jarlborg, Physica C **385**, 513 (2003).

[222] *Magnetism in dense hexagonal iron*, G. Steinle-Neumann, L. Stixrude, and R.E. Cohen, Proc. Nat. Acad. Sci. U.S.A. **101**, 33 (2004).

[223] *The axial ratio of HCP iron at the conditions of the earth's inner core*, C.M.S. Gannarelli, D. Alfe, and M.J. Gillan, Phys. Earth Planet. Inter. **152**, 67 (2005).

[224] *First-principles thermoelasticity of BCC iron under pressure*, X. Sha and R.E. Cohen, Phys. Rev. B **74**, 214111 (2006).

[225] *Iron at earth-core conditions*, P. Modak, A.K. Verma, R.S. Rao, B.K. Godwal, and R. Jeanloz, J. Mater. Sci. **41**, 1523 (2006).

[226] *Thermal effects on lattice strain in ϵ-Fe under pressure*, X. Sha and R.E. Cohen, Phys. Rev. B **74**, 064103 (2006).

[227] *Stability of the body-centered-tetragonal phase of Fe at high pressure: ground-state energies, phonon spectra, and molecular dynamics simulations*, A.B. Belonoshko, E.I. Isaev, N.V. Skorodumova, and B. Johansson, Phys. Rev. B **74**, 214102 (2006).

[228] *Analytic bond-order potential for BCC and FCC iron — comparison with established embedded-atom method potentials*, M. Müller, P. Erhart, and K. Albe, J. Phys. Condens. Matter **19**, 326220 (2007).

[229] *Stability of the HCP phase and temperature variation of the axial ratio of iron near earth-core conditions*, P. Modak, A.K. Verma, R.S. Rao, B.K. Godwal, L. Stixrude, and R. Jeanloz, J. Phys. Condens. Matter **19**, 016208 (2007).

[230] *The lattice expansion of iron*, Z.S. Basinski, W. Hume-Rothery, and A.L. Sutton, Proc. Roy. Soc. London Sect A **229**, 459 (1954).

[231] *Lattice parameter anomalies at the curie point of pure iron*, N. Ridley and H. Stuart, Brit. J. Appl. Phys. **1**, 1291 (1968).

[232] *Temperature dependence of the elastic constants in α-iron single crystals: relationship to spin order and diffusion anomalies*, D.J. Dever, J. Appl. Phys. **43**, 3293 (1972).

[233] *Elastic properties of metals and alloys I, iron nickel and iron-nickel alloys*, H.M. Leadbetter and R.P. Reed, J. Phys. Chem. Ref. Data **2**, 531 (1973).

[234] *Neutron scattering experiments on itinerant electron magnets*, C.G. Windsor, Physica B **91**, 119 (1977).

[235] *Experimental determination of the phonon and electron components of the thermal conductivity of BCC iron*, R.K. Williams, D.W. Yardbrough, J.W. Masey, T.K. Holder, and R.S. Graves, J. Appl. Phys. **52**, 5167 (1981).

[236] *Raman spectroscopy of iron to 152 GPa: implications for earth's inner core*, S. Merkel, A.F. Goncharov, H.K. Mao, P. Gillet, and R.J. Hemley, Science **288**, 1626 (2000).

[237] *Sound velocities in iron to 110 GPa*, G. Fiquet, J. Badro, F. Guyot, H. Requardt, and M. Krisch, Science **291**, 468 (2001).

[238] *On optical phonons and elasticity in the HCP transition metals Fe, Ru, and Re at high pressure*, H. Olijynk, A.P. Jephcoat, and K. Refson, Europhys. Lett. **53**, 504 (2001).

[239] *Raman spectroscopy of metals, high-temperature superconductors and related materials under high pressure*, A.F. Goncharov and V.V. Struzhkin, J. Raman Spectrosc. **34**, 532 (2003).

[240] *Elastic anisotropy in textured HCP-iron to 112 GPa from sound wave propagation measurements*, D. Antonangeli, F. Occelli, H. Requardt, J. Badro, G. Fiquet, and M. Kirsch, Earth Planet. Sci. Lett. **225**, 243 (2004).

[241] *High-resolution angle-resolved photoemission spectroscopy of iron: a study of the self-energy*, X.Y. Cui, K. Shimada, M. Hoesch, Y. Sakisaka, H. Kato, Y. Aiura, S. Negishi, M. Higashiguchi, Y. Miura, H. Namatame, and M. Taniguchi, J. Magn. Magn. Mater. **310**, 1617 (2007).

[242] http://en.wikipedia.org/wiki/Iron, December 17$^{\text{th}}$, 2008.

[243] *Lattice dynamics and thermodynamics of BCC iron under pressure: first-principles linear response study*, X. Sha and R.E. Cohen, Phys. Rev. B **73**, 104303 (2006).

[244] *Some measurements of phonon dispersion relations in iron*, G.G.E. Low, Proc. Phys. Soc. **79**, 479 (1962).

[245] *Lattice vibrations in iron at 296 K*, B.N. Brockhouse, H.E. Abou-Helal, and E.D. Hallman, Solid State Commun. **5**, 211 (1967).

[246] *Normal vibrations in α-iron*, J. Bergsma, C. van Dijk, and D. Toccheti, Phys. Lett. A **24**, 270 (1967).

[247] *Phonon dispersion relation for iron*, V.J. Minkiewicz, G. Shirane, and R. Nathans, Phys. Rev. **162**, 528 (1967).

[248] *Phonon softening and martensitic transformation in α-iron*, J. Neuhaus, W. Petry, and A. Krimmel, Physica B **234-236**, 897 (1997).

[249] *The scattering of thermal neutrons by iron*, A.M. Vallêra, PhD. Thesis, Cambridge University (1977).

[250] *Lattice dynamics of γ-Fe*, J. Zaretsky and C. Stassis, Phys. Rev. B **35**, 4500 (1987).

[251] *Phonon dispersion curves by inelastic neutron scattering to 12 GPa'*, S. Klotz, Z. Krystallogr. **216**, 420 (2001).

[252] *Phonon dispersion of BCC iron to 10 GPa*, S. Klotz and M. Braden, Phys. Rev. Lett. **85**, 3209 (2001).

[253] *Critical and spin-wave scattering of neutrons from iron*, M.F. Collins, J. Minkiewicz, R. Nathans, L. Passell, and G. Shirane, Phys. Rev. **179**, 417 (1969).

[254] S. Boronkay and M.F. Collins, Int. J. Magn. **4**, 205 (1973).

[255] *Neutron-scattering study of the magnon energies and intensities in iron*, M. Yethiraj, R.A. Robinson, D.S. Sivia, J.W. Lynn, and H.A. Mook, Phys. Rev. B **43**, 2565 (1991).

[256] *Measurements of the magnetic excitations above T_C in iron and nickel*, H.A. Mook and J.W. Lynn, J. Appl. Phys **57**, 3006 (1985).

[257] *Neutron scattering study of the magnetic excitations in ferromagnetic iron at high energy transfers*, C.K. Loong, J.M. Carpenter, J.W. Lynn, R.A. Robinson, and H.A. Mook, J. Appl. Phys **55**, 1895 (1984).

[258] *Temperature dependence of the magnetic excitations in iron*, J.W. Lynn, Phys. Rev. B **11**, 2624 (1975).

[259] *Magnons and magnon-phonon interactions in iron*, R.F. Sabiryanov and S.S. Jaswal, Phys. Rev. Lett. **83**, 2062 (1999).

[260] *Magnetic effects in transverse elastic constants of BCC Fe(Si)*, J.M. Alves and A.M. Vallêra, J. Magn. Magn. Mater. **157/158**, 378 (1996)., 378 (1996).

[261] *Neutron scattering measurements of phonons in iron above and below T_C*, S.K. Satija, R.P. Comès, and G. Shirane, Phys. Rev. B **32**, 3309 (1985).

[262] *Temperature dependence of nuclear forward scattering of synchotron radiation in α-$^{5}7Fe$*, U. Bergmann, S.D. Shastri, D.P. Siddons, B.W. Batterman, and J.B. Hastings, Phys. Rev. B **50**, 5957 (1994).

[263] *Measuring velocity of sound with nuclear resonant inelastic x-ray scattering*, M.Y. Hu, W. Sturhahn, T. Toellner, P.D. Mannheim, D.E. Brown, J. Zhao and E.E. Alp, Phys. Rev. B **67**, 094304 (2003).

[264] *Temperature dependence of nuclear inelastic absorption of synchotron radiation in α-$^{5}7Fe$*, A.I. Chumakov, R. Rüffer, A.Q.R. Baron, H. Grünsteudel, and H.F. Grünsteudel, Phys. Rev. B **54**, R9596 (1996).

[265] *Temperature dependence of phonon energy spectra with nuclear resonant scattering of synchotron radiation*, M. Seto, Y. Yoda, S. Kikuta, X.W. Zhang, and M. Ando Nuovo Cimento D **18**, 381 (1996).

[266] *Single-nucleus quantum beats excited by synchotron radiation*, A.Q.R. Baron, A.I. Chumakov, R. Rüffer, H. Grünsteudel, H.F. Grünsteudel, and O. Leupold, Europhys. Lett. **34**, 331 (1996).

[267] *Electron emission from ^{57}Fe nuclei excited with synchotron radiation*, W. Sturhahn, K.W. Quast, T.S. Toellner, E.E. Alp, J. Metge, and E. Gerdau, Phys. Rev. B **53**, 171 (1996).

[268] *Inelastic nuclear resonant scattering with sub-meV energy resolution*, T.S. Toellner, M.Y. Hu, W. Sturhahn, K. Quast, and E.E. Alp, Appl. Phys. Lett. **71**, 2112 (1997).

[269] *Phonon density of states measured by inelastic nuclear resonant scattering*, W. Sturhahn, T.S. Toellner, E.E. Alp, X. Zhang, M. Ando, Y. Yoda, S. Kikuta, M. Seto, C.W. Kimball, and B. Dabrowski, Phys. Rev. Lett. **74**, 3832 (1995).

[270] *Experimental aspects of inelastic nuclear resonance scattering*, A.I. Chumakov and W. Sturhahn, Hyperfine Interact. **123/124**, 781 (1999).

[271] *Phonon spectroscopy with nuclear inelastic scattering of synchotron radiation*, A.I. Chumakov, Phys. Stat. Sol. B **215**, 165 (1999).

[272] *Lattice dynamics and inelastic nuclear resonant x-ray scattering*, E.E. Alp, W. Sturhahn, and T.S. Toellner, Hyperfine Interact. **135**, 295 (2001).

[273] *Lattice dynamics and inelastic nuclear resonant x-ray scattering*, E.E. Alp, W. Sturhahn, and T.S. Toellner, J. Phys. Condens. Matter **13**, 7645 (2001).

[274] *Vibrational dynamics studies by nuclear resonant inelastic x-ray scattering*, E.E. Alp, W. Sturhahn, T.S. Toellner, J. Zhao, M. Hu, and D.E. Brown, Hyperfine Interact. **144/145**, 3 (2002).

[275] *Nuclear inelastic scattering*, R. Rüffer and A.I. Chumakov, Hyperfine Ineract. **128**, 255 (2000).

[276] *Nuclear resonant scattering at high pressure and high temperature*, J. Zhao, W. Sturhahn, J.F. Lin, G. Shen, E.E. Alp, and H.K. Mao, High Press. Res. **24**, 447 (2004).

[277] *Phonon density of states in iron at high pressures and high temperatures*, G. Shen, W. Sturhahn, E.E. Alp, J. Zhao, T.S. Toellner, V.B. Prakapenka, Y. Meng, and H.R. Mao, Phys. Chem. Minerals **31**, 353 (2004).

[278] *Density of phonon states in iron at high pressure*, R. Lübbers, H.F. Grünsteudel, A.I. Chumakov, G. Wortman, Science **287**, 1250 (2000).

[279] *High-pressure studies of magnetism and lattice dynamics by nuclear resonant scattering of synchotron radiation*, G. Wortmann, K. Rupprecht, and H. Giefers, Hyperfine Interact. **144/145**, 103 (2002).

[280] *Phonon density of states and elastic properties of Fe-based materials under compression*, V.V. Struzhkin, H.K. Mao, W.L. Mao, R.J. Hemley, W. Sturhahn, E. Alp, C. l'Abbe, M.Y. Hu, and D. Errandonea, Hyperfine Interact. **153**, 3 (2004).

[281] *Phonon density of iron up to 153 GPa*, H.K. Mao, J. Xu, V.V. Struzhkin, J. Shu, R.J. Hemley, W. Sturhahn, M.Y. Hu, E.E. Alp, L. Vocaldo, D. Alfè, G.D. Price, M.J. Gillan, M. Schwoerer-Böhning, D. Häusermann, P. Eng, G. Shen, H. Giefers, R. Lübbers, and G. Wortmann, Science **292**, 914 (2001).

[282] *Sound velocities of hot dense iron: Birch's law revisited*, J.-F. Lin, W. Sturhahn, J. Zhao, G. Shen, H.K. Mao, R.J. Hemley, Science **308**, 1892 (2005).

[283] *The effects of high pressure on the vibrational and magnetic properties of iron-based materials*, A. Papandrew, PhD. Thesis, California Institute of Technology (2006).

[284] *Nuclear resonant spectroscopy*, W. Sturhahn, J. Phys. Condens. Matter **16**, S497 (2004).

[285] *Introduction to nuclear resonant scattering with synchotron radiation*, W. Sturhahn, E.E. Alp, T.S. Toellner, P. Hession, M. Hu, and J. Sutter, Hyperfine Interact. **113**, 47 (1998).

[286] *Theoretical aspects of incoherent nuclear resonant scattering*, W. Sturhahn and V.G. Kohn, Hyperfine Interact **123/124**, 367 (1999).

[287] *Crystal monochromator with a resolution beyond* 10^8, T.S. Toellner, M.Y. Hu, W. Sturhahn, G. Bortel, E.E. Alp, and J. Zhao, J. Synchotron Rad. **8**, 1082 (2001).

[288] *A high-resolution monochromator for inelastic nuclear resonant scattering experiments using* ^{119}Sn, M.Y. Hu, T.S. Toellner, W. Sturhahn, P.M. Hession, J.P. Sutter, and E.E. Alp, Nucl. Intrum. Methods Phys. Res. Sect. A **430**, 271 (1999).

[289] *High-energy-resolution monochromator for* ^{83}Kr *nuclear resonant scattering*, J.Y. Zhao, T.S. Toellner, M.Y. Hu, W. Sturhahn, E.E. Alp, G.Y. Shen, and H.K. Mao, Rev. Sci. Instrum. **73**, 1608 (2002).

[290] *A water-cooled compound refractive lens as a white beam collimator*, J.Y. Zhao, E.E. Alp, T.S. Toellner, W. Sturhahn, H. Sinn, and D. Shu, Rev. Sci. Instrum. **73**, 1611 (2002).

[291] *An inelastic x-ray spectrometer with 2.2 meV energy resolution*, H. Sinn, E.E. Alp, J. Barraza, G. Bortel, E. Burkel, D. Shu, W. Sturhahn, J.P. Sutter, T.S. Toellner, and J. Zhao, Nucl. Instrum. Methods Phys. Res. Sect. A **467-468**, 1545 (2001).

[292] *CONUSS and PHOENIX: evaluation of nuclear resonant scattering data*, W. Sturhahn, Hyperfine Interact. **125**, 149 (2000).

[293] http://www.scipy.org/

[294] *Interference between one- and multiphonon processes in the scattering of neutrons and x-rays by crystals*, R.A. Cowley, E.C. Svensson, and W.J.L. Buyers, Phys. Rev. Lett. **23**, 525 (1969).

[295] *Elastic constants of iron from 4.2 to 300 degrees K*, J.A. Rayne and B.S. Chandrasekhar, Phys. Rev. **122**, 1714 (1961).

[296] *Elastic-moduli and internal-friction of low-carbon and stainless-steels as a function of temperature*, M. Fukuhara and A. Sanpei, ISIJ International **33(4)**, 508 (1993).

[297] *Components of the thermodynamic functions of iron*, R.J. Weiss and K.J. Tauer, Phys. Rev. **102**, 1490 (1956).

[298] http://en.wikipedia.org/wiki/Gershgorin_circle_theorem, December 17$^{\text{th}}$, 2008.

[299] *The occurrence of singularities in the elastic frequency distribution of a crystal*, L. Van Hove, Phys. Rev. **89**, 1189 (1953).

[300] *Dynamics of simple lattices*, H.B. Rosenstock, Phys. Rev. **97**, 290 (1955).

[301] *Critical points and lattice vibration spectra*, J.C. Phillips, Phys. Rev. **104**, 1263 (1956).

[302] *Critical points in three dimensions*, H.B. Rosenstock, J. Phys. Chem. Solids **2**, 44 (1957).

[303] The Theory of Transformations in Metals and Alloys, J.W. Christian, Pergamon Press Ltd., New York, 1981.

[304] Physical Metallurgy, P. Haasen, Cambridge University Press, Great Britain, 1992.

[305] A. Larose and B.N. Brockhouse, NRC-CISTI Depository of Unpublished Data **617**, 1976.

[306] Analytical Mechanics, G.R. Fowles and G.L. Cassiday, Harcourt College Publishers, Fort Worth, 1999.

[307] *Thermal agitation of electric charge in conductors*, H. Nyquist, Phys. Rev. **32**, 110 (1928).

[308] *Inversibility and generalized noise*, H.B. Callen and T.A. Welton, Phys. Rev. **83**, 34 (1951).

[309] *Fluctuation dissipation theorem*, J. Weber, Phys. Rev. **101**, 1620 (1956).

[310] *The fluctuation-dissipation theorem*, R. Kubo, Rep. Prog. Phys. **29**, 255 (1966).

[311] *On the derivation of the fluctuation-dissipation theorem*, B.U. Felderhof, J. Phys. A **11**, 921 (1978).

[312] http://en.wikipedia.org/wiki/Fluctuation_dissipation_theorem, December 17$^{\text{th}}$, 2008.

[313] Crystals, Defects, and Microstrutures: Modeling Across Scales, R. Phillips, Cambridge University Press, New York, 2001.

[314] *Simulations moléculaires et leur analyse*, G.R. Kneller, J. Phys. IV **130**, 155 (2005).

[315] Understanding Molecular Simulation: From Algorithms to Applications, D. Frenkel and B. Smit, Academic Press, San Diego, 2002.

[316] *Computer "experiments" on classical fluids I. Thermodynamical properties of Lennard-Jones molecules*, L. Verlet, Phys. Rev. **159**, 98 (1967).

[317] *Constant pressure molecular dynamics algorithms*, G.J. Martyna, D.J. Tobias, and M.L. Klein, J. Chem. Phys. **101**, 4177 (1994).

[318] *Isothermal-isobaric computer simulations of melting and crystallization of a Lennard-Jones system.*, S. Nosé and F. Yonezawa, J. Chem. Phys. **84**, 1803 (1986).

[319] *Constant-pressure equations of motion*, W.G. Hoover, Phys. Rev. A **34**, 2499 (1986).

[320] *Molecular dynamics simulations at constant pressure and/or temperature*, H.C. Andersen, J. Chem. Phys. **72**, 2384 (1980).

[321] *A unified formulation of the constant temperature molecular dynamics methods*, S. Nosé, J. Chem. Phys. **81**, 511 (1984).

[322] *A molecular dynamics method for simulations in the canonical ensemble*, S. Nosé, Mol. Phys. **52**, 255 (1984).

[323] *Canonical dynamics: equilibrium phase-space distributions*, W.G. Hoover, Phys. Rev. A **31**, 1695 (1985).

[324] *An extension of the canonical ensemble molecular dynamics method*, S. Nosé, Mol. Phys. **57**, 187 (1986).

[325] *Constant-temperature molecular dynamics*, S. Nosé, J. Phys. Condens. Matter **2**, SA115 (1990).

[326] *Collective motions in liquids with a normal mode approach*, T.-M.W. Wu and R.F. Loring, J. Chem. Phys. **99**, 8936 (1993).

[327] *Computer simulation of the lattice dynamics of solids*, J.M. Dickey and A. Paskin, Phys. Rev. **188**, 1407 (1969).

[328] *Computing memory functions from molecular dynamics simulations*, G.R. Kneller and K. Hinsen, J. Chem. Phys. **24**, 11096 (2001).

[329] *Density of states and the velocity autocorrelation function derived from quench studies*, G.S. Grest, S.R. Nagel, A. Rahman, and T.A. Witten Jr., J. Chem. Phys. **74**, 3532 (1981).

[330] *Free energy and vibrational entropy difference between ordered and disordered Ni_3Al*, R. Ravelo, J. Aguilar, M. Baskes, J.E. Angelo, B. Fultz, and B.L. Holian, Phys. Rev. B **57**, 862 (1998).

[331] *Studies of non linear problems*, E. Fermi, J. Pasta, and S. Ulam, Document LA-1940, (1955).

[332] *GULP - a computer program for the symmetry adapted simulation of solids*, J.D. Gale, JCS Faraday Trans. **93**, 629 (1997).

[333] *GULP: capabilities and prospects*, J.D. Gale, Z. Kristallogr. **220**, 552 (2005).

[334] *Empirical potential derivation for ionic materials*, J.D. Gale, Phil. Mag. B **73**, 3, (1996).

[335] *The General Utility Lattice Program (GULP)*, J.D. Gale and A.L. Rohl, Mol. Simul. **29**, 291 (2003).

[336] *nMoldyn, a program package for the calculation and analysis of neutron scattering spectra from MD simulations*, G.R. Kneller, V. Keiner, M. Kneller, and M. Schiller, Comp. Phys. Comm. **91**, 191 (1995).

[337] *nMoldyn : a program package for a neutron scattering oriented analysis of molecular dynamics simulations*, T. Róg, K. Murzyn, K. Hinsen, and G.R. Kneller, J. Comp. Chem. **24**, 657 (2003).

[338] *Tight-binding potentials for transition metals and alloys*, F. Cleri and V. Rosato, Phys. Rev. B **48**, 22 (1993).

[339] Single Crystal Elastic Constants and Calculated Aggregated Properties, G. Simmons and H. Wang, MIT Press, Cambridge, 1971.

[340] *Compression of Ag and phase-transformation of NaCl*, L. Liu, W.A. Bassett, J. Appl. Phys. **44**, 1475 (1975).

[341] *Absolute prazisionsbestimmung von gitterkonstanten an germanium- und aluminium-einkristallen mit elektroneninterferenzen*, W. Witt, Z. Naturforsch. A **22**, 92 (1967).

[342] *Lattice spacings of gold-palladium alloys*, A. Maeland and T.B. Flanagan, Can. J. Phys. **42**, 2364 (1964).

[343] *Lattice parameters, densities, expansion coefficients and perfection of structure of Cu and of Cu-In α phase*, M.E. Straumanis and L.S. Yu, Acta Cryst. A **25**, 676 (1969).

[344] *Determination of thermal expansion of germanium, rhodium and iridium by x-rays*, H.P. Singh, Acta Cryst. A **24**, 469 (1968).

[345] *Lattice parameters of binary nickel cobalt alloys*, A. Taylor, J. Inst. Metals **77**, 585 (1950).

[346] *A redetermination of the lattice constant of lead*, H.P. Klug, J. Am. Chem. Soc. **68**, 1493 (1946).

[347] *Effect of temperature on lattice parameters of some silver-palladium alloys*, C.N. Rao and K.K. Rao, Can. J. Phys. **42**, 1336 (1964).

[348] *High-temperature thermal expansion of Pt, Ta, Mo and W measured by x-ray diffraction*, Y. Waseda, K. Hirata, and M. Ohtani, High Temp. High Press. **7**, 221 (1975).

[349] *A neutron measurement of the effect of a magnetic field on phonon lifetimes in niobium*, R. Pynn and J.D. Axe, J. Phys. F: Metal Phys. **4**, 1898 (1974).

[350] *Neutron-scattering study of phonon linewidths in Pd*, R. Youngblood, Y. Noda, and G. Shirane, Phys. Rev. B **19**, 6016 (1979).

[351] *Temperature dependence of the Raman spectrum in lithium oxide single crystal*, Y. Ishii, T. Nagasaki, H. Watanabe, and H. Ohno, J. Am. Ceram. Soc. **74**, 2324 (1991).

[352] *Temperature dependence of Raman scattering in ZnO*, R. Cuscó, E. Alarcón-Lladó, J. Ibáñez, L. Artús, J. Jiménez, B. Wang, and M.J. Callahan, Phys. Rev. B **75**, 165202 (2007).

[353] *Anharmonic interactions in beryllium oxide*, G. Morell, W. Pérez, E. Ching-Prado, and R.S. Katiyar, Phys. Rev. B **53**, 5388 (1996).

[354] *Raman study on anharmonicity of hafnia*, C. Li, M. McKerns, and B. Fultz — in preparation.

[355] *A universal equation of state for solids*, P. Vine, J. Ferrante, J.R. Smith, and J.H. Rose, J. Phys. C: Solid State Phys. **19**, L467 (1986).

[356] *Nuclear equation of state from scaling relations for solids*J.H. Rose, J.P. Vary, and J.R. Smith, Phys. Rev. Lett. **53**, 344 (1984).

[357] *Scaling relations in the equation of state, thermal expansion, and melting of metals*, F. Guinea, J.H. Rose, J.R. Smith, and J. Ferrante, Appl. Phys. Lett. **44**, 53 (1984).

[358] *Temperature effects on the universal equation of state of solids*, P. Vinet, J.R. Smith, J. Ferrante, J.H. Rose, Phys. Rev. B **35**, 1945 (1987).

[359] *Universal binding energy curves for metals and bimetallic interfaces*, J.H. Rose, J. Ferrante, and J.R. Smith, Phys. Rev. Lett. **47**, 675 (1981).

[360] *Universal features of the equation of state of metals*, J.H. Rose, J.R. Smith, F. Guinea, and J. Ferrante, Phys. Rev. B **29**, 2963 (1984).

[361] *Universal features of the equation of state of solids*, P. Vinet, J.H. Rose, J. Ferrante, and J.R. Smith, J. Phys. Condens. Matter **1**, 1941 (1989).

[362] Electronic Structure of Materials, A.P. Sutton, Clarendon Press, Oxford, 1993.

[363] *The calculation of molecular natural frequencies*, F.A. Lindemann, Phys. Z. **11**, 609 (1910).

[364] Data Analysis: A Bayesian Tutorial, D.S. Sivia, Oxford University Press, Oxford, 2006.

[365] *The number of good reflections in a powder pattern*, D.S. Sivia, J. Appl. Crys. **33**, 1295 (2000).

[366] *A Bayesian approach to phase extension*, D.S. Sivia and W.I.F. David, J. Phys. Chem. Solids **62**, 2119 (2001).

[367] *Background estimation using a robust Bayesian analysis*, W.I.F. David and D.S. Sivia, J. Appl. Crys. **34**, 318 (2001).

[368] *Molecular spectroscopy and Bayesian spectral analysis — how many lines are there?*, D.S. Sivia and C.J. Carlile, J. Chem. Phys. **96**, 170 (1991).

[369] *The Bayesian approach to reflectivity data*, D.S. Sivia and J.R.P. Webster, Physica B **248**, 327 (1998).

[370] *McStas 1.1: a tool for building neutron Monte Carlo simulations*, K. Lefmann, K. Nielsen, A. Tennant, B. Lake, Physica B **276**, 152 (2000).